

1993

Investigation into the Microstructure, Magnetic Properties and Read/write Performance of Thin-film Media for Perpendicular Recording Computer Disks

PAN, GENHUA

<http://hdl.handle.net/10026.1/2363>

<http://dx.doi.org/10.24382/3655>

University of Plymouth

All content in PEARL is protected by copyright law. Author manuscripts are made available in accordance with publisher policies. Please cite only the published version using the details provided on the item record or document. In the absence of an open licence (e.g. Creative Commons), permissions for further reuse of content should be sought from the publisher or author.

**Investigation into the Microstructure, Magnetic
Properties and Read/write Performance of
Thin-film Media for Perpendicular Recording
Computer Disks**

by

GENHUA PAN

A thesis submitted to the University of Plymouth
in partial fulfilment for the degree of
DOCTOR OF PHILOSOPHY

School of Electronic, Communication and Electrical Engineering
Faculty of Technology

In collaborating with
Pilkington Group Research
Pilkington PLC, Pilkington Technology Centre

April, 1993

This copy of the thesis has been supplied on condition that anyone who consults it is understood to recognise that its copyright rests with its author and that no quotation from the thesis and no information derived from it may be published without the author's prior written consent.

Copyright ©1993 by Genhua Pan.

INVESTIGATION INTO THE MICROSTRUCTURE, MAGNETIC PROPERTIES AND READ/WRITE PERFORMANCE OF THIN-FILM MEDIA FOR PERPENDICULAR RECORDING COMPUTER DISKS

by Genhua Pan

ABSTRACT Pronounced effect of underlayers on the squareness and slope T of the perpendicular loops of very thin CoCr films was observed. Experimental and theoretical studies suggest that, depending on the film microstructure, there are two origins on the anomalous shearing of perpendicular loops of Co-based perpendicular films: the columnar shape anisotropy and the wall-motion-like magnetization reversal process. For films with larger intercolumnar separation, the contribution of the columnar shape anisotropy to the total demagnetizing factor is mainly responsible for the deshearing of the loops. For continuous perpendicular films, the intergranular exchange coupling controls the magnetization reversal process and the wall-motion-like reversal explains the anomalous shearing of the hysteresis loop. The square and desheared perpendicular loops of very thin CoCr films originated from their strong perpendicular anisotropy and large intergranular nonmagnetic separation.

Study of the orientation relationship between the Co-based films and their underlayers suggested that the texture of the very thin CoCr and CoCrTa films is determined by the thermodynamic nature of hcp Co crystal itself and the nature of the underlayers or substrates on which it grows. Amorphous underlayers provide "neutral" substrate surfaces for the [0002] self-oriented growth of hcp Co-based films. Hcp Ti and [111] textural fcc Pt, Au underlayers favour the [0002] oriented epitaxial growth. [100] or [110] textural bcc Cr underlayers favour the [10 $\bar{1}$ 0] oriented growth.

The perpendicular coercivity of a Co-based medium is determined by its crystalline anisotropy and intergranular exchange coupling, and can be largely affected by the morphology of its underlayers. The larger perpendicular coercivity of the CoCrTa films on Ti underlayers was mainly due to the large grain diameter which results in a reduction in the intergranular exchange coupling constant. The difference between the surface and bulk coercivity of the CoCrTa films on Ti underlayers was attributed to the improvement of the crystallographic orientation of the hcp Co crystals and the development of large grains as the film grows thicker, which causes the reduction in the surface intergranular exchange coupling due to large grains as well as large intergranular separation.

Co₈₄Nb₁₂Fe₄ amorphous films were investigated as back-layers for double layer media. Very low coercivity down to 0.0125 Oe was achieved for films of 10000 Å-thick with a saturation magnetic induction of 11 kG. The thickness dependence of coercivity follows the Néel formula for films thicker than 400 Å.

A D_{50} density of 160 KFRPI was achieved for the 2000 Å-thick medium on Pt underlayers using MIG heads of gap length 0.15 μm. Experimental and theoretical analyses of the read/write processes show both the achieved D_{50} density and the reproduced output level for these media were head field and head-medium spacing limited. Lower medium noise and higher SNR were achieved by the media with Ti underlayers, which supports the intergranular exchange coupling noise theory.

Contents

Abstract	ii
Contents	iii
List of Figures	v
List of tables	viii
Acknowledgement	ix
Declaration	x
Introduction	1
1 Background to the investigation	4
1.1 Principles of magnetics	4
1.1.1 Magnetic field parameters	4
1.1.2 Hysteresis properties	6
1.1.3 Energy terms in ferromagnet	10
1.1.4 Magnetization reversal in thin films	16
1.2 Principles of magnetic recording	21
1.2.1 The fundamental processes and modes of magnetic recording	21
1.2.2 Writing field of magnetic heads	23
1.2.3 Theory of write process	26
1.2.4 Theory of read process	30
1.2.5 Medium noise	35
1.3 Thin film growth models	38
1.3.1 Nucleation and growth of thin films	38
1.3.2 Microstructure zone model	41
2 Experimental techniques	44
2.1 Thin film deposition by sputtering	44
2.2 Magnetic measurements	47
2.2.1 Vibration Sample Magnetometer	47
2.2.2 Magneto-optic Kerr effect loop plotter	48
2.2.3 Torque magnetometer	49

2.3	Microstructure and texture examinations	51
2.3.1	Miller-Bravais indices	51
2.3.2	X-ray diffraction	53
2.3.3	Electron diffraction and transmission electron microscopy	56
2.3.4	Scanning electron microscope	60
2.4	Domain observation by Lorentz microscopy	61
2.5	Film composition analysis	64
2.6	Differential thermal analysis	65
3	Results and discussion	67
3.1	Underlayer effect on Co-based media	67
3.1.1	Dependence of MOKE loops on CoCr thickness	68
3.1.2	X-ray diffraction study of Ti/CoCr films	72
3.1.3	Effect of Ti underlayer thickness	74
3.1.4	Very thin CoCr film on different underlayers	80
3.1.5	X-ray diffraction study of Au/CoCr films	82
3.1.6	Electron diffraction study of film texture	84
3.1.7	Crystallographic microstructure examination by TEM	93
3.1.8	AES depth profiling of very thin CoCr films	93
3.1.9	Magnetic domains of very thin CoCr films	97
3.1.10	Physical morphology examination of CoCr films by HRSEM	101
3.1.11	CoCrTa films on Pt, Au and Ti underlayers	102
3.1.12	Correlation of magnetic properties with microstructure	110
3.1.13	The shearing of perpendicular loops	114
3.1.14	Origin of underlayer effect on orientation	120
3.2	CoNbFe soft magnetic backlayer	125
3.2.1	Magnetic properties of CoNbFe films	126
3.2.2	Thermal stability	134
3.2.3	Summary	135
3.3	Read/write using MIG heads	136
3.3.1	Experimental measurement of bit density response	138
3.3.2	Analysis of the recording and reproducing process	144
3.3.3	Medium noise measurement	152
3.3.4	Summary	154
4	Conclusions and future work	155
4.1	Conclusions	155
4.2	Future work	158
	Bibliography	
A	Publications	165

List of Figures

1.1	Hysteresis loop showing magnetic parameters.	7
1.2	Schematic illustration for the measurement of $M_r(H)$ and $M_d(H)$ curves.	9
1.3	Calculated coercivity of perpendicular anisotropy thin films with S-W particles (solid curve), single S-W particle (dotted curve) and single curling particle (dashed curve). (after Zhu and Bertram)	17
1.4	Simulated hysteresis loops for films with different interparticle exchange coupling strength. (after Zhu and Bertram)	19
1.5	Schematic drawing of the fundamental magnetic recording processes.	21
1.6	Schematic drawing of head-medium configurations of perpendicular recording.	22
1.7	Longitudinal and perpendicular components of a Karlquist head field.	24
1.8	The arctangent transition model.	27
1.9	Schematic illustration for demagnetizing field distribution along the longitudinal step-like transition(a) and perpendicular step-like transition(b).	29
1.10	Isolated waveforms reproduced by ring head from: (a) longitudinal transition, (b) perpendicular transition and (c) in-between.	32
1.11	Typical frequency response curves for square-wave recording in terms of (a) peak-to-peak amplitude for symmetrical single-pulse waveforms, (b) peak-to-peak amplitude for antisymmetrical di-pulse waveforms, and (c) rms or fundamental frequency component.	33
1.12	Schematic drawing of three different modes of growth: (a) Layer growth, (b) Stranski-Krastanov growth, (c) island growth. after Reichelt	40
1.13	Microstructure zone model proposed by Thornton	41
2.1	Schematic drawing of sputtering apparatus of planar diode type.	45
2.2	Schematic drawing of a vibrating sample magnetometer	48
2.3	Schematic diagram of the polar Kerr loop plotter. (after Mahvan)	49
2.4	Schematic diagram of the directions of H and M_s and their angles respect to the film normal for a torque measurement.	50
2.5	The arrangement of the axes for the hexagonal system in this work (a), and the schematic drawing of the low index planes and directions in hcp(b).	52
2.6	Schematic diagram of x-ray diffractometer	54
2.7	JEOL 2000FX Transmission Electron Microscope.	57
2.8	Simplified schematic diagram of an electron diffraction camera.	58
2.9	Various emissions are produced when a high energy electron beam bombards the surface of a specimen.	60

2.10	Schematic drawing of the formation of Fresnel contrast of a magnetic thin film with 180° domain walls. (after Chapman)	62
2.11	Schematic drawing of formation of Foucault contrast through displacement of the objective aperture. (after Chapman)	63
2.12	Schematic diagram showing how the interaction of x-ray with an atom produces photo-electrons, Auger electrons and fluorescent x-ray emissions.	65
2.13	Schematic drawing of the DTA apparatus.	66
3.1	Perpendicular M-H loops of different thickness CoCr films with and without Ti underlayers.	69
3.2	Measured hysteresis loop slope T of CoCr films as a function of film thickness.	70
3.3	Perpendicular remanence ratio of CoCr films as a function of film thickness.	71
3.4	X-ray diffraction patterns of 160 Å-thick CoCr films with and without Ti underlayers.	73
3.5	Effect of Ti underlayer thickness on perpendicular MOKE loops of 160 Å-thick CoCr films.	75
3.6	Effect of Ti underlayer thickness on perpendicular magnetic properties and (0002) intensity of 160 Å-thick CoCr films.	76
3.7	M-H loops of 160 Å-thick CoCr films with and without Ti underlayers measured by VSM.	77
3.8	Torque curves of 160 Å-thick CoCr films with and without Ti underlayers.	78
3.9	Perpendicular MOKE loops of 80 Å-thick CoCr films deposited on different underlayers, y-axis is arbitrary unit, but in the same scale.	81
3.10	X-ray diffraction pattern of Au/CoCr(80Å) films.	82
3.11	Schematic representation of hcp (0002) and fcc (111) lattice planes and the lattice misfit calculation.	83
3.12	Schematic drawings of SAD patterns for hcp and bcc films with texture of (a) [0002], (b) [11 $\bar{2}$ 0], (c) [10 $\bar{1}$ 0], and (d) [110].	85
3.13	SAD patterns of 160 Å-thick CoCr films deposited on Ti, Cr, Cu and C underlayers.	87
3.14	TEM bright field images of 160 Å-thick CoCr films on (a) Ti, (b) Cr and (c) C underlayers.	91
3.15	TEM bright field images of Ti and Cr underlayers.	92
3.16	AES depth profiling of very thin CoCr films on (a) Ti and (b) Au underlayers.	94
3.17	Fresnel images of the 160Å CoCr films on (a) Ti, (b) Cr and (c) C underlayers, at demagnetized state with specimen untilted and 20° tilted.	96
3.18	HRSEM micrographs of fractured cross sections of CoCr (2400 Å) on (a) Ti underlayer, and (b) glass.	98
3.19	HRSEM micrographs of top surface of CoCr(2400 Å) on (a) Ti underlayer, and (b) glass.	99
3.20	HRSEM micrographs of top surface of CoCr(160 Å) on (a) Ti underlayer, and (b) glass.	100
3.21	X-ray diffraction patterns of CoCrTa films on Pt (a) and Ti (b) underlayers.	103
3.22	HRSEM micrographs of top surfaces of 2000 Å-thick CoCrTa films on Ti (a) and Pt (b) underlayers.	106
3.23	Thickness dependence of perpendicular coercivity of CoCrTa films on Pt and Ti underlayers measured by MOKE and VSM.	108

3.24	Typical VSM perpendicular (solid curves) and in-plane hysteresis loops (dashed curves) of CoCrTa films (2000Å) on (a) Ti and (b) Pt underlayers.	109
3.25	Hysteresis loop slope T of CoCr films as a function of film thickness, dotted curves are calculated by particulate model.	117
3.26	Thickness dependence of coercivity H_c and anisotropy field H_k of amorphous CoNbFe films.	127
3.27	Substrate bias effect on H_c and H_k of 4600 Å-thick CoNbFe films.	129
3.28	Sputtering power dependence of H_c and H_k of CoNbFe films(8500Å), also shown the deposition rate and final substrate temperature.	130
3.29	DTA curves for CoNbFe films at heating rate of 5 and 10 °C/min respectively.	132
3.30	Annealing temperature dependence of H_c and H_k of CoNbFe films.	133
3.31	Readback voltage versus write current for the disks with 2000 Å-thick CoCrTa media on Pt and Ti underlayers. MIG head gap length is 0.15μm.	137
3.32	Bit density response(fundamentals) of different thickness of CoCrTa media on Pt underlayers measured by narrow gap MIG head.	139
3.33	Bit density response(fundamentals) of different thickness CoCrTa media on Ti underlayers measured by narrow gap MIG head.	140
3.34	Bit density response(peak-to-peak) of different thickness CoCrTa media on Pt and on Ti underlayers measured by wide gap MIG head.	142
3.35	Typical isolated waveforms measured for disk D1 and D2 at 0.25 MHz by MIG head with gap length of 0.15μm and 0.30μm respectively.	143
3.36	The recorded perpendicular magnetization amplitude as a function of the bit density calculated for disks D1, D2, D3 and D4.	149
3.37	Comparison of calculated and measured bit density response curves.	150
3.38	Schematic illustration of the increase of head-medium spacing by a small tilting of the MIG head along the track-width direction (a) or along the medium moving direction (b).	151

List of Tables

2.1	<i>d</i> spacing and 2θ values for lattice planes of hcp Co, hcp Ti, fcc Pt and fcc Au for x-ray diffraction using C_uK_α radiation.	55
3.1	Thickness dependence of (0002) reflection peak intensity of CoCr films with and without Ti underlayers.	74
3.2	Summary of SAD patterns C/Ti(300Å)/CoCr(160Å) films with specimen untilted and tilted.	88
3.3	Summary of SAD patterns C/Cr(300Å)/CoCr(160Å) films with specimen untilted and tilted.	88
3.4	Summary of SAD patterns C/Cu(300Å)/CoCr(160Å) films with specimen untilted and tilted.	89
3.5	Summary of SAD patterns C/CoCr(160Å) films with specimen untilted and tilted.	89
3.6	$\Delta\theta_{50}$ of different thickness CoCrTa on Pt, Au and Ti underlayers.	105
3.7	Summary of the properties of six single-layer disks	136
3.8	Maximum writeable coercivity by MIG heads with gap length of 0.15 and 0.30 μm for media of different thickness.	145
3.9	Results of medium noise measurement for disks D1, D2, D3 and D4.	153

Acknowledgement

I would like to express my gratitude to all those people and organisations who have been associated with this project, in particular,

My supervisors Professor D.J. Mapps (Director of Studies) and Dr. M.A. Akhter of the school of Electronic, Communication and Electrical Engineering, for their constant support, encouragement and guidance throughout the project.

Professor J.N. Chapman and the electron microscopy group of Department of Physics and Astronomy, The University of Glasgow for their collaboration in the TEM study.

Professor J.C. Lodder and Mr. P. ten Berge of MESA, Twente University, The Netherlands, for their collaboration in the magnetic measurement.

Dr. J. Bradshaw of Pilkington Group Research for his help in the SEM observation and AES depth profiling.

Dr. K. Hayashi and the magnetic materials research group for the three-month training in SONY Corporation Research Centre, Yokohama, Japan.

Mr. S. Onodera, and Mr. N. Honda of SONY Corporation Sendai Technology Centre, and Mr. N. Darragh of CRIST, for their collaboration in the recording measurement.

Mr. B. Lakey and the EM Unit of the University of Plymouth for training the use of equipment and for their technical assistance.

All the staff within the CRIST for their support and friendship.

The Science and Engineering Research Council and Pilkington Group Research, Pilkington PLC, for their financial support.

I would also like to thank my wife Jianhua, son Qi and my parents for their love and support.

Declaration

At no time during the registration for the degree of Doctor of Philosophy has the author been registered for any other University award.

This study was financed with the aid of a research fund from the Science and Engineering Research Council, and carried out in collaboration with the Pilkington Group Research, Pilkington plc, Pilkington Technology Centre.

A programme of advanced study was undertaken, which included the extensive reading of literature relevant to the research project, an advanced course on applied magnetism and magnetic recording, supervised trainings in transmission electron microscopy, electron diffraction and Lorentz microscopy, a three-month industry training in SONY Corporation Research Centre, Yokohama, Japan, and attendance of international conferences and seminars on magnetics and magnetic recording.

Some of the work contained in this thesis has been presented at several international conferences and published in the relevant journals. Copies of published papers are included in appendix A of this thesis.

Presentations and conferences attended:

The Intermag'90 in Brighton, UK; the 35th MMM conference in San Diego, USA; the 5th Joint MMM-Intermag conference in Pittsburgh, USA; the 13th ICMFS in Glasgow, UK; the PMRC'91 in Iwate, Japan; the 15th Conference on magnetism in Japan; the MRM'92 in Perugia, Italy; and the INTERMAG'93 in Stockholm, Sweden.

External contacts:

Twente University, the Netherlands; Glasgow University; Pilkington Group Research; SONY Corporation Research Centre, Yokohama, Japan and SONY corporation Sendai Technology Centre, Sendai, Japan.

Genhua Pan



Date 15-4-1993

To My Motherland

Introduction

The magnetic recording technology has been developing very fast towards the higher density, larger capacity, higher data access rate, smaller volume and lower costs. The introduction of thin film technology for the fabrication of thin-film media and heads in the recent years made the increase of the areal density into the 1 gigabit/in² regime possible [1, 2, 3] by the conventional longitudinal magnetic recording technology. However, in the longitudinal recording the minimum recording transition length (l_{min}) of a recording medium is always limited by the self-demagnetization in the recording transition and a self-demagnetization dominated minimum transition length [5] is given by,

$$l_{min} = \frac{2\pi M_r \delta}{H_c}, \quad (0.1)$$

where M_r is the remanent magnetization, δ is the film thickness and H_c is the coercivity of the recording medium. In order to achieve high density (small l_{min}), a recording medium must have small thickness (δ), low remanent magnetization (M_r) and high coercivity (H_c). But, the small δ and low M_r will lead to a small playback signal and therefore degrade the signal-to-noise performance against head and electronics noise. This is shown by equation 0.2 [4].

$$V_{peak} = \frac{4N\eta W v \delta M_r}{\pi g} \tan^{-1} \left[\frac{g}{2(d+a)} \right], \quad (0.2)$$

where N is the number of turns of the reproducing head, η is the head efficiency, W is the track width, v is the head-to-media velocity, g is the head gap, d is the head-medium spacing and a is the transition parameter.

In the gigabit/in² longitudinal recording system, a desired signal-to-noise ratio was achieved by the use of high H_c media with thick(1000Å) Cr underlayers [1, 6, 7]. The typical values of the medium parameters are as follows [1, 2]:

$$\delta = 230 \text{ \AA}, H_c = 1.1 \sim 2.0 \text{ kOe and } M_r \delta = 0.7 \times 10^{-3} \text{ emu/cm}^2.$$

A further increase in the recording density means a further reduction of the film thickness and remanent magnetization or a further increase of the coercivity of the recording media. The further smaller thickness and remanent magnetization will certainly cause degrading of the signal-to-noise ratio. Additionally, there would be concerns about the integrity of a film if the thickness is further reduced [5]. The increase of the coercivity of the recording media is limited by the saturation magnetization of the head materials. All these limit the further breakthrough of the recording density in the conventional longitudinal recording technology.

Following the historic paper given by Iwasaki and Nakamura on circular mode magnetization [8], numerous researchers have been involved in a new recording technology, perpendicular recording. One of the major advantages of such a recording mode over the conventional longitudinal recording is that the demagnetizing field at the recording transition is zero [9], which is essentially suitable for high density recording. The ultimate areal density of perpendicular recording, as predicted by Y. Nakamura recently [17], would be 1 Gbits/mm².

The project was proposed to meet such a technical challenge. The aim of this work was to develop desired perpendicular recording media for very high density

perpendicular recording computer disks, and to make a comprehensive understanding of the correlation of film microstructure, magnetic properties and recording performance.

Following the introduction, chapter 1 covers the fundamental theories of magnetism, magnetic recording and thin film growth process, which are important to this work.

Chapter 2 gives the experimental techniques for thin film deposition, magnetic measurement, microstructural examination, magnetic domain observation, film composition analysis and thermal stability analysis.

Chapter 3 presents the detailed results and discussions of this investigation. It contains three major parts:

(1) the effect of underlayers on the magnetic properties, microstructure and crystallographic orientation of Co-based perpendicular media. The following major issues were investigated in this part: the origin of underlayer effect on orientation, the anomalous shearing of perpendicular loops, the square perpendicular loops, the perpendicular coercivity and the difference of surface and bulk coercivity.

(2) study of amorphous CoNbFe soft magnetic backlayer for double-layered disks;

(3) experimental and theoretical analysis of the read/write process, bit density response and medium noise of single-layer media and their correlation with the film microstructure and magnetic properties.

The final chapter draws conclusions based on the results of the project and presents proposals for the possible future work of the perpendicular recording media.

The cgs-emu system of units is used in this thesis.

Chapter 1

Background to the investigation

1.1 Principles of magnetics

1.1.1 Magnetic field parameters

The magnetization M

Magnetization is a property which arises from the motion of electrons within atoms. Depending on its electronic structure, an atom may or may not have an atomic magnetic moment. The spontaneous magnetization in magnetic materials, according to Weiss's molecular field theory [19] and Heisenberg [18] quantum mechanical exchange theory, originates from the exchange interaction between the spin electrons of the neighbouring atoms, which produces an internal quantum mechanical force by which the individual atomic moments are aligned into a parallel or anti-parallel state, known as magnetic ordering.

Magnetic materials can be classified as ferromagnet, anti-ferromagnet and ferrimagnet according to their magnetic ordering. For thin-film magnetic recording media, we are mainly concerned with ferromagnet in which the neighbour atomic

moments everywhere within a magnetic domain have a parallel magnetic ordering.

The magnetization vector \mathbf{M} of magnetic material is defined as the vector sum of the atomic moments per unit volume:

$$\mathbf{M} = \frac{1}{V} \sum_{i=1}^N \boldsymbol{\mu}_i, \quad (1.1)$$

where V is the volume of the magnetic material, $\boldsymbol{\mu}$ is the atomic magnetic moment, N is the number of atomic moments in volume V . The unit of \mathbf{M} in the cgs-emu unit system is emu/cm³.

In a large applied field, the magnetization at all parts of a ferromagnet is parallel. In the absence of magnetic field, only the magnetization within a domain is parallel and uniform and a ferromagnetic specimen as a whole may exhibit no magnetization because of the random orientation of the domain magnetization. The value of magnetization of a single domain is called the spontaneous magnetization, or the saturation magnetization, M_s .

Saturation magnetization M_s of a magnetic material depends on the temperature, being a maximum at absolute zero and vanishing at a critical temperature T_c , called Curie temperature.

Magnetic field intensity \mathbf{H}

The magnetic field intensity vector \mathbf{H} is defined as the force the magnetic pole exerts on a unit positive pole [20]. There are two contributing sources of magnetic field: electric current I and magnetic poles or magnetic charges ρ .

The magnetic field produced by electric current I passing through a conductor l obeys Ampère's law:

$$\oint \mathbf{H} \cdot d\mathbf{l} = I. \quad (1.2)$$

The magnetic field produced by magnetic poles is given by [21],

$$\mathbf{H} = \int_V \frac{\rho \mathbf{r}}{|\mathbf{r}|^3} dV, \quad (1.3)$$

where \mathbf{r} is a position unit vector, V is the volume of the magnetic material and ρ is the magnetic pole density which is defined as the divergence of magnetization \mathbf{M} ,

$$\rho = \nabla \cdot \mathbf{M}. \quad (1.4)$$

Equations 1.4 and 1.3 are very useful in the computation of demagnetizing field of recording transition, medium noise and head field distribution.

Magnetic induction \mathbf{B}

The magnetic flux density or magnetic induction vector \mathbf{B} is defined as,

$$\mathbf{B} = \mathbf{H} + 4\pi\mathbf{M}, \quad (1.5)$$

where the unit of \mathbf{B} is gauss(G); \mathbf{H} , oersteds(Oe); and \mathbf{M} , emu/cm³; or $4\pi\mathbf{M}$, gauss in the cgs-emu unit system. The forms of equation correlating these parameters differ in different system of units.

1.1.2 Hysteresis properties

If a magnetic specimen is cycled by an alternating magnetic field sufficiently strong to saturate the specimen, we get a major hysteresis loop as shown in figure 1.1. The magnetic recording performance of a medium is closely related to the shape of the loop and various magnetic parameters of interest in magnetic recording, such as coercivity H_c , remanence coercivity H_{cr} , remanent magnetization M_r , saturation magnetization M_s , and remanence squareness S , are defined at various points of a loop, as also shown in figure 1.1.

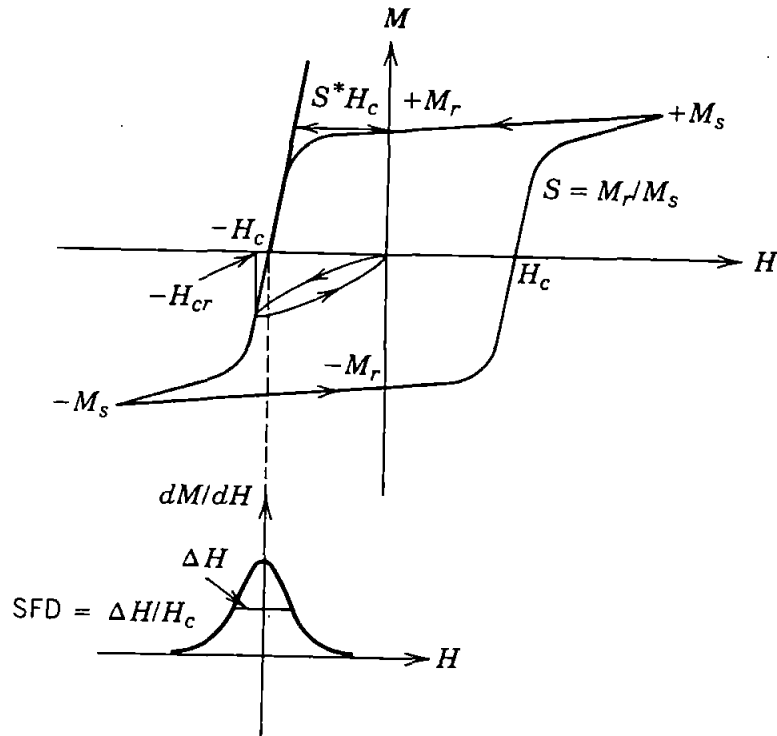


Figure 1.1: Hysteresis loop showing magnetic parameters.

For digital magnetic recording media, an open and rectangular loop is always desirable in order to get a sharp switching between the two discrete magnetization states. Such properties are frequently described in terms of remanence squareness (S), switching field distribution (SFD) and coercivity squareness S^* . The SFD measures the narrowness of the range over which the domain magnetization reverses or switches as a function of applied field H . It is defined as the half-amplitude width, ΔH_{50} , when normalised by H_c , of the derivative dM/dH of a hysteresis loop centred about H_c and is given by: [21]

$$SFD = \frac{\Delta H_{50}}{H_c}, \quad (1.6)$$

or alternatively by:

$$SFD = \frac{H_{-M_r/2} - H_{M_r/2}}{H_c}. \quad (1.7)$$

The S^* is another commonly used term to characterize the distribution of switching field and is defined for a hysteresis loop such that at $H = -H_c$,

$$\frac{dM}{dH} = \frac{Mr}{(1 - S^*)H_c}. \quad (1.8)$$

A value of S^* close to unity is desirable for a sharp switching. However, it had been reported that a high S^* medium exhibits strong intergranular exchange coupling and high medium noise [6].

Apart from the above hysteresis properties defined by the major loop, the remanence curves are recently being used to characterize the intergranular interaction of the longitudinal recording media [25, 23, 24, 26]. As shown in figure 1.2(a), when a positive field H_1 is applied to an initially ac demagnetized ferromagnet and then removed, we get a remanence value of $M_r(H_1)$. For a larger field H_i we get $M_r(H_i)$. If the process is progressively repeated until the saturation is reached, we can plot a curve of M_r as a function of applied field H . Such a curve is called isothermal remanent magnetization curve, or $M_r(H)$ curve.

Similarly, we get a dc demagnetization remanent magnetization curve $M_d(H)$, as shown in figure 1.2(b), by reversing a field to $-H_i$ from the positive dc saturation state, with the remanent magnetization $M_d(H_i)$ recorded as a function of reversing field until negative saturation has been reached.

The $M_r(H)$ and $M_d(H)$ curves can be used to characterize the nature of interparticle or intergranular interactions for recording media [23, 24, 25, 26]. According to Wohlfarth [27], the $M_r(H)$ curve of a single domain particle or noninteraction particles obeys the following relation with its corresponding $M_d(H)$ curve,

$$M_d(H) = 1 - 2M_r(H). \quad (1.9)$$

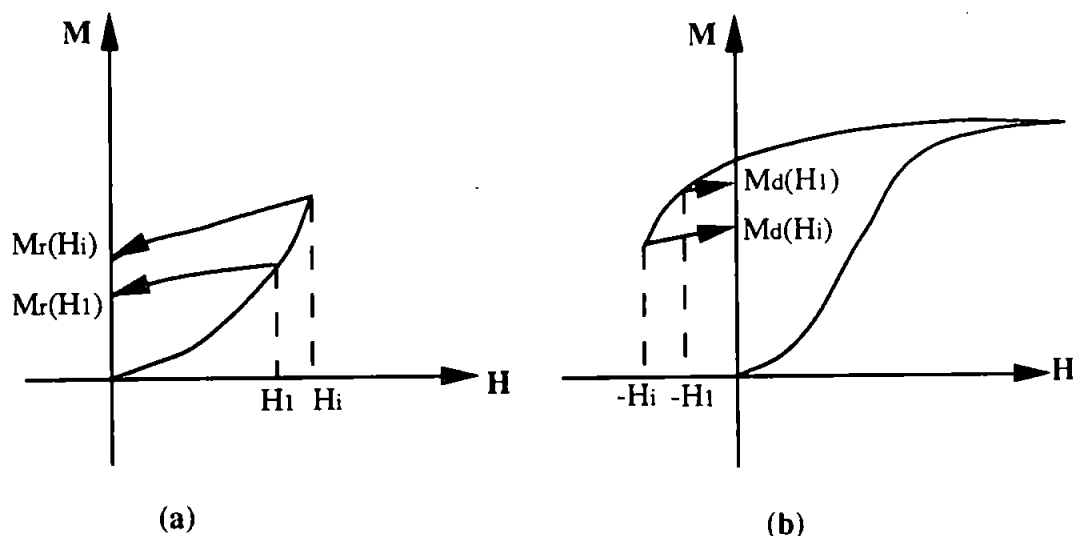


Figure 1.2: Schematic illustration for the measurement of $M_r(H)$ and $M_d(H)$ curves.

Henkel [28] investigated the nature of particle interactions by plotting $M_d(H)$ versus $M_r(H)$ and suggested that the particle interactions could be characterized by a parameter ΔM , which is the deviation from the the Wohlfarth relation and is given by,

$$\Delta M = M_d(H) - (1 - 2M_r(H)). \quad (1.10)$$

Positive values of ΔM are interpreted as a result of stabilizing interactions. Conversely, negative values of ΔM are due to destabilizing interactions [23]. Specifically, a positive value of ΔM indicates the existence of the intergranular exchange interaction and a negative value of ΔM indicates weak or no intergranular exchange interaction, as predicted by Beardsley and Zhu from their computer simulation [26]. However, it is very difficult to apply such a measurement to the perpendicular recording media because of the unpredictable shearing of the perpendicular loops.

1.1.3 Energy terms in ferromagnet

The study of energy interaction in ferromagnets forms the basis of ferromagnetism. The theoretical calculation of domain configuration, magnetization process and magnetization reversal process of ferromagnets and the computer simulation of medium noise of the recording media [6, 22] are of typical samples of such applications.

There exist different kinds of energies in a thin film recording medium, such as exchange energy E_{exc} , magnetocrystalline anisotropy energy E_{cry} , magnetoelastic energy E_{ela} , magnetostatic energy E_{sta} and intergranular interaction energy E_{int} . The total energy E_{tot} in a medium is, therefore, the sum of these various energies as given by,

$$E_{tot} = E_{exc} + E_{cry} + E_{ela} + E_{sta} + E_{int}. \quad (1.11)$$

A stable magnetization distribution of a specimen is a state in which the sum of various energies E_{tot} is minimised. The following discussion outlines the main energy terms of interest in magnetic recording medium.

(a) Exchange energy

The spontaneous magnetization of magnetic materials, as discussed previously, originates from the exchange interaction of the neighbouring electron spin moments. The exchange energy of spin moments of neighbouring atoms is given by:

$$E_{exc} = -2 \sum_{i < j} A_{ij} \mathbf{S}_i \cdot \mathbf{S}_j, \quad (1.12)$$

where \mathbf{S}_i and \mathbf{S}_j are the atomic spin moments of neighbouring atoms and A_{ij} is the exchange integral of neighbouring atoms.

Thin film recording medium is composed of closely packed columns or grains.

The exchange interaction in a film may differ in respect to the position of interest. Within each grain the exchange interaction is normally assumed to be uniform and therefore $A_{ij} = A$, $S_i = S_j = S$, and equation 1.12 can be written by:

$$E_{exc} = -2S^2 A \sum_{i < j} \cos \Phi_{ij}, \quad (1.13)$$

where Φ_{ij} is the angle between the neighbour atomic spin moments.

The exchange interaction between grains, or in the grain boundaries, however, will depend on the intergranular boundary conditions, such as intergranular non-magnetic separation, surface defects, etc.. The intergranular exchange interaction energy will be further discussed later in this section.

(b) Magnetocrystalline anisotropy energy

In single crystal ferromagnets the orientation of atomic moments in every domain are strongly crystallographic directional dependent. In cobalt, for example, which has a hexagonal close packed (hcp) structure, the domain magnetic moments align parallel to the c-axis, or the [0001] axis. It is very much easier to magnetize a single crystal Co to saturation along the [0001] axis or easy axis than along the [10 $\bar{1}$ 0] axis or hard axis. This phenomenon is known as magnetocrystalline anisotropy. The magnetocrystalline anisotropy energy E_{cry} is defined as the energy required to magnetize a single crystal sample to saturation along a specific axis:

$$E_{cry} = \int_0^{M_s} H dM \quad (1.14)$$

In practice, the magnetocrystalline anisotropy energy is measured in terms of anisotropy energy constant K , which is a relative energy required, in ergs/cm³, to rotate the magnetic moment from the easy direction to hard direction. For hcp Co,

it is defined by:

$$K = \frac{1}{V} \left(\int_{0[10\bar{1}0]}^{M_s} H dM - \int_{0[0001]}^{M_s} H dM \right). \quad (1.15)$$

Considering the symmetry of crystals, the uniaxial magnetocrystalline anisotropy energy is expressed mathematically in a series of powers of $\sin\theta$, where θ is the angle between the magnetization vector and the $[0001]$ axis,

$$E_K = K_1 \sin^2\theta + K_2 \sin^4\theta + \dots, \quad (1.16)$$

E_K is the magnetocrystalline anisotropy energy density (ergs/cm³), K_1 , K_2 and \dots , are the anisotropy constants (ergs/cm³). Usually the first term (K_1) is sufficient to express the actual anisotropy energy. For the single hcp Co crystal at room temperature $K_1 = 4.12 \times 10^6$ ergs/cm³.

The perpendicular recording medium is normally a Co-based hcp polycrystalline thin film. The total magnetocrystalline anisotropy constant of the film is a vector sum of that of all the individual hcp crystals. It is therefore very important to have a strong perpendicular *c*-axis orientation of all the crystals in the film in order to get a large perpendicular magnetocrystalline anisotropy constant, or in other words, to have a strong perpendicular anisotropy film.

(c) Magnetoelastic energy

The magnetocrystalline anisotropy energy discussed above is based on perfect single crystal. In reality, ferromagnetic crystals are subject to changes in dimension caused by the spontaneous magnetization or by stress in the specimen, which will in turn cause a change in the magnetocrystalline anisotropy energy in ferromagnets. Anisotropy caused by stress is called stress induced anisotropy. The magnetoelastic

energy E_{ela} is introduced to account for such a change in anisotropy associated with the change in dimension of ferromagnets and, for the simplest case in which the magnetostriction is isotropic, is given by:

$$E_{ela} = -\frac{3}{2}\sigma\lambda_s\cos^2\theta, \quad (1.17)$$

where σ is the stress in the ferromagnet, λ_s is the saturation magnetostriction coefficient, and θ is the angle between the stress σ and the saturation magnetization M_s .

(d) Magnetostatic energy

The magnetostatic energy, which include external field energy E_H and demagnetization energy E_d , is due to the interaction between the ferromagnet and the magnetic field.

(1) External field energy E_H

For a given ferromagnet with magnetization \mathbf{M} in an applied field \mathbf{H} , the external applied field energy is given by:

$$E_H = -\mathbf{M}\cdot\mathbf{H} = -M_s H \cos\theta, \quad (1.18)$$

where θ is the angle between \mathbf{M} and \mathbf{H} . E_H is a minimum when $\theta = 0^\circ$, and maximum when $\theta = 180^\circ$. $E_H = 0$ when applied field $H = 0$. The external applied field energy is sometimes called Zeeman energy.

(2) Demagnetizing energy E_d

When a ferromagnet is magnetized in an external field \mathbf{H} , it generates an internal field opposing the magnetization of the ferromagnet because of the magnetic charges arising from the divergence of the magnetization. This field is called demagnetizing

field \mathbf{H}_d . Using equation 1.3, we have,

$$\mathbf{H}_d(\mathbf{r}) = - \int \frac{\rho \mathbf{r}}{|\mathbf{r}|^3} dV. \quad (1.19)$$

Equation 1.19 is useful in the calculation of demagnetizing field distribution in the recording transition.

If a ferromagnet is uniformly magnetized, the algebraic form of H_d is given by:

$$H_d = -NM, \quad (1.20)$$

where N is the demagnetizing coefficient taking values from 0 to 4π (from 0 to 1 in the standard international unit system, SI unit) depending on the shape and size of the specimen and the direction concerned with. For a thin-film recording medium, the demagnetizing coefficient within the x, y plane is 0, and along the z axis is 4π which causes the shearing of the perpendicular M-H loops.

The demagnetization energy E_d measures the interaction between the ferromagnet and the demagnetizing field \mathbf{H}_d . It, therefore, uses similar expression as for the E_H but in an integrated form because the demagnetizing field H_d is a function of magnetization M . For a ferromagnet with uniform magnetization it is given by :

$$E_d = - \int_0^M H_d dM = \frac{1}{2} NM^2. \quad (1.21)$$

For a perpendicular recording thin film the demagnetizing coefficient normal to the film plane is 4π , we have,

$$E_d = 2\pi M^2. \quad (1.22)$$

The demagnetization energy E_d depends on the shape of the specimen and is called shape anisotropy energy. The demagnetization energy is a key factor, as mentioned in the Introduction, which limits the recording density of longitudinal magnetic recording media [8, 9].

(e) Intergranular interaction energy

One of the major differences between the thin-film recording media and the conventional particulate recording media is that the grains in a thin-film medium are closely packed. This brings about strong interactions between grains in the thin-film media, which have been considered to be a major source of recording transition noise [7, 6, 22]. Such intergranular interactions can be described in terms of intergranular interaction energy E_{int} , which includes intergranular exchange coupling energy $E_{exc}(\mathbf{r}_i)$ and intergranular magnetostatic interaction energy $E_{mag}(\mathbf{r}_i)$.

(1) Intergranular exchange coupling energy $E_{exc}(\mathbf{r}_i)$

The intergranular exchange coupling energy is due to the exchange interaction between the neighbour magnetization of grains, which is a short range order interaction energy and depends strongly on the intergranular separation and the diameter of the grains. For the i th grain in a film, its intergranular exchange energy with its nearest neighbour(n.n.) [22, 49] is given by

$$E_{exc}(\mathbf{r}_i) = -\frac{2A^*}{M^2 D^2} \mathbf{M}_i \cdot \sum_{n.n.} \mathbf{M}_j, \quad (1.23)$$

where \mathbf{r}_i is the position vector, A^* is the effective intergranular exchange energy constant (for a fully exchange coupled films $A^* = A$), M is the mean magnetization of the sample, D is the grain diameter, \mathbf{M}_i and \mathbf{M}_j are the magnetization of the i th and j th grains and the summation is over the nearest-neighbor grains.

(2) Intergranular magnetostatic interaction energy $E_{mag}(\mathbf{r}_i)$

The intergranular magnetostatic interaction energy is due to the magnetostatic interaction between grains in a film. Such an interaction is a function of magnetic pole density ($\rho = -\nabla \cdot \mathbf{M}$). For the i th grain in a film, the magnetostatic interaction

energy is,

$$E_{mag}(\mathbf{r}_i) = \int \int dV_i dV_j \left(\frac{\rho_i \rho_j}{r_i - r_j} \right). \quad (1.24)$$

For a film with a given magnetization, the intergranular magnetostatic interaction energy is a function of $\frac{\delta}{D}$, and $\frac{d}{D}$ [49], where δ is the film thickness, d is the intergranular non-magnetic separation and D is the grain diameter.

1.1.4 Magnetization reversal in thin films

It is important to study the magnetization reversal mechanism in order to understand the physics of magnetic recording process. Extensive experimental [31, 32, 33] and theoretical [22] studies had been undertaken in recent years on this subject.

The magnetization reversal process of the recording media can be classified as domain wall motion and magnetization rotation mechanism. Wall motion reversal process normally happens in a magnetically continuous film, which often gives rise to a small coercivity and is not a desired reversal process for recording media. The rotation reversal process is typical to a single-domain particle or particulate media where no domain wall exists or domain wall motion is prohibited by the non-magnetic separation or grain boundaries. Rotation reversal process often gives rise to high coercivity.

Stoner-Wohlfarth coherent rotation [29] and curling [30] are the two classical rotation magnetization reversal models for an isolated cylindrical particle, of which Stoner-Wohlfarth coherent rotation is the simplest case where only the magneto-crystalline anisotropy energy and external field energy terms were considered. The curling or incoherent rotation model considered other energy terms, such as exchange energy and magneto-static energy. The coercivity of an isolated particle with Stoner-

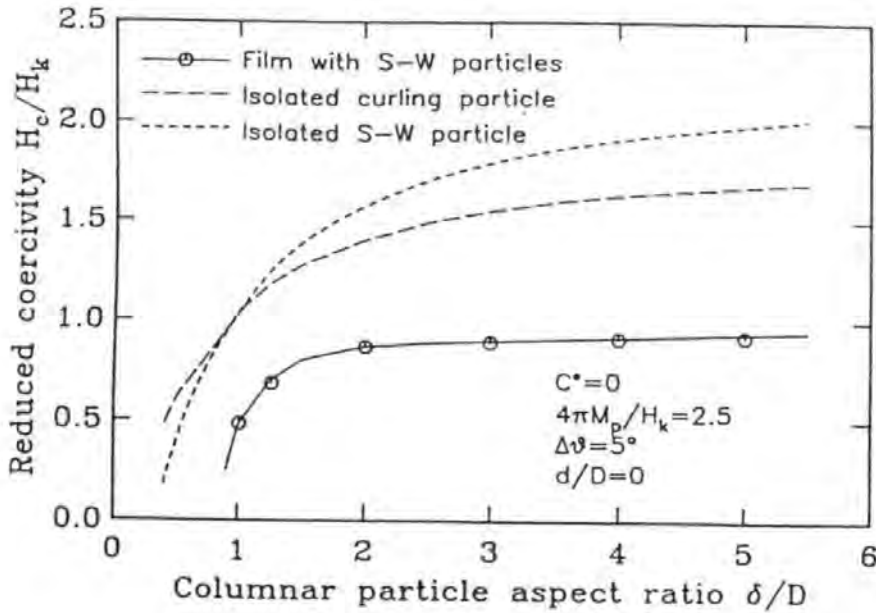


Figure 1.3: Calculated coercivity of perpendicular anisotropy thin films with S-W particles (solid curve), single S-W particle (dotted curve) and single curling particle (dashed curve). (after Zhu and Bertram)

Wohlfarth coherent rotation, which is approximately equal to the nucleation field, is given by,

$$H_c^{s-w} = H_k \left[1 + (N_b - N_a) \frac{M_s}{H_k} \right], \quad (1.25)$$

and the coercivity for curling reversal is

$$H_c^{curl} = H_k \left(1 + \frac{1.08\pi A}{(D/2)^2 K} - \frac{N_a M_s}{H_k} \right), \quad (1.26)$$

where H_k is the crystalline anisotropy field, N_a and N_b are the demagnetizing coefficients along the crystalline easy and hard axes respectively, A is the exchange energy constant, D is the particle diameter and K is the crystalline anisotropy constant.

For thin film recording media, the reversal process is more complicated than an

isolated single domain particle. More energy terms need to be considered, especially, the intergranular exchange coupling energy and the intergranular magneto-static interaction energy.

Numerical micromagnetic computer simulation of the magnetization reversal in perpendicular recording CoCr medium has been presented by Zhu and Bertram [22]. The model used a 2D array of hexagonal columnar particles. Each column is considered to be a single crystal with perpendicular uniaxial crystalline anisotropy. Their results showed that the reversal process in the film without interparticle exchange coupling (film consists of S-W particles) is characterized by coherent magnetization rotation of chain particles followed by incoherent magnetization reversal in the chain. Figure 1.3 shows the calculated coercivity of the perpendicular anisotropy films with S-W particles as a function of the particle aspect ratio δ/D . The coercivities of an isolated particle for uniform rotation and curling are also plotted in the figure. It shows that the coercivity of such a film is approximately equal to the perpendicular crystalline anisotropy and is much less than the coercivity of the isolated Stoner-Wohlfarth particle and the isolated curling particle. They attributed such a reduction in the coercivity to the collective behaviour of the magnetization reversal process in the film. The collective magnetization rotation yields lower nucleation fields.

By considering the intergranular exchange coupling, the reversal process would be different with different intergranular exchange coupling strength. The strength of the intergranular exchange coupling in a medium can be expressed in terms of intergranular exchange coupling constant C^* , or intergranular exchange coupling

field reduced by the crystalline anisotropy field, which is defined as follows [49],

$$C^* = \frac{A^*}{KD^2}, \quad (1.27)$$

where A^* is the effective intergranular exchange coupling energy constant, K is the crystalline anisotropy constant and D is the grain diameter.

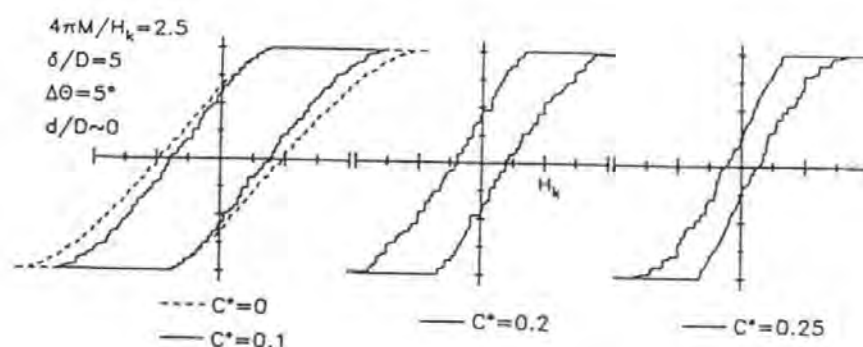


Figure 1.4: Simulated hysteresis loops for films with different interparticle exchange coupling strength. (after Zhu and Bertram)

For a film with weak interparticle exchange coupling ($C^* \leq 0.1$), the reversal process is similar to a nonexchange coupled film ($C^* = 0$), and its maximum perpendicular coercivity will be less than its perpendicular crystalline anisotropy constant. In the case of strong exchange coupling, the magnetization reversal process is characterized by initial coherent magnetization rotation and incoherent reversal followed by wall-motion-like expansion. This is because the intergranular exchange coupling

reduces the nucleation field of the particles at the boundaries of the reversed domains. The shape of the hysteresis loops depends strongly on the strength of the intergranular exchange coupling of the film. The perpendicular coercivity reduces significantly with increase of C^* . Figure 1.4 gives three simulated hysteresis loops for $C^* = 0.1$, $C^* = 0.2$ and $C^* = 0.25$ respectively. A hysteresis loop for $C^* = 0$ is shown as the dashed curve.

1.2 Principles of magnetic recording

1.2.1 The fundamental processes and modes of magnetic recording

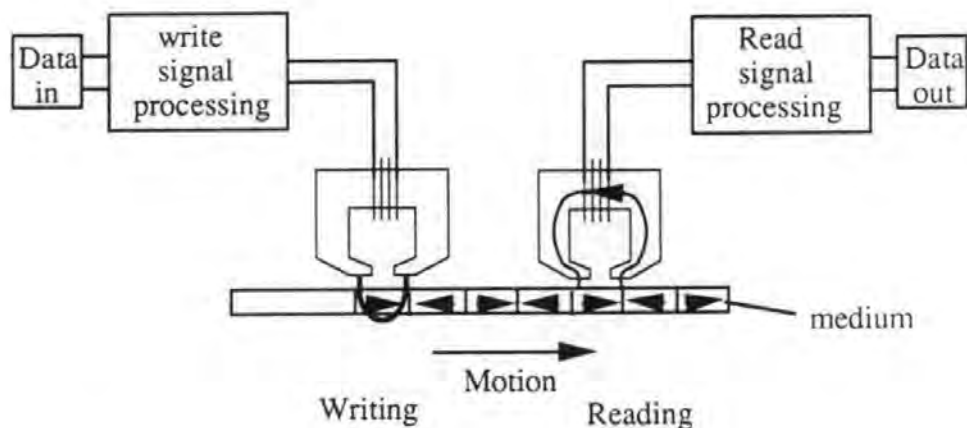


Figure 1.5: Schematic drawing of the fundamental magnetic recording processes.

The fundamental processes of magnetic recording is depicted in figure 1.5. The information to be stored is first encoded and converted by signal processing into the writing current of the recording head. When the writing current passes through the coil of an inductive head, it produces a magnetic field, a portion of which, fringing out around the gap, magnetizes the recording medium passing beneath the gap to form a "recorded" magnetization pattern in the medium. The information is thus stored in the medium and can be kept indefinitely if the media is not exposed to magnetic fields strong enough to magnetize the medium.

The recorded information can be reproduced by a replay head (or the same inductive head). As shown in figure 1.5, when the replay head passes over a recorded

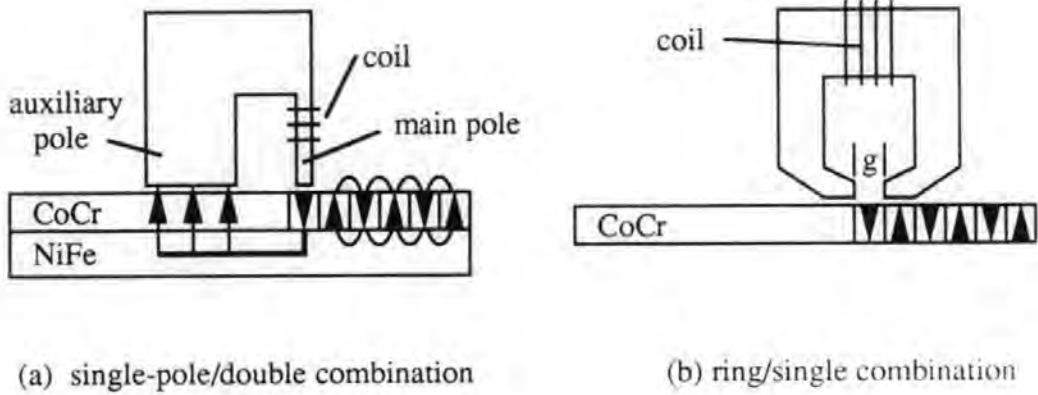


Figure 1.6: Schematic drawing of head-medium configurations of perpendicular recording.

magnetization pattern, the surface flux from the magnetized pattern is intercepted by the head core, and a voltage is induced in the coil, which is, by Faraday's law, proportional to the rate of change of this flux. The induced voltage is then reconstructed by signal processing into the original signal.

The magnetization pattern can be recorded longitudinally or perpendicularly to the film plane depending on the recording mode used, or in other words, depending on the type of head and medium used. The combination of a ring head and a medium with in-plane anisotropy tends to produce a recorded magnetization which is predominantly longitudinal. This is known as the longitudinal recording. An alternative of this is the perpendicular recording [8] by which the magnetization is perpendicularly recorded by using the head-medium configurations as shown in figure 1.6. The perpendicular orientation of the recorded magnetization exhibits zero demagnetizing field at the recording transition which is one of the major ad-

vantages of the perpendicular recording mode over the longitudinal recording [9]. The perpendicular recording can be realised simply, as shown in figure 1.6(a), by using the same ring type head as in the longitudinal recording, and a single-layer medium with perpendicular anisotropy, known as ring/single combination. With such a head-medium configuration, it is also possible to record the magnetization oriented obliquely to the film plane if the medium has an oblique anisotropy [34, 35]. The oblique recording exhibits weaker transition demagnetization in the medium and sharper oblique head field distribution and therefore better recording performance than the longitudinal recording [34]. The genuine perpendicular recording head-medium configuration is the single-pole head and double-layer medium configuration, as shown in figure 1.6(b), known as single-pole/double combination, where a sharp perpendicular writing field is produced by the strong magnetic interaction between the single-pole head and the soft magnetic backlayer. The back layer serves as a magnetic path during the writing and playback processes. Other head/medium combinations, such as ring/double combination, was also being used [12].

1.2.2 Writing field of magnetic heads

Various magnetic heads have been used for magnetic recording. The magnetic heads for longitudinal recording are designed to produce greater longitudinal field component H_x and for perpendicular recording, greater perpendicular field component H_y . The precise calculation of the magnetic field produced by a real head is rather complicated and involves numerical computation [38, 39]. The most commonly used analytical solution for the field in front of the write-gap g of a ring head is due to Karlquist [36]. The longitudinal field component H_x and the perpendicular field

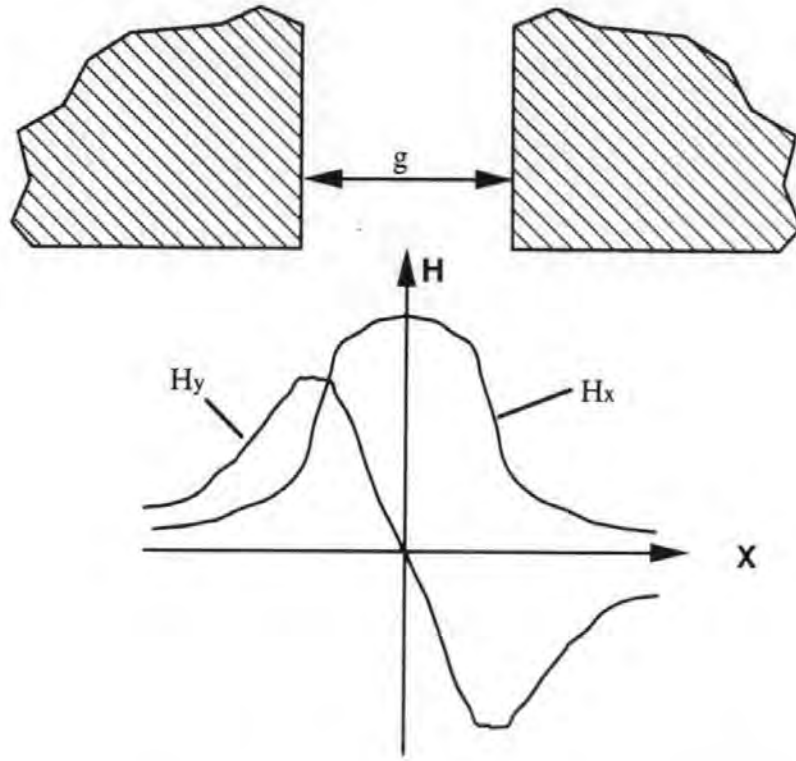


Figure 1.7: Longitudinal and perpendicular components of a Karlquist head field.

component H_y of a Karlquist head are given by equations 1.28 and 1.29 and plotted in figure 1.7.

$$H_x(x, y) = \frac{H_g}{\pi} \left[\tan^{-1} \left(\frac{g/2 + x}{y} \right) + \tan^{-1} \left(\frac{g/2 - x}{y} \right) \right], \quad (1.28)$$

$$H_y(x, y) = \frac{H_g}{2\pi} \ln \left[\frac{y^2 + (g/2 + x)^2}{y^2 + (g/2 - x)^2} \right], \quad (1.29)$$

where H_g is the deep gap field, x and y is the longitudinal and vertical co-ordinator respectively. The origin is set at the centre of the gap on the head surface.

The maximum longitudinal component is obtained when $x=0$ (in the central plane of the deep gap) and is given by,

$$H_x(max) = \frac{2H_g}{\pi} \tan^{-1} \left(\frac{g}{2y} \right), \quad (1.30)$$

and the maximum perpendicular component is obtained when $x=g/2$ and is given by,

$$H_y(max) = \frac{H_g}{2\pi} \ln \frac{y^2 + g^2}{y^2}. \quad (1.31)$$

It can be seen from figure 1.7 and equations 1.30 and 1.31 that the strength of the maximum head field depends strongly on the vertical distance from the head. The closer the medium to the head, the greater magnetic field the medium will be subject to.

Karlquist equation may also apply to the single-pole head [39, 43, 8]. The x and y components of field produced by single-pole head are simply given by,

$$H_x^{sp}(x, y) = -H_y(x, y), \quad (1.32)$$

$$H_y^{sp}(x, y) = H_x(x, y), \quad (1.33)$$

where $H_y(x, y)$ and $H_x(x, y)$ are y and x components of ring head given by equations 1.29 and 1.28 respectively. The deep gap field H_g for single-pole head is interpreted as the y component of field just under the pole face [43] and the gap length is substituted for the pole thickness T. The y component of the single-pole head field can be strongly enhanced by the existence of an infinite-permeability soft magnetic backlayer [47].

From equations 1.30 and 1.31 it can be seen that the writing field of a recording head is proportional to the deep gap field H_g . The deep gap field of a writing head is a function of writing current I, number of turns of the coil N, its write efficiency η_w and its gap length g, and is given by,

$$H_g = 4\pi \times 10^{-3} \eta_w \frac{NI}{g} \quad (1.34)$$

The maximum deep gap field a head can produce is limited by the saturation magnetization of the head material. Head saturation occurs when $H_g \geq 0.5B_s$ for ferrite heads and $H_g \geq 0.8B_s$ for MIG heads [5]. This criteria together with equations 1.30 and 1.31 can be used to estimate the maximum writeable coercivity of a medium with a specific head used [5].

1.2.3 Theory of write process

The write process converts an electrical signal current by the writing-head to an equivalent magnetization on the medium. The major target of the write process design in digital magnetic recording is to write data on the medium as closely as possible. The ideal situation for this is that the two discrete magnetization states in the medium exhibit a step-like reversal upon switching the direction of writing current. In reality, however, such a reversal is strongly affected by the head field gradient, properties of the medium, and, for longitudinal recording in particular, by the self-demagnetizing nature in the recorded transition. Such a transition region eventually limits the ultimate recording density. It has been a major research topic to relate the transition length with the recording head geometry, writing current, and magnetic properties of the recording medium. However, no completely satisfied theoretical model has yet been developed mainly because of the highly nonlinear nature of the write process and the complexity of the medium self-demagnetizing phenomenon. The most commonly used model in the digital magnetic recording is the Williams-Comstock model [42], and its simplified version known as Middleton-Wright transition [43].

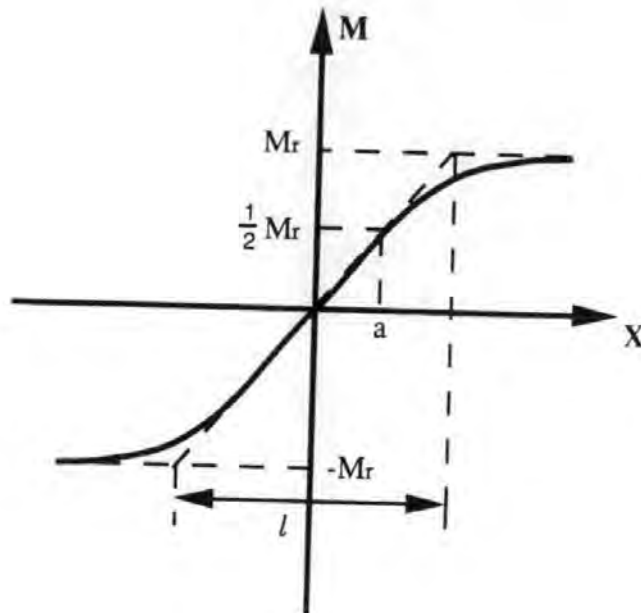


Figure 1.8: The arctangent transition model.

(a) Longitudinal transition

The variation of recorded magnetization in the x direction of the transition for longitudinal recording medium is best described by an arctangent function,

$$M_x = \frac{2}{\pi} M_r \tan^{-1}\left(\frac{x}{a}\right), \quad (1.35)$$

where a is the transition parameter, by which the transition length l is defined as $l = \pi a$. Figure 1.8 illustrates the arctangent transition model for longitudinal recording medium.

The demagnetizing field for an arctangent transition can be calculated from the divergence of magnetization by equation 1.19, [21]

$$H_d = \frac{M_r \delta x}{\pi(x^2 + a^2)}. \quad (1.36)$$

The maximum value of demagnetizing field $H_{d,max}$ occurs at $x = a$,

$$H_{d,max} = \pm \frac{M_r \delta}{2\pi a} \quad (1.37)$$

From equation 1.37 it can be seen the maximum demagnetizing field in the longitudinal transition increases as the recording density increase. If the transition is self-demagnetization dominated, the minimum transition length l_{min} is obtained when $H_c = H_{d,max}$,

$$l_{min} = \frac{2\pi M_r \delta}{H_c} \quad (1.38)$$

In Williams-Comstock model [42] the relation of the transition length with the head field gradient, self-demagnetizing field gradient and properties of recording medium is obtained by equating the differentiation of equation 1.35 with the following function,

$$\frac{dM_x}{dx} = \frac{dM}{dH} \left(\frac{dH_h}{dx} + \frac{dH_d}{dx} \right), \quad (1.39)$$

where the total field H is the sum of head field H_h and the self-demagnetizing field H_d . dM/dH is the slope of M-H loop at $H = -H_c$, as shown in equation 1.8, which reflects the contribution of medium parameters to the transition parameter.

The minimum transition parameter a is calculated by the maximum head field gradient and maximum demagnetizing field gradient and is given by,

$$a = 2\sqrt{\frac{M_r}{H_c} \delta \left(d + \frac{\delta}{2} \right)} \quad (1.40)$$

The Williams-Comstock model contains a few simplifications. The real write process is more complicated. However, the W-C model is very useful because it revealed the correlation of the transition length with the head and medium parameters. We can see from equations 1.38 and 1.40 that a small value of transition length requires a high value of H_c , a thin medium and a small head-medium spacing.

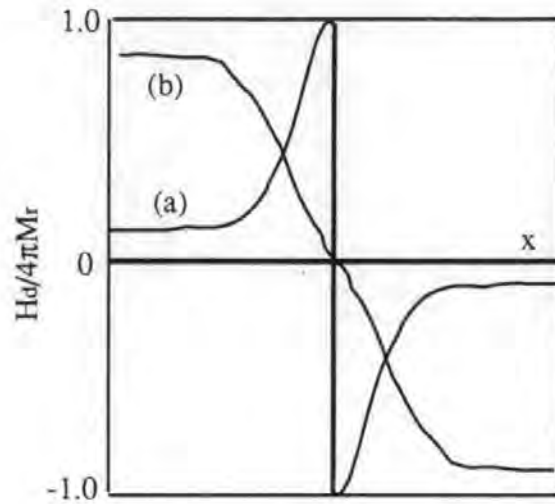


Figure 1.9: Schematic illustration for demagnetizing field distribution along the longitudinal step-like transition(a) and perpendicular step-like transition(b).

(b) Perpendicular transition

The perpendicular recording was first proposed by Iwasaki [8] from his study on transition demagnetization phenomenon in the longitudinal recording medium. One of the fundamental differences of the perpendicular recording from the longitudinal one is the distribution of the demagnetizing field in the recording transition. The demagnetizing field in the perpendicular transition can be calculated from equations 1.3 and 1.4 if the magnetization distribution in the transition is known. Figure 1.9 shows the demagnetizing field distribution for a longitudinal step-like transition (a) and perpendicular step-like transition (b) [9]. It can be seen that the demagnetizing field in the perpendicular step-like transition is zero in the centre of transition and $4\pi M_y$ away from the centre whilst in the case of longitudinal step-like transition, the demagnetizing field is maximum in the centre of transition and zero away from the transition. Therefore it is possible to realise step-like transition (zero transition

length) in the perpendicular recording from the point of view of transition demagnetization. The ultimate recording density for perpendicular recording would no longer be transition demagnetization limited.

The demagnetizing field away from the perpendicular transition shears the perpendicular loop, resulting in reduced output and unstable recorded magnetization [39]. It is therefore important in the perpendicular recording to make the recording media have coercivity H_c high enough to cancel such a demagnetizing effect. A soft magnetic backlayer reduces the the surface magnetic pole of the recording medium and therefore allows us to use media with lower coercivity [12].

Middleton and Wright [43] have used the Williams-comstock model to compare the transition length for perpendicular and longitudinal recording and concluded that very narrow transition length could be realised in perpendicular recording.

1.2.4 Theory of read process

The read process is devoted to study the head-medium interaction relating to the readback voltage, signal losses and the signal waveforms. In contrast to the write process, the read process, or reproducing process is almost completely understood. This is mainly because the flux density levels are so low in the reading head that the process may be considered to be linear.

The readback voltage calculation is simply based on the Faraday's law,

$$e(t) = -N \frac{d\Phi}{dt} = -N \frac{d\Phi}{dx} \frac{dx}{dt} = -Nv \frac{d\Phi}{dx}, \quad (1.41)$$

where N is the number of turns on the reproducing head, v is the head-medium relative velocity in cm/sec, Φ is the flux passing through the head, which is generated by the written magnetization in the recording medium.

A conventional method to calculate the head flux function was first proposed by Wallace [44]. The importance of Wallace's method is that it correlated successfully the readback signals with the parameters of head, medium and the recording system and revealed a number of important features that are characteristics of magnetic recording, such as spacing-loss, thickness-loss and gap-loss.

A more general and powerful approach to the head flux function Φ is the application of the reciprocity theorem to the reading process [21, 37, 39]. The reciprocity theorem gives the head flux function as,

$$\Phi = \iiint \mathbf{M}(\mathbf{r}) \cdot \mathbf{H}(\mathbf{r}) d^3\mathbf{r}, \quad (1.42)$$

where $\mathbf{M}(\mathbf{r})$ is the magnetization distribution function in the medium, $\mathbf{H}(\mathbf{r})$ is the head field function.

If the head field function and the magnetization distribution function are known, the reproducing voltage and reproducing waveform can be calculated immediately by equations 1.42 and 1.41.

For perpendicular recording, the readback voltage can be written by the reciprocity theorem as, [45]

$$e(t) = K \frac{\partial}{\partial s} \int_d^{d+\delta} dy \int_{-\infty}^{\infty} \mathbf{H}_y(x, y) \cdot \mathbf{M}_y(x - s, y) dx, \quad (1.43)$$

where $s = vt$, $\mathbf{H}_y(x, y)$ is the perpendicular component of the head field function, $\mathbf{M}_y(x - s, y)$ is the recorded magnetization in the medium, d is the head-medium spacing and δ is the thickness of medium.

The readback voltage expression derived from the reciprocity integral method for a perpendicular single-layer medium with sinusoidal recorded magnetization using

a ring head is given by [46],

$$e(t) = -2K M_r e^{-2\pi d/\lambda} (1 - e^{-2\pi\delta/\lambda}) G_a(\lambda, g) \sin(2\pi vt/\lambda), \quad (1.44)$$

where d is the head-medium spacing, λ is the wavelength, δ is the thickness of the medium and g , the gap length of the ring head. Equation 1.44 contains spacing-loss function, thickness-loss function and gap-loss function which are quite similar to that in the longitudinal recording derived by Wallace [44].

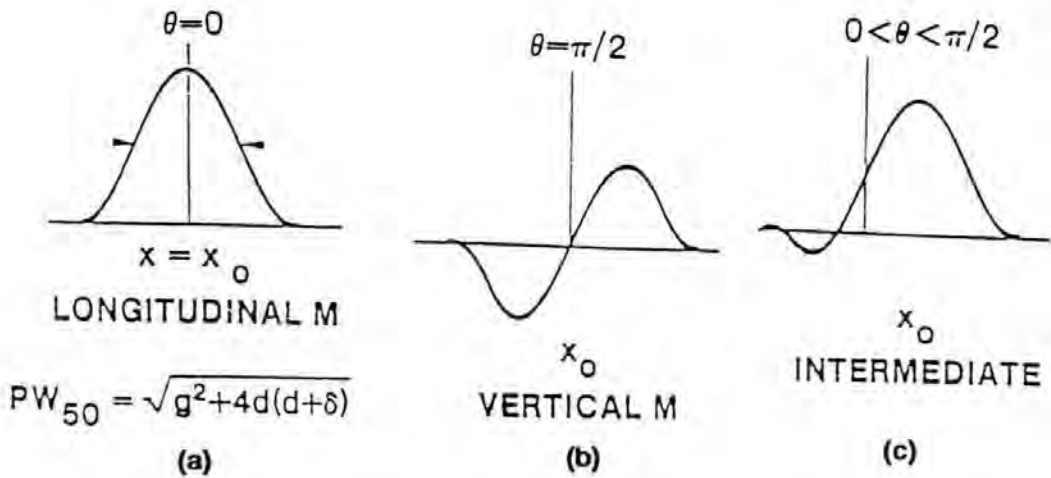


Figure 1.10: Isolated waveforms reproduced by ring head from: (a) longitudinal transition, (b) perpendicular transition and (c) in-between. (after Bertram)

The reproduced waveform will strongly depend on the type of transition, the orientation of the recorded magnetization and the type of head used. Figure 1.10 gives the isolated waveforms reproduced by a ring head from a perfect longitudinally recorded magnetization transition (a) and a perfect perpendicularly recorded magnetization transition (b) [49]. If the recorded magnetization is obliquely oriented, the reproduced waveform will be an asymmetrical di-pulse, as shown in figure 1.10(c), composed of both the longitudinal and perpendicular components. The reproduced

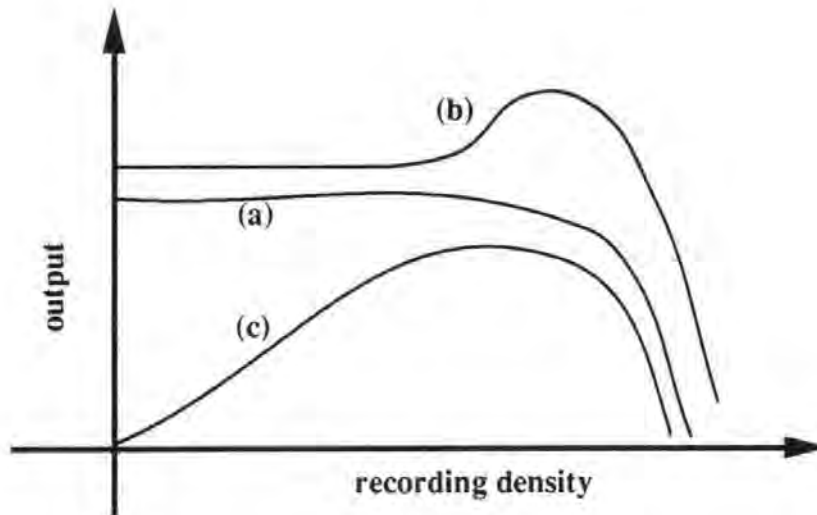


Figure 1.11: Typical frequency response curves for square-wave recording in terms of (a) peak-to-peak amplitude for symmetrical single-pulse waveforms, (b) peak-to-peak amplitude for antisymmetrical di-pulse waveforms, and (c) rms or fundamental frequency component.

waveform by a single-pole/double combination has the similar shape to that of ring head and longitudinal medium combination, as shown in figure 1.10(a).

The frequency response of reproduced voltage in square wave digital recording is often measured in terms of peak-to-peak amplitude or in root mean square(rms). The peak-to-peak amplitude of the reproduced waveform at low density for a recorded square wave magnetization is constant. However, as the recording density increases, the pulses begin to overlap causing changes in the peak amplitude and peak shift [47, 40, 41]. For the symmetrical single-pulse waveforms, as shown in figure 1.10(a), the pulse superposition or pulse crowding will give reduced output. The peak

voltage-frequency response curve for such waveforms is shown by curve (a) in figure 1.11. The point where this peak voltage has fallen to 50 percent is denoted D_{50} or -6dB density. Because D_{50} depends on the shape of the waveform, the pulse width of such a waveform PW_{50} is often used to estimate the -6dB density. The PW_{50} depends on the properties of medium and head, and head-medium spacing. The smaller head-medium spacing, smaller transition length and smaller head gap length will give smaller PW_{50} and consequently higher recording density.

For the antisymmetrical di-pulse waveforms, which are obtained in perpendicular recording with ring/single combination or ring/double combination, the pulse crowding will initially give a peak voltage rising before the falling starts in the peak voltage-frequency response curve as shown by curve (b) in figure 1.11. If the di-pulses are asymmetrical, the pulse crowding will cause peak shift [41].

The rms of a square wave function is equal to the fundamental component of its Fourier transfer function and its amplitude at wavenumber k ($k = \frac{2\pi}{\lambda}$) may be approximated by, [49]

$$e(k) = 4\pi \times 10^{-8} N v M \eta W \delta \frac{1 - e^{-k\delta}}{k\delta} e^{-k(d+a)} \frac{\sin(1.136kg/2)}{1.136kg/2}, \quad (1.45)$$

where N is number of turns, η is the head efficiency, W is the track width and other symbols are the same as defined previously. Equation 1.45 is valid only for single-layer medium [47].

The frequency response curves in terms of fundamentals or rms is shown by curve (c) in figure 1.11. This resembles the Wallace curve for sinusoidal wave [47].

It had been shown from the study of write and read process that a small head-medium spacing is always advantageous to high density recording (small transition length, high output and narrow reproduced waveform. This brought about the novel

idea of contact recording where the head-medium spacing is nearly zero [48].

1.2.5 Medium noise

The overall reliability of a digital recording system is determined by its bit error rate. Noise causes bit shift [21] and is one of the major error sources in a peak detection digital recording system. There are three types of noise sources: head noise, electronic noise and medium noise. Here we are only concerned with the medium noise as ultimate limits in magnetic storage are perceived as related to the inherent signal to noise capability of the media [21].

Medium noise is classified into two categories: the additive noise which comes from uncorrelated sources and the multiplicative noise (modulation noise) which comes from correlated sources. Additive noise adds on a power (or voltage-squared) basis (nP^2) because it comes from random, uncorrelated processes and is normally described in terms of total noise power (NP) and noise power spectrum (NPS). The noise power spectrum can be compared with the signal power spectrum leading to the narrow-band signal-to-noise ratio $(SNR)_n$ and the wide-band signal-to-noise ratio $(SNR)_w$ [37].

The noise properties are quite different between particulate media and thin film media, and between longitudinal media and perpendicular media [37, 21, 26].

Noise in particulate media had been thoroughly investigated during the 60s and 70s [37, 50, 51, 52]. The most interesting physical interpretation for the particulate medium noise is due to Mallinson[37] for the wide-band signal-to-noise ratio expression at high bit density,

$$(SNR)_w = \frac{nW\lambda_{min}^2}{2\pi} \quad (1.46)$$

where n is the number of particles per unit volume, W is the track width, λ_{\min} is the minimum wavelength. Equation 1.46 simply states that the wide-band SNR for particulate media is equal to the number of particles in a volume of size " $W \frac{\lambda_{\min}}{\pi} \frac{\lambda_{\min}}{2}$ ". This volume is known as effective medium volume sensed by head at any instant. Equation 1.46 also suggests that if the system is medium noise limited, from the SNR considerations, the better way to increase the areal density is to increase the track density rather than to increase the linear bit density.

Noise in thin film media has been studied intensively in recent years, particularly for longitudinal media [7, 6, 26, 53, 56]. It had been concluded that the intergranular exchange coupling, which significantly enhances the size of magnetic structures and results in large-size domains away from saturation, is the origin of thin film medium noise. Large irregular magnetic domains in the recorded transition of high noise media have been observed by Lorentz electron microscopy [55, 56]. The noise power reduced by the magnetization (M) and thickness of a medium (δ) is given by the following equation [49],

$$\frac{NP}{(M\delta)^2} = D^2 \mathcal{F}\left[C^*, \frac{M}{H_K} \mathcal{G}\left(\frac{\delta}{D}, \frac{d}{D}\right)\right]. \quad (1.47)$$

where D is the grain diameter, C^* is the intergranular exchange coupling constant as defined by equation 1.27, $\mathcal{G}\left(\frac{\delta}{D}, \frac{d}{D}\right)$ is the intergranular magnetostatic interaction energy function and d is the intergranular non-magnetic separation. Equation 1.47 tells that, for a medium with given grain diameter, the reduction of intergranular exchange coupling energy constant A^* will lead to the reduction of the medium noise power; For a medium with given thickness, zero intergranular exchange coupling ($A^* = 0$) and strong crystalline anisotropy (large H_K), the noise power decreases as the grain diameter reduces. However, if A^* is not equal to zero, or the crystalline

anisotropy is not strong enough, the reduction of grain diameter will lead to very complicated effects on the noise power because it also leads to the increase of intergranular exchange coupling as $C^* = \frac{A^*}{KD^2}$ and intergranular magnetostatic coupling $\mathcal{G}(\frac{\delta}{D}, \frac{d}{D})$.

There are distinct differences of the noise characteristics between longitudinal and perpendicular thin film media. For longitudinal thin film media, noise occurs mainly at the transition centres and increases with increasing recording density. In contrast to this, medium noise in perpendicular films occurs away from the transition centres and decreases with increasing recording density [26].

1.3 Thin film growth models

1.3.1 Nucleation and growth of thin films

The film formation process is normally distinguished into the following stages: the transport of coating species to the surface of substrate, the condensation, nucleation and growth of these species on the substrate surface and finally the movement of coating atoms to their final position by bulk diffusion [57]. The microstructure of the deposited coatings may be dominated by one or more of these stages depending on the deposition conditions.

The transport stage for the case of sputtering is controlled by apparatus geometry, working gas pressure and chamber base pressure.

The condensation process involves the adsorption, desorption and diffusion of coating atoms on the surface. For the sputtering process, the probability of desorption of coating atoms is very low. Thus most of the sputtered atoms normally transfer sufficient energy to the substrate on their arrival so that they become loosely bonded species known as adatoms. The adatoms diffuse over the surface, exchange energy with the substrate atoms until they become trapped at low energy sites or desorbed by evaporation or sputtering. The diffusion of adatoms over the surface is determined by its diffusion constant which depends on the nature of the material and the substrate temperature.

As the coating process proceeds, the nucleation of the film starts and the condensed adatoms combine to form nuclei. The film nucleation process involves the surface diffusion of adatoms to the low energy nucleation sites and the formation and growth of nuclei on the substrate surface. Thus the nucleation process will depend

on the adatom mobility and the adatom-substrate interaction and is controlled by the following three parameters [58]: E_a , the adsorption energy between the adatoms and the substrate which determines the adhesion between deposit and substrate; E_d , the surface diffusion energy required to transfer an adatom to the adjacent adsorption site, which determines the mobility of adatoms; and E_b , the binding energy between coating atoms, which determines the cohesion between the coating atoms.

According to the classical theory of nucleation, the following three different growth mechanisms may take place depending on the interaction energies between atoms of the deposit and atoms of the substrate [59].

(a) Layer growth (LG, 2D, van der Merwe) takes place if E_a (adhesion) is much higher than E_b (cohesion). In such a case, films grow layer-by-layer.

(b) Island growth (IG, 3D, Volmer-Weber) takes place from the beginning of condensation, if E_b (cohesion) is greater than E_a (adhesion).

(c) Straski-Krastanov growth (SK) takes place, where the nucleation starts with a layer growth (2D) and then develops into an island growth (3D). The SK growth mechanism is characterized by an interfacial energy which increases with the thickness of growing layers. Such a growth mechanism is often seen in the epitaxial growth films [60, 61] in the presence of lattice misfit, where the elastic strain energy of the ML and the misfit energy of interfacial registry increases with the initial layer thickness so that the ML condition may be violated beyond a critical number of layers. As a consequence, a transition from 2D to 3D growth may occur.

Figure 1.12 is the schematic drawing of the three different modes of film growth, where θ is the coverage in monolayers.

The mode of the initial nucleation and the atomic arrangement in the nuclei

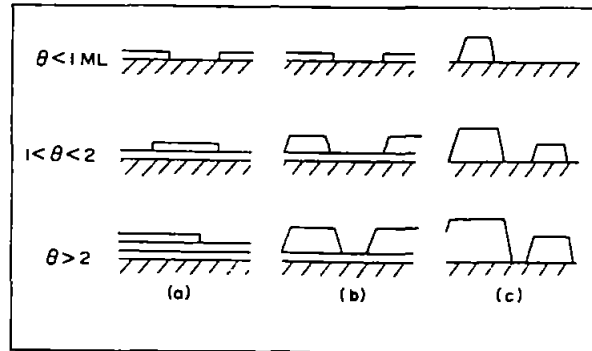


Figure 1.12: Schematic drawing of three different modes of growth: (a) Layer growth, (b) Stranski-Krastanov growth, (c) island growth. after Reichelt.

will significantly influence the microstructure and crystallographic orientation of the over-growth films, especially for coatings deposited at low substrate temperatures. For the case of island growth, the initially nucleated islands grow in number as well as in size as the coating process proceeds until they coalesce with each other to form larger islands or finally a continuous film. The coalescence process of the sputter-deposited coating is limited by the low mobility of coating atoms at low substrate temperature. As a result of this, a rough surface morphology forms at this very early growth stage which introduces an atomic shadowing effect on the arriving coating flux and consequently may result in a columnar growth structure of the over-growth. The grain size of the film will be determined by the number of initial nuclei and the mobility of coating atoms. If the mobility of the coating atoms is low, the high nucleation rate will result in a fine grain film.

The preferred crystallographic orientation can occur in this initial nucleation

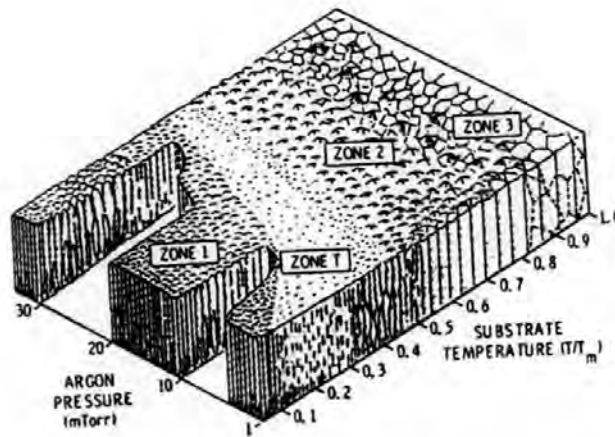


Figure 1.13: Microstructure zone model proposed by Thornton

stage if the formation of such nuclei with preferred orientation decreases the free energy. A particular application of this is the epitaxial growth of oriented or single-crystal films, where the crystallographic orientation of the over-growth has a strong relation with that of the substrate. The epitaxial growth conditions involve clean surfaces, nature of the substrate, modest deposition rate and elevated substrate temperature [58].

1.3.2 Microstructure zone model

Once a continuous coating is formed, growth proceeds similarly by adatoms arriving and diffusing over the coating surface until they become trapped in low energy sites, but with the surface of the growing coating serves as substrate. The arrival sites of the coating species may be affected by the morphology of the local growing

coating surfaces and by the incident angles. This phenomenon is known as atomic shadowing. The incorporated atoms in the growing coating will be further adjusted to their final position within the lattice by bulk diffusion.

According to Thornton [57], the adatom surface diffusion, the atomic shadowing and the bulk diffusion are the three most important factors, one of which may dominate the final film microstructure depending on the substrate temperature. At low substrate temperatures, the bulk diffusion may not have significant effect on the coating microstructure. The coating microstructure is dominated by the atomic shadowing which depends on apparatus configuration, substrate surface morphology and working gas pressure. At intermediate temperatures, the atomic shadowing is compensated for by surface adatom diffusion. The surface diffusion will dominate. As the substrate temperature increases, the bulk diffusion becomes increasingly important. The bulk diffusion becomes dominant so that a coating loses all memory of the earlier steps in its growth.

A classical structure zone model [58], which was proposed by Thornton to describe the general relationship between the microstructure of sputter-deposited coatings and the most prominent deposition parameters, is shown in figure 1.13. The microstructure of the sputter-deposited coatings at low substrate temperature is characterized by a typical zone 1 structure which exhibits a columnar growth defined by voided open boundaries. The columnar growth is further enhanced by the higher working gas pressure. Such a columnar growth structure is a fundamental consequence of atomic shadowing acting in concert with the low adatom mobility at low substrate temperature. As the substrate temperature increases, the microstructure of the coating changes gradually to zone T, zone 2 and zone 3 structure, as depicted

in figure 1.13, as a result of the increasing influence of surface diffusion and bulk diffusion.

For the deposition of CoCr-based perpendicular recording media, a low substrate temperature is often used. Therefore the microstructure of the CoCr films is characterized by the zone 1 columnar structure with voided column boundaries.

Chapter 2

Experimental techniques

2.1 Thin film deposition by sputtering

CoCr, CoCrTa films and their underlayers, CoNbFe soft magnetic backlayers and Carbon overcoatings investigated in this work were deposited by rf-planar diode sputtering or rf-planar magnetron sputtering. The schematic drawing of the rf-planar diode sputtering apparatus used in this work is shown in figure 2.1. It consists of a vacuum chamber, target and substrate electrode, a vacuum pump system, an rf power supply and its impedance matching network. The target and substrate, which are connected to the rf power supply, reverse cathode-anode roles on each half of rf cycle. However, sputtering occurs only on the target surface because the voltage drops on the substrate electrode is very small due to the considerably larger area of the substrate electrode than the target electrode [57]. A negative potential is thus produced on the target surface, which serves as the sputtering potential. The chamber is evacuated by a diffusion pump system equipped with a liquid Nitrogen trap to a base pressure of below 2×10^{-7} Torr, then is backfilled with Ar gas prior

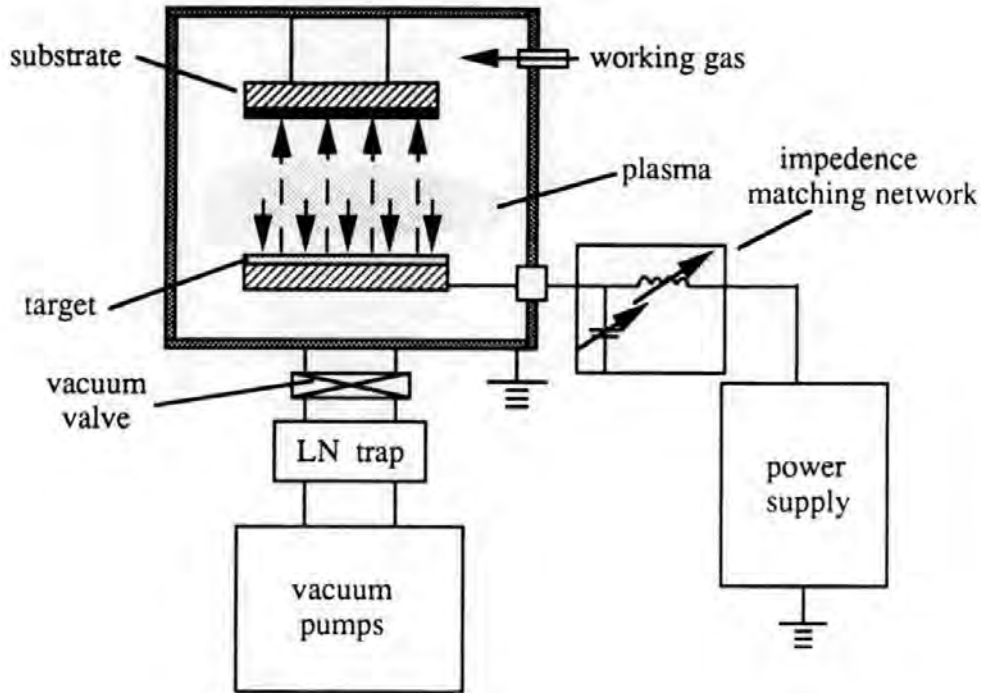


Figure 2.1: Schematic drawing of sputtering apparatus of planar diode type.

to sputtering. When an rf voltage is applied between the target and substrate by the RF power supply through a matching network, a plasma which contains Ar ions and electrons is produced. The Ar ions accelerated by the negative potential of the target bombard the target with sufficient energy resulting in the ejection of target materials from its surface. The substrates are placed in front of the target so that they intercept the flux of sputtered atoms to form coatings. At the same time, the electrons are accelerated towards the substrates to produce large amount of substrate heating. For this reason the substrates are normally water-cooled.

The deposition rate can be significantly increased by the use of magnetron sputtering. In the planar magnetron sputtering, both the magnetic field B above the

target surface and the electric field E across the dark space act on the moving plasma electrons causing the drift of electrons along the $E \times B$ direction [58]. As a result of this, the plasma electrons are confined in the vicinity of the target surface, resulting in a high density electron region. The confined electrons transfer most of their energy to the plasma to produce large number of Ar ions which are then accelerated by the cathode potential towards the target surface to produce more sputtering. The highest density of electrons, according to Spencer [63], is in the region where the B field is parallel to the target surface. Accordingly, the maximum sputtering of the target will be beneath this region. The by-product of the magnetron sputtering is the low substrate heating because of the confinement of the plasma electrons in the vicinity of the target surface.

A substrate bias can be applied during the sputtering process. This is realized in rf sputtering system by adding an impedance to the substrate electrode circuit so that the potential of this electrode relative to the plasma can be controlled for purpose of bias sputtering [57]. The bias sputtering provides a low energy ion bombardment to the growing coatings, which may increase the mobility of coating adatoms or remove the light element impurities from the surface of a growing coating [58].

Pure metal targets, composite targets and alloy targets were used in this study. A good quality target is a precondition for the deposition of films with desired properties. The heat-sintered target is cheap but useless because of its high porosity. Vacuum cast targets produce better quality films. Ti, Pt, Au and Cr underlayers were deposited by vacuum-cast pure metal targets. Carbon overcoatings were deposited by a graphite carbon target with purity of 99.9% and density of 1.83 g/cm^3 .

The CoCr films were deposited by a composite target which consists of an 8" cobalt plate with purity of 99.99% and pieces of 1cm^2 chromium uniformly arranged on the top of the cobalt plate to give the desired film composition. The CoNbFe films were also deposited by a composite target using the same cobalt plate with small Nb and Fe pieces on the top surface. Alloy targets were used in the later stage for the CoCr, CoNbFe films as well as CoCrTa films. The relation of the composition of the deposited films with that of target depends strongly on the sputtering yield of each constituent in the alloy, the sputtering power [62] and the type of sputtering apparatus. It is found in this study that the composition of the alloy films deposited by rf-planar sputtering is nearly the same as that of the alloy target. The composition of the films deposited by rf-planar magnetron sputtering may be different from that of the alloy target depending on the material and sputtering power used. This phenomenon may be explained by the effects of strong bulk diffusion in the target because of the high target temperature in the case of magnetron sputtering and the selective sputtering of surface atoms with different sputtering yield [62].

2.2 Magnetic measurements

2.2.1 Vibration Sample Magnetometer

The Vibrating Sample Magnetometer (VSM) is a commonly used instrument for the measurement of M-H loops, magnetization curves and remanence curves of recording media. Figure 2.2 is a schematic drawing of the VSM used in this work. The magnetic field of up to 10,000 Oe is produced by an electromagnet. The sample is suspended on a nonmagnetic rod, which vibrates vertically to the magnetic field at

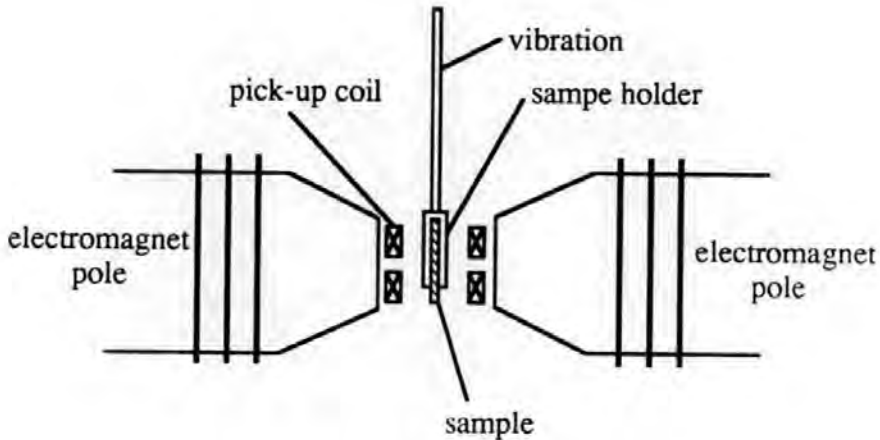


Figure 2.2: Schematic drawing of a vibrating sample magnetometer

certain frequency. When the sample vibrates, it produces an induced voltage in the pick-up coils which is proportional to the magnetization of the sample.

2.2.2 Magneto-optic Kerr effect loop plotter

There are three kinds of Kerr magneto-optic effects: longitudinal Kerr effect, transverse Kerr effect and polar Kerr effect [64]. In this work a transverse Kerr effect system is used for the measurement of CoNbFe soft magnetic films and a polar Kerr effect system [64] is used for the measurement of perpendicular recording media. Figure 2.3 is a schematic diagram of the polar Kerr loop plotter. A 3mW He-Ne laser ($\lambda = 6328 \text{ \AA}$) is used as a light source. An electromagnet with a bore in the centre of the pole is used to produce applied field up to 10,000 Oe and at the same time to allow the passage of the laser beam at an angle of 2° from vertical axis.

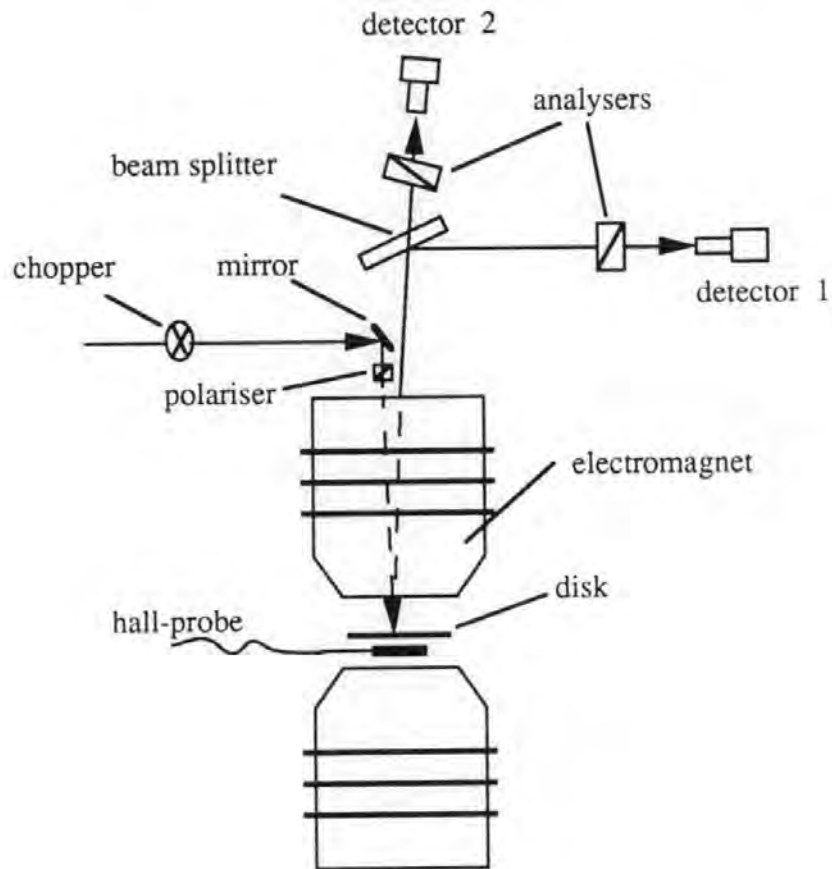


Figure 2.3: Schematic diagram of the polar Kerr loop plotter. (after Mahvan)

The polar Kerr rotation is detected by two detectors and their output is fed to a differential amplifier by which an improved S/N ratio is achieved.

2.2.3 Torque magnetometer

The uniaxial anisotropy constant K_u and the saturation magnetization M_s of thin film recording media can be determined by means of Torque curve measurement. The torque curve of a specimen is correlated with the anisotropy constant and saturation magnetization by considering the magnetic energy equilibrium in the specimen.

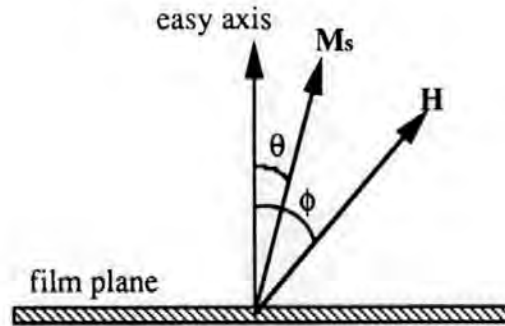


Figure 2.4: Schematic diagram of the directions of \mathbf{H} and \mathbf{M}_s and their angles respect to the film normal for a torque measurement.

When a CoCr thin film specimen is suspended in a uniform field \mathbf{H} at an angle ϕ with respect to the magnetization easy direction of the specimen, as shown in figure 2.4, the saturation magnetization of the specimen \mathbf{M}_s makes an angle of θ with the easy axis. The torque experienced by a specimen with volume V is,

$$L = V\mathbf{M}_s \times \mathbf{H} = VM_s H \sin(\theta - \phi) \quad (2.1)$$

The magnetic energy in the specimen is given by,

$$E = E_h + E_k = -VM_s H \cos(\theta - \phi) + KV \sin^2 \theta, \quad (2.2)$$

where E_h is the applied field energy, E_k is the anisotropy energy and K is the effective anisotropy constant which is defined as

$$K = K_u - 2\pi M_s^2, \quad (2.3)$$

where K_u is the uniaxial anisotropy energy constant, $2\pi M_s^2$ is the shape anisotropy energy along the film normal as given by equation 1.22.

For equilibrium the energy must be at a minimum with respect to θ :

$$\frac{\partial E}{\partial \theta} = VM_s H \sin(\theta - \phi) - KV \sin 2\theta = 0. \quad (2.4)$$

From equations 2.1 and 2.4 we have,

$$L = KV \sin 2\theta. \quad (2.5)$$

Since at high fields: $\theta = \phi$, we have,

$$L = KV \sin 2\phi. \quad (2.6)$$

From equation 2.6 it can be seen that for a uniaxial anisotropy film, torque L is a function of $\sin 2\phi$. The maximum torque, $L_{max} = KV$ occurs at $\phi = 45^\circ$.

For a real film the maximum torque may not occur at $\phi = 45^\circ$ because of the anisotropy dispersion. If L_{max} occurs at angle ϕ_m , from the differentiation $\partial L / \partial \phi = 0$ we will have [65],

$$\left(\frac{L_{max}}{H}\right)^2 = \frac{(VM_s)^2}{2} \left(1 + \frac{KV \sin 2\phi_m}{L_{max}}\right). \quad (2.7)$$

By plotting $(L_{max}/H)^2$ versus $\sin 2\phi_m$, the M_s and K_u can be determined.

2.3 Microstructure and texture examinations

2.3.1 Miller-Bravais indices

The planes and zone axes of fcc and bcc crystals are normally indexed by a three-digit index scheme, known as Miller indices $\{hkl\}$. For the hcp crystals, such as hcp Co and hcp Ti, the three-digit Miller indices is also applicable. However, a four-digit index scheme, known as Miller-Bravais indices $\{hkil\}$, is more convenient

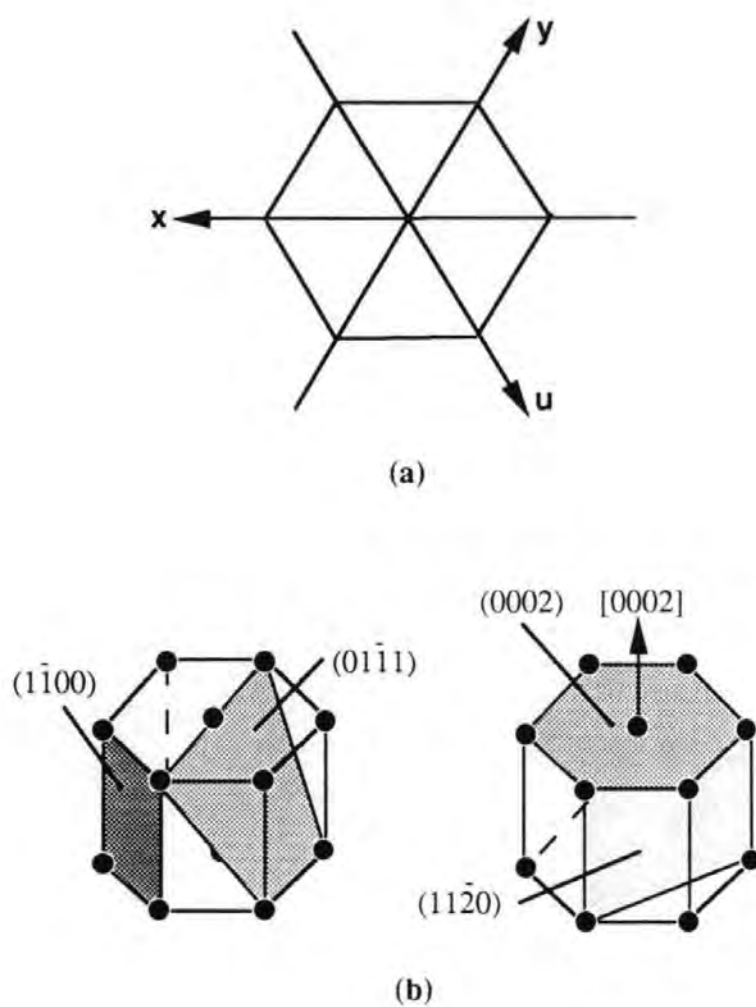


Figure 2.5: The arrangement of the axes for the hexagonal system in this work (a), and the schematic drawing of the low index planes and directions in hcp(b).

and straightforward, in which the symmetry relationship between the planes of each family can be obviously shown.

In the Miller-bravais indices, the vertical z axis is in the centre of hexagonal plane. There are two possibilities in arranging the three horizontal axes x , y and u , which may result in different indices for the same set of planes. Figure 2.5(a) shows the axis system used in this work. Figure 2.5(b) gives a schematic diagram of the low index planes and direction in hcp crystals designated by the Miller-bravais indices.

Because three-dimensional geometry can not be described in terms of four independent parameters, h , k and i must be interrelated. Actually, h , k and i have the following relation, $h + k + i = 0$. Thus, a given three-digit Miller index (hkl) for an hcp crystal can be extended to a four-digit Miller-Bravais index ($hkil$) by $i = -(h + k)$. For example, the three-digit Miller index (100) will become ($10\bar{1}0$) in four-digit Miller-Bravais index.

2.3.2 X-ray diffraction

X-ray diffraction was used to determine the film microstructure and the texture. Figure 2.6 is a schematic diagram of the x-ray diffractometer. When a monochromatic x-ray beam with wavelength λ impinges on a polycrystalline thin-film sample with an angle θ with respect to the film plane, the lattice planes in the sample with spacing d , diffract the x-ray to form a diffraction pattern if the Bragg law is satisfied.

$$n\lambda = 2d\sin\theta. \quad (2.8)$$

The deflected beam is detected by a counter located in the 2θ position. In order to detect deflected beams from different lattice planes, the sample and the detector are rotatable and the rotation of the sample and the detector is coupled so that when

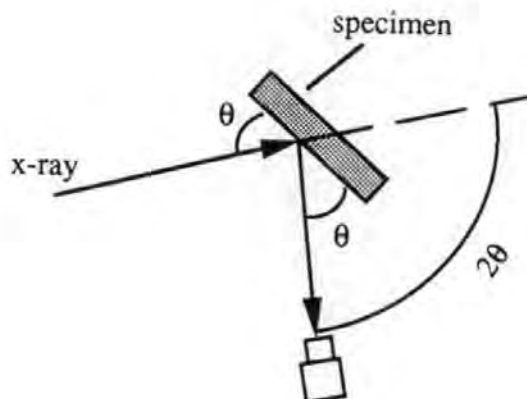


Figure 2.6: Schematic diagram of x-ray diffractometer

the sample plane is in the θ angle position with respect to the incident beam, the detector is always in the 2θ angle position.

An x-ray diffraction pattern measures the intensity of the deflected beam as a function of 2θ angle. From the values of 2θ of the diffraction peaks one can determine the corresponding d spacing and hence the crystal structure. From the number of peaks and the intensity of the peaks one can determine the crystal orientation or film texture.

The C_uK_α radiation ($\lambda = 1.54\text{\AA}$) was used for the x-ray diffraction in this work. Because the d spacing of lattice planes is of the same order of magnitude of λ , it can be seen from equation 2.8 that the θ angle for the first order ($n=1$) x-ray diffraction is in the range of $15 - 60^\circ$. Table 2.1 lists the 2θ angles and their corresponding d spacing values for the lattice planes of hcp Co, hcp Ti, fcc Pt and fcc Au.

The dispersion of the c-axis orientation of the Co-based media can be measured in terms of $\Delta\theta_{50}$ which is the half pulse width of the c-axis rocking curve. To

Table 2.1: d spacing and 2θ values for lattice planes of hcp Co, hcp Ti, fcc Pt and fcc Au for x-ray diffraction using C_uK_α radiation.

	hk.l	2θ ($^\circ$)	$d(\text{\AA})$
hcp Co	10 $\bar{1}0$	41.57	2.170
	0002	44.47	2.035
	01 $\bar{1}1$	47.42	1.915
	01 $\bar{1}2$	62.51	1.484
hcp Ti	10 $\bar{1}0$	35.08	2.555
	0002	38.39	2.342
	01 $\bar{1}1$	40.15	2.243
	01 $\bar{1}2$	52.99	1.726
fcc Pt	111	39.75	2.265
	002	46.21	1.962
	022	67.44	1.387
	222	85.63	1.133
fcc Au	111	38.17	2.355
	002	44.37	2.039
	022	64.55	1.442
	222	81.72	1.177

measure the c-axis rocking curve of the hcp Co crystals, the detector is fixed at the 2θ (44.7°) position and de-coupled from the rotation of the specimen and the specimen is rotated from $\theta - \Delta\theta$ to $\theta + \Delta\theta$.

2.3.3 Electron diffraction and transmission electron microscopy

Transmission electron microscope is a powerful instrument for the study of thin film microstructure and texture. The crystallographical texture of recording media can be determined by electron diffraction patterns with TEM. Moreover, the modern high resolution TEM provides us an effective means to resolve the microstructure of grains and grain boundaries at atomic level. Figure 2.7 is a picture of the JEOL 2000FX Transmission Electron Microscope used in this work. The accelerating voltage of the JEOL 2000FX system is 200KV.

(a) Electron diffraction

The electron diffraction is also based on Bragg law. The difference of electron diffraction from the x-ray diffraction is in that the Bragg angle θ in the electron diffraction is very small, less than 1 or 2° . This is because the wavelength λ of an electron beam is much smaller than that of an x-ray beam ($\lambda = 0.025\text{\AA}$ when the accelerating voltage is 200KV). In the transmission electron microscope, the electron beam travels perpendicular to the plane of a specimen, therefore only those lattice planes which are near parallel to the film normal contribute to the electron diffraction patterns. Consider an hcp Co polycrystalline specimen with strong $[0001]$ texture, the main reflection rings of such a specimen will be $(10\bar{1}0)$, $(11\bar{2}0)$, $(20\bar{2}0)$, \dots , $\{hki0\}$, all of which are contributed from the lattice planes parallel to the film

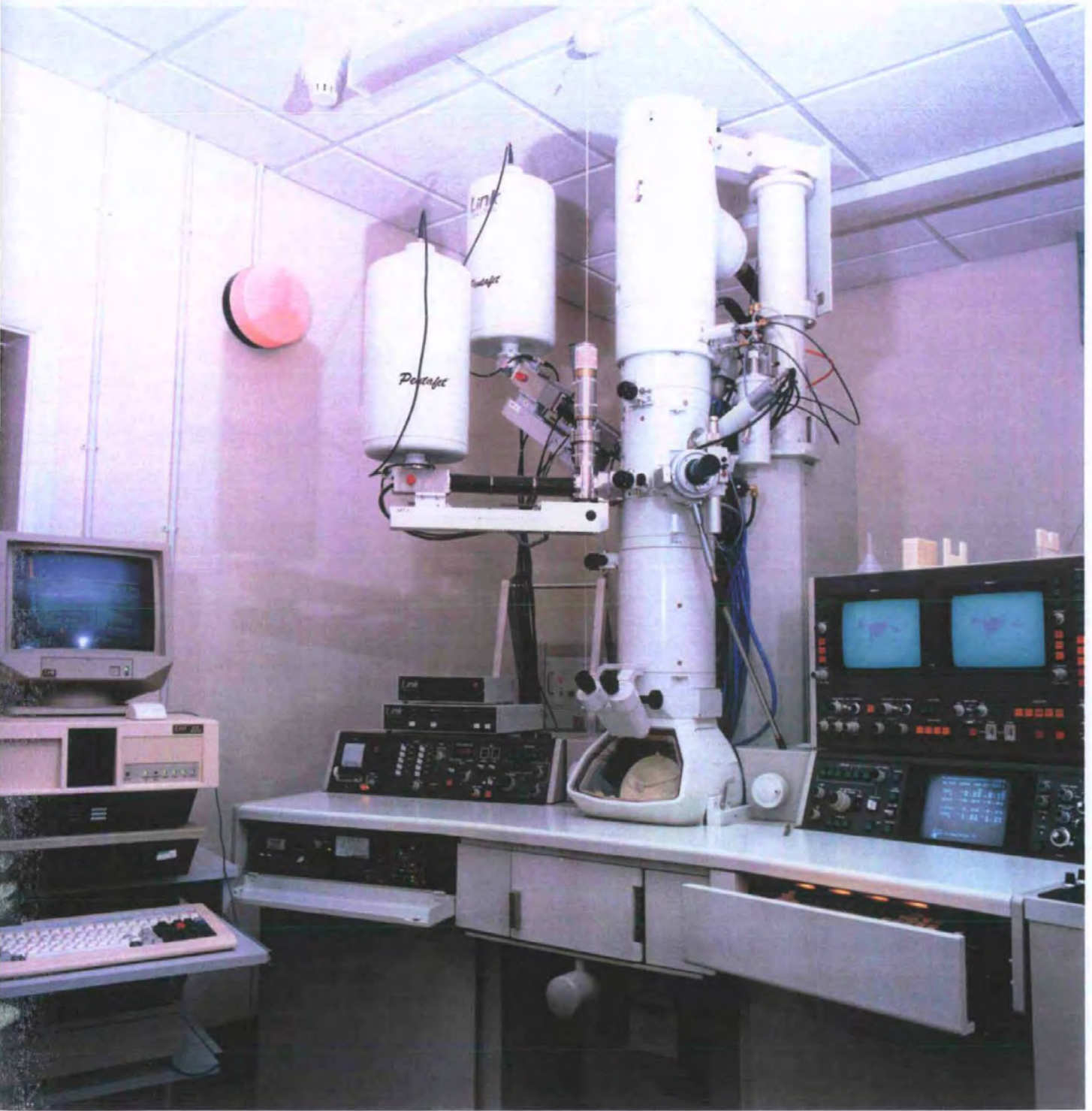


Figure 2.7: JEOL 2000FX Transmission Electron Microscope.

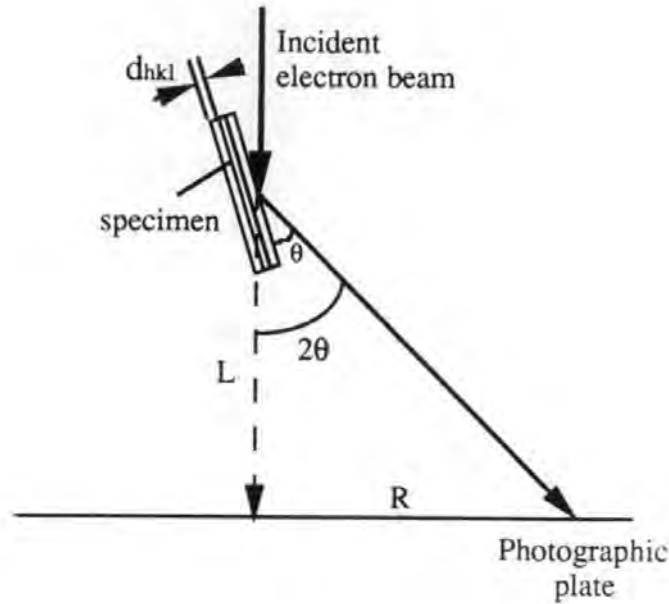


Figure 2.8: Simplified schematic diagram of an electron diffraction camera.

normal. Reflection rings of (0002) , $(01\bar{1}1)$, \dots , $\{hkil\}$ ($l \neq 0$) would not appear. The expected diffraction patterns for the $[0002]$, $[11\bar{2}0]$ and $[10\bar{1}0]$ textural hcp Co polycrystalline films will be further discussed in chapter 3.

The principle for the index of a diffraction pattern is depicted in figure 2.8. When an electron beam with wavelength λ strikes a specimen with incident angle θ , a diffraction pattern is formed on the photographic plate at distance R from the centre of the diffraction pattern. The distance between the specimen and the plate, the camera length, is designated L . The Bragg law states that,

$$\lambda = 2d\sin\theta, \quad (2.9)$$

and by simple geometry we have,

$$\tan 2\theta = R/L. \quad (2.10)$$

With approximation of $\tan 2\theta = 2\sin\theta$ for very small θ , we have,

$$Rd = \lambda L. \quad (2.11)$$

In equation 2.11, if R can be measured from a particular diffraction ring, L can be calibrated by a known crystalline specimen and λ can be obtained from the accelerating voltage of the electron beam, then the d-spacing d of the set of lattice planes giving rise to that diffraction ring can be determined.

(b) TEM images

Apart from the electron diffraction, TEM micrographs(images) is another important technique to study the film microstructure. There are two important mechanisms which produce image contrast in the transmission electron microscope: amplitude contrast and phase contrast. Amplitude contrast arises from the removal of part of the diffracted beam (bright field image), or alternatively the transmitted beam (dark field image) by the objective aperture. Improvement in image contrast can be obtained through use of smaller apertures, but at the expense of resolution since the scattered electrons carry the detailed information about the specimen. Amplitude contrast is the dominant mechanism in resolving structure detail $\geq 15\text{\AA}$. The phase contrast is produced by interference between the transmitted and diffracted electron beams at the image point. Phase contrast is the dominant mechanism for structure detail $\leq 10\text{\AA}$ and is important in lattice resolution studies. The lens aberration is one of the major causes in limiting the phase contrast resolution.

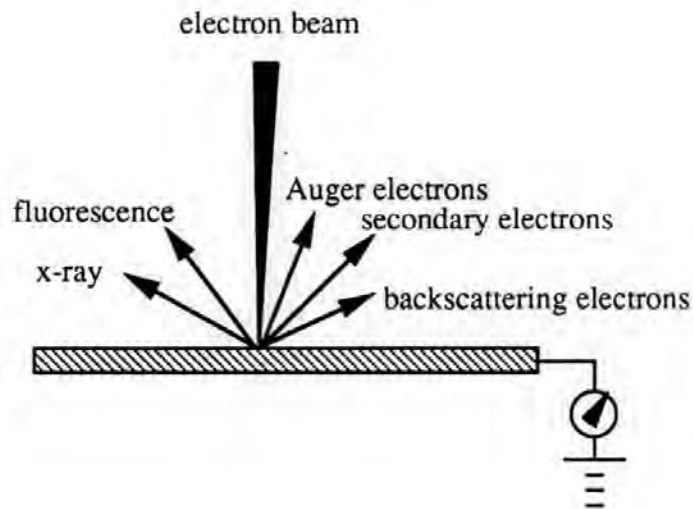


Figure 2.9: Various emissions are produced when a high energy electron beam bombards the surface of a specimen.

(c) Specimen preparation

The underlayers and CoCr films for TEM study were deposited by rf-sputtering on to glass disk substrates which were precoated with Carbon films. The films were then floated off from the substrates by water and placed in foldable Cu grids for TEM examinations. The thickness of underlayers is 300\AA and CoCr films, 160\AA .

2.3.4 Scanning electron microscope

The scanning electron microscope (SEM) is a useful instrument for the study of the surface or cross section morphology of the recording media at high magnification. Images are formed in the SEM by a quite different mechanism from that in TEM. In TEM images are formed by an objective lens. However, no objective lens is used in

SEM. Images are build up point by point in a way similar to that used in television display.

As shown in figure 2.9, when a high energy electron beam bombards the surface of a specimen in an SEM, various electrons, characteristic x-rays, etc. are emitted from the specimen surface as a result of the interaction of the electron beam with the specimen. The SEM may utilize any of a number of different types of signal to produce an image from a specimen. In each case the microscope will be employed in a particular operation mode [66]. The most common operation mode for high resolution SEM is the emissive mode in which the secondary electrons are used to form SEM images. Because the secondary electrons are very sensitive to the topography of the specimen, the dominant contrast provided by the emissive mode is the topographical contrast [66]. The SEM images so obtained are particularly useful in resolving the physical columnar structure and the columnar diameter of the sputtered films. However, they do not provide any information about the crystallographic structure of the specimen. The columnar structure is superimposed on a microstructure which may be polycrystalline or amorphous [57].

One of the advantages of SEM is the ease of specimen preparation. No special requirement is normally needed for the preparation of the recording medium specimen for SEM. However, In order to get a high resolution image, a conducting layer, such as Gold coating, is sometimes required.

2.4 Domain observation by Lorentz microscopy

The interaction of the electrons with the magnetization of the specimen in a TEM can be used to detect magnetic domain structures. As the observed contrast could

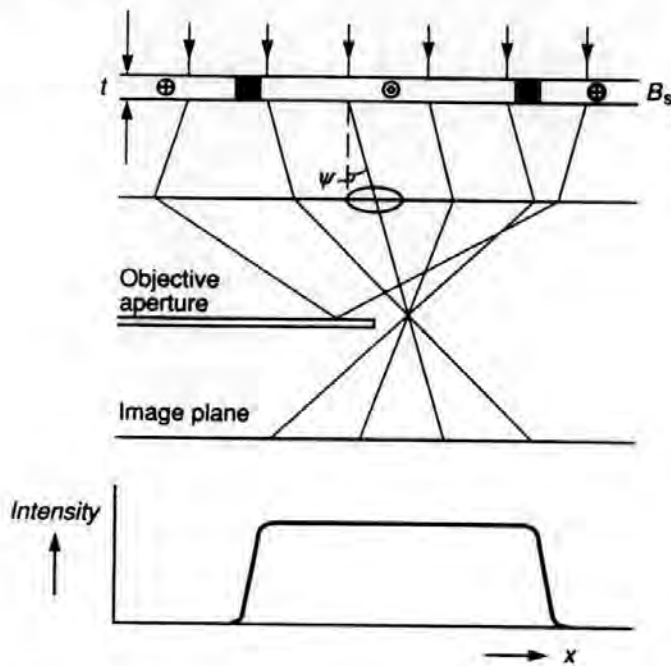


Figure 2.11: Schematic drawing of formation of Foucault contrast through displacement of the objective aperture. (after Chapman)

distance ΔZ . In the JEOL 2000FX TEM, the objective lens is actually switched off in the Lorentz mode in order that the magnetic specimen is in the magnetic field free space. The objective-mini(OM) is the image forming lens. With the objective lens switched off the magnification and resolution is considerably reduced. The maximum magnification of 1000X can be achieved if the free lens mode is employed. For the examination of perpendicular recording media, the specimen is tilted through an angle in order to get sufficient in-plane magnetization component.

Figure 2.11 is the schematic diagram showing the generation of the Foucault contrast. As shown in the figure, the electron beams deflected by the magnetic domains magnetized in one direction are cut off by displacing the objective aperture. These domains are then dark in the final image and the domains magnetized in the opposite direction are bright. Domain walls in the Foucault image appear as

boundaries between dark and bright areas. The main advantage of the Foucault mode is its ability to complement very simply the Fresnel images by providing information on the orientation of magnetization within specific domains [68].

2.5 Film composition analysis

The energy dispersive analysis by x-rays (EDAX) and the Auger Electron Spectroscopy (AES) were used in this work to determine the composition of the recording media. These instruments are based on the principle that when an area of a specimen is bombarded with high energy electrons or x-rays, the absorption of high energy beam by atoms in specimen results in the emission of photo-electrons, Auger electrons and fluorescent x-rays. Figure 2.12 is a schematic diagram showing how the interaction of x-ray with an atom produces photo-electrons, Auger electrons and characteristic x-ray emissions. The wavelength of such emissions depends on the nature of atoms in the specimen and is used for qualitative analysis. The intensity of such emissions depends on the number of atoms and is used for quantitative analysis.

The EDAX used in this work was not suitable for the analysis of light elements ($Z < 10$). A thicker film ($1 \mu\text{m}$) is also required in order to get the results free from the substrate interference. For the analysis of light elements and very thin films the AES is more powerful. Another advantage of AES is that it can be used to do the depth profiling if combined with a sputtering gun, which is a useful technique to study the composition distribution of thin films through the film depth. The thickness resolution of the AES is about 5\AA to 50\AA .

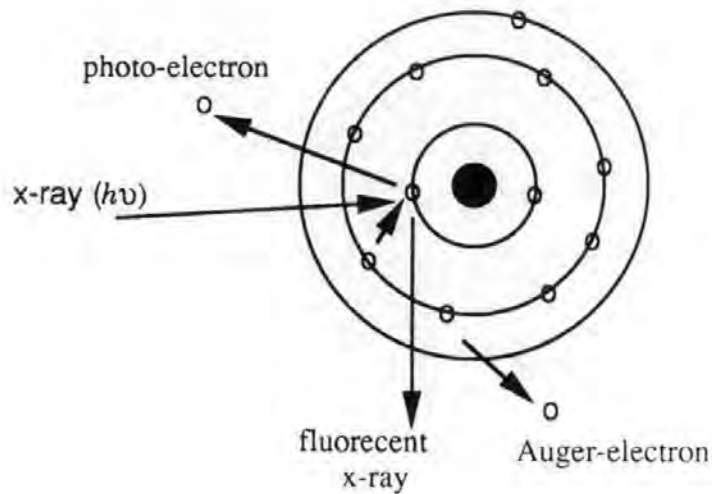


Figure 2.12: Schematic diagram showing how the interaction of x-ray with an atom produces photo-electrons, Auger electrons and fluorescent x-ray emissions.

2.6 Differential thermal analysis

The crystallisation temperature of the amorphous CoNbFe films was measured by a differential thermal analysis (DTA) techniques. Figure 2.13 is the schematic drawing of the DTA apparatus. CoNbFe films of 5 mg which were peeled off from glass substrate are put in the micro-environment cup and heated by a furnace winding at a specific heating rate during the test. The heat flow in the specimen is measured by a calorimeter in the micro-environment cup and recorded by an X-Y plotter as a function of specimen temperature. When crystallisation occurs in the specimen as temperature increases, the latent heat is evolved because of the phase change and

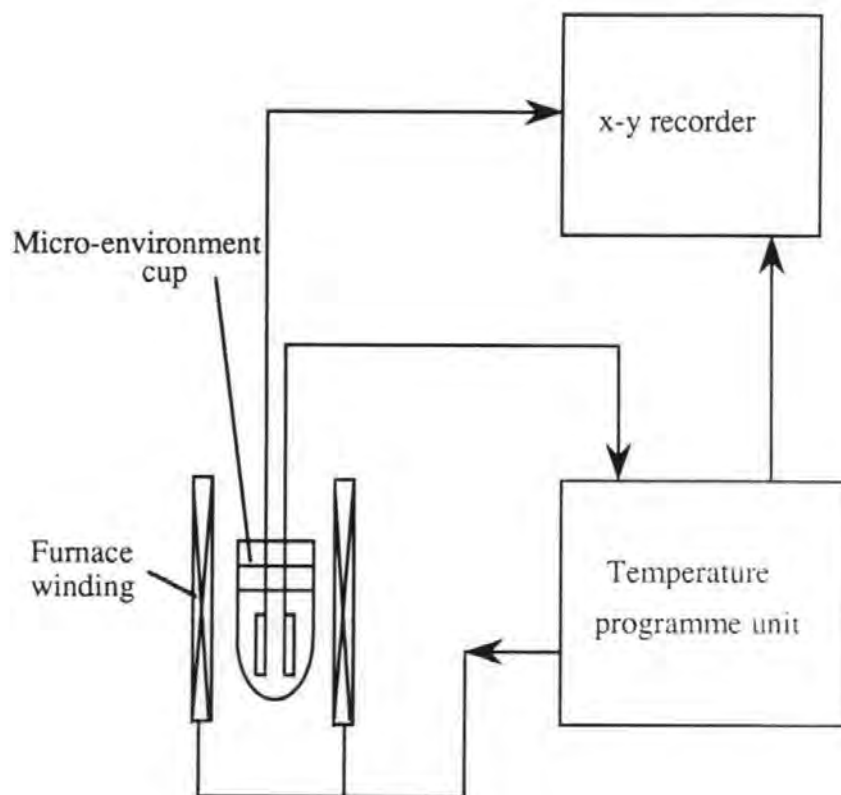


Figure 2.13: Schematic drawing of the DTA apparatus.

is recorded by the X-Y plotter as a pulse peak in the heat flow - temperature plot.

The crystallisation temperature is thus determined from such a plot.

Chapter 3

Results and discussion

3.1 Underlayer effect on Co-based media

This section presents the detailed experimental studies of CoCr and CoCrTa perpendicular recording media deposited on various kinds of underlayers. The CoCr films and their underlayers studied in this section were deposited by rf-sputtering on to chemically strengthened glass disk substrates. A -100 v substrate bias was used during the deposition unless otherwise stated. The base pressure of the sputtering chamber was below 2×10^{-7} Torr. Ar pressure was 3 mTorr. The Cr content of the CoCr films was 22 at%. The CoCrTa films and their underlayers were deposited by rf-magnetron sputtering. No substrate bias was used during this sputtering.

Results presented include magnetic measurement of these media by MOKE, VSM and torque magnetometer, texture examination by x-ray diffraction patterns, rocking curves and TEM electron diffraction, physical and crystallographic microstructure examination by TEM, HRSEM and AES, and micromagnetic examination by Lorentz microscopy. Experimental results are discussed in conjunction with the re-

cent theoretical development in the related subject. Special attention is paid to the thin film growth process, orientation relationship between the Co-based media and their underlayers, the correlation of the magnetic properties, such as coercivity, squareness and shearing of the loops, with the film microstructure and texture.

3.1.1 Dependence of MOKE loops on CoCr thickness

Figure 3.1 shows the typical perpendicular MOKE loops of the four different thickness CoCr films with Ti underlayers (solid curve) and without Ti underlayers (dashed curve). The Ti underlayer thickness was 600 Å. From these hysteresis loops one can see that for the 1600 Å-thick CoCr films, the principal difference of the MOKE loop of the CoCr films with and without Ti underlayer is only in the "shoulder" of the loop. CoCr films deposited on Ti underlayers exhibit a bigger "shoulder" in its perpendicular loops. The similar results have been reported by M. Futamoto and his colleagues [74]. However, when the CoCr films get thinner, the Ti underlayer effects on the perpendicular loops become pronounced. There are two major effects: the shearing of the perpendicular loop and the squareness of the perpendicular loop. For CoCr films deposited directly on glass disk substrates, the perpendicular loops are always sheared and the squareness becomes smaller as film thickness reduces. On the other hand, for CoCr films deposited on Ti underlayers, their perpendicular loops become steeper and squarer as the CoCr film thickness reduces. As shown in figure 3.1, an 80 Å-thick CoCr film and a 160 Å-thick CoCr film deposited on Ti underlayer exhibits nearly square perpendicular hysteresis loops. The shearing of the loop is very small and the perpendicular remanence ratio is near unity.

Wielinga et al have proposed to use the slope $T (= 4\pi dM/dH_{M=0})$ of the per-

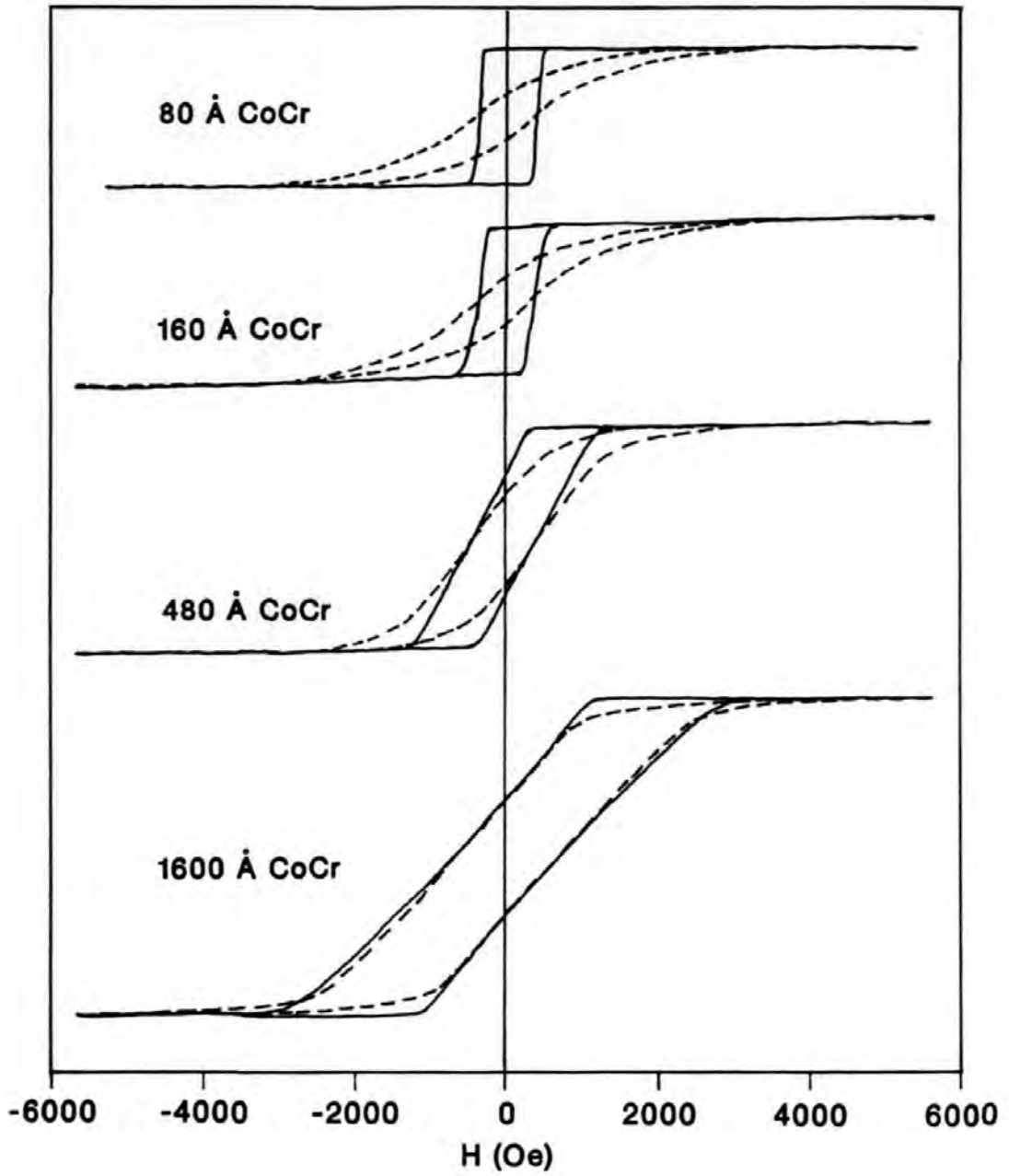


Figure 3.1: Perpendicular M-H loops of different thickness CoCr films with and without Ti underlayers.

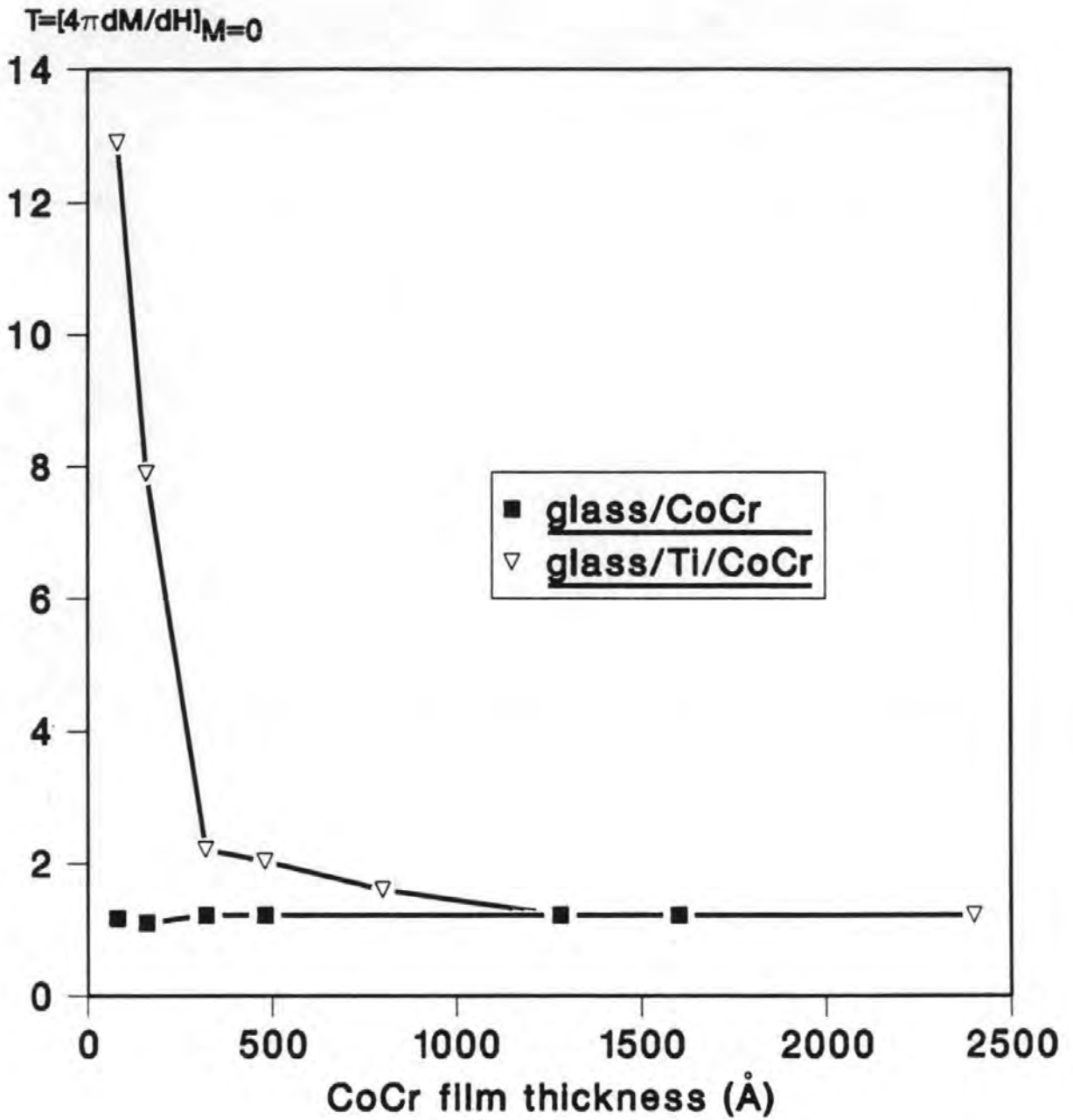


Figure 3.2: Measured hysteresis loop slope T of CoCr films as a function of film thickness.

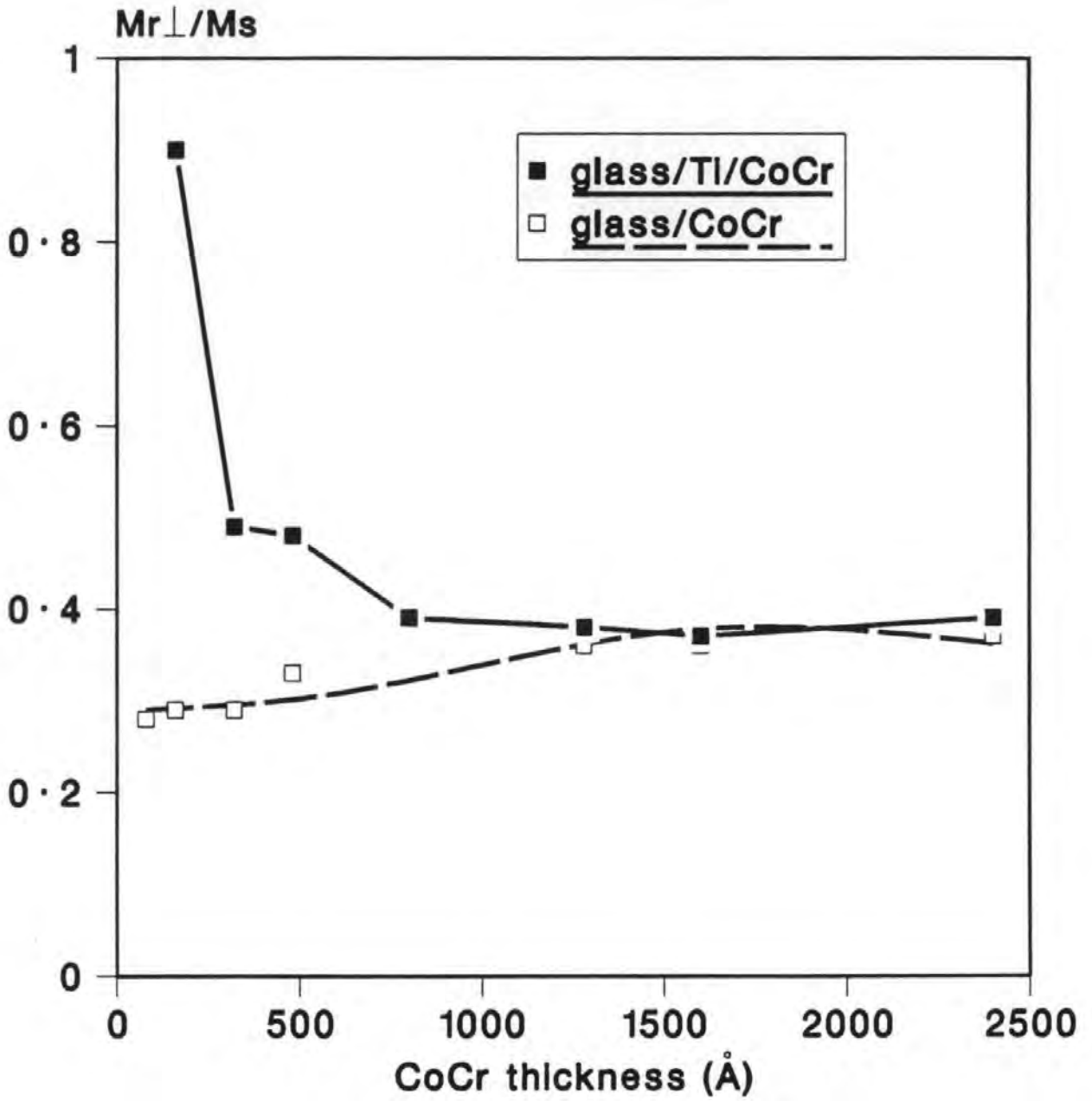


Figure 3.3: Perpendicular remanence ratio of CoCr films as a function of film thickness.

perpendicular loops to indicate the shearing of the perpendicular loops [69]. The same method is used in this work to describe the shearing of the perpendicular loops. Figure 3.2 is the dependence of the slope T on the film thickness. The dependence of perpendicular remanence ratio on the CoCr film thickness is plotted in figure 3.3. It can be seen from figures 3.2 and 3.3 that the Ti underlayer effects on the magnetic properties become very pronounced in the thinner film region. The slope T of the perpendicular loop of an 80 Å-thick CoCr film with Ti underlayer is about 13 and perpendicular remanence ratio 0.9, while for the same thickness CoCr film without Ti underlayer, only about 1.2 and 0.28. However, no significant underlayer effect on the perpendicular coercivity was observed at any thickness.

3.1.2 X-ray diffraction study of Ti/CoCr films

The x-ray diffraction patterns in figure 3.4 show that the CoCr films have an hcp structure with a main reflection peak of (0002) and the Ti underlayer has an hcp structure with a main reflection peak of (10 $\bar{1}$ 0). The (0002) reflection peak intensity of different thickness CoCr films with and without Ti underlayers is shown in table 3.1, from which one can see that the (0002) peak intensity of any thickness CoCr films deposited on Ti underlayers is much higher than that without Ti underlayers, which suggests the CoCr films deposited on Ti underlayers have better c-axis orientation. The better c-axis orientation appears to result in a bigger "shoulder" for perpendicular hysteresis loops of thick CoCr films and desheared, square loops for the thin ones.

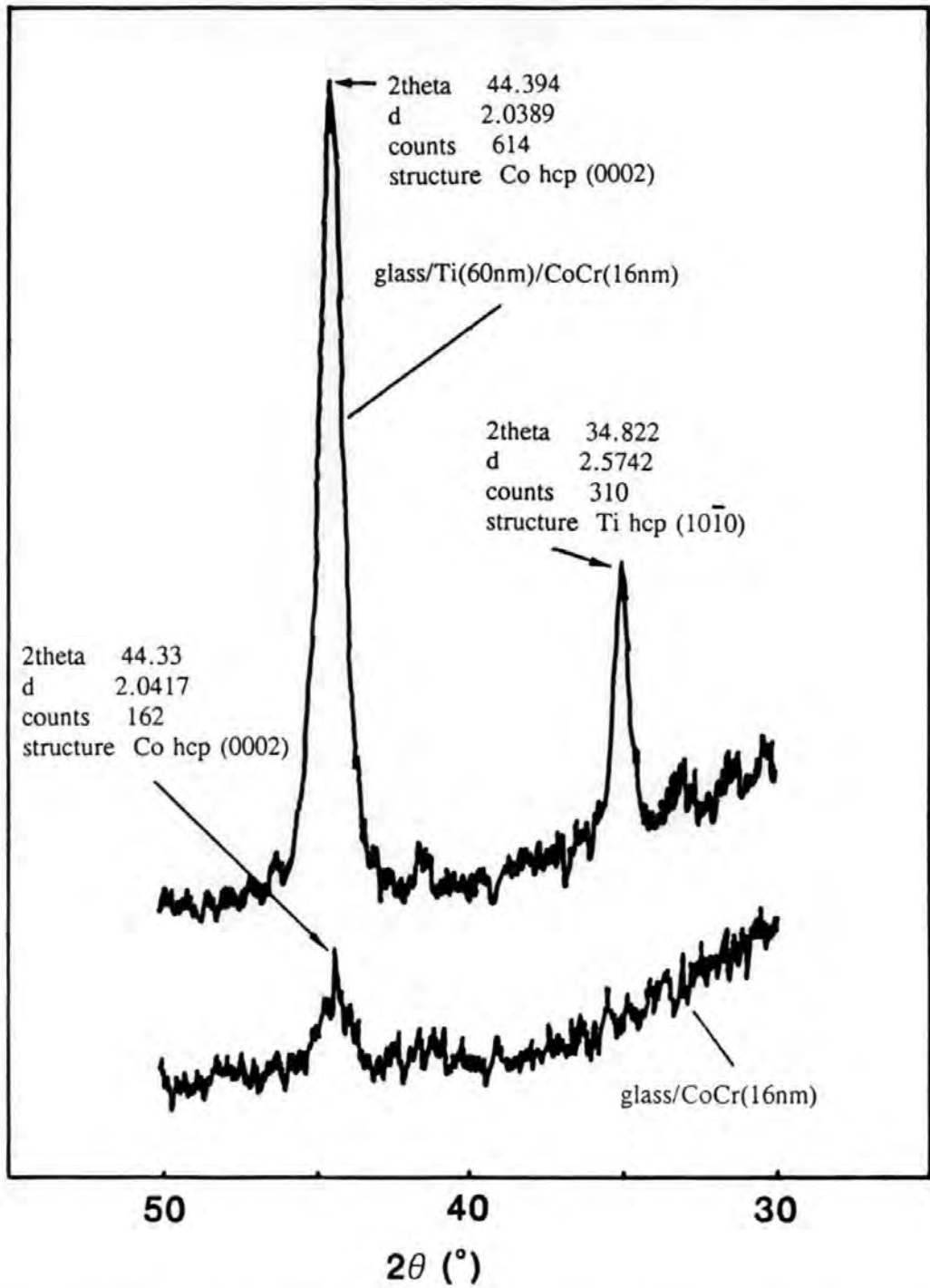


Figure 3.4: X-ray diffraction patterns of 160 Å-thick CoCr films with and without Ti underlayers.

Table 3.1: Thickness dependence of (0002) reflection peak intensity of CoCr films with and without Ti underlayers.

Film thickness	160 Å	640 Å	960 Å	1280 Å	1920 Å
I(0002) (cps) glass/Ti/CoCr	614	1,548	4,474	4,670	11,710
I(0002) (cps) glass/CoCr	162	934	1,778	1,946	3,824

3.1.3 Effect of Ti underlayer thickness

The effect of Ti underlayer thickness on the magnetic properties of very small thickness CoCr films (160 Å) is shown in figure 3.5 and 3.6. The perpendicular remanence ratio and the slope T can be in some degree changed by the existence of even a very thin Ti underlayer. This change is again related to the improvement of the (0002) orientation of the CoCr films, reaching the maximum at the Ti thickness of about 250 Å. Very thin CoCr films deposited on 250 or 600 Å-thick Ti underlayers exhibit little difference in their perpendicular loops. Therefore, a 250 Å-thick Ti underlayer is sufficient to provide a good substrate condition for the growth of highly (0002) oriented CoCr films. It can also be seen from figure 3.6 that the coercivity of a 160 Å-thick CoCr film is about 300 Oe and not affected by the Ti underlayer thickness.

The perpendicular M-H loops of 160 Å-thick CoCr films with and without Ti underlayers were also measured by VSM and results are shown in figure 3.7. The

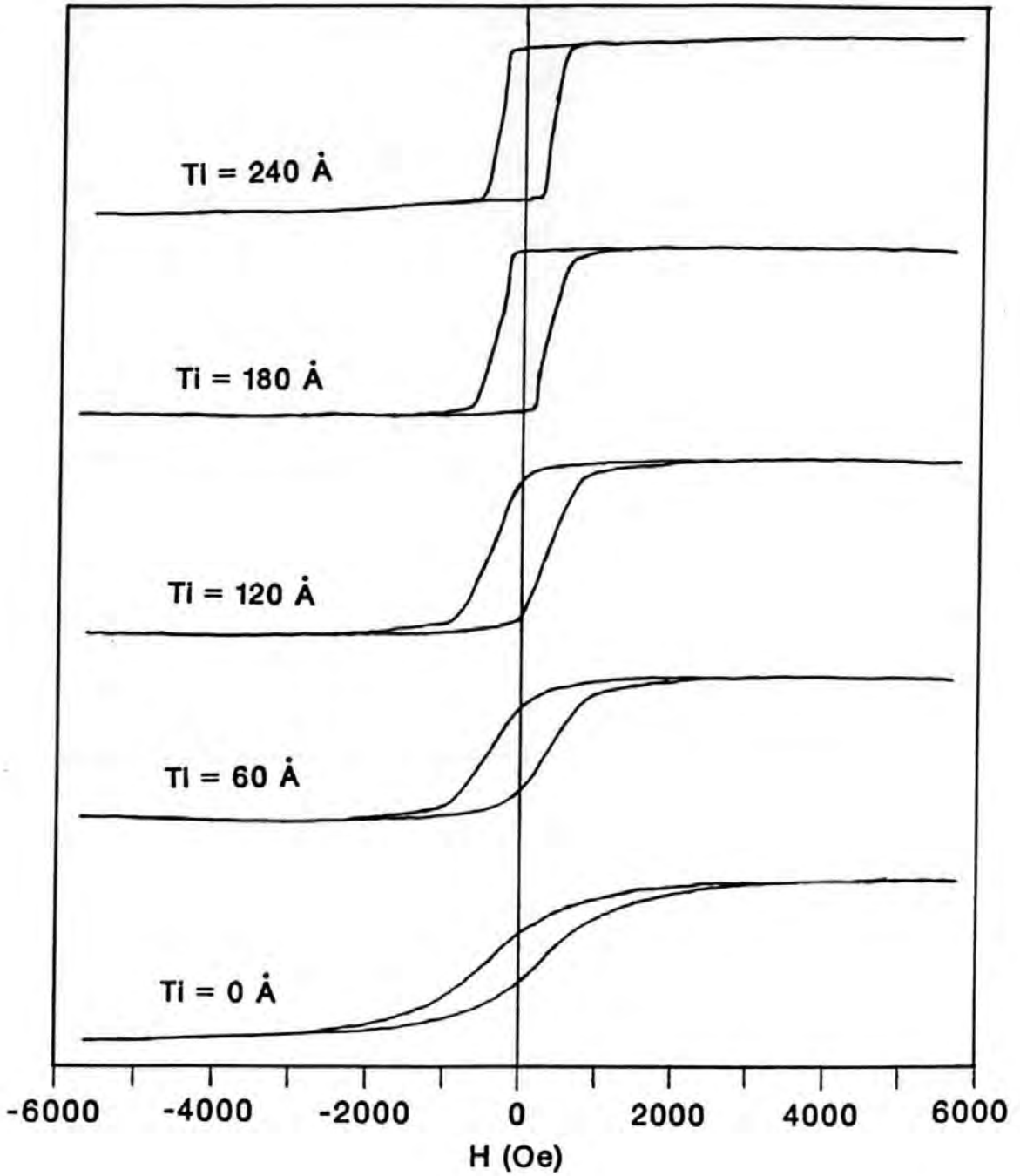


Figure 3.5: Effect of Ti underlayer thickness on perpendicular MOKE loops of 160 Å-thick CoCr films.

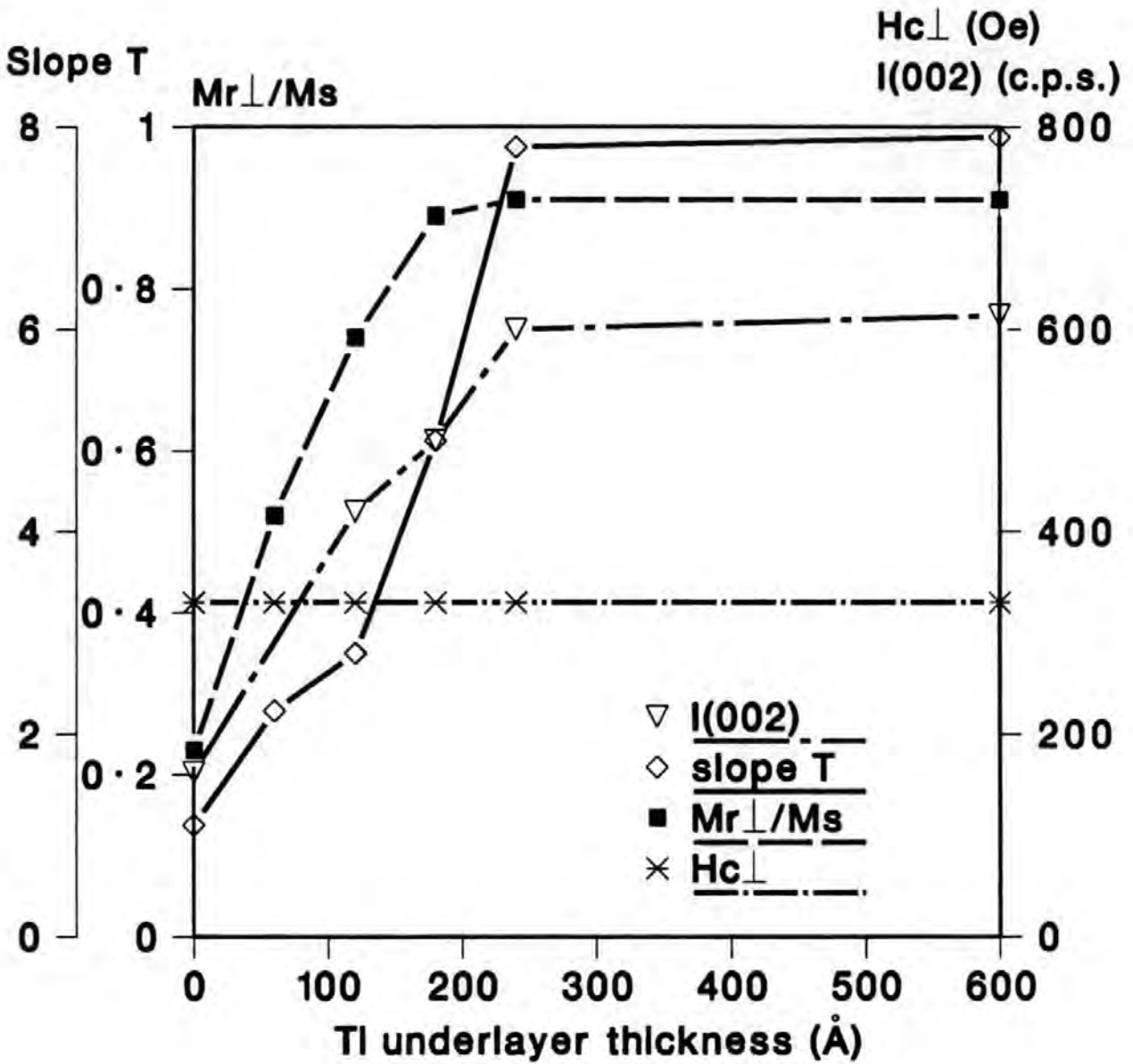


Figure 3.6: Effect of Ti underlayer thickness on perpendicular magnetic properties and $I(002)$ intensity of 160 Å-thick CoCr films.

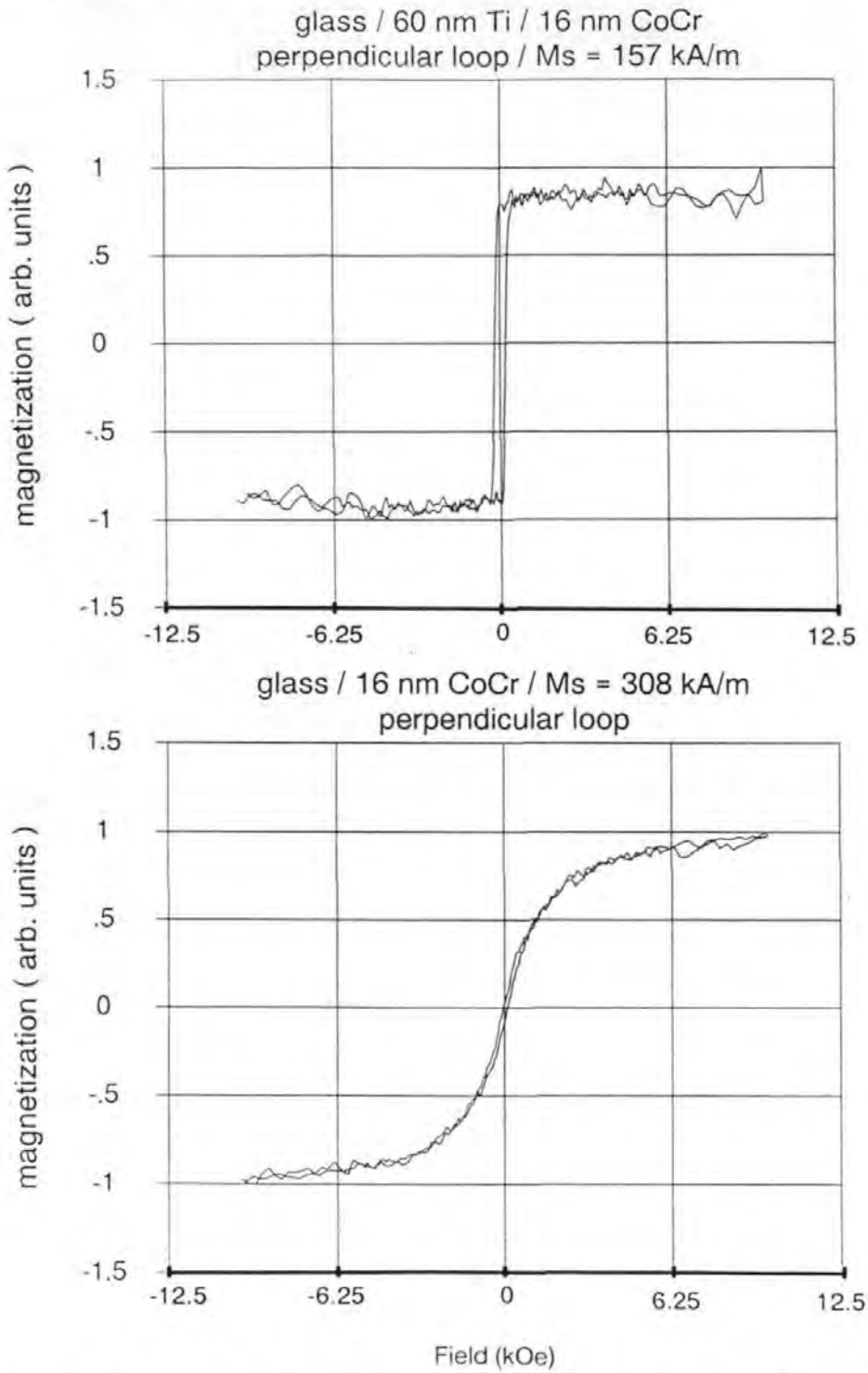


Figure 3.7: M-H loops of 160 Å-thick CoCr films with and without Ti underlayers measured by VSM.

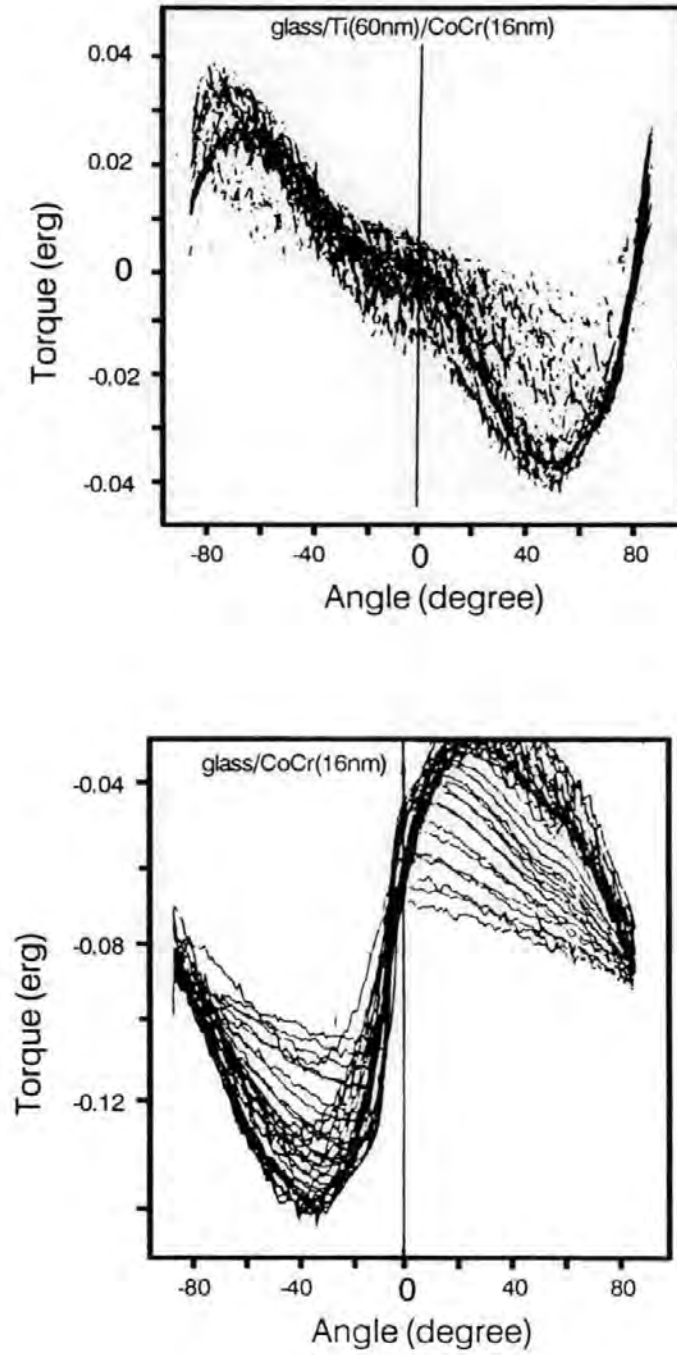


Figure 3.8: Torque curves of 160 Å-thick CoCr films with and without Ti underlayers.

VSM perpendicular M-H loop for the 160 Å-thick CoCr film on Ti is nearly square and unsheared whilst the loop for the same thickness CoCr film deposited without underlayer is thin, curved and sheared. These results are nearly in agreement with the corresponding MOKE loops except the coercivity value.

Figure 3.8 is the torque magnetometer measurement of the 160 Å-thick CoCr films with and without Ti underlayers. Torque curves for both samples are initiated with the applied field in the plane of sample. Under these conditions, torque curves which start at zero degree with a negative slope indicate an anisotropy perpendicular to the film plane and with a positive slope, an anisotropy in the plane of the film. As shown in figure 3.8 the CoCr on glass exhibits a typical in-plane anisotropy torque curve, while the CoCr film on Ti exhibits a perpendicular anisotropy torque curve. The magnetization easy axis of such a thin CoCr film is switched from the in-plane direction to perpendicular direction by the existence of Ti underlayer. These results are in a good agreement with the x-ray diffraction studies.

In summary, the experimental results so far show that very thin CoCr films deposited on Ti underlayers exhibit nearly square and de-sheared perpendicular loops. X-ray diffraction study shows that the Ti underlayers greatly improve the [0002] orientation of the hcp CoCr films though the Ti underlayer itself has a [10 $\bar{1}$ 0] texture. Torque curve measurement indicates that the very thin CoCr without underlayer exhibits an in-plane anisotropy whilst with Ti underlayer exhibits a perpendicular anisotropy.

It has been reported by several authors that the (0002) oriented hcp structure Ti and Ti-M alloy underlayers or amorphous-like Ge underlayers [74, 101] could greatly improve the c-axis orientation of CoCr films. An epitaxial growth model

had been proposed for this effect. However, the Ti underlayer used in this study, which has a strong effect on the [0002] texture of CoCr films, is not (0002) oriented, its main reflection peak of x-ray diffraction pattern is (10 $\bar{1}$ 0). A similar result has been reported by D. Jeanniot et al [77]. It seems that the high (0002) orientation of the underlayer is not essential for the growth of highly (0002) oriented CoCr films. More detailed studies are necessary to clarify the growth mechanism of CoCr film on underlayers.

3.1.4 Very thin CoCr film on different underlayers

Further experimental study of the very thin CoCr films deposited on other underlayers was undertaken. Figure 3.9 shows the perpendicular MOKE loops of the 80 Å-thick CoCr films on various underlayers. It can be seen from figure 3.9 that the squareness, slope and shape of the MOKE loops of the same thickness CoCr films depend strongly on the underlayers. The loops shown in the figure can be roughly classified into four categories: square and unsheared, square and sheared, curve-shaped, and, thin and flat. The 80 Å-thick CoCr films on Ti and Au exhibit unsheared square perpendicular loops though the height of the two loops is different, which is believed to be caused by the underlayer enhancement effect on the magneto-optic signals [67]. The 80 Å-thick CoCr films deposited on Carbon, Al underlayers or on amorphous Si substrate exhibit square and sheared MOKE loops. The CoCr deposited on Cu underlayers exhibits a curve-shaped MOKE loop and the CoCr on Cr underlayer shows a thin and flat perpendicular loop.

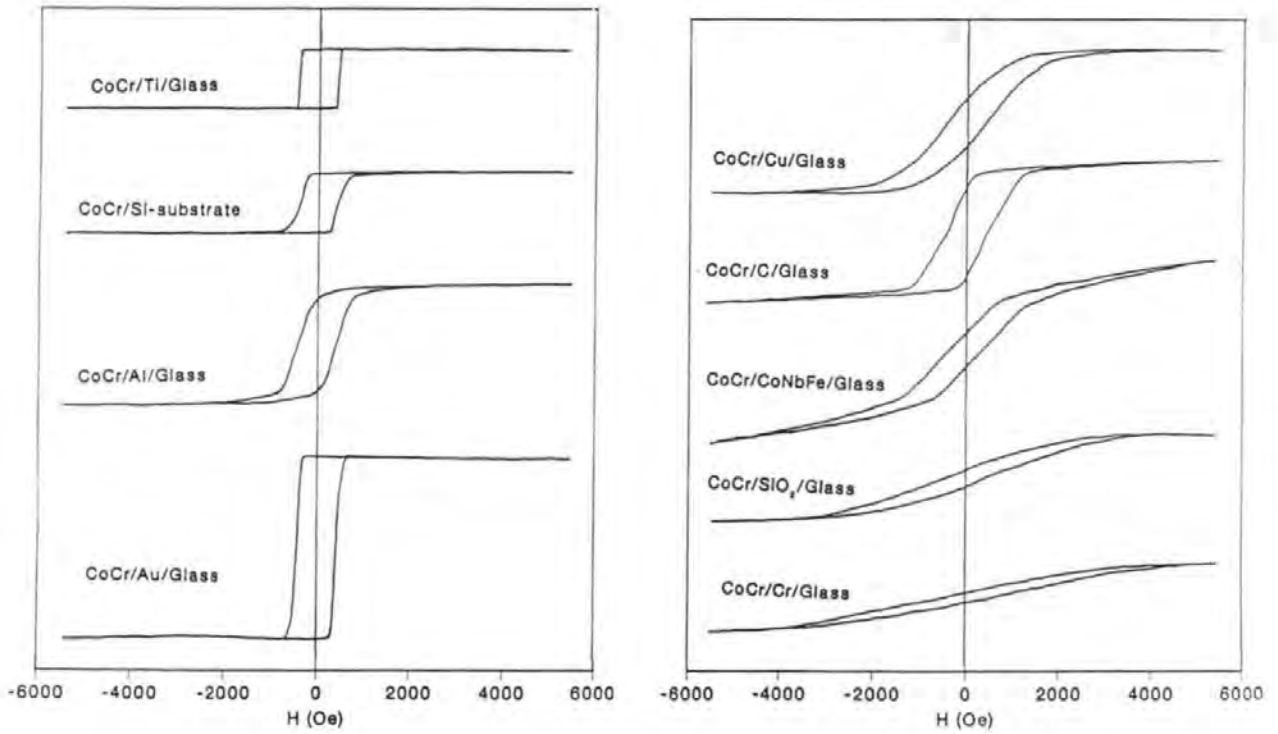


Figure 3.9: Perpendicular MOKE loops of 80 Å-thick CoCr films deposited on different underlayers, y-axis is arbitrary unit, but in the same scale.

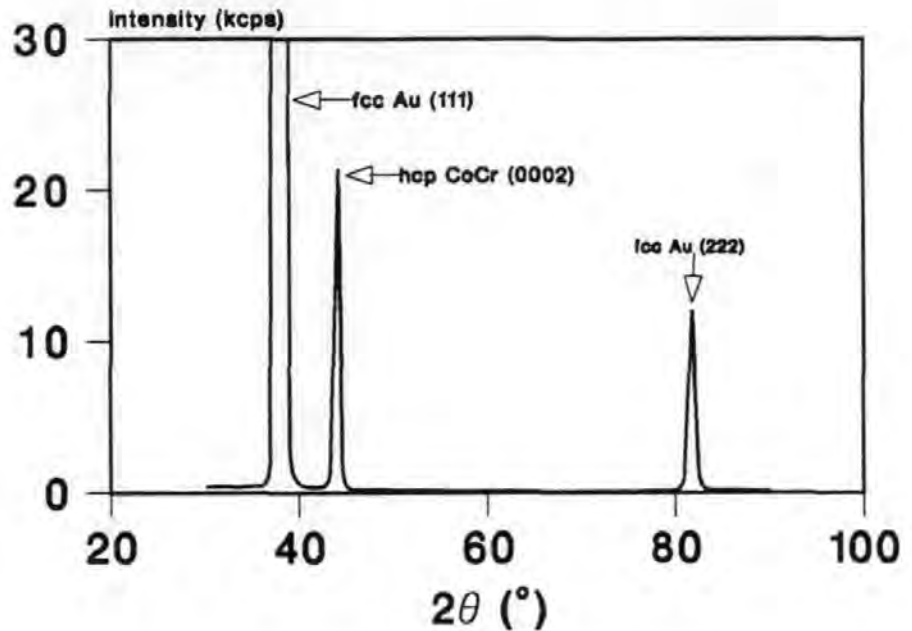
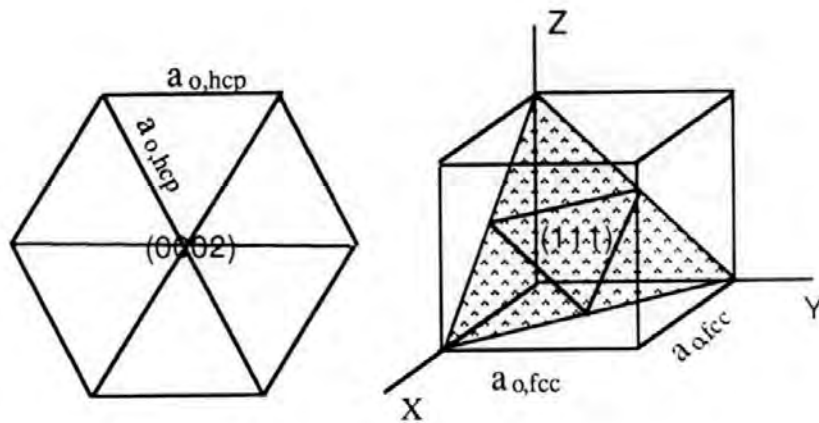


Figure 3.10: X-ray diffraction pattern of Au/CoCr(80Å) films.

3.1.5 X-ray diffraction patterns of Au/CoCr films

Figure 3.10 is the x-ray diffraction pattern of the Au(500Å)/CoCr(80Å) films which exhibit a rectangular unsheared perpendicular loop as shown in figure 3.9. It can be seen from the x-ray diffraction that the Au underlayer has a very strong fcc [111] texture and the very thin CoCr film on the Au underlayer has a strong hcp [0002] texture. It was found in our experiment that the [111] texture of the Au underlayer is essential for the growth of the very thin [0002] textural CoCr films. Such an orientation relation may be attributed to the "epitaxial growth" mechanism. This is depicted in figure 3.11. As shown by the figure, when the hcp CoCr films deposit on fcc [111] textural Au, the (0002) hexagonal lattice pattern appears to match the fcc (111) lattice pattern in spite of their large lattice misfit (15%).



$$\text{misfit} = \frac{a_{o,hcp} - \frac{\sqrt{2}}{2} a_{o,fcc}}{a_{o,hcp}}$$

Figure 3.11: Schematic representation of hcp (0002) and fcc (111) lattice planes and the lattice misfit calculation.

3.1.6 Electron diffraction study of film texture

In order to understand the textural relations between the CoCr films and their underlayers, the 160 Å-thick CoCr films on Ti, C, Cr and Cu underlayers were studied by TEM selected area diffraction (SAD). For the preparation of the TEM specimen, the CoCr films and their underlayers were deposited on glass disk substrates with precoated Carbon layers. The films were then floated off the substrates in water. The hysteresis loops of these films were examined by magneto-optic Kerr loop plotter after deposition and no significant difference from the loops shown in figure 3.9 was observed. The thickness of underlayers in all cases was 300 Å.

The C/Ti/CoCr, C/Cr/CoCr, C/Cu/CoCr and C/CoCr films were examined by selected area electron diffraction with specimen untilted and tilted with 30°. The SAD patterns of these films are shown in figure 3.13 and are indexed in tables 3.2 to 3.5.

As discussed in section 2.3.3, in electron diffraction only those planes which are near parallel to the incident electron beam contribute to the diffraction patterns. If we consider an hcp Co polycrystalline film with strong [0002] texture, the SAD pattern for such a specimen will be as shown in figure 3.12(a). The main reflection rings are $(10\bar{1}0)$, $(11\bar{2}0)$ and $(20\bar{2}0)$, ..., $(hki0)$, all of which are contributed from the lattice planes parallel to the film normal. Reflection rings of (0002) , $(01\bar{1}1)$, ..., $\{hkil\} (l \neq 0)$ would not appear. When the specimen is tilted through 30°, the $\{hki0\}$ rings break into arcs along the diameter parallel to the tilting axis and extra arcs, such as $(01\bar{1}1)$ would also appear along the perpendicular diameter because the $(10\bar{1}0)$ planes make an angle of 28° with the c-axis. The schematic drawings of SAD patterns of the $[11\bar{2}0]$ and $[10\bar{1}0]$ textural hcp polycrystalline films are shown

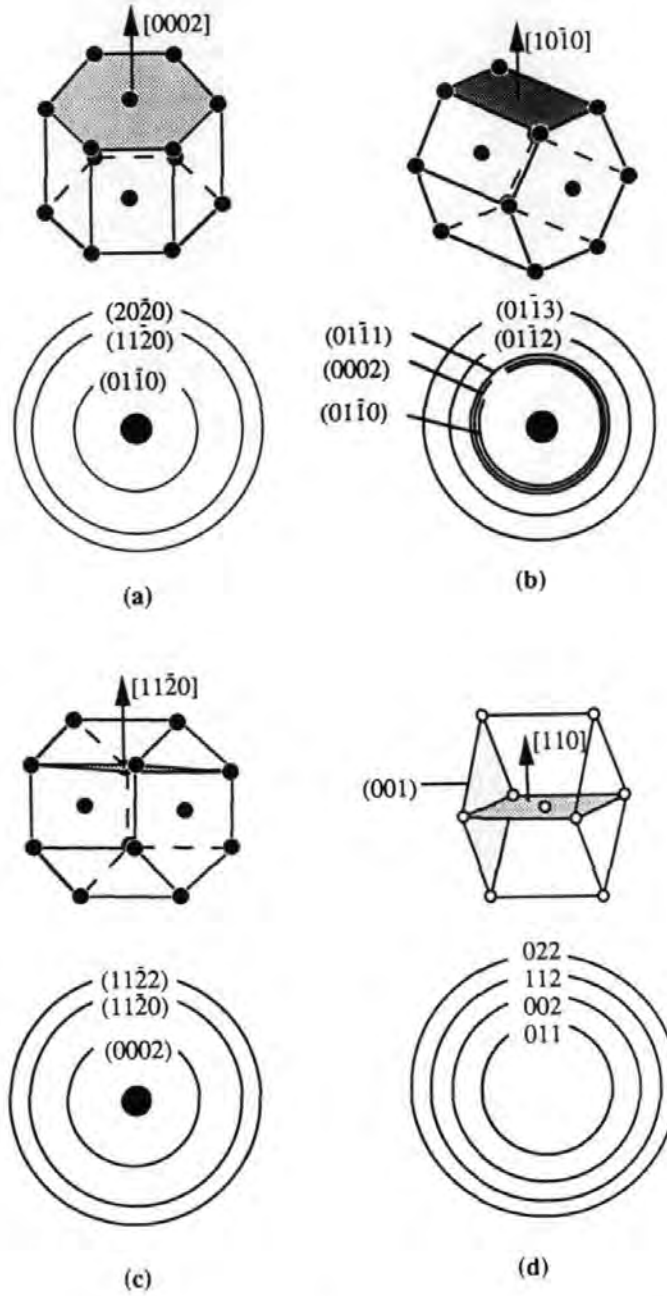


Figure 3.12: Schematic drawings of SAD patterns for hcp and bcc films with texture of (a) $[0002]$, (b) $[11\bar{2}0]$, (c) $[10\bar{1}0]$, and (d) $[110]$.

in figures 3.12(b) and (c) respectively. When we observe the SAD patterns of the $[11\bar{2}0]$ and $[10\bar{1}0]$ textural Co films with specimen tilted, it is more difficult to predict when arcs would occur for every family of planes because of the complex of angles with each family. However, one of the obvious features for such textural films is that the (0002) ring will break into arcs along the diameter parallel to the tilting axis. The SAD pattern for the $[110]$ textural bcc polycrystalline films is shown in figure 3.12(d).

It can be seen from figure 3.13 and tables 3.2 to 3.5 that the diffraction patterns of CoCr films on Ti and C underlayers with specimen untilted and tilted are as expected from a strong $[0002]$ textural hcp Co film. The main reflection rings of the hcp Co on both patterns are $(10\bar{1}0)$, $(11\bar{2}0)$ and $(20\bar{2}0)$ when untilted. Diffraction rings of the form $(000l)$, where $l \neq 0$, are not seen. When specimen was tilted at 30° , the $(10\bar{1}0)$, $(11\bar{2}0)$ and $(20\bar{2}0)$ rings are broken into arcs along the parallel diameter of the tilting axis. Extra arcs, such as $(01\bar{1}1)$, appear along the perpendicular diameter. The c-axis of such a film is therefore perpendicular to the film plane.

The CoCr film on Cr shows a mixed $[11\bar{2}0]$ and $[10\bar{1}0]$ zone axis pattern. When specimen was tilted, arcs from the (0002) planes can be seen. The c-axis of such a film is lying in the film plane.

The CoCr on Cu has no texture. Reflection rings from all zone axes are present on the SAD pattern. When tilted, the diffraction pattern remains unchanged.

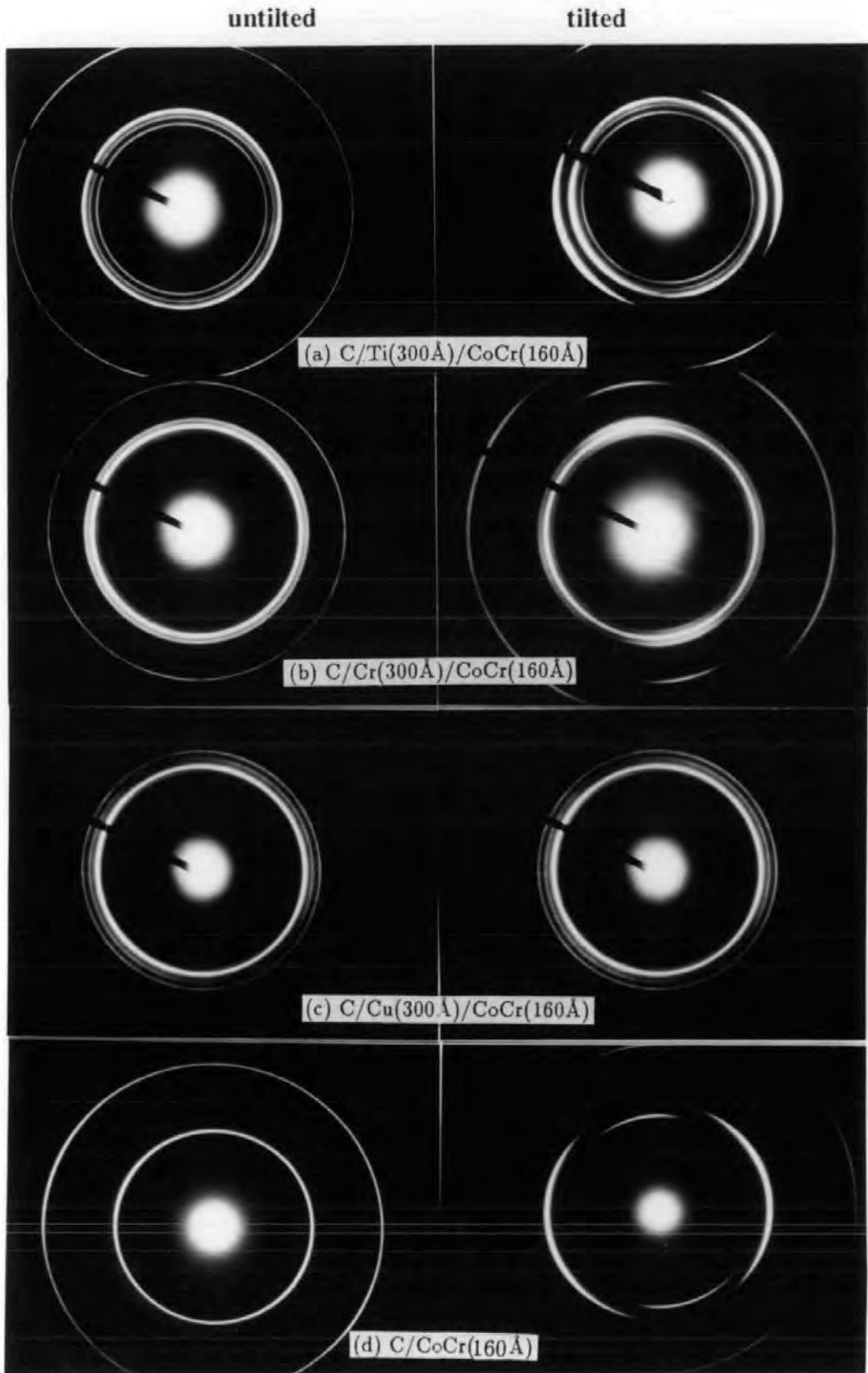


Figure 3.13: SAD patterns of 160 Å-thick CoCr films deposited on Ti, Cr, Cu and C underlayers.

Table 3.2: Summary of SAD patterns C/Ti(300Å)/CoCr(160Å) films with specimen un-tilted and tilted.

Ring	Diameter	Plane spacing [Å]		Structure	<i>hkil</i>	Untilted	Tilted
		measured	ASTM				
1	29.0	2.544	2.555	Ti hcp	10 $\bar{1}$ 0	medium ring	ring & arcs
2	31.5	2.342	2.342	Ti hcp	0002	medium ring	unchanged
3	32.9	2.242	2.243	Ti hcp	01 $\bar{1}$ 1	very weak ring	strong arcs \perp
4	34.0	2.170	2.170	Co hcp	10 $\bar{1}$ 0	strong ring	strong arcs
5	38.5	1.916	1.915	Co hcp	01 $\bar{1}$ 1	invisible	strong arcs \perp
6	42.9	1.72	1.72	Ti hcp	01 $\bar{1}$ 2	invisible	weak arcs \perp
7	50.2	1.470	1.475	Ti hcp	11 $\bar{2}$ 0	medium ring	medium arcs
8	55.2	1.337	1.332	Ti hcp	01 $\bar{1}$ 3	very weak ring	unchanged
9	58.6	1.259	1.253	Co hcp	11 $\bar{2}$ 0	strong ring	strong arcs
10	67.5	1.093	1.085	Co hcp	20 $\bar{2}$ 0	very weak ring	weak ring & arcs

Table 3.3: Summary of SAD patterns C/Cr(300Å)/CoCr(160Å) films with specimen un-tilted and tilted.

Ring	Diameter	Plane spacing [Å]		Structure	<i>hkil</i>	Untilted	Tilted
		measured	ASTM				
1	34.0	2.170	2.170	Co hcp	10 $\bar{1}$ 0	weak ring	unchanged
2	36.2	2.04	2.04	Cr bcc	011	strong ring	ring & arcs
3	36.2	2.038	2.035	Co hcp	0002	strong ring	ring & arcs
4	38.5	1.916	1.915	Co hcp	01 $\bar{1}$ 1	strong ring	ring & arcs
5	49.8	1.481	1.484	Co hcp	01 $\bar{1}$ 2	weak ring	weak arcs
6	51.0	1.447	1.443	Cr bcc	002	strong ring	strong arcs
7	58.6	1.259	1.253	Co hcp	11 $\bar{2}$ 0	weak ring	unchanged
8	62.4	1.182	1.178	Cr bcc	112	weak ring	medium arcs \perp
9	63.8	1.156	1.15	Co hcp	01 $\bar{1}$ 3	weak ring	unchanged
10	69	1.07	1.067	Co hcp	11 $\bar{2}$ 2	very weak ring	unchanged
11	72	1.02	1.02	Cr bcc	022	weak ring	ring & arcs

Table 3.4: Summary of SAD patterns C/Cu(300Å)/CoCr(160Å) films with specimen un-tilted and tilted.

Ring	Diameter	Plane spacing (Å)		Structure	<i>hkil</i>	Untilted	Tilted
		measured	ASTM				
1	34.0	2.170	2.170	Co hcp	10 $\bar{1}$ 0	weak ring	unchanged
2	35.3	2.09	2.087	Cu fcc	111	strong ring	unchanged
3	36.0	2.049	2.038	Co hcp	0002	medium ring	unchanged
4	38.5	1.916	1.915	Co hcp	01 $\bar{1}$ 1	weak ring	unchanged
5	41.0	1.80	1.808	Cu fcc	002	medium ring	unchanged
6	57.8	1.276	1.278	Cu fcc	022	medium ring	unchanged
7	58.6	1.259	1.253	Co hcp	11 $\bar{2}$ 0	medium ring	unchanged
8	68.0	1.085	1.085	Co hcp	20 $\bar{2}$ 0	medium ring	unchanged
9	69.4	1.063	1.067	Co hcp	11 $\bar{2}$ 2	weak ring	unchanged
10	71.0	1.039	1.044	Cu fcc	222	weak ring	unchanged

Table 3.5: Summary of SAD patterns C/CoCr(160Å) films with specimen un-tilted and tilted.

Ring	Diameter	Plane spacing (Å)		Structure	<i>hkil</i>	Untilted	Tilted
		measured	ASTM				
1	27	2.17	2.17	Co hcp	10 $\bar{1}$ 0	strong ring	strong arcs
2	28.8	2.034	2.035	Co hcp	0002	faint	faint
3	30.5	1.92	1.915	Co hcp	01 $\bar{1}$ 1	faint	strong arcs ⊥
4	46.6	1.257	1.253	Co hcp	11 $\bar{2}$ 0	strong ring	strong arcs
5	53.8	1.089	1.085	Co hcp	20 $\bar{2}$ 0	medium ring	medium arcs
6	55	1.065	1.068	Co hcp	11 $\bar{2}$ 2	faint	strong arcs ⊥
7	61.2	0.957	0.957	Co hcp	02 $\bar{2}$ 2	invisible	weak arcs ⊥
8	71.6	0.818	0.82	Co hcp	12 $\bar{3}$ 0	weak ring	medium arcs

The underlayer structure can also be clarified from these diffraction patterns. The Ti underlayer on carbon has a preferred hcp [0002] texture. The C underlayer is amorphous. The Cr underlayer has a preferred bcc [110] or [100] texture and the Cu underlayer has a fcc structure with no texture. The texture of the Ti underlayer on carbon is obviously different from the texture of Ti deposited on glass which exhibit a $[10\bar{1}0]$ texture, as seen in figure 3.4. Such a difference may be attributed to the effect of precoated Carbon layers. However the CoCr films on both kinds of Ti underlayers exhibit [0002] texture. This would certainly give rise to the complexity of the textural relations between the underlayers and CoCr films.

The relationship of the underlayer texture and the CoCr texture obtained from the electron diffraction study is summarised as follows:

$$\begin{aligned} & \text{C(amorphous)/Ti[0002]/CoCr[0002]}, \quad \text{C(amorphous)/CoCr[0002]}, \\ & \quad \text{C(amorphous)/Cr[110]_{bcc}/CoCr}([10\bar{1}0] + [11\bar{2}0]), \\ & \quad \text{C(amorphous)/Cu(no texture)/CoCr(no texture)}. \end{aligned}$$

It is concluded from these electron diffraction studies that the thin and flat perpendicular loop(hard-axis type loop) of the C/Cr/CoCr films is due to the in-plane texture of the CoCr films, which explains why the Cr/CoCr films can be used as longitudinal recording media. The curve-shaped perpendicular loop of C/Cu/CoCr is due to its random easy axis(c-axis) orientation. The square or near square perpendicular loop of such very thin films is related to the excellent c-axis texture of the CoCr films. However, it is difficult to tell from the electron diffraction patterns that there is any textural difference in the C/Ti/CoCr films which exhibit a square and unsheared loop and the C/CoCr films which exhibit a square but sheared loop.

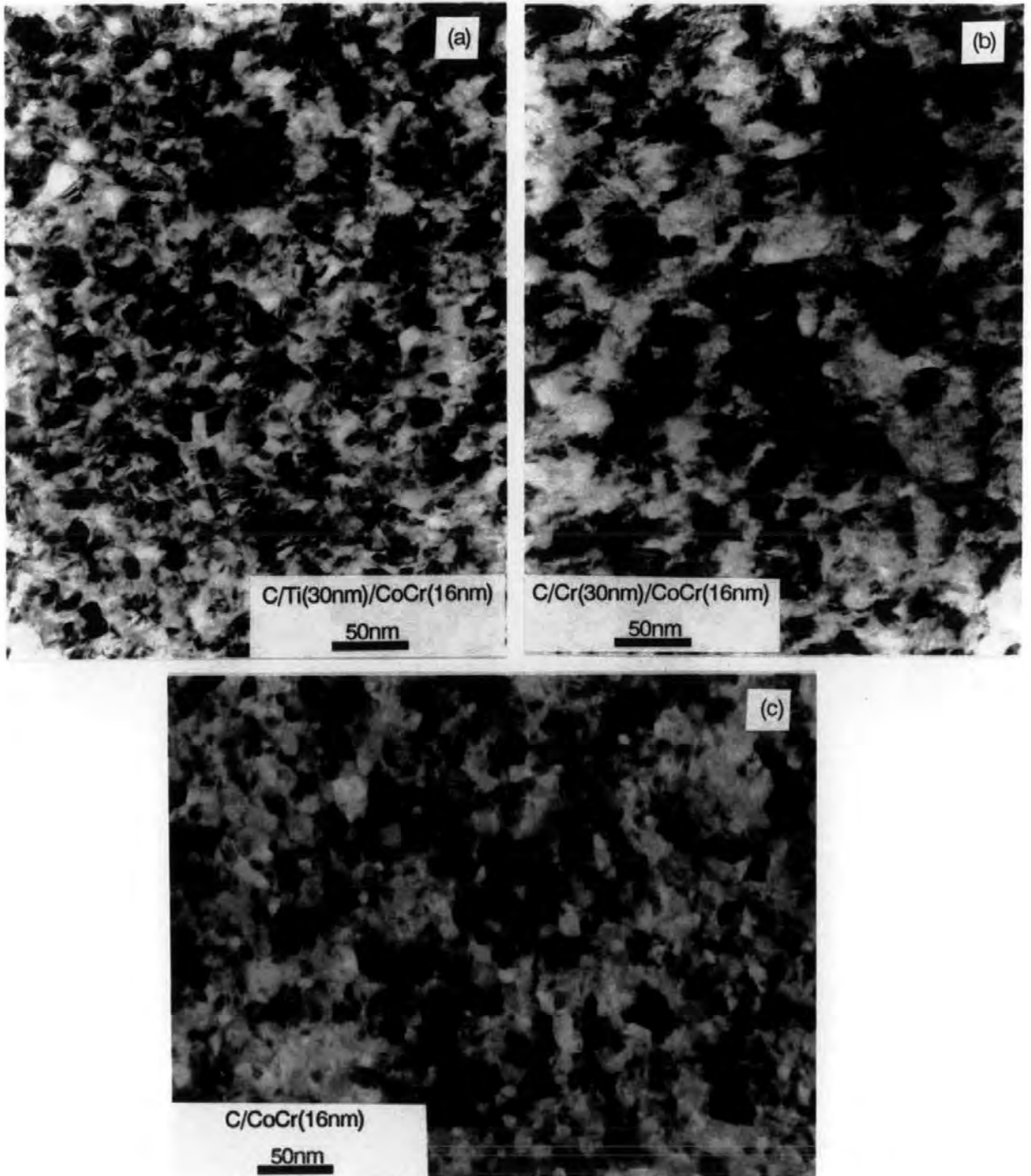


Figure 3.14: TEM bright field images of 160 Å-thick CoCr films on (a) Ti, (b) Cr and (c) C underlayers.

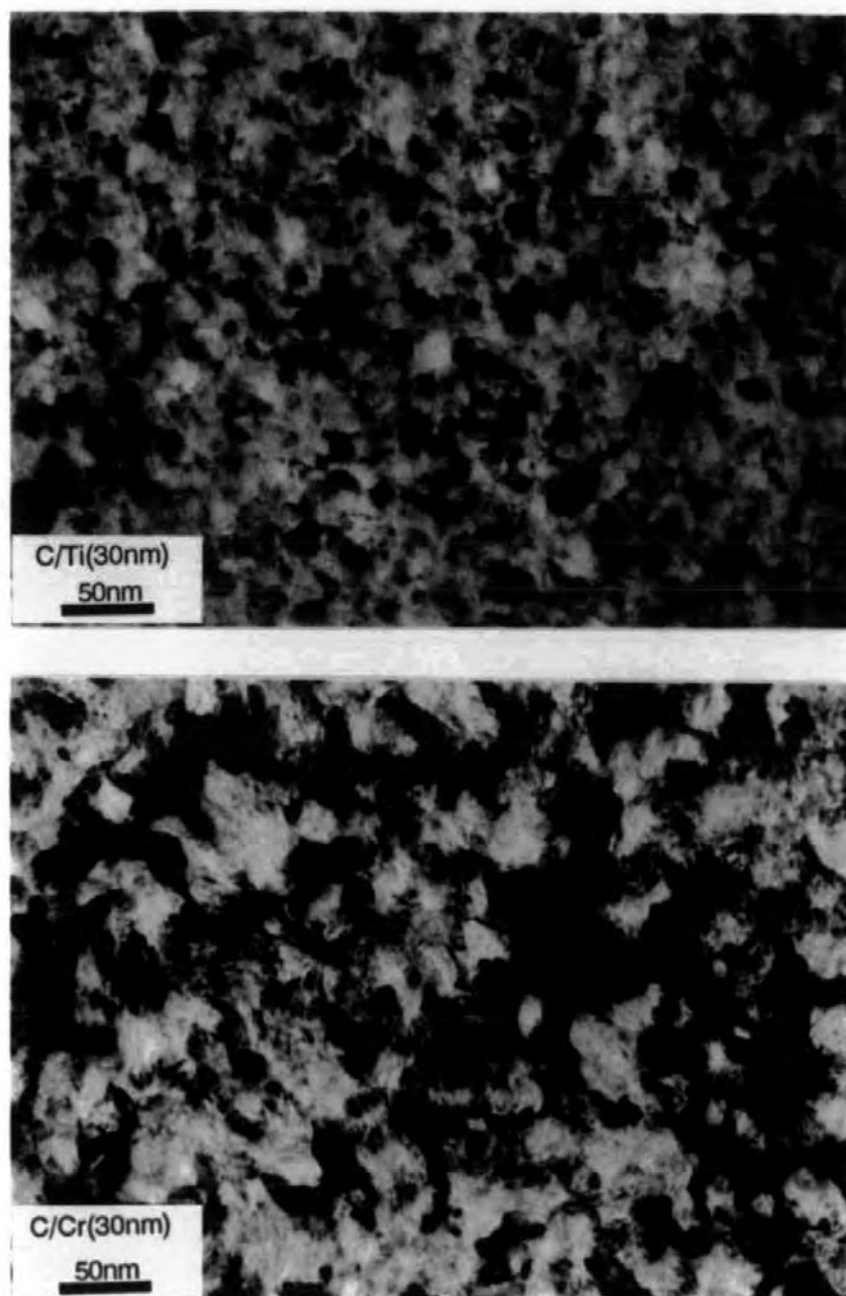


Figure 3.15: TEM bright field images of Ti and Cr underlayers.

3.1.7 Crystallographic microstructure examination by TEM

Figure 3.14 is the TEM bright field images of C/Ti/CoCr, C/Cr/CoCr, and C/CoCr films corresponding to the films in figure 3.13 (a), (b) and (d) respectively. The bright field images of Ti/CoCr and Cr/CoCr have contributions from both the CoCr and underlayers. For comparison, the bright field images for the same thickness of Ti and Cr underlayer deposited in the same condition are given in figure 3.15. It can be seen from figure 3.14(a) that the Ti/CoCr films have very well defined grains with grain size varying from 50 Å to 250 Å. The average grain size is about 100 Å. Striations can be seen on some grains which indicate the stacking faults of the crystals [88]. The bright field image of the Ti underlayer (figure 3.15(a)) shows the similar grain structure with smaller grain size. This may suggest that the top CoCr film replicated the grain morphology of the Ti underlayers. Stacking faults can also be observed for the Ti underlayer. In the case of Cr/CoCr, the grains are not very well defined (figure 3.14(b)) and can not be easily identified. If we compare the bright field image of Cr/CoCr with that of Cr underlayer(figure 3.15(b)), they again appear to be quite similar. The CoCr deposited on Carbon underlayer has very well defined and densely packed grains (figure 3.14(c)). The grain size is slightly smaller than that of Ti/CoCr films. The stacking faults are negligible for such films.

3.1.8 AES depth profiling of very thin CoCr films

The Auger electron microscopy (AES) depth profiling was used to investigate the composition distribution along the film depth of the 80 Å-thick CoCr films on Ti (300 Å) and Au (500 Å) underlayers. The two specimens were the same as those in figure 3.9 with Ti and Au underlayers. The removal rate for each film was 135

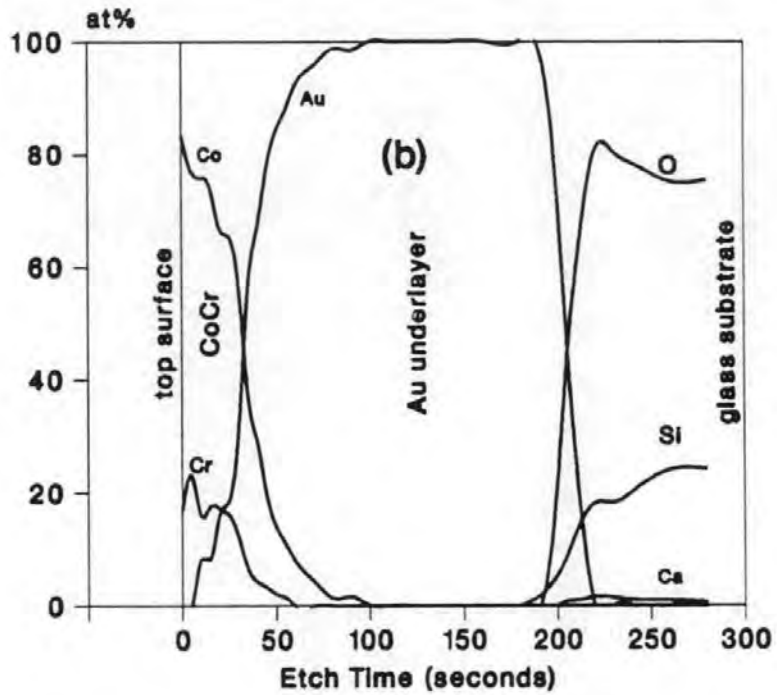
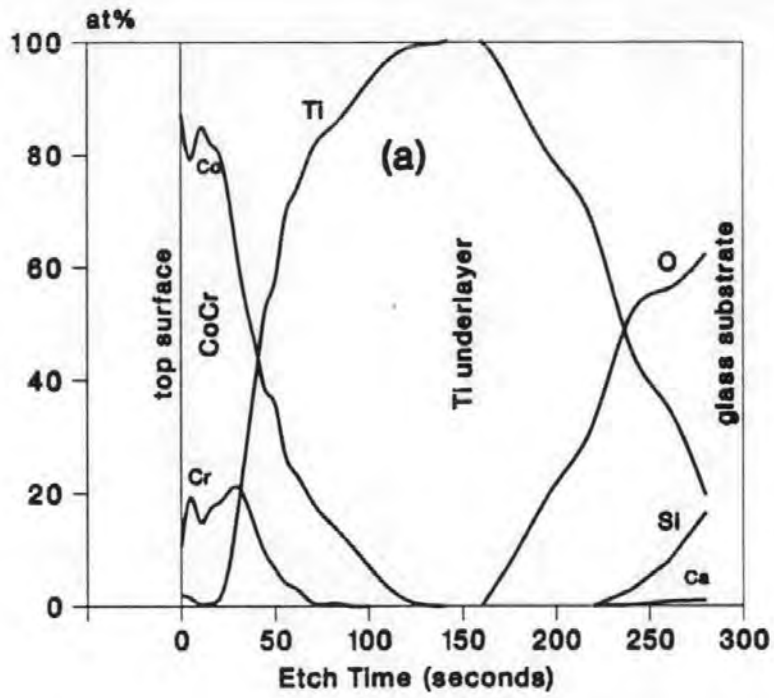


Figure 3.16: AES depth profiling of very thin CoCr films on (a) Ti) and (b) Au underlayers.

Å/min for CoCr, 127 Å/min for Ti and 226 Å/min for Au.

Figure 3.16 shows the atomic composition versus the etching time for the two samples. There was some contamination detected on the surface of the two samples such as Oxygen and Carbon but are not shown in this figure.

In figure 3.16 (a), the Ti underlayer has a long tail into the CoCr films, so does the CoCr well into the Ti underlayer. There are two possible reasons for such tails; the surface diffusion of each element and the response of the AES measurement to the non-flatness of the CoCr-Ti interface. If we now pay attention to the CoCr-Au interface in figure 3.16 (b), similar tails are also seen. However, for the interfaces of Au-glass and Ti-glass, the pictures are different. The Au-glass interface is very sharp which suggests the glass surface is actually very flat and there is also very little diffusion in the Au-glass interface, whilst the Ti-glass interface is quite similar to the CoCr-Ti interface where long tails are seen, which obviously indicates that the diffusion in the Ti-glass interface is quite active. Because the glass surface is very flat and the Au is not diffusion active, the tails detected in the CoCr-Au interface would represent the surface roughness of the Au underlayer which was developed during the films growth process due to the columnar growth nature of sputter-coated films [57]. The surface roughness estimated from the tail length is about 150 Å, greater than the CoCr film thickness. Therefore, CoCr films with such a small thickness are very likely not continuous. The tails in the CoCr-Ti interface may also be caused by the surface roughness of the Ti underlayer though the interface diffusion is not negligible in this case. In conclusion, the very thin CoCr films on the Au and Ti underlayers may not be physically continuous due to the surface roughness of the underlayers developed during the film growth process. Further discussion

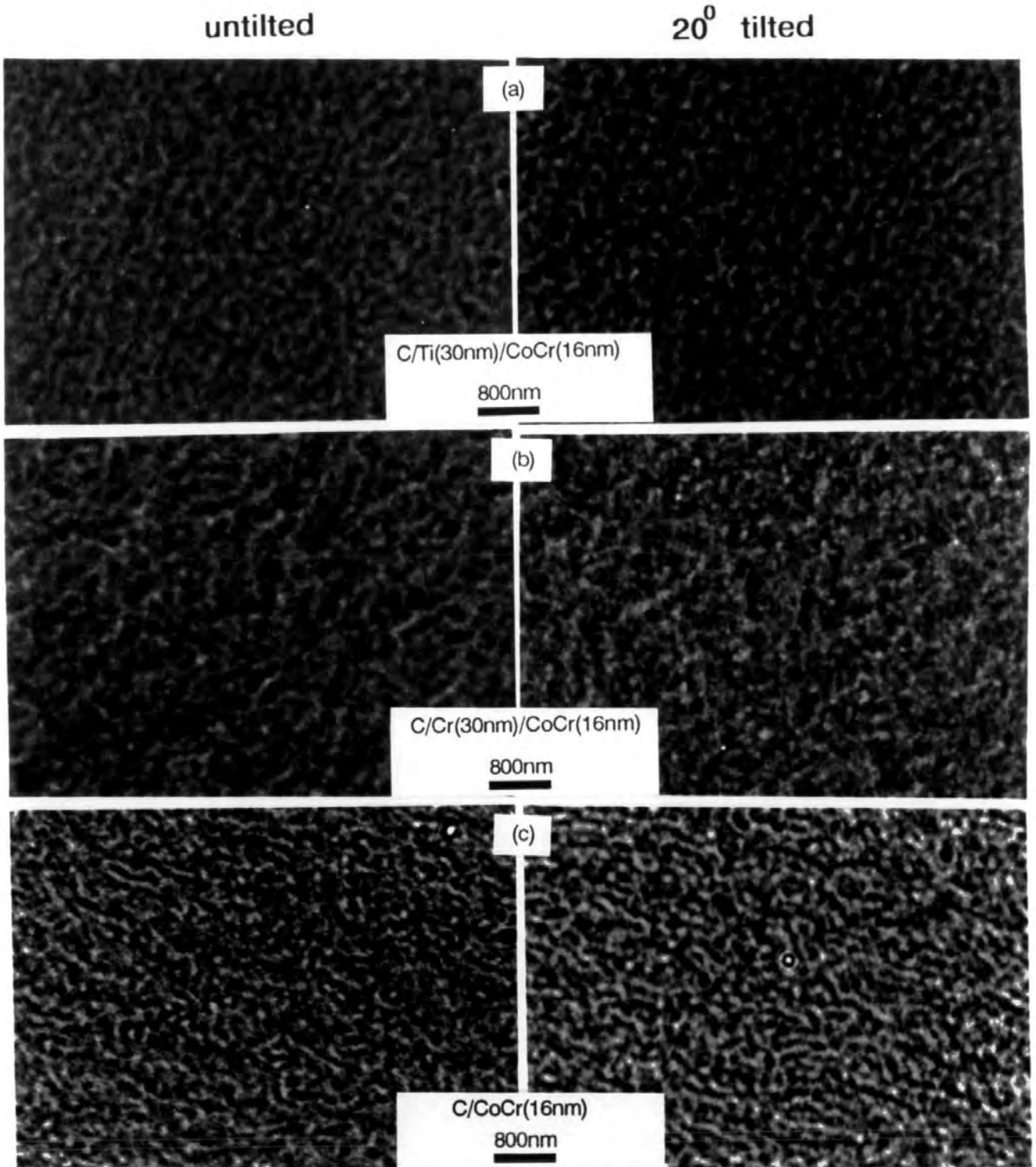


Figure 3.17: Fresnel images of the 160Å CoCr films on (a) Ti, (b) Cr and (c) C underlayers, at demagnetized state with specimen untilted and 20° tilted.

will be given on these AES depth profiling results in comparison with the surface morphology examinations of the CoCr films by HRSEM.

3.1.9 Magnetic domains of very thin CoCr films

The micromagnetic structure of the very thin CoCr films deposited on Ti, Cr and C underlayers was studied by Lorentz transmission electron microscopy at demagnetized state. The Fresnel images with specimen untilted and 20° tilted are shown in figure 3.17. All these samples show fine domain structure which are quite similar to those reported by Yeh et al[91] for very thin CoCrTa films on Cr underlayers. The tilting of the specimen makes no difference to the domain contrast of the CoCr film on Cr underlayer. However, for the CoCr films on Ti and C underlayers, the domain contrast is increased by tilting the specimen at 20°. This further proves that the very thin CoCr films on Ti and C underlayers exhibit strong perpendicular anisotropy and the CoCr film on Cr underlayer exhibits in-plane anisotropy.

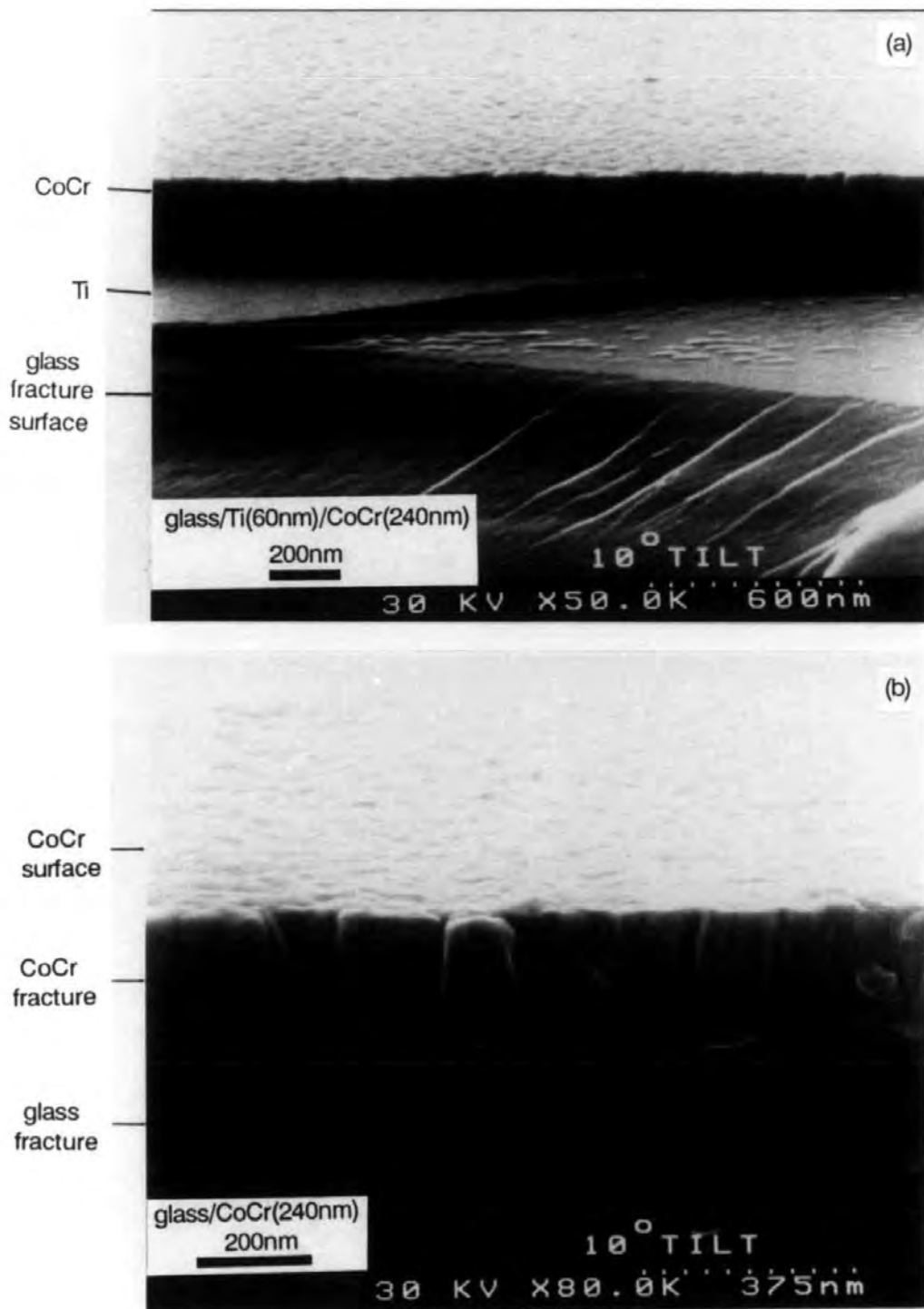


Figure 3.18: HRSEM micrographs of fractured cross sections of CoCr (2400 Å) on (a) Ti underlayer, and (b) glass.

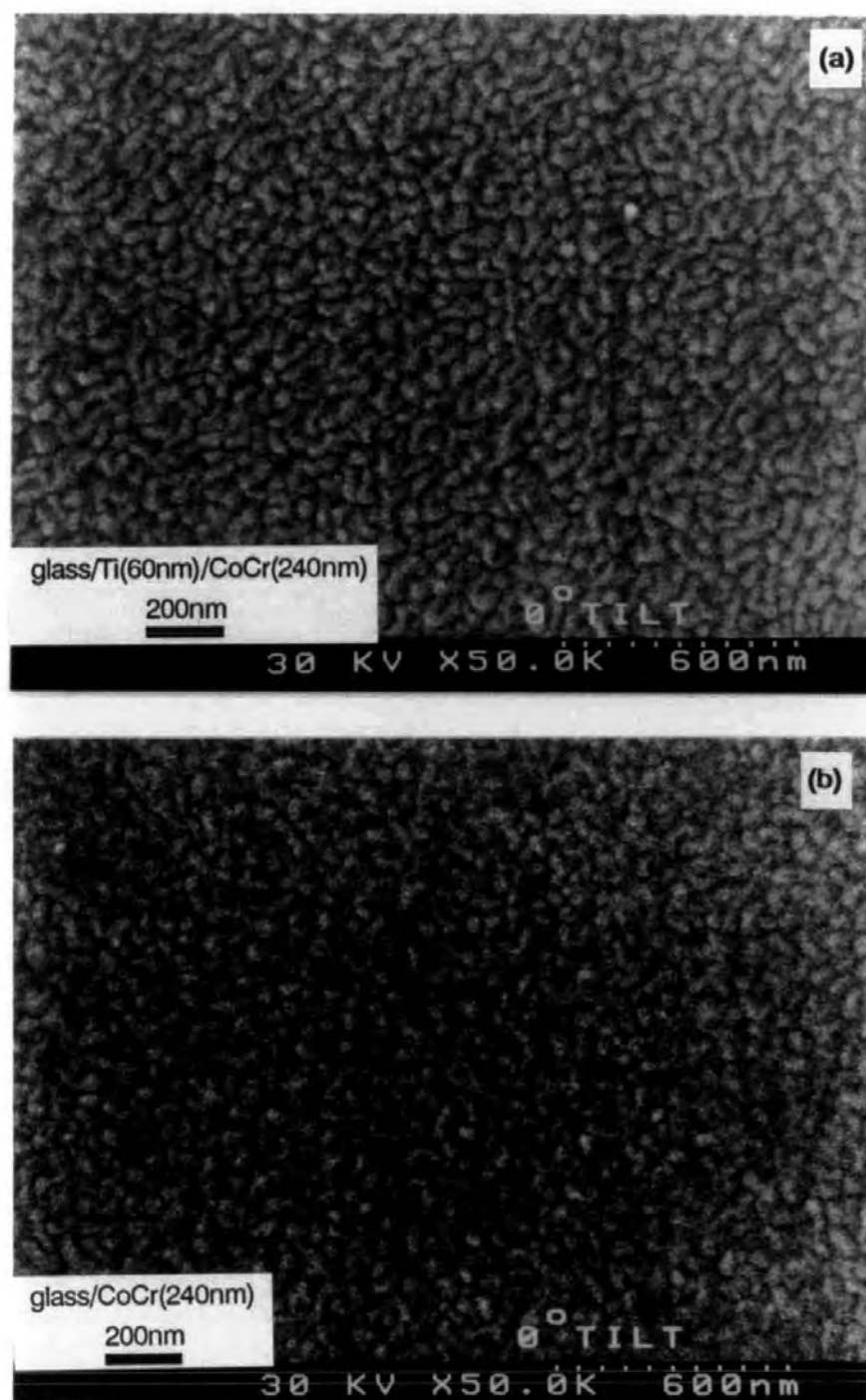


Figure 3.19: HRSEM micrographs of top surface of CoCr(2400 Å) on (a) Ti underlayer, and (b) glass.

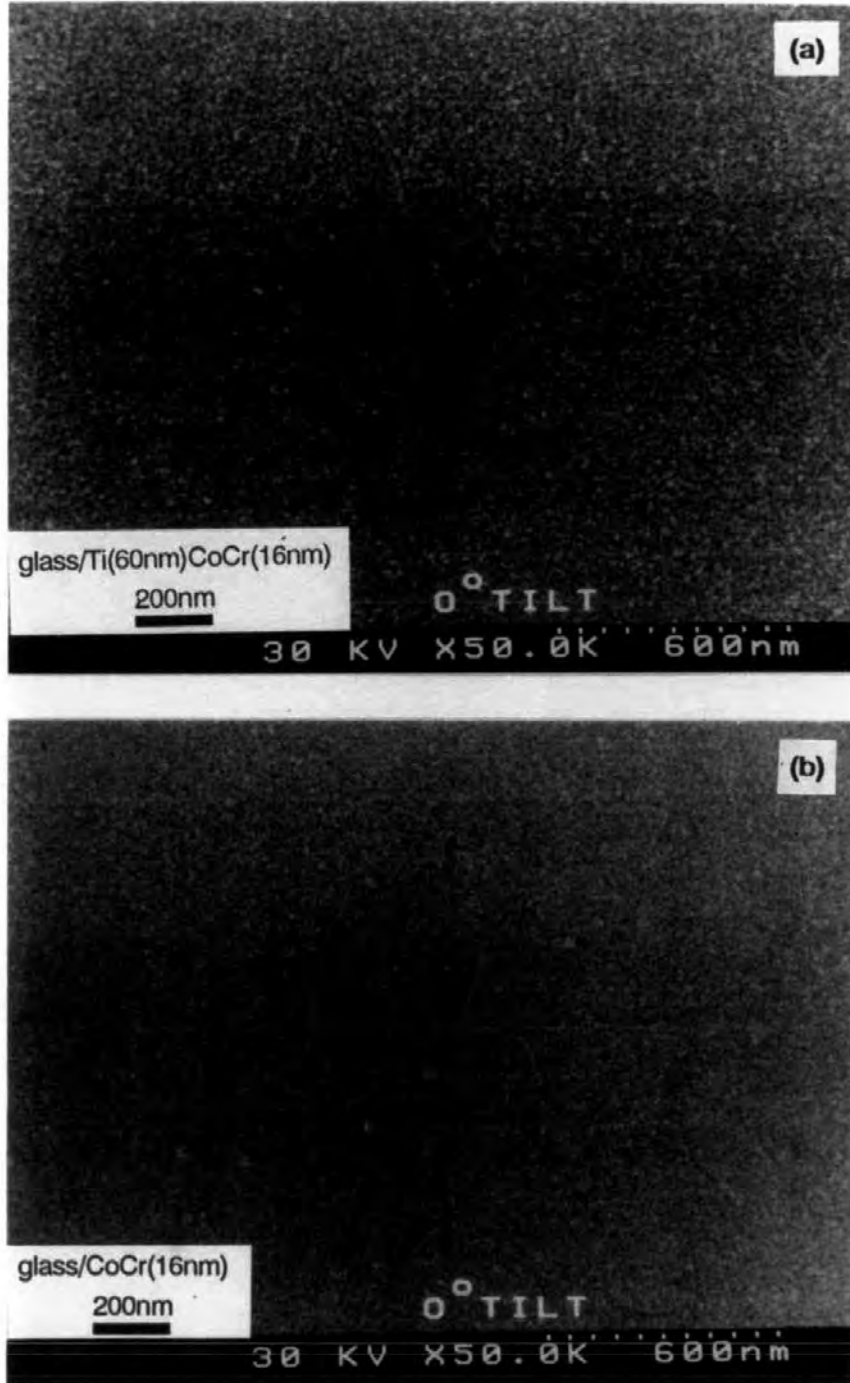


Figure 3.20: HRSEM micrographs of top surface of CoCr(160 Å) on (a) Ti underlayer, and (b) glass.

3.1.10 Physical morphology examination of CoCr films by HRSEM

Figure 3.18 is the HRSEM micrographs of the fractured cross sections of Ti(600Å)/CoCr(2400Å) and CoCr(2400Å) films on glass substrates. These micrographs revealed that both the CoCr films with and without Ti underlayers exhibit a columnar structure which corresponding to Thornton's zone 1 structure, as shown in figure 1.13. Such a structure is expected for a sputter-deposited coating on unheated substrates where the adatom mobility is limited. The columnar structure is a fundamental consequence of atomic shadowing acting in concert with the low adatom mobility [57]. It is not adequate to associate such a columnar structure with the crystallographic c-axis texture of the hcp CoCr films as claimed by some authors. As a result of such a columnar growth, the top surface of the CoCr is quite rough as shown in the figures. The surface morphology of the Ti underlayer can also be seen in figure 3.18(a), which is smoother than the surface of the CoCr films because of its finer columns due to its small thickness (600 Å).

Figure 3.19 is the HRSEM micrographs of the CoCr top surfaces of the two samples at the magnification of 50,000X, which shows an acicular and "worm-like" surface structure. The average column diameter of both CoCr films is around 400 Å. It can also be seen that the columns of CoCr on glass is not as elongated as those formed on Ti underlayer. This is probably due to the contribution of the Ti underlayer to the surface roughness. The HRSEM micrographs in figure 3.20 support this view.

Figure 3.20 shows the top surface HRSEM micrographs for the very thin CoCr films(160Å) with and without Ti underlayers. Very fine grains less than 100 Å in diameter can be seen from the top surface of the 160 Å-thick CoCr films on

Ti underlayers, which are in good agreement with the TEM bright field image. However, the same thickness CoCr on glass shows a very smooth surface. The grain size is not discernible at such a magnification. This may suggest that the fine grains seen in figure 3.20(a) represent the roughness of 600 Å-thick Ti underlayer resulted from its columnar growth.

It is therefore concluded that both the CoCr film and the Ti underlayer exhibit a columnar growth mechanism during the film growth process. Surface roughness develops during the film growth process due to the columnar growth nature. The column diameter and the surface roughness increase with the film thickness. And the top CoCr coatings always replicate the surface morphology of underlayers. This supports the AES depth profiling results which suggest the very thin CoCr films on Ti and Au are not physically continuous due to the surface roughness of the underlayers. Such a surface roughness is obviously the consequence of the columnar growth. The physical separation between columns may be partly responsible for the deshearing of the perpendicular loops of very thin CoCr films, which will be further discussed in section 3.1.13.

3.1.11 CoCrTa films on Pt, Au and Ti underlayers

CoCrTa films have been proposed as longitudinal recording media because of the high in-plane coercivity and low recording noise when deposited on Cr underlayers [80, 81, 82]. It has also been reported by Howard [83], Tamai and et al [84] that the addition of as little as 2 at.% Ta into the CoCr films could greatly increase the perpendicular coercivity of the media. This section presents the experimental study on CoCrTa films deposited on Pt, Au and Ti underlayers by RF-magnetron

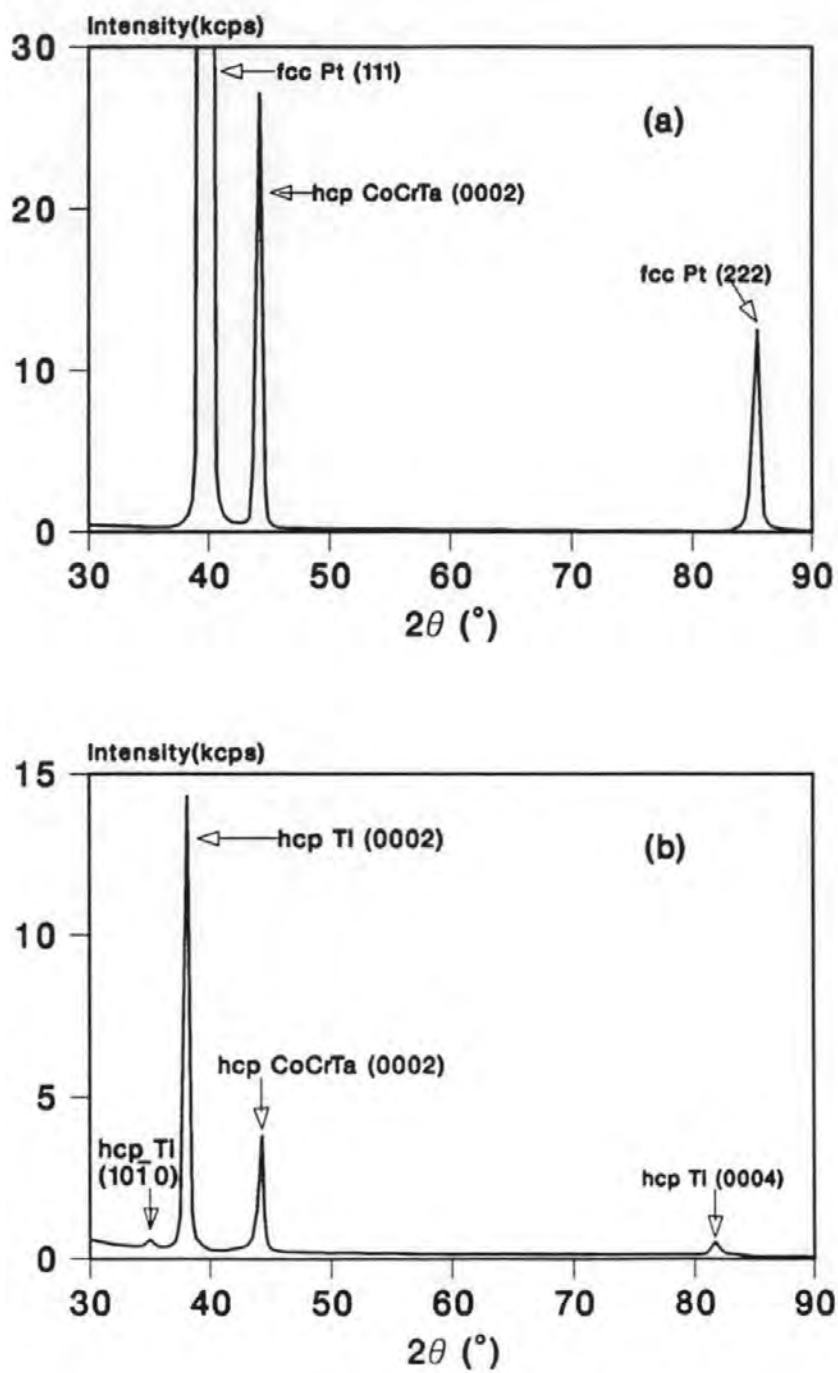


Figure 3.21: X-ray diffraction patterns of CoCrTa films on Pt (a) and Ti (b) underlayers.

sputtering. The CoCrTa were deposited by an alloy target with composition of $\text{Co}_{78.5}\text{Cr}_{17.5}\text{Ta}_4$. The film composition analysed by EDAX was $\text{Co}_{79}\text{Cr}_{18}\text{Ta}_3$. The deposition rate at 300W sputtering power was 670 Å/m for CoCrTa, 900 Å/m for Pt, 300 Å/m for Ti and 1900 Å/m for Au respectively. The saturation magnetization of the CoCrTa film is 540 emu/cc, independent of the underlayers used.

(a) Film texture and microstructure

Figure 3.21(a) shows the x-ray diffraction pattern of 440 Å-thick CoCrTa films deposited on Pt underlayers. The Pt underlayer thickness is 900 Å. X-ray diffraction shows that CoCrTa films deposited on fcc Pt, fcc Au and hcp Ti all exhibit strong [0002] texture. The Pt and Au underlayers exhibit a very strong [111] texture. The orientation relation of the CoCrTa films with Pt and Au underlayers is quite similar to that of CoCr films with Au underlayers(see figure 3.11). It was also found that the [111] texture of the Pt and Au underlayers is essential for the growth of [0002] textural CoCrTa films.

Figure 3.21(b) is the x-ray diffraction pattern of 440 Å-thick CoCrTa on Ti underlayer. The Ti underlayer deposited on glass disk substrate in this experiment has a preferred [0002] texture with a very weak $(10\bar{1}0)$ peak, which is different from the results as shown in figure 3.4, where the Ti underlayer has a $[10\bar{1}0]$ texture. Such a difference may be explained by the different Ti target and also the different sputtering equipment used in those two cases. However, the texture of the Ti underlayer of this experiment is quite similar to the one deposited on precoated Carbon layers for TEM study as shown in figure 3.13. In spite of the textural difference of the Ti underlayers, the Co-based films deposited on these Ti underlayers all have a good

[0002] orientation. It appears that the texture of the hcp underlayer does not play any important role in determining the texture of the Co-based films.

Table 3.6: $\Delta\theta_{50}$ of different thickness CoCrTa on Pt, Au and Ti underlayers.

CoCrTa film thickness	220 Å	440 Å	880 Å	2000 Å
$\Delta\theta_{50}$ OF CoCrTa on Pt	4.6	4.6	4.9	4.9
$\Delta\theta_{50}$ OF CoCrTa on Au	4.9	5	5.1	4.8
$\Delta\theta_{50}$ OF CoCrTa on Ti	10.5	8.8	4.8	4.9

The $\Delta\theta_{50}$ of the [0002] peak of different thickness of CoCrTa films on 900 Å-thick Pt, Au and Ti underlayers is shown in table 3.6. CoCrTa films deposited on Pt and Au underlayers show very small $\Delta\theta_{50}$ at any film thickness while the films deposited on Ti underlayers have relatively larger $\Delta\theta_{50}$ in the thinner film region. The $\Delta\theta_{50}$ approaches to the similar value as that on Pt underlayers when films grow thicker.

Figure 3.22 is the top surface view of the HRSEM micrographs for 2000 Å-thick CoCrTa films on Ti and Pt underlayers. The thickness of both underlayers was 900 Å. The obvious difference in the microstructure of these two films is the column diameter. The average column diameter is 500 Å for the 2000 Å-thick CoCrTa on Ti, and 250 Å for the same thickness CoCrTa on Pt. Such a difference in column

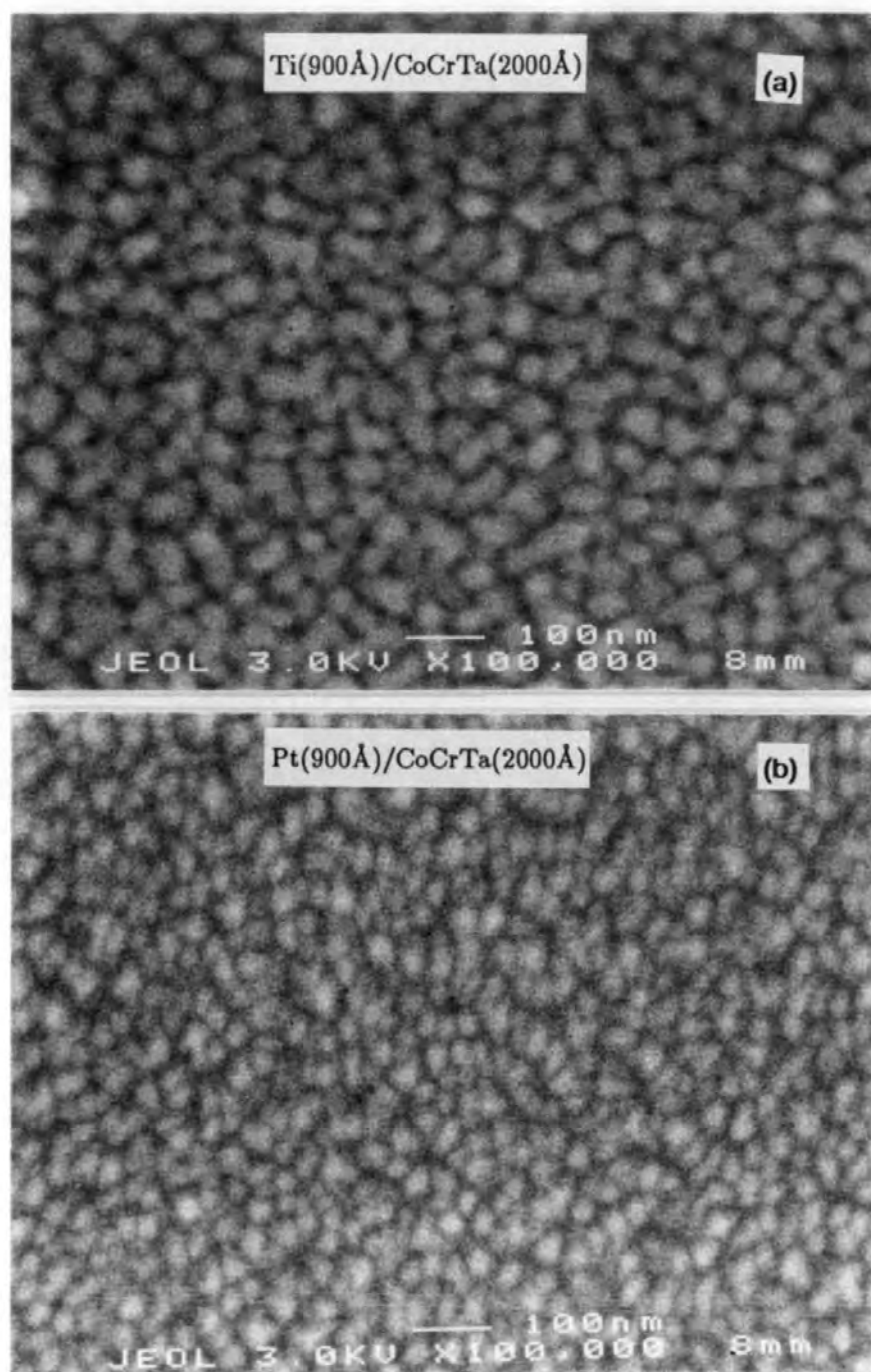


Figure 3.22: HRSEM micrographs of top surfaces of 2000 Å-thick CoCrTa films on Ti (a) and Pt (b) underlayers.

diameter may be attributed to the different grain morphology of the two underlayers which is determined by the nature of the underlayer material. One of the distinct differences of these two underlayers is the deposition rate. The high deposition rate of Pt (900 Å/m) may results in a fine grain structure under the low substrate temperature condition.

(b) Magnetic properties

The perpendicular coercivity of the CoCrTa films on Pt and Ti underlayers was measured by MOKE and VSM and results are shown in figure 3.23. The coercivity of both films is a strong function of film thickness. At very small thickness, both films exhibit small coercivity. As the film thickness increases, the coercivity of both films increases. However, the coercivities of CoCrTa films on Ti are much larger than that of CoCrTa on Pt films either by MOKE or by VSM. It is also noticeable from figure 3.23 that for the CoCrTa films deposited on Pt underlayers, the MOKE coercivity and VSM coercivity are nearly the same while for the films deposited on Ti underlayers, the MOKE coercivity is larger than the VSM coercivity. This is especially true in film thickness region of 400 Å to 1500 Å.

The shape of the perpendicular hysteresis loops of these films strongly relies on the underlayers used. The CoCrTa films deposited on Ti underlayers exhibit fat perpendicular loops with rounded "shoulder" and the films on Pt and Au underlayers exhibit thin, "waisted" loops with well defined "shoulder". The slope T of the hysteresis loops of CoCrTa films on Ti, Pt and Au underlayers is also a function of film thickness, increasing with the decrease of film thickness. For films with intermediate thickness, the slope T is not equal to unity. Figure 3.24 shows the typical VSM hys-

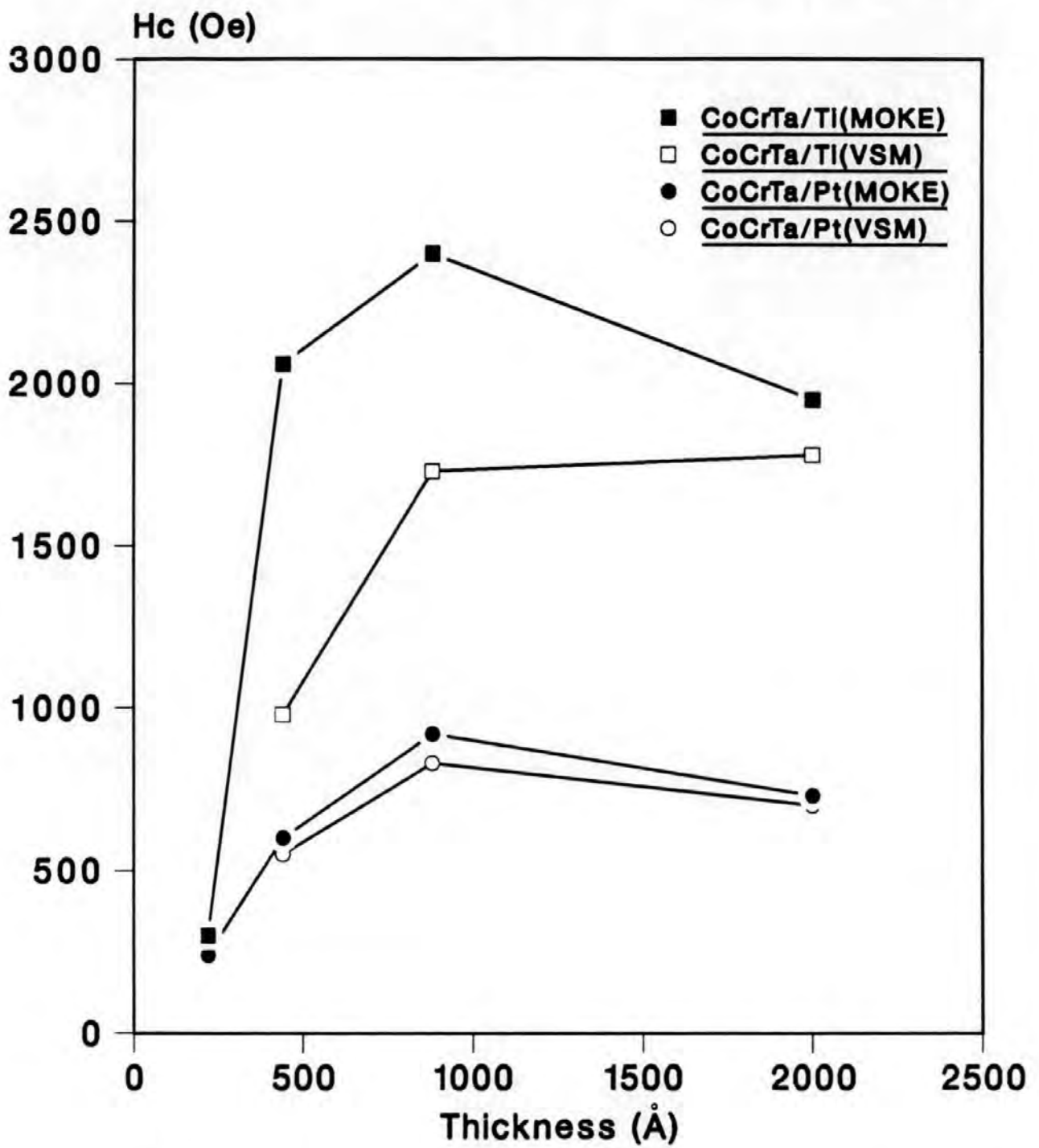


Figure 3.23: Thickness dependence of perpendicular coercivity of CoCrTa films on Pt and Ti underlayers measured by MOKE and VSM.

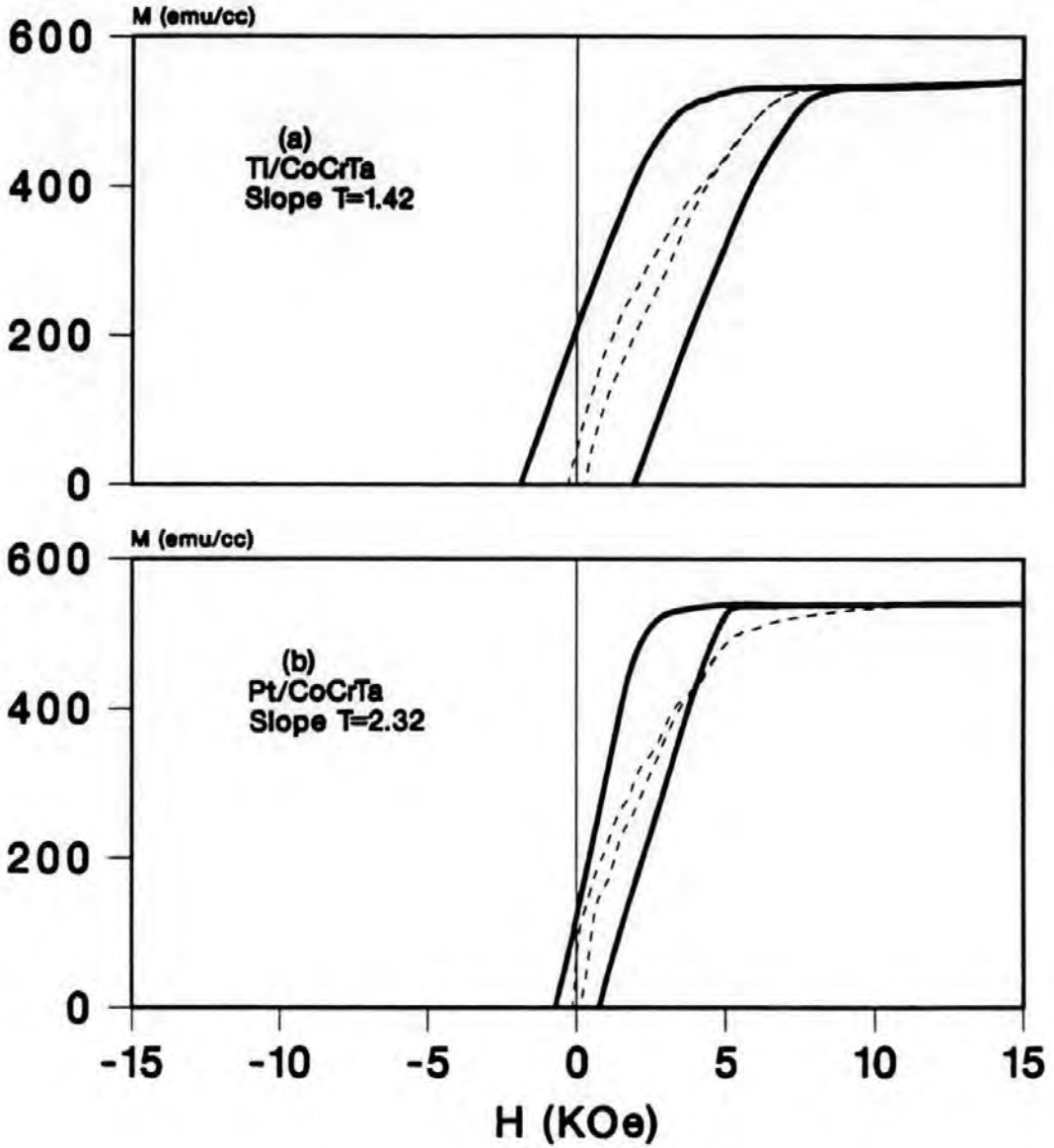


Figure 3.24: Typical VSM perpendicular (solid curves) and in-plane hysteresis loops (dashed curves) of CoCrTa films (2000\AA) on (a) Ti and (b) Pt underlayers.

teresis loops of the Ti(900Å)/CoCrTa(2000Å) and Pt(900Å)/CoCrTa(2000Å) films. The perpendicular coercivity of these two films is 2000 Oe and 700 Oe respectively. Slope T for the 2000 Å-thick CoCrTa on Ti is 1.42 while for the same thickness CoCrTa on Pt is 2.32.

3.1.12 Correlation of magnetic properties with microstructure

It has been seen from section 3.1.11 that there are distinct differences in the magnetic properties, such as perpendicular coercivity, MOKE and VSM coercivity, shape of perpendicular hysteresis loops and slope of hysteresis loops, between the CoCrTa films deposited on Pt and the CoCrTa films on Ti underlayers. The correlation of the magnetic properties with the film microstructure will be discussed in this section in conjunction with the recent theoretical development in the numerical micromagnetic computer simulation for the Co-based perpendicular media [22].

(a) Perpendicular coercivity and shape of M-H loops

The perpendicular coercivity of the Co-based films with thickness greater than a few hundred Å, as discussed in section 1.1.4, is closely related to the shape of the hysteresis loops which is in turn determined by the film microstructure. As seen in figure 1.4, a weak intergranular exchange coupling film exhibits a fat loop with a rounded "shoulder" whilst a strong intergranular exchange coupling film exhibits a thin, "waisted" loop with a well defined "shoulder". The coercivity decreases with increase of intergranular exchange coupling constant. If we compare the loops shown in figure 3.24 with figure 1.4, apparently, the CoCrTa on Ti exhibits a weak intergranular exchange coupling loop whilst the CoCrTa on Pt, a stronger inter-

granular exchange coupling loop. The difference in magnetic properties of these two films can therefore be attributed to the difference in the intergranular exchange coupling constant. The intergranular exchange coupling constant C^* is defined by equation 1.27, which is proportional to A^* , $\frac{1}{K}$ and $\frac{1}{D^2}$, where A^* is the intergranular exchange energy constant which is a function of intergranular non-magnetic separation, K is the perpendicular crystalline anisotropy constant which depends on the [0002] orientation of the grains and D is the grain diameter. As has been shown in figure 3.22, the grain diameter of the 2000 Å-thick CoCrTa film on Pt underlayer is only half of that on Ti underlayer. Such a difference in grain size will make a significant difference in the intergranular exchange coupling constant. If we ignore the effect of A^* and K on C^* of the two films for the moment, the intergranular exchange coupling constant of the 2000 Å-thick CoCrTa on Pt, by equation 1.27, will be four times of that on Ti due to the difference in their grain diameter. Therefore, the smaller grain diameter of the CoCrTa films on Pt could be the major reason for its stronger intergranular exchange coupling constant. The CoCrTa films on Pt may also have larger C^* because of the reduced atomic shadowing effect by the fine grains which will result in smaller intergranular non-magnetic separation or larger A^* . The better [0002] orientation of CoCrTa films on Pt will lead to a slight reduction of the intergranular exchange coupling constant. However, the net result would be that the CoCrTa films on Pt have stronger intergranular exchange coupling than the CoCrTa films on Ti.

The well defined "shoulder" in the perpendicular loop, according to Zhu and Bertram [22], is a consequence of the change in the nucleation field during the magnetization reversal process. For a strong intergranular exchange coupling film, the

magnetization reversal process starts with an initial nucleation. The initial nucleation field is not affected by the intergranular exchange coupling field. However, the intergranular exchange coupling field reduces the nucleation field of the grains at the boundaries of the reversed domains. After the first reversed domain nucleates, the sum of the external applied field and the local demagnetizing field significantly exceeds the nucleation field for the domain wall motion. Therefore, the reversed domain expands almost without any change of the applied field and a "shoulder" in the beginning of the reversal point on the hysteresis loop results. Evidence of the Bloch wall motion was observed in the computer simulation. Big "shoulders" have been seen from the loops of Pt/CoCrTa and Au/CoCrTa films of any thickness. They are all in line with smaller perpendicular coercivity in comparison with the coercivity of Ti/CoCrTa films. This supports the intergranular exchange coupling theory. The "well defined shoulders" are also observed in the CoCr films on Ti underlayers, as shown in figure 3.1, but the coercivity of such films is about the same value as that of the CoCr films without Ti underlayers which exhibit loops with rounded "shoulders". This is due to the fact that the perpendicular crystalline anisotropy of the the CoCr films without underlayers is very weak, they therefore exhibit small perpendicular coercivity. The comparison of the perpendicular coercivity as a function of the intergranular exchange coupling can only be made for films with the similar perpendicular crystalline anisotropy constant.

It was also predicted by the computer simulation[22] that the reduction of the nucleation field also makes the slope T of the hysteresis loop ($T = 4\pi[dM/dH]_{M=0}$) no longer equal to unity as in the zero or weak intergranular exchange coupling films. The change of slope T has been seen in the CoCrTa films on Pt underlayers

($T = 2.32$), which supports the computer simulation. However, the slope T of the 2000 Å-thick CoCrTa films on Ti is not equal to unity either ($T = 1.47$) as it would have been if predicted by the computer simulation for a weak intergranular exchange coupling film. Such a discrepancy will be further discussed in section 3.1.13 in comparison with the particulate model proposed by Chang and Fredkin [71].

(b) Surface and bulk coercivity

As has been shown in figure 3.23, The MOKE coercivity of the CoCrTa films on Ti is much larger than the VSM coercivity. It was believed that the MOKE coercivity is a measure of surface coercivity and the VSM coercivity, a measure of bulk [90]. The difference of surface and bulk coercivity may indicate the non-uniform magnetization reversal through the depth of the film. As has been discussed in section 1.1.4, the perpendicular coercivity is a function of the perpendicular crystalline anisotropy constant K and intergranular exchange coupling constant C^* of the film. For a zero or weak intergranular exchange coupling films, the maximum perpendicular coercivity is equal to or less than the perpendicular crystalline anisotropy constant. An increase in the intergranular exchange coupling will significantly reduces the perpendicular coercivity. If we apply such a coercivity theory to different depth layers of the Ti/CoCrTa films, we may speculate that the difference in the surface and bulk coercivity of the films is caused by the change in the perpendicular crystalline anisotropy constant and intergranular exchange coupling constant through the depth of the film. This appears to be strongly supported by the experimental results. As shown in table 3.6, the [0002] orientation of the CoCrTa films on Ti improves as the film grows thicker. The improvement of [0002] orientation will increase the per-

pendicular crystalline anisotropy constant and hence the perpendicular coercivity. Another fact is the larger grain diameter of the 2000 Å-thick CoCrTa films on Ti, which may suggest that the grains in the CoCrTa on Ti grow much faster in diameter than that on Pt underlayers. As has been seen from equation 1.27, larger surface grain diameter reduces the intergranular exchange coupling constant C^* , which will in turn increase the surface coercivity. The larger surface grains may also result in a larger intergranular separation or smaller A^* on the film surface due to the enhanced shadowing effect, which reduces the C^* and increases the surface coercivity further. Therefore, it is concluded that the larger surface coercivity of the CoCrTa films on Ti underlayers is caused by the improvement of the crystallographic orientation of the hcp Co crystals and by the development of large grains as the film grows thicker which results in a reduction in the intergranular exchange coupling constant due to large grain diameter and possible large intergranular separation.

3.1.13 The shearing of perpendicular loops

One of the most interesting phenomena observed in this work is the square and desheared perpendicular loops of very thin CoCr films deposited on Ti or Au underlayers. The shearing of the perpendicular loops of those films also depends on the film thickness (figure 3.1). Unsheared square loops or less sheared near square loops were obtained for very thin CoCr films on Ti, Au and other underlayers (figure 3.9).

Normally, the perpendicular loops of CoCr films are sheared because of the demagnetizing field along the film normal. The slope T of the loop at coercivity is equal to unity. Any deviation from this is considered to be anomalous. The anomaly of the shearing of perpendicular loops has been reported by other authors [69] for

CoCr films thicker than 250 Å. There were various theoretical models to explain this phenomenon.

The first theoretical work to explain the anomalous shearing of the loops of CoCr films was proposed by Wielinga and Lodder [69] based on the stripe domain model. Their calculation showed that the slope of the hysteresis loops of CoCr films increases as the film thickness reduces. The calculated results fit well with their experimental measurements. They attributed such an anomaly to the wall-motion-like magnetization reversal process of the CoCr media. This appears to be strongly supported by Zhu and Bertram's computer simulation results in which they claimed, as discussed in section 3.1.11, the intergranular exchange coupling reduces the nucleation field of the particles at the boundaries of the reversed domains and causes wall-motion-like reversal at lower nucleation field after the first reversed domain nucleates. Consequently, a "shoulder" and an anomalous shearing of the loop results. However, since both the stripe domain model and the computer simulation are based on Bloch walls which exist only in films thicker than 400 Å [69], it would not be adequate to apply them to the very thin films which exhibit square loops.

Two particulate models were proposed later by Wielinga and Lodder [70], and by Chang and Fredkin [71] respectively based on the column structure of the CoCr films and taking account of the non-magnetic separation between columns. Both models showed that the slope of the perpendicular hysteresis loops of CoCr films is a strong function of the thickness and intercolumnar non-magnetic separation of the film, particularly when the film is very thin, and concluded that the anomalous shearing is caused by the contribution of the columnar shape anisotropy to the total perpendicular shape anisotropy of the films.

In Chang and Fredkin's model [71] the structure of the perpendicular medium is simulated by ferromagnetic single domain columns which are arranged as concentric circles with intercolumnar non-magnetic separation a . The intrinsic saturation magnetization of the columns is equal to M_s and uniformly perpendicular. For such a film structure the perpendicular demagnetizing factor N_z^F , which is different from that of continuous perpendicular films, is defined by,

$$N_z^F = 4\pi - \{[N_z(D + 2a) - N_z(D)] + [N_z(3d + 4a) - N_z(3d + 2a)] + \dots\}, \quad (3.1)$$

where $N_{z(x)}$ ($x = D+2a, 3D+2a, 3D+4a, \dots$) is the demagnetization factor taking the form for an ellipsoid. D is the column diameter and "a" is the non-magnetic gap between columns.

The slope T of the hysteresis loop is given by[71],

$$T^{-1} = \frac{D}{4\pi(D + a)} \{4\pi - [N_z(D + 2a) + [N_z(3D + 4a) - N_z(3D + 2a)] + \dots\} \quad (3.2)$$

It has been shown that the perpendicular demagnetizing factor N_z^F reduces significantly due to the intercolumnar non-magnetic gap of "a", particularly when the film becomes thinner. Because of the reduction in demagnetizing factor, the hysteresis loop of such films becomes desheared.

The calculated hysteresis loop slope T , with "a" values of 0, 10, 20, 30, 40, and 50 Å, are plotted in figure 3.25(dotted curve). For comparison, our experimental data of slope T for CoCr films with and without Ti underlayers are also plotted in the same figure. The results, as depicted in figure 3.25, show that for a columnar structure with zero non-magnetic gap (a continuous perpendicular film), the loop would show a normal shearing and the slope T is equal to unity, independent of the film thickness; and that for a columnar structure with a non-magnetic gap $a \neq 0$, the loop would

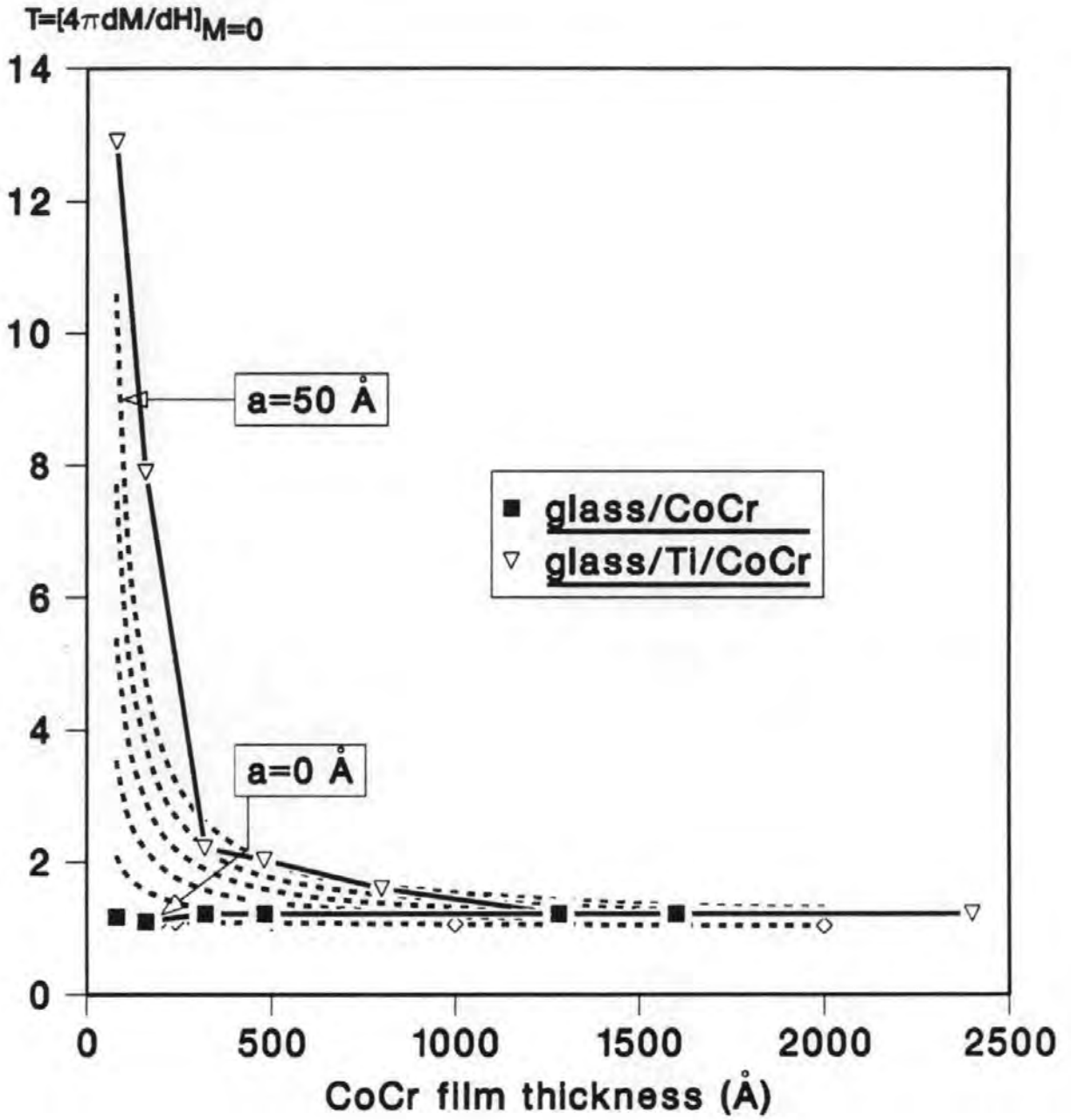


Figure 3.25: Hysteresis loop slope T of CoCr films as a function of film thickness, dotted curves are calculated by particulate model.

show anomalous shearing depending strongly on the film thickness and the value of "a". For very thin particulate films the slope T of the hysteresis loops deviates significantly from 1.0, particularly for films with larger non-magnetic separation "a". As the films become thicker, the slope T falls sharply at first and then gradually approaches to unity. For very thick films, the anomalous shearing caused by the columnar morphology is negligible. For films with intermediate thickness the slope T is still slightly higher than 1.0 because of the subtraction of columnar shape anisotropy to the total demagnetizing factor.

As shown in figure 3.2, the slope T of the CoCr films on Ti underlayers appears to fit with the calculated results by the particulate model with intercolumnar separation greater than 50 Å. For very thin CoCr films the slope T of the hysteresis loop is much higher than 1.0 ($T = 13.0$ for 80 Å-thick film). As the thickness of the films increases, the slope T drops sharply. For films with intermediate thickness, the slope T is slightly higher than 1.0.

As has been shown by our AES depth profiling and HRSEM examination (figures 3.16 and 3.20), the very thin CoCr films (160 Å-thick) deposited on Ti or Au underlayers are not continuous as a result of columnar growth. Therefore, a non-magnetic gap of greater than 50 Å between the columns can be justified. The TEM electron diffraction and x-ray diffraction also show that the very thin CoCr films deposited on Ti or Au underlayers exhibit strong [0002] texture. This satisfies the assumption of the particulate model that the saturation magnetization of the columns is perpendicular to the film plane, which is also supported by our torque magnetometer measurement (figure 3.8) and by the TEM Lorentz micromagnetic examination (figure 3.17). The Ti underlayer thickness effect on the shape of the

loops (figure 3.2) of the 160 Å-thick CoCr films also suggests that a good c-axis orientation is essential for the unsheared square perpendicular loop. It is therefore concluded that the unsheared square perpendicular loop of very thin CoCr films deposited on Ti or Au underlayers originates from their excellent [0002] texture and the intercolumnar non-magnetic separation. The shape anisotropy of the columns of very thin films significantly reduces the perpendicular demagnetizing factor and deshears the perpendicular loop of the CoCr films.

The variation of the shearing of the perpendicular loops shown in figure 3.9 may be attributed to the variation in the c-axis orientation distribution or the variation in the intercolumnar separation for each individual film.

The particulate model would not be valid for the CoCr films without Ti underlayers because of the lack of [0002] texture in such films though the experimental data of such films fit with the calculated curve for films with zero non-magnetic separation (figure 3.25).

The particulate model predicts a normal sheared loop ($T = 1.0$) for continuous perpendicular films and a slightly desheared loop for particulate films. This is obviously in contradiction to the computer simulation results [22] and domain model [69] which predict a desheared loop for continuous due to wall-motion-like reversal, and a normal sheared loop for particulate medium. Such a contradiction is due to the fact that the particulate model takes account of only the columnar shape anisotropy effect on the shearing of the loops whilst the computer simulation or domain model takes account of only the intergranular exchange coupling effect. Therefore, the validity of these two models is limited by its presumed conditions.

The experimental results in this work show that either particulate media (for

instance, CoCrTa on Ti) or continuous films(for instance CoCrTa on Pt) exhibit anomalous shearing in their perpendicular loops. The origin of such a phenomenon for each case is obviously different. For the films with large intergranular separation, such as CoCrTa on Ti or the very thin CoCr films on Ti and Au, the intergranular exchange coupling is negligible. Therefore, the particulate model applies. The anomalous shearing of the perpendicular loops for such films is due to the contribution of columnar shape anisotropy to the total demagnetizing factor. On the other hand, for a continuous film, such as CoCrTa on Pt, the intercolumnar exchange interaction is no longer negligible, the particulate model is therefore not valid. The domain model gives better explanation for such films.

In conclusion, the slope T of the perpendicular hysteresis loops of Co-based perpendicular films can be affected either by the intercolumnar separation or by the magnetization reversal process, depending strongly on the film microstructure. For films with larger intercolumnar separation, the contribution of the column shape anisotropy to the total demagnetizing factor is mainly responsible for the deshearing of the loops. The particulate model applies to such a film structure. For perpendicular films with zero or very small intergranular separation, the intergranular exchange coupling controls the magnetization reversal process and the wall-motion-like reversal explains the anomalous shearing of the hysteresis loop.

3.1.14 Origin of underlayer effect on orientation

The extensive experimental evidences in this study have shown that the very thin CoCr or CoCrTa films deposited on the following underlayers exhibit strong $[0002]$ texture: the hcp Ti with $[0002]$ texture, the hcp Ti with $[10\bar{1}0]$ texture, the fcc

Au with [111] texture, the fcc Pt with [111] texture and the amorphous Carbon underlayers; the very thin CoCr films deposited on amorphous-like glass substrates exhibit a weak [0002] texture and the very thin CoCr films deposited on bcc Cr underlayers show an in-plane c-axis texture. The crystallographic orientation of the the Co-based films is obviously strongly influenced by the underlayers. There has been a considerable interest in the underlayer effect on the orientation of Co-based media for perpendicular recording [74, 75, 76, 77, 78, 79] as well as for longitudinal recording [80]. CoCr films are reported to have an improved [0002] texture when deposited on hcp Ti [74, 77], amorphous Ge and Si [74, 78, 79] underlayers. It is therefore very important to make a good understanding to such a phenomenon.

As we discussed in section 1.3, the crystallographic orientation of a coating is determined by the oriented nucleation on the substrate surface as well as by bulk diffusion. For the very thin CoCr or CoCrTa films deposited by sputtering onto water cooled substrates, We only need to consider the effect of nucleation process because the bulk diffusion is negligible. Generally, in the nucleation process the positions of coating atoms in the initial nuclei will be arranged so that they tend to satisfy the minimum nucleation energy criteria. The minimum nucleation energy tendency is constrained by the surface mobility of the coating adatoms. When the Co-based film nucleates on underlayers, there are two possible mechanisms which will lower the nucleation energy; the epitaxial oriented growth, which depends on the orientation combination of the hcp Co and the underlayers, and the self-oriented growth, which depends on the thermodynamic nature of the hcp Co crystal itself. During the minimum energy competition, the one makes the system nucleation energy lower will survive and become the dominant growth mechanism.

It has been reported by various authors that the (0002) close packed plane of an hcp crystal has the lowest surface energy [74, 80]. Therefore, the CoCr film has the tendency to grow with the c-axis oriented normal to film plane if it is not interfered by the substrate. This is supported by many experimental evidences, observed in this study as well as reported by other authors [92, 8, 80, 91], that the [0002] orientation of CoCr films deposited on glass substrates improved as they grew thicker and that the orientation of CoCrTa films deposited on Cr underlayers changed from $[10\bar{1}0]$ texture when they were very thin to [0002] texture when they grew thicker. The very good [0002] orientation of very thin Co-based films deposited on amorphous C, Si underlayers in this study as well as that deposited on amorphous Ge or Si underlayers reported by other authors [74, 79] may be attributed to such a self-oriented growth mechanism. The amorphous underlayers serve as "neutral" substrate surfaces on which the hcp Co crystals grow freely into the [0002] texture.

When the Co-based films deposited on amorphous-like glass substrates, The situation would be different from that on C, Ge or Si amorphous underlayers. The amorphous glass substrate is not "neutral" because it contains Oxygen atoms which is chemically very active. The oxygen atoms on the glass substrate surface may have a strong bonding with the Co adatoms, which may limit the movement of Co adatoms to the lattice position for self-oriented nucleation. Consequently, the Co atoms on the glass surface would not be able to nucleate freely. In addition, the additives of K and Na in the glass may also form a kind of short range order or micro-crystals which may interfere with the oriented nucleation of Co crystals.

When the Co-based films are deposited on crystalline underlayers, the orientation of the initial nucleation layers will be affected by the crystallographic orientation

of underlayers. The epitaxial growth mechanism apply to such cases. The good [0002] texture of CoCr and CoCrTa films deposited on [0002] textural hcp Ti and on [111] textural fcc Pt or Au, and the [10 $\bar{1}$ 0] texture of CoCr and CoCrTa on [110] or [100] textural bcc Cr underlayers can be attributed to the epitaxial growth mechanism. However, the epitaxial growth is a very complex phenomenon. So far there is no complete theory to predict epitaxial growth in advance from the physical properties of the substrate and the deposit [59]. Experiments have shown that the over-growth appears to exhibit the like-lattice-pattern of underlayers. But, the lattice misfit between the over-growth and the underlayer does not play a decisive role [59] during the epitaxial growth because the elastic energy created by the lattice distortion due to misfit can be easily compensated for by misfit dislocations [60]. The experimental results in this study strongly support this. The large lattice misfit between the (0002) hcp Co and (0002) hcp Ti or (111) fcc Pt and Au appears not to have any effect on the [0002] orientation of the hcp Co. High density stacking faults can also be seen in our TEM bright field images of very thin CoCr films and its underlayers (figure 3.14).

It was found in this study as well as reported by other authors [77] that the [10 $\bar{1}$ 0] textural Ti underlayers is also a good substrate for [0002] textural Co-based films. The reason for that is not clear. One possible explanation is that on the very top surface of the [10 $\bar{1}$ 0] textural Ti underlayers, where the [0002] hcp Co nucleates, there actually exist many (0002) plane lattice patterns because the hcp Ti has the tendency to evolve into the [0002] texture, as the hcp Co does, as the film grows thicker. Those (0002) lattice patterns, which may be too thin and too tiny to be detected by x-ray diffraction or electron diffraction, provide the low energy site for

the oriented nucleation of [0002] textural hcp Co crystals.

In conclusion, the texture of the very thin CoCr and CoCrTa films is determined by the thermodynamic nature of hcp Co crystal itself and the nature of the surface of underlayers or substrates on which it grows. Amorphous underlayers, such as C, Si and Ge provide "neutral" substrate surfaces for the [0002] self-oriented growth of hcp Co-based films. Hcp Ti and [111] textural fcc Pt, Au underlayers favour the [0002] oriented epitaxial growth of hcp Co-based films. [110] or [100] textural bcc Cr underlayers favour the $[10\bar{1}0]$ oriented growth of hcp CoCr or CoCrTa films. Chemically active substrates or random oriented polycrystalline substrates are detrimental to the oriented growth of Co-based films.

3.2 CoNbFe soft magnetic backlayer

Various soft magnetic thin films have been used as "soft" back-layers in perpendicular magnetic recording systems [89, 94]. These films are required to have excellent soft magnetic properties such as high saturation magnetization, small coercivity and high permeability. It has been reported by different authors [95, 96] that CoNbFe amorphous films exhibit much better properties than permalloy and other soft magnetic films, such as zero magnetostriction, very small coercivity, very high saturation magnetization and permeability, good corrosion resistance and high resistivity. In the Co-Nb-Fe system, Nb functions as a glass forming element. It had been reported [100] that the minimum Nb concentration to form a stable amorphous state was about 8 at%. The saturation magnetization of the amorphous films follows a straight line decreasing with the increase of the Nb concentration. Amorphous CoNbFe films with very high saturation magnetic inductance ($B_s=14.3$ kG) had been prepared by H. Sakakima [95]. The saturation magnetostriction of the CoNb binary system is slightly negative and independent of the Nb content of the films. The addition of adequate amount of Fe makes it possible to produce zero magnetostriction amorphous films. The suitable concentration of Fe was reported to be 2 to 4 at% [96].

This section presents a detailed study on the magnetic properties and thermal stability of $\text{Co}_{84}\text{Nb}_{12}\text{Fe}_4$ amorphous films deposited by RF-sputtering on glass substrate.

3.2.1 Magnetic properties of CoNbFe films

The as-deposited $\text{Co}_{88}\text{Nb}_{12}\text{Fe}_4$ films exhibit a uniaxial anisotropy. The saturation magnetic induction is about 11kG. Both the electron diffraction and the x-ray diffraction analysis show that the film structure is amorphous. A very thin Ti adhesion layer could be used to improve the adhesion between the CoNbFe film and the glass disc substrate. No effect of this adhesion layer on the magnetic properties was observed.

Figure 3.26 shows the dependence of coercivity H_c on the thickness of CoNbFe films deposited on chemically strengthened glass disc substrates and on microscope slide substrates without Ti adhesion layer in the thickness range of 30 Å to 13800 Å. The coercivity was measured by transverse Kerr magneto-optic system for the thinner films (from 30 Å to 5000 Å) and by inductive B-H loop plotter for thicker films (from 400 Å to 13800 Å). No significant difference between these two measurements was observed, as can be seen from figure 3.26. The coercivity is also independent of the surface roughness on these two substrates, but a strongly dependent on the film thickness. The value of H_c changes from 14 Oe for 30 Å-thick films to 0.0125 Oe for 13800 Å-thick films.

A theoretical estimate of the thickness dependence of the easy direction coercivity has been made by Néel [98]. Because the domain wall energy is a function of the film thickness, the part of the coercivity which is thickness dependent can be written:

$$H_c(t) = \frac{1}{2M_s} \left[\frac{\partial \sigma_w}{\partial x} + \frac{\sigma_w}{t} \frac{\partial t}{\partial x} \right], \quad (3.3)$$

where t is the film thickness and σ_w is the domain wall thickness.

For Bloch walls with wall motion reversal mechanism, equation 3.3 can be eval-

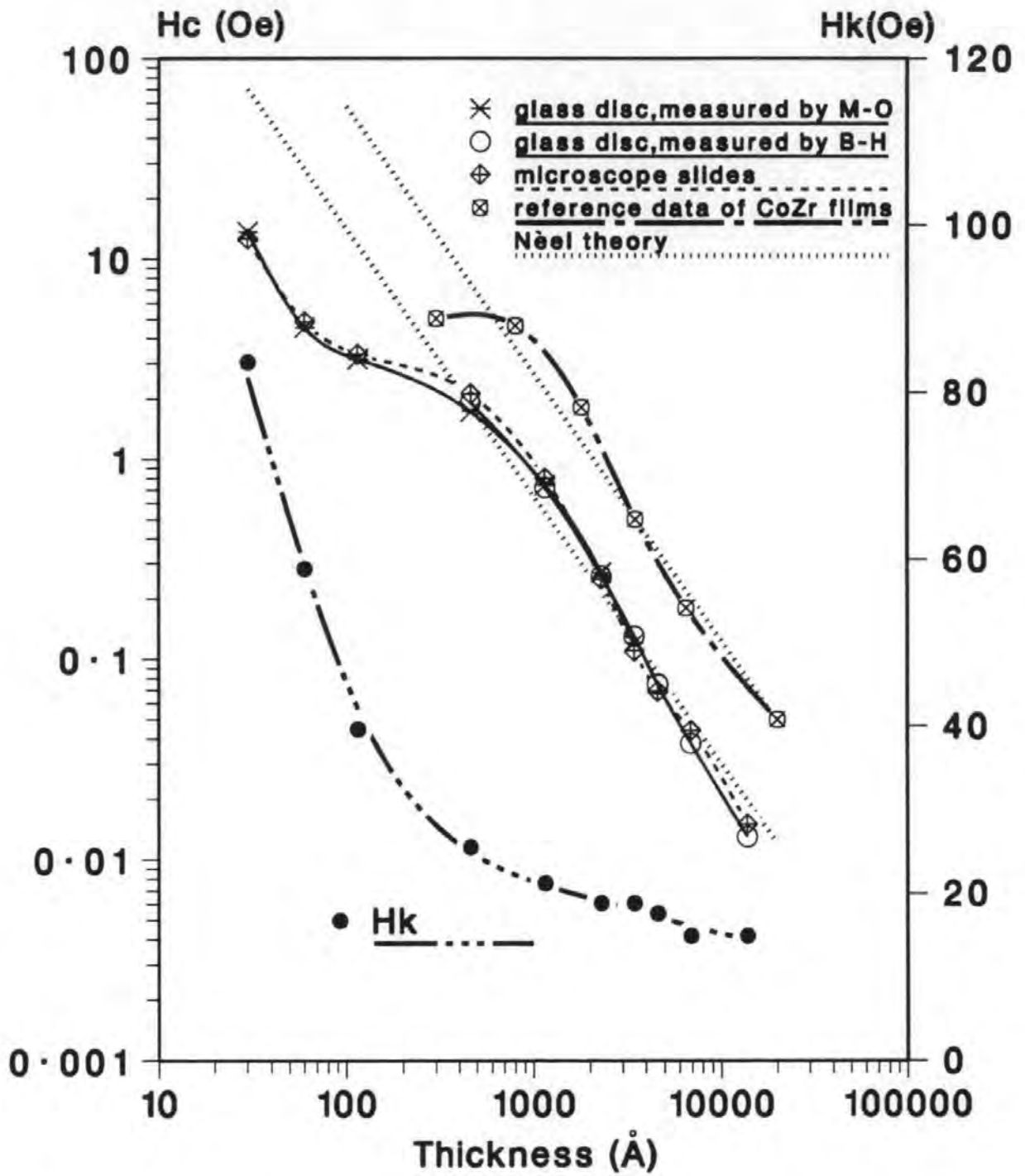


Figure 3.26: Thickness dependence of coercivity H_c and anisotropy field H_k of amorphous CoNbFe films.

uated as,

$$H_c(t) \propto t^{-4/3}. \quad (3.4)$$

The thickness dependence of Néel's theoretical predictions for domain wall motion coercivity is plotted in figure 3.26. The coercivity of CoZr Films [97] is also plotted in the figure for comparison.

As shown in figure 3.26, the thickness dependence of coercivity could be divided into three regions throughout the thickness range. The first region is from 15000 Å to 400 Å, where the experimental coercivity of both CoNbFe and CoZr films approximately follows the Néel formula. The dominant coercivity mechanism for this region could, therefore, be assumed to be wall motion coercivity mechanism as predicted by Néel [97, 98].

The second region is from 400 Å to 100 Å, where the experimental coercivity of both CoNbFe and CoZr films shifts from the $t^{-4/3}$ law, showing less thickness dependence. Jagielinski [97] attributed the deviation from the Néel formula to the existing of Néel wall rather than Bloch wall in this region because for Néel walls, the coercivity was found to be independent of thickness [99] and the Néel wall might be expected to occur in this thickness range according to the wall energy theory [98].

The third region is when films are thinner than 100 Å, where the coercivity of the CoNbFe films increases sharply as film thickness reduces, approximately fitting the $t^{-4/3}$ law again. However, it might not be reasonable to assume the coercivity mechanism to be Néel's wall motion mechanism for this region because Bloch walls might not exist in these extremely thin films due to the very high wall energy. The interface effect on the magnetic domains might be mostly responsible for the sharp increase of coercivity in this region. Further studies are needed to understand this.

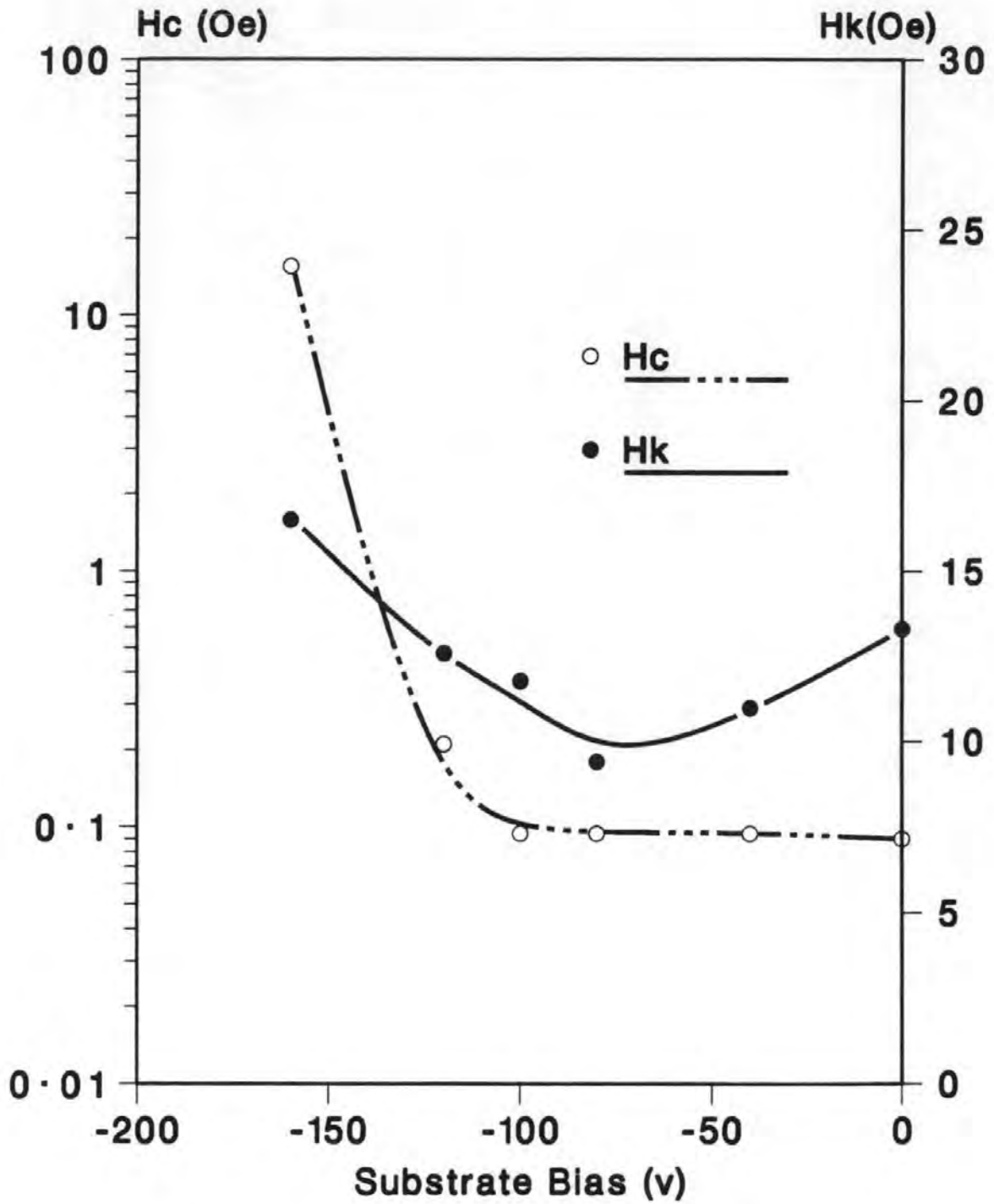


Figure 3.27: Substrate bias effect on H_c and H_k of 4600 Å-thick CoNbFe films.

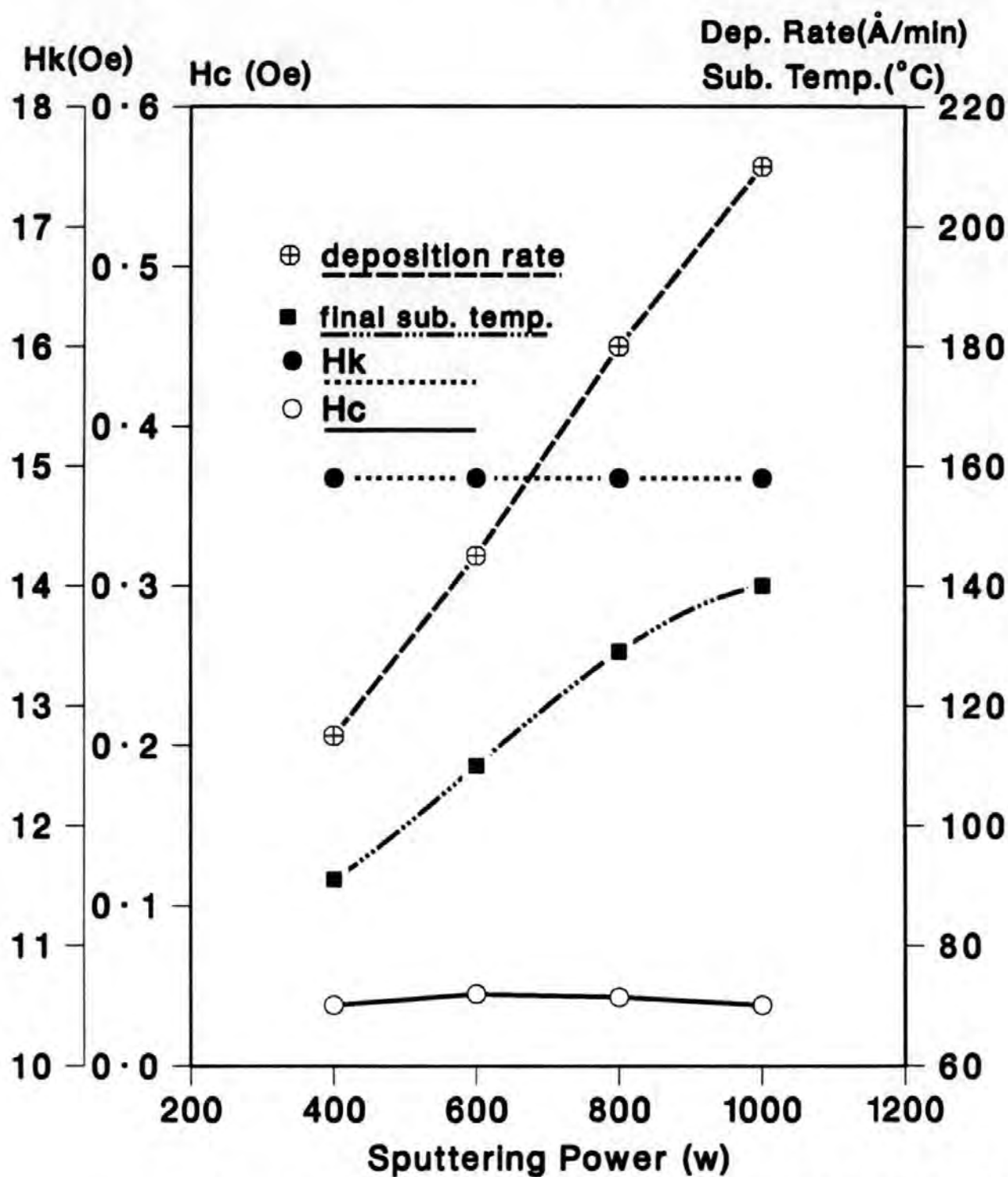


Figure 3.28: Sputtering power dependence of H_c and H_k of CoNbFe films (8500 Å), also shown the deposition rate and final substrate temperature.

The coercivity of *CoNbFe* films is always smaller than that of *CoZr* films in the whole thickness range, as shown in figure 3.26. This could be attributed to the nearly zero saturation magnetostriction of the $\text{Co}_{84}\text{Nb}_{12}\text{Fe}_4$ films due to the addition of the small amount of Fe [95].

The thickness dependence of the anisotropy field H_k is also shown in figure 3.26. The value of H_k changes from 943 Oe for film with thickness of 30 Å to 14 Oe for film with thickness of 10000 Å. The dependence of H_k on film thickness of thinner films is much stronger than that of thick films. No significant effect of the two different substrates on H_k was observed in this study.

Figure 3.27 shows the substrate bias effects on H_c and H_k of 4600 Å-thick as-deposited films. The coercivity of the as-deposited films appears to be not affected by substrate bias when substrate bias is between 0 V and -100V. The anisotropy field H_k shows a slight decrease as the amplitude of the negative substrate bias increases from 0 to 80V. A further increase of negative substrate bias above 100V results in a sharp increase of the coercivity (15 Oe for $V_b = -160\text{V}$) and a slight increase of H_k .

Figure 3.28 shows the sputtering power dependence of H_c and H_k of 8500 Å-thick *CoNbFe* films. These films were made under different sputtering power, but the same thickness by controlling the deposition time. The deposition rate and the final substrate temperature under different sputtering power is also shown in figure 3.28. As can be seen, when sputtering power increases, both the deposition rate and substrate temperature increase. However, the magnetic properties are insensitive to these changes.

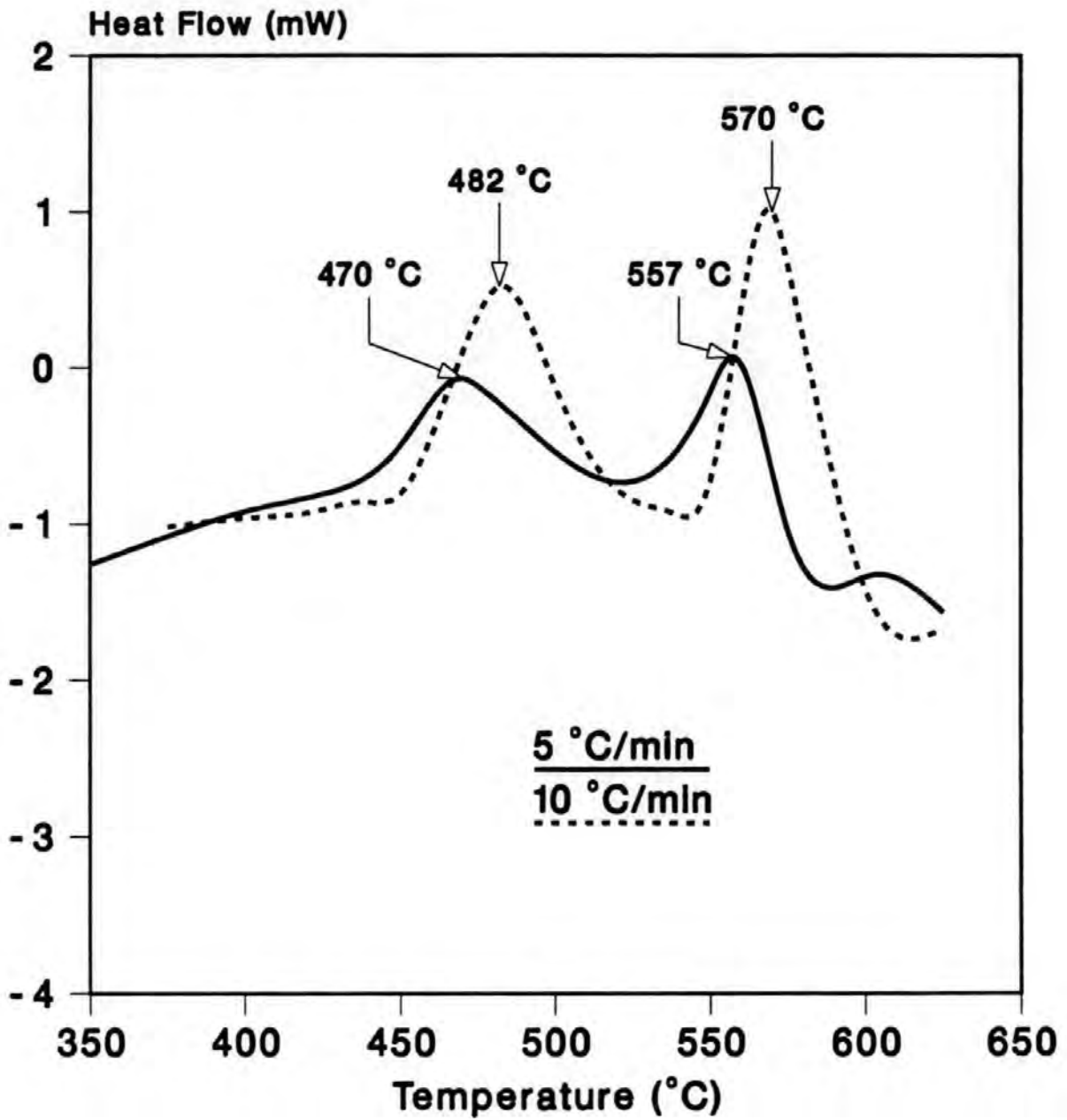


Figure 3.29: DTA curves for CoNbFe films at heating rate of 5 and 10 °C/min respectively.

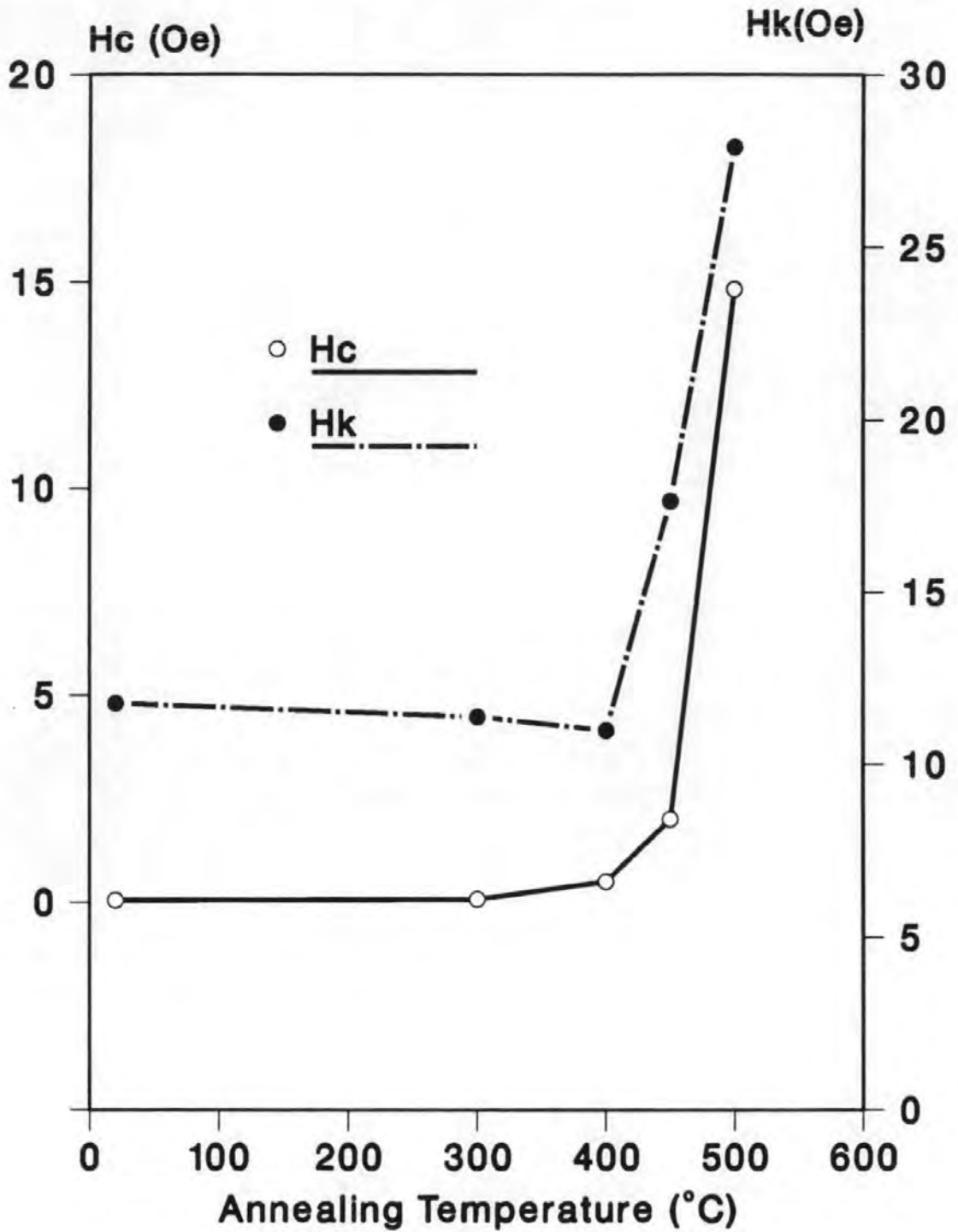


Figure 3.30: Annealing temperature dependence of H_c and H_k of CoNbFe films.

3.2.2 Thermal stability

The thermal stability of the CoNbFe films was studied by Differential Thermal Analysis (DTA) method as well as by thermal annealing. Samples for DTA were 30000 Å-thick films peeled off from a glass disc substrate, about 5 mg in weight for each run. Figure 3.29 shows the DTA curves of the CoNbFe films measured at two different heating rates, i.e. at 5 and 10°C/min. Two main exothermic peaks in each curve were observed at 470°C and 557°C for heating rate of 5°C/min, and at 482°C and 570°C for heating rate of 10°C/min. The first peak is due to the crystallisation of the film from amorphous to crystalline state. The second peak may be due to the phase change from one crystalline state to another. The different peak temperature values at different heating rate reflect some information on the kinetics of the crystallisation process.

The thermal annealing was undertaken by heating samples in an oven with an air atmosphere from room temperature to 300, 400, 450 and 500°C and holding on each temperature for 30 min respectively. The samples for thermal annealing were 10000 Å-thick CoNbFe films deposited on glass disc substrate and coated with an 800 Å-thick SiO_2 top layer to prevent the film from oxidation during annealing. The coercivity H_c and anisotropy field H_k were measured after annealing and results are shown in figure 3.30. From figure 3.30 we can see that the magnetic properties of the films are quite stable when the annealing temperature is below 400°C. A slight decrease of H_k after annealing could be attributed to the stress release by the thermal annealing process. When the annealing temperature increases to 450°C or over, both the H_c and H_k increase sharply. These results agree very well with the DTA results, both of which suggest that crystallisation process occurs in the

CoNbFe films when temperature is above 450°C.

3.2.3 Summary

Co₈₄Nb₁₂Fe₄ amorphous films were deposited by RF-sputtering on to chemically strengthened glass disc substrates as a back-layer for perpendicular magnetic recording computer discs. Very low coercivity down to 0.0125 Oe is achieved for films of 10000 Å-thick with a uniaxial anisotropy field of 14 Oe and saturation magnetic induction of 11 kG. Coercivity and anisotropy field were studied over a thickness range from 30 Å to 15000 Å and found to be a strong function of film thickness. The thickness dependence of coercivity follows Néel formula ($H_c \propto t^{-4/3}$) when films are thicker than 400 Å. A low substrate bias during sputtering has no effect on coercivity and reduces H_k slightly. A high substrate bias (above -120V) is detrimental to the soft magnetic properties of the films. The crystallisation temperature of the amorphous films is about 450°C. The thermal stability of the film is very good from room temperature to 400°C.

3.3 Read/write using MIG heads

The recording performance of 3.5" rigid disks with single-layer CoCrTa media on Ti and Pt underlayers was examined by using 8mm video MIG heads. Two types of MIG heads were used: (1) gap length $0.15 \mu\text{m}$, track width $30\mu\text{m}$, number of turns 20 and saturation magnetization of the metal 14.5 kG; (2) gap length $0.3 \mu\text{m}$, track width $25\mu\text{m}$, number of turns 23 and saturation magnetization of the metal (CoNbFe) 11 kG. A non-flying head supporting mechanism [93] was used for the contact recording experiment. Each disk was coated with an 80 \AA -thick carbon protective film and a liquid lubricant layer. The magnetic properties of the CoCrTa films on Pt and Ti underlayers for these disks are similar to that discussed in the previous section. Typical perpendicular loops of the CoCrTa films of 2000 \AA -thick on Pt and Ti underlayers are as shown in figure 3.24. The properties of the six disks tested are summarized in table 3.7.

Table 3.7: Summary of the properties of six single-layer disks

Disk	Underlayer	CoCrTa(\AA)	$\Delta\theta_{50}(\text{deg})$	Hc(VSM) (Oe)	Hc(M-O) (Oe)
D1	Pt(900 \AA)	2000	4.8	700	730
D2	Ti(900 \AA)	2000	4.8	2000	2060
D3	Pt(900 \AA)	880	4.9	700	750
D4	Ti(900 \AA)	880	5.6	1225	2250
D5	Pt(900 \AA)	440	4.8	500	1125
D6	Ti(900 \AA)	440	8.8	1000	1875

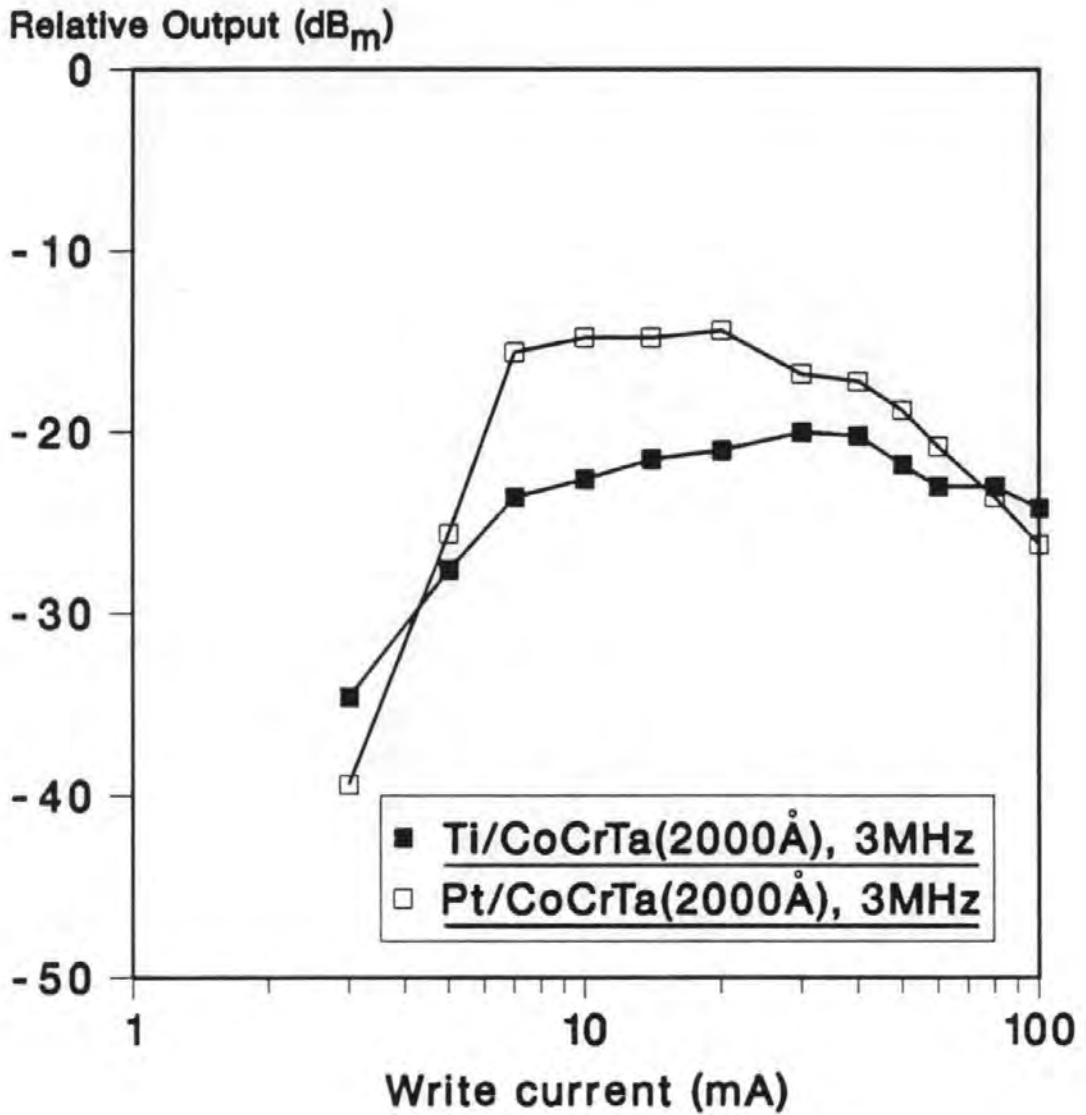


Figure 3.31: Readback voltage versus write current for the disks with 2000 Å-thick CoCrTa media on Pt and Ti underlayers. MIG head gap length is 0.15 μm.

For recording experiment using the MIG heads with gap length of $0.15\mu\text{m}$, the read back voltage was measured by a spectrum analyser in terms of fundamental frequency component. The unit of the readback voltage is dB_m , where the reference voltage was set to $450 \text{ nV}_{0-p}/\mu\text{m}\cdot\text{turn}\cdot\text{m/s}$. The head-medium relative velocity was 3 m/s . The D_{50} density from the fundamental curve is defined as the density at which the output signal is 6 dB lower than the maximum output level. The write current (I_w) for each disk was determined from the input-output curves. The typical input-output curves for the 2000 \AA -thick CoCrTa media on Pt and Ti underlayers are shown in figure 3.31, where the write current corresponding to the maximum output was chosen as I_w .

For recording experiment using the MIG heads with gap length of $0.3\mu\text{m}$, the read-back voltage was measured by an oscilloscope in terms of peak-to-peak amplitude. The head-medium relative velocity was 8.4 m/s . The unit of the read-back voltage is $\text{nV}_{p-p}/\mu\text{m}\cdot\text{turn}\cdot\text{m/s}$. The writing current I_w was also determined from the maximum output point of the input-output curve.

3.3.1 Experimental measurement of bit density response

The bit density response curves of disks D1, D2, D3, D4, D5 and D6, listed in table 3.7, measured by 0.15μ gap length MIG head in terms of fundamentals, are shown in figure 3.32 for CoCrTa media with thickness of 2000, 880 and 440 \AA on Pt underlayers and figure 3.33 for different thickness CoCrTa media on Ti underlayers respectively. It can be seen from figure 3.32 that for CoCrTa on Pt underlayers, the output signal level increases with the CoCrTa film thickness. In low density region, such an increase is proportional to the film thickness. However, the 2000

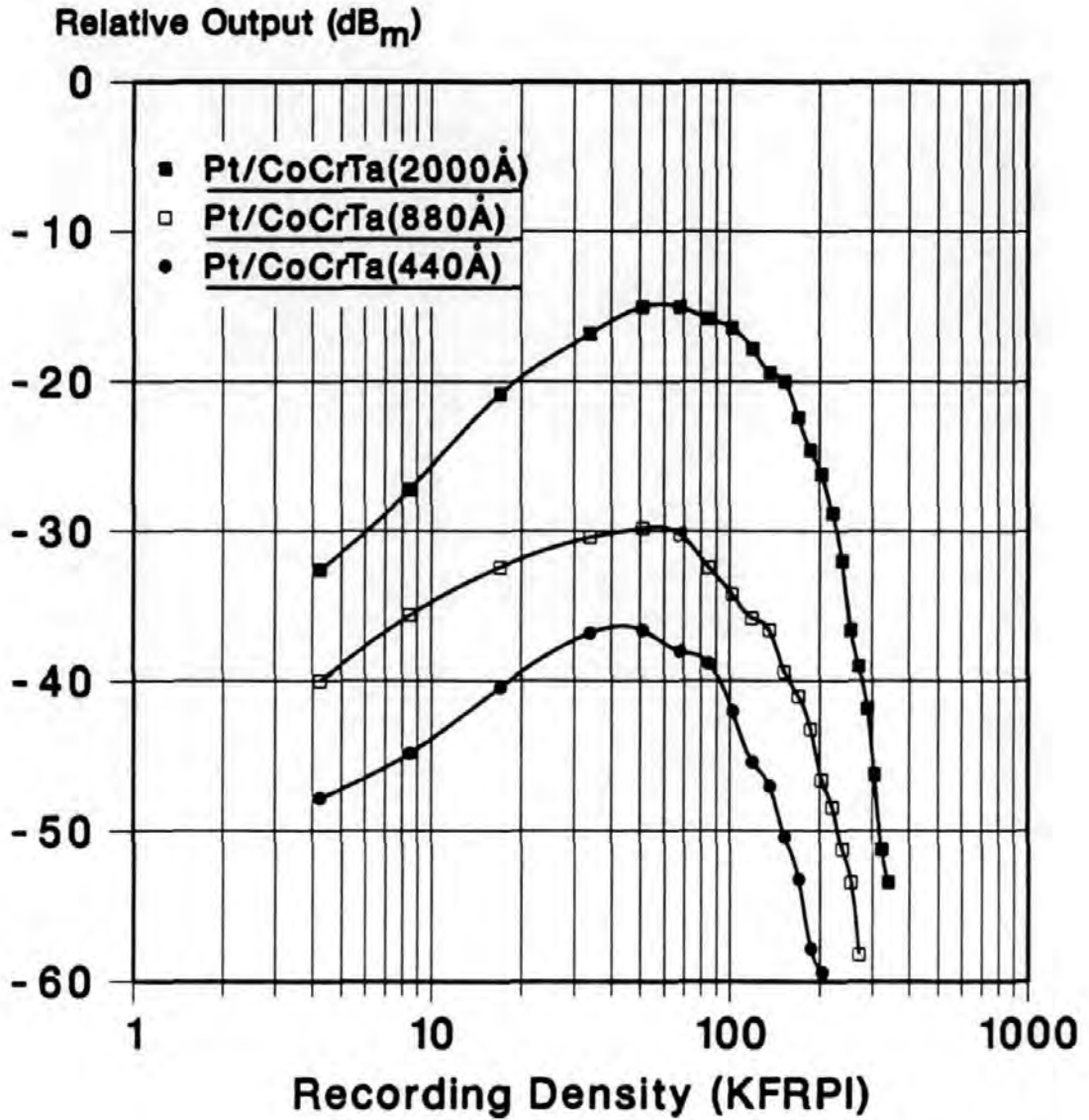


Figure 3.32: Bit density response(fundamentals) of different thickness of CoCrTa media on Pt underlayers measured by narrow gap MIG head.

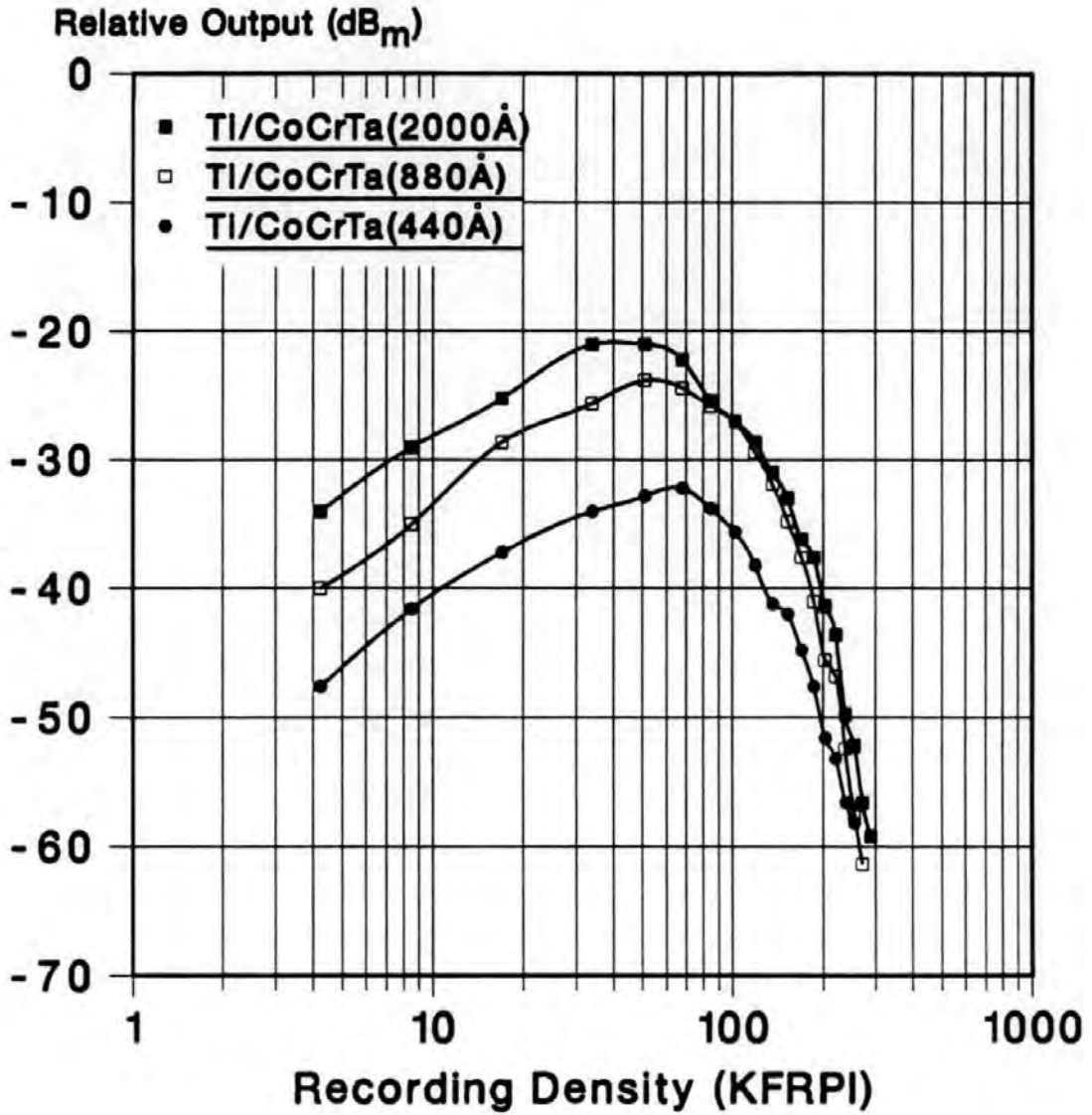


Figure 3.33: Bit density response(fundamentals) of different thickness CoCrTa media on Ti underlayers measured by narrow gap MIG head.

Å-thick medium shows much higher output signals in the high density region than the thinner media, for instance, the difference of the output signal between the 2000 Å-thick medium and 880 Å-thick medium is only 10 dB at 10 KFRPI, but 18 dB at 100 KFRPI. The maximum output for the 2000 Å-thick medium is $80 nV_{0-p}/\mu\text{m}\cdot\text{turn}\cdot\text{m}/\text{s}$ at 68 KFRPI. The D_{50} density for the 2000 Å-thick medium on Pt estimated from the fundamentals is 160 KFRPI, which is equivalent to an areal density of 4 Gb/in² if projected with a track density of 25.4 KTPI. The D_{50} densities for the 880 and 440 Å-thick media are 110 and 100 KFRPI respectively.

The bit density response of the media with thickness of 880 Å and 440 Å on Ti underlayers (figure 3.33) is better than that of the same thickness media on Pt underlayers. The estimated D_{50} densities are 130 and 120 KFRPI respectively. However, for the 2000 Å-thick CoCrTa on Ti, the output voltage is not as high as that of 2000 Å-thick CoCrTa medium on Pt underlayer. The maximum output is 50 % (6dB) lower than that of the same thickness CoCrTa on Pt. The estimated D_{50} is only 110 KFRPI.

The bit density response curves for disks D1, D2, D3 and D4, measured by the 0.3 μm gap length MIG head in terms of peak-to-peak amplitude, is shown in figure 3.34. These curves are initially near flat in low density region. As the bit density increases, all the curves rise and exhibit a voltage peak before the falling starts. This is a result of pulse crowding for di-pulse waveform (figure 3.35). The output voltage level shown in figure 3.34 is proportional to the coercivity and thickness of the media. The 2000 Å-thick CoCrTa on Ti underlayer ($H_c = 2000 \text{ Oe}$) exhibits higher output voltage than the same thickness CoCrTa on Pt underlayer ($H_c = 700 \text{ Oe}$). For the 880 Å-thick media, the one on Ti underlayer also exhibits higher output because of its

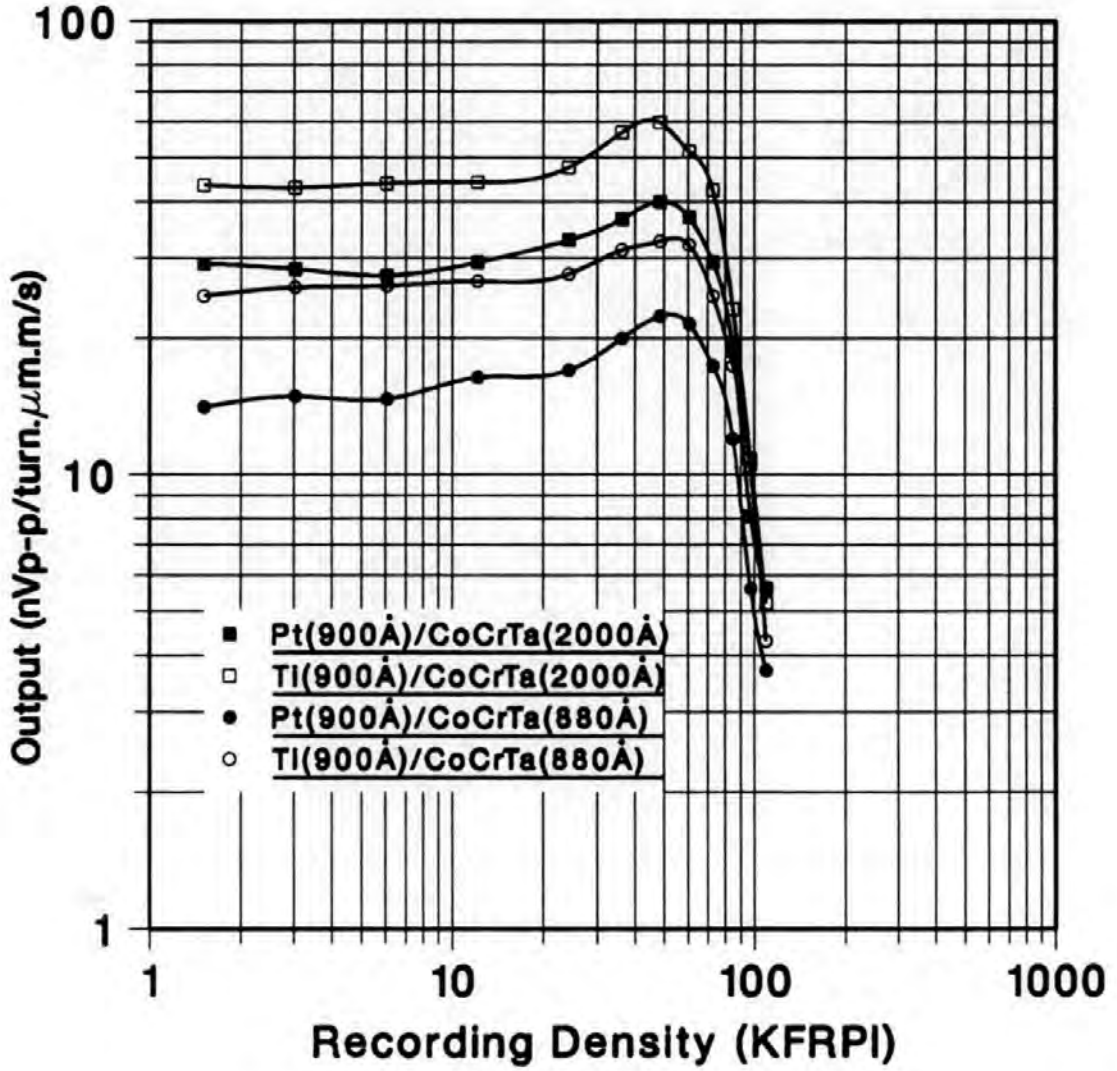


Figure 3.34: Bit density response(peak-to-peak) of different thickness CoCrTa media on Pt and on Ti underlayers measured by wide gap MIG head.

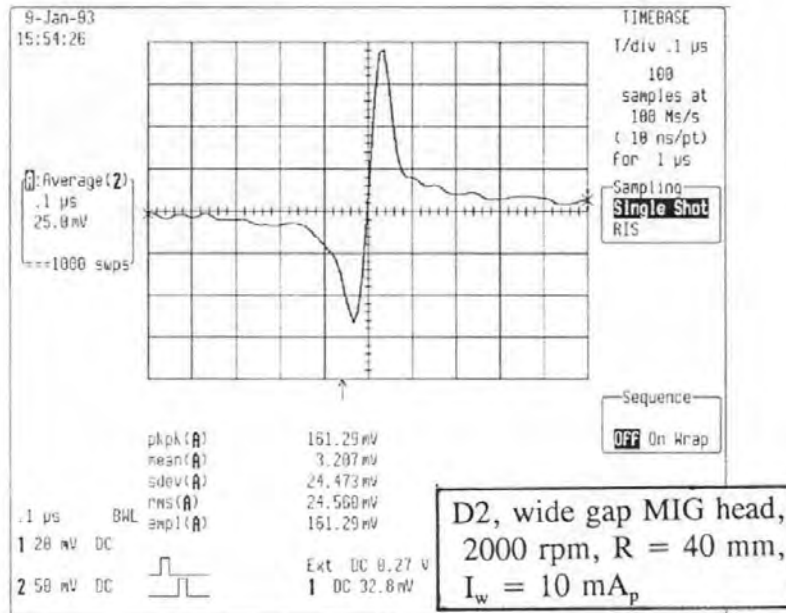
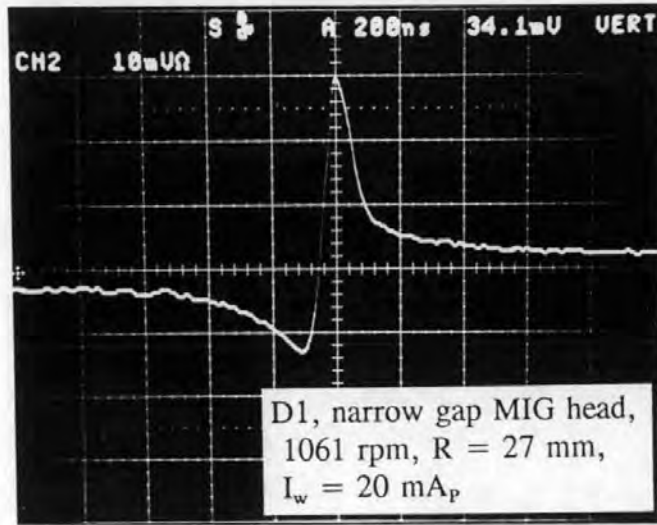


Figure 3.35: Typical isolated waveforms measured for disk D1 and D2 at 0.25 MHz by MIG head with gap length of $0.15 \mu\text{m}$ and $0.30 \mu\text{m}$ respectively.

higher coercivity. The D_{50} density of all four disks has the same value of 90 KFRPI, which is obviously head gap length limited.

All the disks produce quite similar isolated waveforms which are asymmetrical di-pulses with di-pulse ratio varying from 0.50 to 0.70. Typical isolated waveforms measured at 0.25 MHz are shown in figure 3.35(a) for disk D1 with narrow gap MIG head, and figure 3.35(b) for disk D2 with wide gap MIG head. If we compare these waveforms with figure 1.10, they do not match with the reproduced waveform calculated from a perfect perpendicular transition with ring/single combination (figure 1.10(b)). Similar isolated waveforms had been obtained for the ring/single combination by Hokkyo et al [14]. This behaviour was understood to be caused by the asymmetric recorded perpendicular magnetization distribution along the isolated transition due to the perpendicular demagnetizing field away from the transition centre [4, 9].

3.3.2 Analysis of the recording and reproducing process

(a) Maximum writeable medium coercivity by MIG heads

It is assumed for the contact perpendicular recording that the actual magnetization reversal during the writing process is characterized by the intrinsic perpendicular loop [15] because the high permeability head material can significantly reduce the surface magnetic charge and hence deshears the perpendicular loop. Therefore, magnetization reversal takes place when the perpendicular field component of the write head exceeds the coercivity of the medium. If the coercivity of the medium is higher than the maximum field the write head can produce, the information will not be effectively recorded. The maximum writeable medium coercivity of the MIG

Table 3.8: Maximum writeable coercivity by MIG heads with gap length of 0.15 and 0.30 μm for media of different thickness.

Medium thickness	Maximum writable medium coercivity (Oe)	
	$g=0.15\mu\text{m}$, $B_s=14.5\text{kG}$	$g=0.30\mu\text{m}$, $B_s=11\text{kG}$
2000Å	1563	2583
880Å	3010	4003
440Å	4120	4950

heads used in this study is calculated by using Karlquist approximation and is given by,

$$H_c(\text{max}) = \frac{0.8B_s}{2\pi} \ln \frac{(d + \delta)^2 + g^2}{(d + \delta)^2}, \quad (3.5)$$

where the saturation magnetic induction B_s of the metal in the MIG heads is 14.5 kG for heads with gap length of 0.15 μm and 11 kG for the heads with gap length of 0.3 μm respectively, the head-medium spacing d for both cases is assumed to be 300 Å, the thickness of the medium δ is 440, 880 and 2000 Å respectively. The maximum writeable coercivity of the media is calculated with reference to the middle plane of the medium (half thickness plane) and results are summarised in table 3.8. It can be seen from the table that the maximum writeable medium coercivity of a head is a function of head gap length and medium thickness. For media with

thickness of 440 and 880 Å, The maximum writeable coercivity by both types of MIG head is far greater than the actual coercivity of the medium (see table 3.7). Head saturation for these media would not occur. For the medium with thickness of 2000 Å, the maximum writeable coercivity by the MIG head with gap length of $0.15\mu\text{m}$ is only 1563 Oe which is smaller than the actual coercivity of the 2000 Å-thick CoCrTa films on Ti (2000 Oe measured by VSM). Therefore head saturation may occur for such a high coercivity medium. However, if a MIG head with larger gap length ($0.3\mu\text{m}$) is used, head saturation would not occur because, as shown in table 3.8, the maximum writeable medium coercivity for such a head is 2583 Oe which is greater than the actual medium coercivity.

(b) Calculation of bit density response

The reproduced voltage of fundamental frequency level versus bit density for single-layer medium with ring head can be calculated by equation 1.45. For normalised output, it can be written,

$$\frac{e(k)}{NvW\eta} = 4\pi \times 10^{-8} M\delta \frac{1 - e^{-k\delta}}{k\delta} e^{-k(d+a)} \frac{\sin(1.136kg/2)}{1.136kg/2}. \quad (3.6)$$

As discussed in section 1.2.3, the demagnetizing field away from the transition in perpendicular recording shears the perpendicular loop and hence reduces the recorded magnetization amplitude. The recorded perpendicular magnetization amplitude M in perpendicular transition is given by [4],

$$M = T \frac{H_c}{4\pi}, \quad (3.7)$$

where H_c is the coercivity of the medium and T is the slope of the perpendicular hysteresis loop ($T = [\frac{4\pi dM}{dH}]_{M=0}$). For normal sheared perpendicular loop, $T = 1.0$,

therefore, $M = H_c/4\pi$. However, as has been seen in section 3.1.13, T is normally not equal to unity because of the effect of the intercolumn separation on the perpendicular shape anisotropy or the effect of intergranular exchange coupling on the nucleation field during the magnetization reversal. T is also a function of bit density because the demagnetizing field decreases as the bit density increases [4]. It is therefore necessary to consider the above effects on the recorded perpendicular magnetization amplitude for the calculation of bit density response.

By considering the anomalous shearing of the perpendicular loop and the bit density dependence of the demagnetizing coefficient for each bit, the slope $T(k)$ of the hysteresis loop as a function of bit density can be written,

$$T(k) = T \frac{k\delta}{1 - e^{-k\delta}}, \quad (3.8)$$

where k is the wavenumber ($k = 2\pi/\lambda$), T is the slope of perpendicular hysteresis loop measured by VSM, and the dependence of the demagnetizing coefficient on the bit density takes the form proposed by Bertram [4] based on perfect perpendicular sinusoidal magnetization pattern.

The dependence of the recorded perpendicular magnetization amplitude $M(k)$ on the bit density can be calculated by equations 3.8 and 3.7 and is written as,

$$M(k) = \begin{cases} \frac{TH_c}{4\pi} \frac{k\delta}{1 - e^{-k\delta}} & \text{if } M(k) < M_s, \\ M_s & \text{if } M(k) \geq M_s, \end{cases} \quad (3.9)$$

where the perpendicular M-H loop is assumed to be rectangular after the demagnetization correction. The calculated recorded perpendicular magnetization amplitude as a function of bit density for the 2000 and 880 Å-thick CoCrTa films on Pt and Ti underlayers are shown in figure 3.36. The slope T used for calculation is 1.42 for

CoCrTa on Ti and 2.32 for CoCrTa on Pt. Other properties are the same as listed in table 3.7.

It can be seen from figure 3.36 that the recorded magnetization amplitude in all cases increases as the bit density increases. This is a typical feature of perpendicular transition as a result of transition interaction. However, for the thicker films (2000 Å) such increases are much sharper than the thinner ones. The perpendicular coercivity of the medium also makes big difference. For the 2000 Å-thick CoCrTa on Ti ($H_c = 2000$ Oe), the magnetization reaches maximum ($M = M_s$) at 80 KFRPI while for the same thickness CoCrTa on Pt ($H_c = 700$ Oe), the magnetization reaches maximum at 170 KFRPI. It is obvious that a thicker film with larger coercivity is advantageous for high output in perpendicular recording. However this is constrained by the head saturation as discussed a moment ago and also by the medium thickness loss.

The bit density response of the output voltage in terms of fundamentals is calculated by equation 3.6 for the above four disks with MIG head of gap length $0.15 \mu\text{m}$, where the dependence of the recorded perpendicular magnetization amplitude takes the form of equation 3.9. The hysteresis loop slope T was 1.42 for the CoCrTa on Ti and 2.32 for the CoCrTa on Pt. The calculated voltage amplitude was normalised with reference to the measured output voltage of the 2000 Å-thick CoCrTa on Pt at 4.23 KFRPI. The calculated results for disks D1, D2, D3 and D4 are plotted in Figure 3.37 (a), (b), (c) and (d) respectively. The measured data were also plotted in the corresponding figures for comparison. It can be seen from the figure that the calculated output level at low density region matches with the experimental data reasonably well for all the disks except for disk D2. The difference between the calculated and measured appears in the high density region. The most likely

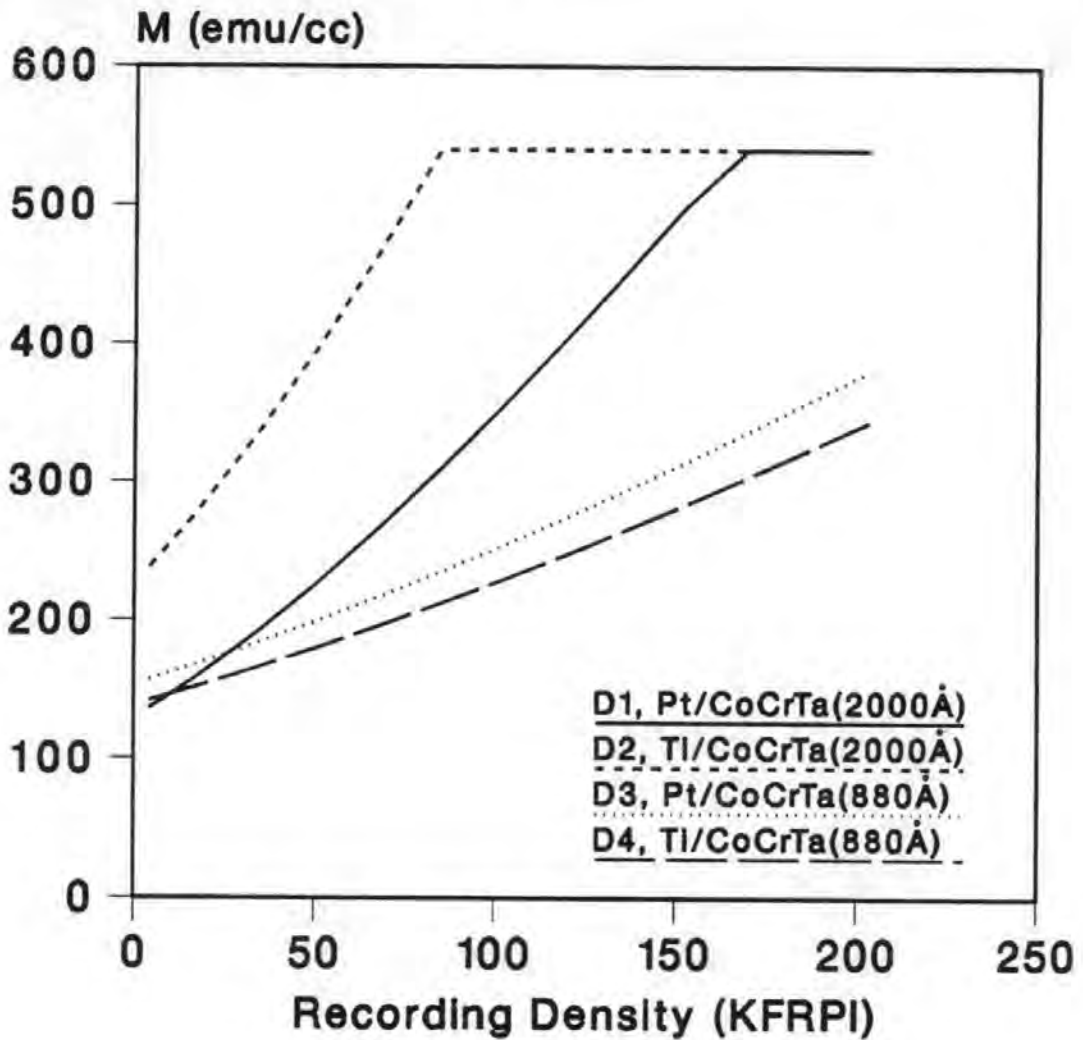


Figure 3.36: The recorded perpendicular magnetization amplitude as a function of the bit density calculated for disks D1, D2, D3 and D4.

reason for that is the spacing loss due to a small tilt of the recording heads. This is shown in figure 3.37 (a), (c) and (d), where the calculated output curves were plotted with different head-medium spacing. It can be seen from these figures that the experimental data in high density region for disks D1, D3 and D4 match closely with the calculated curves for head-medium spacing of 700 Å, 1600 Å and 1000 Å respectively. Such a big variation in the head-medium spacing is possible if consider the effect of the head-tilting during the measurement. It was found during the mea-

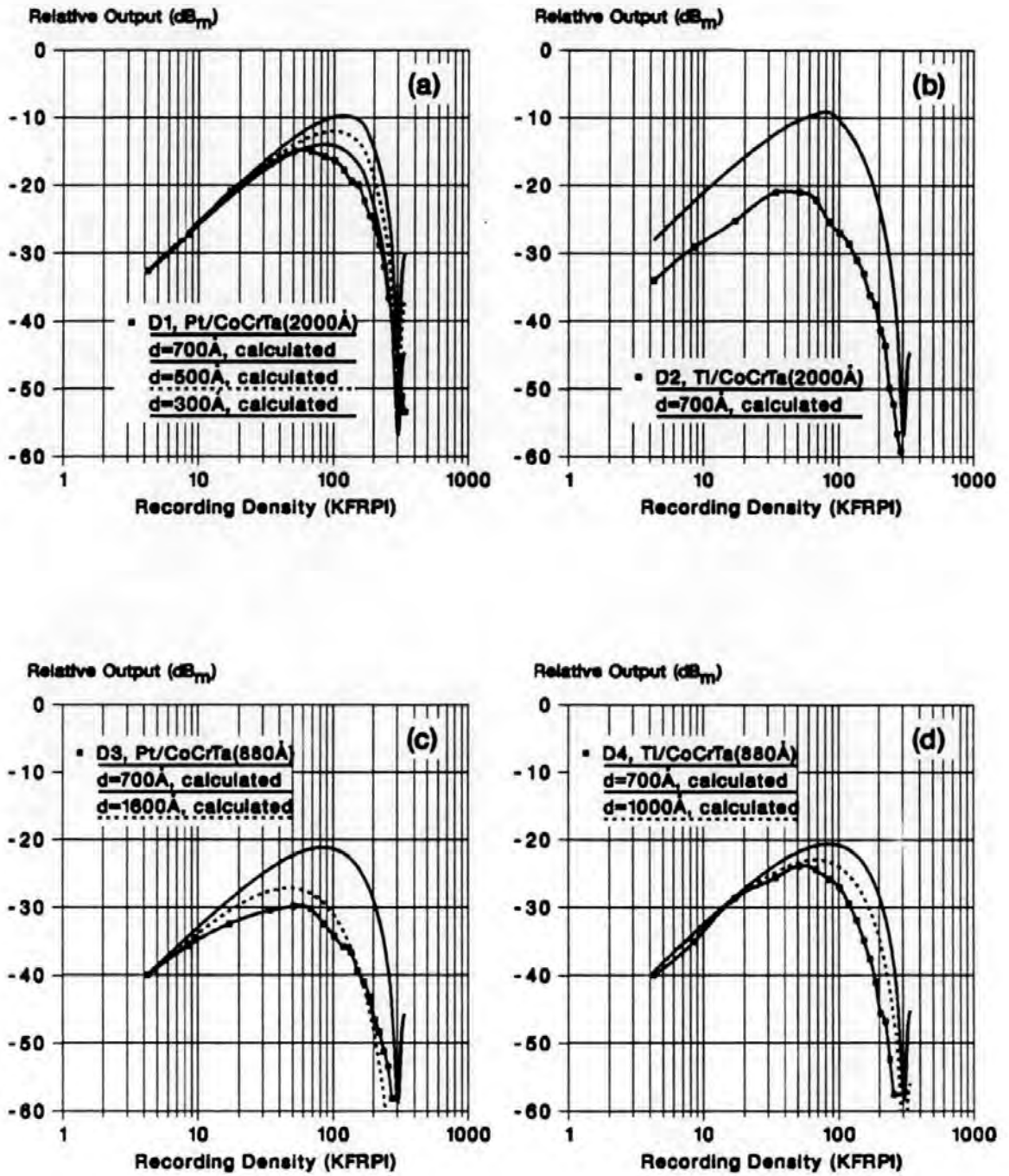
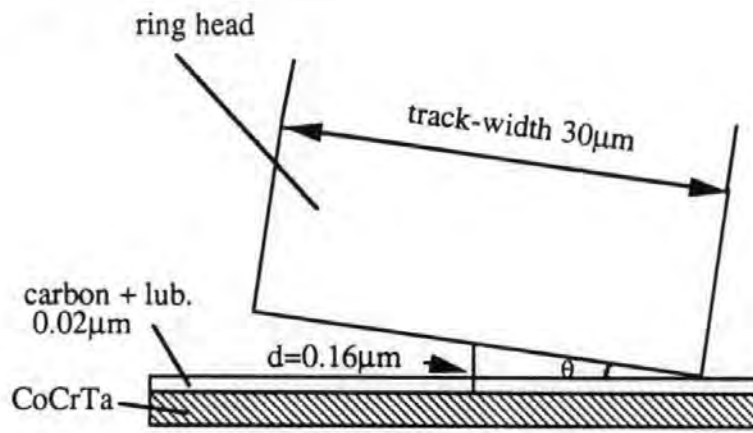
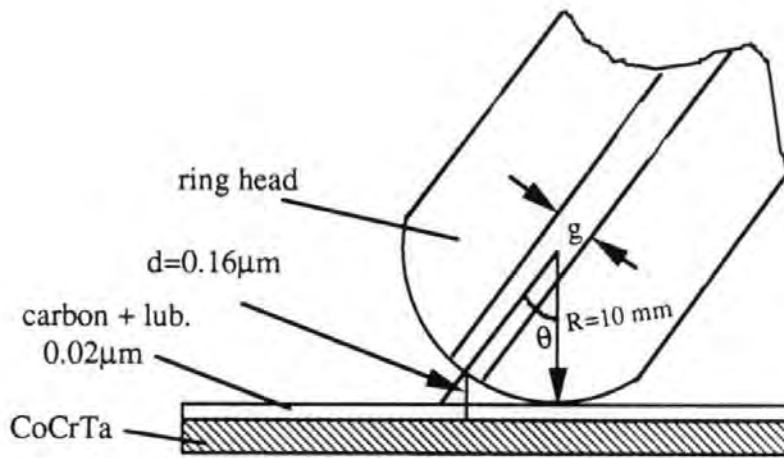


Figure 3.37: Comparison of calculated and measured bit density response curves.



$$\theta = \arcsin 0.14/15 = 0.5 \text{ degree}$$

(a)



$$\theta = \arccos (R-0.14)/R = 0.3 \text{ degree}$$

(b)

Figure 3.38: Schematic illustration of the increase of head-medium spacing by a small tilting of the MIG head along the track-width direction (a) or along the medium moving direction (b).

surement that the output voltage was very sensitive to the head alignment. This can be further demonstrated by figure 3.38(a) and (b). As shown in the figure, either a tilt of 0.5 degree of the head along the track width direction (figure 3.38(a)) or a 0.3 degree along medium moving direction (figure 3.38(b)) will result in a head-medium spacing of 1600 Å for a head with track-width of 30 μm. It is therefore very important to make a very accurate alignment for the MIG head, or considerable spacing loss will occur in the high density region. It can be seen from figure 3.38(a) that a narrower track-width would be advantageous to the reduction of the spacing loss caused by the tilting of heads. The minimum head-medium spacing achieved in the above experiment appears to be greater than 700 Å if estimated from the spacing loss calculation. The head-medium alignment for disks D3 and D4 apparently was not optimised.

The discrepancy between the calculated output and the measured ones for disk D2 (see figure 3.37(b)) was due to the head saturation problem because the 2000 Å-thick CoCrTa on Ti has too high coercivity to be effectively written by the narrow gap MIG head. This has been shown in table 3.5. The medium would give much higher output if a higher saturation magnetization head, or a wide gap head is used. The results obtained by using the wide gap MIG head for this medium given in figure 3.34, which show the 2000 Å-thick CoCrTa medium on Ti exhibited higher output than the same thickness medium on Pt. also confirm that.

3.3.3 Medium noise measurement

The medium noise was measured at the dc erased state. As discussed in section 1.2.5, the perpendicular medium noise decreases with increasing bit density, the dc erased

Table 3.9: Results of medium noise measurement for disks D1, D2, D3 and D4.

Disk	Underlayer	CoCrTa(Å)	Medium noise($\mu\text{V rms}$)	SNR(medium)(dB)	SNR(system)(dB)
D1	Pt(900Å)	2000	2.65	26.4	22.7
D2	Ti(900Å)	2000	0.961	40.6	26.2
D3	Pt(900Å)	880	1.15	29.7	16.7
D4	Ti(900Å)	880	0.402	43.5	21.4

medium noise may therefore represent the maximum medium noise. In the measurement, the total system noise voltage, measured over system bandwidth of 30MHz, was $5.82 \mu\text{V rms}$. The medium noise for all the disks measured are much smaller than the system noise. Results are given in table 3.9 for disks D1, D2, D3 and D4.

As shown in table 3.9, the disks with Ti underlayers exhibit smaller medium noise and higher SNR than the disks with Pt underlayers. This supports Zhu's computer simulation prediction [26] that a stronger intergranular exchange coupling results in a higher medium noise. As has been discussed in section 3.1.12, the CoCrTa media on Ti underlayers are weakly intergranular exchange coupled because of their large grain size and possible large intergranular non-magnetic separation. It is therefore expected to have lower noise for such media. However, as has been seen from our SEM topography in figure 3.22, the grain size of CoCrTa on Pt underlayers is much smaller than that on Ti underlayers. The CoCrTa films on Pt also exhibit better crystallographic orientation, as shown in table 3.6. The smaller grain size and strong perpendicular crystalline anisotropy will, as shown by equation 1.47, favour higher SNR if the intergranular exchange coupling energy constant A^* can be made small enough. Therefore, the CoCrTa/Pt films can still be the favourite candidate for high

density and low noise media if the intergranular exchange coupling can be reduced.

3.3.4 Summary

Contact recording performance of single magnetic layer CoCrTa media with Ti and Pt underlayers on 3.5" glass disks are examined using two types of MIG heads. The achieved D_{50} density is 160 KFRPI for the 2000 Å-thick medium on Pt underlayers using MIG heads of gap length 0.15 μm . The maximum output voltage (fundamentals) is $80 \text{ nV}_{0-p}/\mu\text{m}\cdot\text{turn}\cdot\text{m/s}$ for the same disk. Experimental and theoretical analyses of the read/write processes show both the achievable D_{50} density and the reproduced output level for these media are head field and head-medium spacing limited. Noise measurement shows all the media exhibit noise much lower than the electronic noise. Lower medium noise and higher SNR are achieved by the media with Ti underlayers, which supports the intergranular exchange coupling noise theory.

Chapter 4

Conclusions and future work

4.1 Conclusions

Pronounced effect of underlayers on the squareness and anomalous shearing of the perpendicular loops of very thin CoCr films was observed by MOKE and VSM measurements. The shearing of the perpendicular loops also depends on the film thickness, especially when the film is very thin. It was found by x-ray diffraction, electron diffraction, Lorentz micromagnetic examination and torque curve measurement that the very thin CoCr films with square and desheared perpendicular loops exhibit excellent perpendicular c-axis orientation and strong perpendicular anisotropy. Film microstructure examination by HRSEM, TEM and Auger depth profiling suggests a columnar growth and discontinuous nature of the very thin CoCr films. Experimental results were compared with the recent particulate model and domain model. It was concluded that the square and desheared perpendicular loops of very thin CoCr films originated from their strong perpendicular anisotropy and large intergranular nonmagnetic separation. The slope T of the perpendicular hysteresis loops

of Co-based perpendicular films can be affected either by the intercolumn separation or by the magnetization reversal process, depending on the film microstructure. For films with larger intercolumn separation, the contribution of the column shape anisotropy to the total demagnetizing factor is mainly responsible for the deshearing of the loops. The particulate model applies to such a film structure. For perpendicular films with zero or very small intergranular separation, the intergranular exchange coupling controls the magnetization reversal process and the wall-motion-like reversal explains the anomalous shearing of the hysteresis loop. This was also supported by the experimental results of CoCrTa films on Pt and Ti underlayers.

Study of the orientation relationship between the Co-based films and their underlayers suggests that the texture of the very thin CoCr and CoCrTa films is determined by the thermodynamic nature of hcp Co crystal itself and the nature of the surface of underlayers or substrates on which it grows. Amorphous underlayers, such as C, Si and Ge provide "neutral" substrate surfaces for the [0002] self-oriented growth of hcp Co-based films. Hcp Ti and [111] textural fcc Pt, Au underlayers favour the [0002] oriented epitaxial growth. [110] or [100] textural bcc Cr underlayers favour the [10 $\bar{1}$ 0] oriented growth. Chemically active substrates or random oriented polycrystalline substrates are detrimental to the oriented growth of Co-based films.

The CoCrTa films on Ti underlayers exhibit much larger perpendicular coercivity than the same films on Pt underlayers. The magnetic and microstructure measurements for these films support the intergranular exchange coupling theory, and suggest that the larger perpendicular coercivity of the CoCrTa films on Ti was mainly due to the large grain diameter and possible large intercolumnar separation

in the film, which results in a reduction in the intergranular exchange coupling constant. The big difference between the surface and bulk coercivity of the CoCrTa films on Ti underlayers was attributed to the improvement of the crystallographic orientation of the hcp Co crystals and the development of large grains as the film grows thicker which caused the reduction in the surface intergranular exchange coupling due to large grains as well as large intergranular separation.

$\text{Co}_{84}\text{Nb}_{12}\text{Fe}_4$ amorphous films were investigated as a back-layer for double layer media. Very low coercivity down to 0.0125 Oe was achieved for films of 10000 Å-thick with a uniaxial anisotropy field of 14 Oe and saturation magnetic induction of 11 kG. Coercivity and anisotropy field were studied over a thickness range from 30 Å to 15000 Å and found to be a strong function of film thickness. The thickness dependence of coercivity follows the Néel formula when film thickness is greater than 400 Å. The crystallisation temperature of the amorphous films is about 450°C. The CoNbFe amorphous films exhibit good thermal stability when temperature is below 400°C.

Contact recording performance of single magnetic layer CoCrTa media with Ti and Pt underlayers on 3.5" glass disks are examined using two types of MIG heads. The achieved D_{50} density is 160 KFRPI for the 2000 Å-thick medium on Pt underlayers using MIG heads of gap length 0.15 μm. The maximum output voltage (fundamentals) is $80 \text{ nV}_{0-p}/\mu\text{m}\cdot\text{turn}\cdot\text{m/s}$ for the same disk. Experimental and theoretical analyses of the read/write processes show both the achievable D_{50} density and the reproduced output level for these media were head field and head-medium spacing limited. Noise measurement shows all the media exhibit noise much lower than the electronic noise. Lower medium noise and higher SNR were achieved by

the media with Ti underlayers, which supports the intergranular exchange coupling noise theory.

4.2 Future work

The CoCrTa film on Pt underlayer exhibits excellent perpendicular crystallographic c-axis orientation and fine grains. Further development of such films towards the lower intergranular exchange coupling would be of interest to the future very high density and low noise media. It is also necessary to undertake further microstructural and micromagnetic examinations of these films by high resolution TEM and high resolution Lorentz microscopy and to combine such studies with the medium noise measurement, particularly, the observation of intergranular nonmagnetic separation by HRTEM lattice images and the observation of micromagnetic structure of the films with different noise performance.

The CoNbFe films exhibit very good soft magnetic properties which can be used as a soft magnetic backlayer for double layer media. Limited experimental results in this work have shown that there was a significant difference in the perpendicular coercivities of the Co-based media deposited on Ti or Pt underlayers with the amorphous CoNbFe films and deposited on the same thickness Ti or Pt underlayers without CoNbFe films. This may be due to the difference in the grain morphology caused by the existence of amorphous CoNbFe films. Further experimental study is needed to understand such a phenomenon as well as the effect of CoNbFe films on the reproduced voltage and noise performance of the Co-based media.

Results in this work have shown that the recording performance of the disks was head field and head-medium spacing limited. High linear density requires narrow

gap ring heads or narrow pole width single pole heads. However, the write field of a head would be significantly reduced by the narrower gap. On the other hand, low noise media always requires recording heads with high write field because of the high coercivity of the media. As a result of this, there would be two options in the development of the future recording heads: (1) to use head material with very high saturation magnetization for the writing heads, which would be able to produce high writing field even with narrow gap; and (2) to use head material with high sensitivity for the reproducing heads, such as giant magnetoresistive material, which would allow the use of very thin recording media. This would ease the needs for high writing field for the writing head because of the relatively larger writeable medium coercivity for thinner media.

Bibliography

- [1] T. Yogi, C. Tsang, T.A. Ngugen, K. Ju, G.L. Gorman and G. Castillo, *IEEE Trans. Magn.*, Vol.26, No.5, 2271(1990).
- [2] C. Tsang, M. Chen, T. Yogi and K. Ju, *IEEE Trans. Magn.*, Vol.26, No.5, 1689(1990).
- [3] C. Tsang, *J. Appl. Phys.*, 69(8), 5393(1991).
- [4] H.N. Bertram, *Proceedings of IEEE*, Vol.74, No.11, 1494(1986).
- [5] M.H. Kryder, "Proceedings of the Symposium on Magnetic Materials, Process and devices", *Proceedings Vol.90-8*, 25(1990).
- [6] J-G. Zhu and H.N. Bertram, *IEEE Trans. Magn.*, Vol.26, No.5, 2140(1990).
- [7] T. Chen and T. Yamashita, *IEEE Trans. Magn.*, Vol.24, No.6, 2700(1988).
- [8] S. Iwasaki and Y. Nakamura, *IEEE Trans. Magn.*, MAG-13, No.5, 1272(1977).
- [9] T. Susuki and S. Iwasaki, *IEEE Trans. Magn.*, Mag-18, No.2, 769(1982).
- [10] S. Iwasaki, *IEEE Trans. Magn.*, MAG-16, No.1, 71(1980).
- [11] S. Iwasaki, *IEEE Trans. Magn.*, MAG-16, No.5, 1111(1980).
- [12] S. Iwasaki, *J. Appl. Phys.* 69(8), 4739(1991).
- [13] J. Hokkyo and F.Kugiya, *J. Magn. Soci. Japan*, Vol.13, No.S1, 1(1989).
- [14] J. Hokkyo, K. Hayakawa, I. Saito, S. Satake, K. Shirane, N. Honda, T. Shimamura and T. saito, *IEEE Trans. Magn.*, Vol . MAG-18, No.6, 1203(1982).
- [15] K. Ouchi, *J. Magn. Soci. Japan*, Vol.13, No.S1, 611(1989).
- [16] S. Iwasaki, Y. Nakamura and K. Ouchi, *IEEE Trans. Magn.*, MAG-15, No.6, 1456(1979).
- [17] Y. Nakamura, *J Magn. Soci. Japan*, Vol.15, No.S2, 497(1991).
- [18] W. Heisenberg, *Z. Physik*, Vol. 49, 619(1928).

- [19] P. Weiss, *J Phys.*, Vol. 6, 661(1907).
- [20] A. H. Morrish, "Physical principles of magnetism" (John Wiley & Sons, Inc., London, 1965).
- [21] A. Hoagland and J. Monson, "Digital Magnetic Recording" (Wiley-interscience, New York, 1991).
- [22] J-G. Zhu and H.N. Bertram, *J. Appl. Phys.*, 66(3), 1291(1989).
- [23] P.I. Mayo, R.M. Erkkila, A. Bradbury and R.W. Chantrell, *IEEE Trans. Magn.*, Vol.26, No.5, 1894(1990).
- [24] P.I. Mayo, K. O'Grady, J.A. Cambridge, I.L. Sanders, T. Yogi, P.E. Kelly and R.W. Chantrell, *J. Appl. Phys.*, Vol. 69, 4733(1991).
- [25] K. O'Grady, *IEEE Trans. Magn.*, Vol. 26, No. 5, 1870(1990).
- [26] I.A. Beardsley and J-G. Zhu, *IEEE Trans. Magn.*, Vol. 27, No. 6, 5037(1991).
- [27] E.P. Wohlfarth, *J. Appl. Phys.*, 29, 595(1958).
- [28] O. Henkel, *Phys. Stat. Sol.*, 7, 919(1964).
- [29] E.C. Stoner and E.P. Wohlfarth, *Phil. Trans. R. Soc.(London)*, Ser. A240, 599(1948).
- [30] E.H. Frei, S. Shtrikman and D. Treves, *Phys. Rev.*, 106, 446(1957).
- [31] J.C. Lodder and C.Z. Li, *J. Magn. Soc. Japan*, Vol. 13, No. S1, 659(1989).
- [32] J.C. Lodder and C.Z. Li, *IEEE Trans. Magn*, Vol. 25, No. 5, 4174(1989).
- [33] G.T.A. Huysmans and J.C. Lodder, *J. Appl. Phys.*, 64(4), 2016(1988).
- [34] I. Tagawa, Y. Shimitzu and Y. Nakamura, *J. Magn. Soci. Japan*, Vol.15, No.S2, 827(1991).
- [35] K. Tohma, Y. Kawawake and R. Sugita, *J. Magn. Soci. Japan*, Vol.15, No.S2, 15(1991).
- [36] O. Karlquist, *Trans. Roy. Inst. Technol. Stockholm*, 86(1954).
- [37] J.C. Mallinson, "The Foundations of Magnetic Recording" (Academic Press, Inc. San Diego, 1987).
- [38] F. Jorgensen, "The Complete Handbook of Magnetic Recording" (Tab Books Inc., 1980).
- [39] Robert M. White, "Introduction to magnetic recording" (IEEE Press, New York, 1985).
- [40] M. Kusunoki, H. Ohashi, M. Fujiki, Y. Ito, *IEEE Trans. Magn.*, MAG-23, No.5, 2076(1987).

- [41] I. Saito, S. Satake, K. Kawazoe and J. Hokkyo, *IEEE Trans. Magn.*, MAG-20, No.5, 903(1984).
- [42] M.L. Williams and R.L. Comstock, 17th Annual AIP Conf. Proc., Part 1, No. 5, 738(1971).
- [43] B.K. Middleton and C.D. Wright, *IERE Conf. Proc.*, Vol. 54, 181(1982).
- [44] R.L. Wallace, *Bell Syst. Tech. J.*, Vol. 30, 1145(1957).
- [45] S. Iwasaki and J. Hokkyo, "Perpendicular Magnetic Recording", (Ohmsha, Ltd, Tokyo Japan, 1991).
- [46] S. Satake, N. Honda and J. Hokkyo, *J. Magn. Society Japan*, Vol. 8, No. 2, 81(1984).
- [47] C. Denis Mee, Eric D. Daniel, "Magnetic Recording Handbook, Technology and Application", (McGraw-Hill Publishing Company, New York, 1988).
- [48] H. Hamilton, *J. Magn. Soc. Japan*, Vol.15, No.S2, 483(1991).
- [49] N. Bertram, NATO-ASI Summer School on Applied Magnetism, July 1992.
- [50] E.D. Daniel, *J. Audio Eng. Soc.*, Vol.20, No.2, 92(1972).
- [51] J.C. Mallinson, *IEEE Trans. Magn.*, Vol. MAG-5, No.3, 182(1969).
- [52] L. Thurlings, *IEEE Trans. Magn.*, Vol. MAG-16, No.3, 507(1980).
- [53] J-G. Zhu and H.N. Bertram, *IEEE Trans. Magn.*, Vol. 24, No.6, 2706(1988).
- [54] J-G. Zhu and H.N. Bertram, *J. Appl. Phys.*, 69(8), 6084(1991).
- [55] H. Aoi, R. Tsuchiya, Y. Shiroishi and H. Matzuyama, *IEEE Trans. Magn.*, Vol. 24, No.6, 2715(1988).
- [56] R.P. Ferrier, *IEEE Trans. Magn.* Vol.25, No.5, 3387(1989).
- [57] J.A. Thornton, *J. Vac. Sci. Technol.* A4(6), 3059(1986).
- [58] John A. Thornton, "Evaporation and Sputtering" (Noyes Publications, Park Ridge, NJ, 1984).
- [59] K. Reichelt, *Vacuum*, Vol.38, No.12, 1083(1988).
- [60] William A. Tiller, "The Science of crystallisation: microscopic interfacial phenomena" (Cambridge University Press, Cambridge, 1991).
- [61] J.H. van der Merwe and E. Bauer, *Physical Review (B)* Vol.39, No.6, 3632(1989).
- [62] K. Hayashi, M. Hayakawa, Y. Ochiai, H. Matsuda, W. Ishikawa, Y. Iwasaki and K. Aso, *J. Appl. Phys.* 61(8), 2983(1987).
- [63] A.G. Spencer, C.A. Bishop and R.P. Howson, *Vacuum* 37, No 3/4, 366(1987).
- [64] N. Mahvan, PhD thesis, 1988.

- [65] T. Wielinga, *J. Appl. Phys.* 50(7), 4888(1979).
- [66] P.J. Grundy and G.A. Jones, "Electron Microscopy in the Study of Materials" (Edward Arnold, Bristol, 1976).
- [67] J. Zak, E.R. Moog, C. Liu and S.D. Bader, *JMMM*, Vol. 89, 107(1990).
- [68] J.N. Chapman, *J. Phys. D: Appl. Phys.*, Vol.17, 623(1984).
- [69] T. Wielinga, J.C. Lodder and J. Worst, *IEEE Trans. Magn.*, MAG-18, 1107(1982).
- [70] T. Wielinga and J.C. Lodder, *Phys. Stat. Sol.*, Vol.(a)96, 255(1986).
- [71] C.R. Chang and D.R. Fredkin, *IEEE Trans. Magn.*, MAG-23, 2052(1987).
- [72] J.C. Lodder, T. Wielinga and J. Worst, *Thin Solid Films*, Vol.101, 61(1983).
- [73] H.S. Gill and T. Yamashita, *IEEE Trans. Magn.*, MAG-20, 776(1984)
- [74] M. Futamoto, Y. Honda, H. Kakibayashi and K. Yoshida, *IEEE Trans. Magn.*, MAG-21, 1426(1985).
- [75] T. Tanaka and H. Masuya, *Japan. J. Appl. Phys.*, 26(6), 897(1987).
- [76] O. Kitakami, Y. Ogawa, H. Fujiwara, F. Kugiya and M. Suzuki, *IEEE Trans. Magn.*, MAG-25, 2607(1989).
- [77] D. Jeannot and J. Bouchand, *IEEE Trans. Magn.*, MAG-24, 2356(1988).
- [78] C.P.G. Schrauwen and J.P.C. Bernardis, *IEEE Trans. Magn.*, MAG-24, 1901(1988).
- [79] H. Cura and A. Lenhart, *J. Magnetism and Magnetic Materials*, Vol 83, 72(1990).
- [80] Y. Hsu, J.M. Sivertsen and J.H. Judy, *IEEE Trans. Magn.*, Vol.26, No.5, 1599(1990).
- [81] J.C. Allen, R.D. Fisher, *IEEE Trans. Magn.*, MAG-23, 122(1987).
- [82] R.D. Fisher, J.C. Allen, J.L. Pressesky, *IEEE Trans. Magn.*, MAG-22, 352(1986).
- [83] J.K. Howard, *J. Vac. Sci. Technol.* A4(6), 2975(1986).
- [84] H. Tamai, K. Tagami and H. Hayashida, *IEEE Trans. Magn.*, MAG-24, 2347(1988).
- [85] J. Zak, E.R. Moog, C. Liu and S.D. Bader, *J. Magnetism and Magnetic Materials*, Vol. 89, 107(1990).
- [86] B.E.P. Beeston, R.W. Horne and R. Markham, "Electron Diffraction and Optical Diffraction Techniques" (North-Holland/American Elsevier, 1972).
- [87] P.B. Hirsch, A.Howie, R.B. Nicholson and D.W. Pashley, "Electron Microscopy of Thin Crystals" (Butterworths, London, 1965).
- [88] J.W. Edington, "Interpretation of transmission electron micrographs" (The Macmillan Press Ltd, London,1975).

- [89] K. Ouchi and S. Iwasaki, *J. Apply. Phys.*, 57(1), 4013(1985).
- [90] D.J. Mapps, N. Mahvan and M.A. Akhter, *IEEE Trans. Magn.*, Vol.25, No.5, 4192(1989).
- [91] T. Yeh, J.M. Sivertsen and J.H. Judy, *IEEE Trans. Magn.*, Vol.26, No.5, 1590(1990).
- [92] C. Byun, J.M. Sivertsen and J.H. Judy, *J. Appl. Phys.*, 57(1), 3997(1985).
- [93] S. Onodera, S. Okijima, K. Nakamura and S. Iwasaki, *J. Magn. Soci. Japan*, Vol.15, No.S2, 287(1991).
- [94] M. Takahashi, H. Uwazumi, T. Miyazuki, T. Sato, M. Takahashi and T. Wakiyama, *J. Magn. Soci. Japan*, Vol.13, No. S1, 743(1989).
- [95] H. Sakakima, *IEEE Trans. Magn. MAG-19*, No.2, 131(1983).
- [96] G. Pan, A.G. Spencer and R.P. Howson, *IEEE Trans. Magn.*, Vol.27, No.1 664(1991).
- [97] T. Jagielinski, *J. Appl. Phys.*, 61(8), 3237(1987).
- [98] M. Prutton, "Thin Ferromagnetic Films" (Butterworths, London, 1962).
- [99] R. F. Soohoo, "Magnetic Thin Films" (Harper & Row, New York, 1965).
- [100] H. Fujimori, N.S. Kazama, K. Hirose, J. Zhang, H. Morita, I. Sato and H. Sugawara, *J. Appl. Phys.*, 55(6), 1796(1984).
- [101] Y. Matsuda, Y. Shiroishi, T. Shimotsu and K. Takagi, *J. Magn. Soci. Japan*, Vol. 13, Supplement S1, 391(1989).

Appendix A

Publications

In-contact magnetic recording performance of Pt/CoCrTa thin films on glass computer disks *

D.J. Mapps ^a, G. Pan ^a, M.A. Akhter ^a, S. Onodera ^b and A. Okabe ^c

^a Centre for Research in Information Storage Technology, University of Plymouth, Plymouth, Devon PL4 8AA, UK

^b Sony Magnetic Products Inc., 3-4-1 Sakuragi, Tagajo-shi, Miyagi-ken 985, Japan

^c Sony Corporation Research Center, 174 Fujitsuka-cho, Hodogaya-ku, Yokohama 240, Japan

CoCrTa films deposited on fcc Pt and Au underlayers show excellent *c*-axis orientation. The 'epitaxial-growth' mechanism may explain the origin of such an effect. The perpendicular MOKE and VSM coercivity, shape of hysteresis loops and contact recording results of such media are investigated and discussed together with the film structure. A first peak D_{50} of 160 kFRPI has been realized by a single-layer Pt/CoCrTa rigid disk using an in-contact MIG head.

1. Introduction

In the search for extremely high density recording media for both longitudinal and perpendicular magnetic recording, underlayers are found to be very important in improving the film orientation and in reducing the recording noise [1,2]. For perpendicular recording in particular, comprehensive studies have been undertaken in recent years in order to find the best underlayer for Co-based perpendicular media and to understand the origin of the underlayer effect [2,3]. In this paper we report our recent study of CoCrTa films deposited on Pt, Au and Ti underlayers and the in-contact magnetic recording performance of such media.

2. Experimental

CoCrTa films, their underlayers and carbon protective layers were deposited onto 3.5" glass computer disk substrates by rf-magnetron sputtering in the same evacuation. The base pressure of the system is 3×10^{-7} Torr. Sputtering Ar pressure was 4 mTorr. An alloy target of $\text{Co}_{78.5}\text{Cr}_{17.5}\text{Ta}_4$ was used for the deposition of CoCrTa films, which produces CoCrTa films with composition of $\text{Co}_{79}\text{Cr}_{18}\text{Ta}_3$ analyzed by EDAX. The film structure and crystal orientation was studied by x-ray diffraction pattern, rocking curve method and scanning electron microscope (SEM). The magnetic properties of the CoCrTa films were measured by VSM and magneto-optic Kerr effect (MOKE) system. A non-fly-

ing head supporting mechanism [4] and a MIG head with gap length of 0.15 μm , track width of 30 μm and saturation magnetization of the metal of 14.5 kG were used in the in-contact recording experiment. The recording tests were performed on 3.5 in. single-magnetic-layer disks coated with an 80 Å thick carbon layer and a liquid lubricant layer. The relative head-medium velocity was 3 m/s.

3. Results and discussion

3.1. Crystal orientation

X-ray diffraction shows that CoCrTa films deposited on fcc Pt, fcc Au and hcp Ti all exhibit strong [0002] texture. The Pt and Au underlayers exhibit a very strong [111] texture. The Ti underlayer has a preferred [0002] texture with a very weak (10 $\bar{1}$ 0) peak. Figure 1 shows a typical X-ray diffraction pattern of 440 Å thick CoCrTa films deposited on Pt underlayers. The Pt underlayer thickness is 900 Å. It has been reported by various authors [2,3] that the hcp Ti underlayer improves the [0002] texture of CoCr films because of the 'epitaxial growth' of hcp Co on the [0002] textural hcp Ti. The effect of fcc Pt and Au underlayers on the texture of CoCrTa films may also be attributed to such 'epitaxial growth' mechanism because of the similarity of the lattice patterns of fcc (111) plane and hcp (0002) as shown in fig. 2, in spite of their lattice misfit. We found in our experiment that the [111] texture of the Pt and Au underlayer is essential for the growth of [0002] textural CoCrTa films.

Table 1 summarizes the thickness dependence of $\Delta\theta_{50}$ of CoCrTa films on 900 Å thick Pt, Au and Ti underlayers. CoCrTa films deposited on Pt and Au underlayers show very small $\Delta\theta_{50}$ at any film thickness while the films deposited on Ti underlayers have rela-

Correspondence to: Dr. G. Pan, Centre for Research in Information Storage Technology, University of Plymouth, Plymouth, Devon PL4 8AA, UK.

* This work was carried out at the Sony Research Centre, Yokohama, Japan, under the 'Sony Sabbatical Chair' scheme.

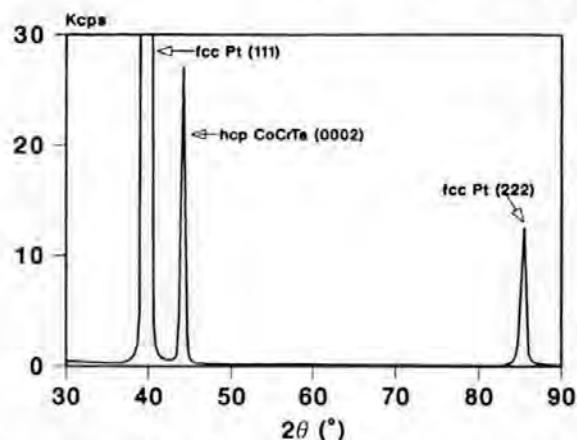


Fig. 1. X-ray diffraction pattern of 440 Å thick CoCrTa film deposited on Pt underlayer, using CuK α radiation (30 kV, 100 mA, 1.5405 Å wavelength).

tively larger $\Delta\theta_{50}$ in the thinner film region. This is perhaps due to the less strong [0002] texture of the hcp Ti underlayers in this experiment.

3.2. Magnetic properties

The perpendicular coercivity of the CoCrTa films on Pt and Ti underlayers were measured by MOKE and by VSM, and results are shown in fig. 3. In these measurements we find that for the CoCrTa films deposited on Pt underlayers, the MOKE coercivity and VSM coercivity are nearly the same, while for the films deposited on Ti underlayers, the MOKE coercivity is much larger than the VSM coercivity. This is especially

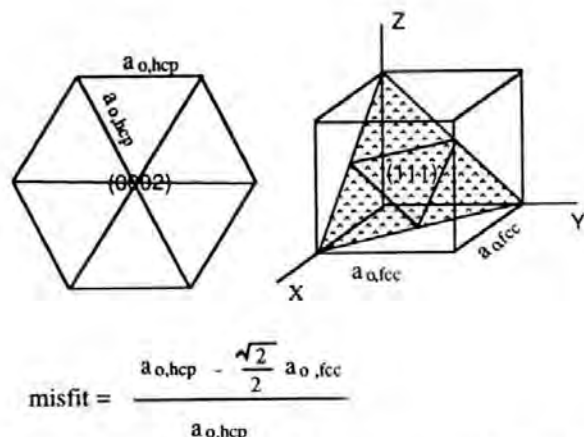


Fig. 2. Schematic representation of hcp (0002) and fcc (111) lattice plane, and the lattice misfit calculation for the [0002] textural hcp CoCrTa on the [111] textural fcc Pt or Au underlayers.

Table 1

$\Delta\theta_{50}$ of different thicknesses of CoCrTa films on Pt, Au, Ti underlayers

CoCrTa film thickness	220 Å	440 Å	880 Å	2000 Å
$\Delta\theta_{50}$ of CoCrTa on Pt	4.6	4.6	4.9	4.9
$\Delta\theta_{50}$ of CoCrTa on Au	4.9	5	5.1	4.8
$\Delta\theta_{50}$ of CoCrTa on Ti	10.5	8.8	4.8	4.9

true in film thickness region 400–1500 Å. It was believed that the MOKE coercivity is a measure of surface coercivity and the VSM coercivity is a measure of bulk [5]. One possible explanation to this phenomenon may be that the orientation distribution through the depth of the film thickness of these two films is different. In the case of Ti/CoCrTa, as shown in table 1, the surface film has better [0002] orientation than the bottom films. This may cause the non-uniformity of the magnetic properties of the film through the depth of the film thickness. In the case of Pt/CoCrTa, the crystal orientation of the films through the depth of the film thickness is very uniform, consequently, the film also has uniform magnetic properties through the entire film thickness.

In fig. 3 it is also noticeable that the Ti/CoCrTa films exhibit larger coercivity than the Pt/CoCrTa films. Figure 4 shows the typical VSM hysteresis loops of the Ti/CoCrTa and Pt/CoCrTa at the film thickness of 2000 Å. The CoCrTa deposited on Pt exhibits a

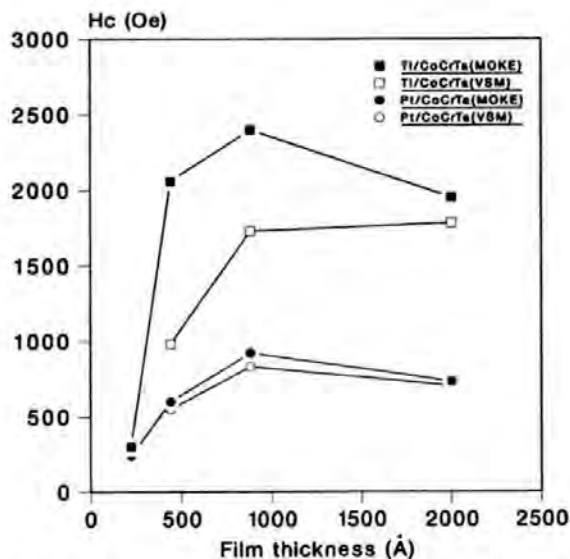


Fig. 3. Thickness dependence of perpendicular coercivity of CoCrTa films deposited on Pt and Ti underlayers measured by MOKE and VSM.

thin, 'waisted loop' with a well-defined 'shoulder' and the films on Ti have a fat loop with a rounded 'shoulder'. The perpendicular coercivities of Pt/CoCrTa and Ti/CoCrTa are 700 and 2000 Oe, respectively. CoCrTa films on Au underlayers show similar behaviour as that of Pt/CoCrTa films. It has been proposed by Zhu and Bertram [6] from their computer simulation that the shape of the perpendicular loop and the perpendicular coercivity of the CoCr films are determined mainly by the intergranular exchange coupling of the films. A weak exchange coupled film shows a fat loop with a rounded 'shoulder' whilst a strong exchange coupled film exhibits a thin, 'waisted loop' with a well defined 'shoulder' and the coercivity decreases with the increase in the exchange coupling constant. The shape of the loops and the perpendicular coercivity shown in fig. 4 apparently indicate that the grains of CoCrTa on Ti are weakly exchange-coupled and that on Pt are more strongly exchange-coupled. Our SEM examination of these two films shows that the Pt/CoCrTa films have a smaller grains than the Ti/CoCrTa films. As shown in fig. 5, the average grain size is 250 Å for the 2000 Å thick CoCrTa films on a 900 Å thick Pt underlayer, and 500 Å for the same thickness CoCrTa on a 900 Å thick Ti underlayer. The different grain (or column) size of the two films may be due to the replication of the different grain morphology of the two different underlayers. However, it is still

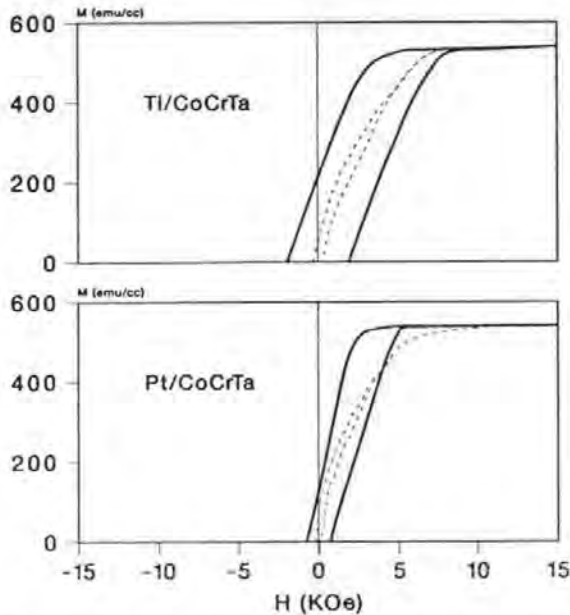


Fig. 4. Typical VSM perpendicular (solid lines) and in-plane (dashed lines) hysteresis loops of the Ti/CoCrTa and Pt/CoCrTa at film thickness of 2000 Å.

not certain that whether the differences in the shape of the hysteresis loop and the perpendicular coercivity of the two films are associated with such a difference in the grain or column size which may give rise to a different intergranular exchange coupling, or it is due to the difference of the Cr segregation in CoCrTa films occurred on the two different underlayers. More microstructural examinations are needed to understand this.

There are various approaches reported in recent years to change the perpendicular coercivity of CoCr- or Co-based perpendicular films, namely, to increase the sputtering Ar pressure, which enhances the columnar morphology of the CoCr films [7]; to add non-magnetic additives, such as Ta [8], which promotes the selective segregation of the non-magnetic elements around the grain boundaries; to increase the substrate temperature [9] during deposition, which enhances the Cr segregation around the grain boundaries; and most recently, to form non-magnetic gaps between columns by introducing B(O) in a Co-based perpendicular film [10]. This study suggests that the underlayer is another important factor that causes a change in film morphology and hence perpendicular coercivity and shape of hysteresis loops.

3.3. In-contact recording

Figure 6 shows the bit density response of three single-layered Pt/CoCrTa disks with medium thickness of 440, 880 and 2000 Å, and one single-layer Ti/CoCrTa disk with medium thickness of 2000 Å, respectively. The output signal level and the D_{50} of three disks with Pt underlayers increase with CoCrTa film thickness. In a low-density region such an increase is proportional to the medium thickness. However, the 2000 Å thick medium shows much higher output signals in the high recording density region than the thinner media; for instance, the difference in the output signals of the 2000 and 880 Å thick media is only 10 dB at 10 kFRPI, but 18 dB at 100 kFRPI. The achieved D_{50} of the 2000 Å thick medium is 160 KFRPI and maximum output is 80 nV_{0-p}/μm · turn · m/s at 68 kFRPI. It has been proposed by Iwasaki [11] that the optimum thickness of the single-layer perpendicular recording medium is the one which equals to the head gap length, in this work, 0.15 μm. It is not clear that whether the good recording performance of the 2000 Å thick CoCrTa medium is related to such a phenomenon.

The bit density response of the 2000 Å thick CoCrTa medium on Ti underlayer ($D_{50} = 120$ kFRPI) is not as high as that of 2000 Å thick CoCrTa medium on Pt underlayer, particularly in the higher-density region.

There are three major differences between these two media, the crystal orientation distribution, the shape of hysteresis loop or perpendicular coercivity and the grain size, as shown in table 1 and figs. 3–5. The better orientation and smaller grain size of the medium on Pt underlayer may favour a better bit density response [12]. On the other hand, the weak intergranular exchange coupling of the medium on Ti underlayer is desirable for a high-density recording medium. A high

coercivity is also favourable for a better bit density response if the writing head can write effectively on the high-coercivity medium. More experimental studies are needed in order to clarify the effects of the above properties on the bit density response and on the signal-to-noise ratio.

The authors gratefully acknowledge Tetsuya Yamamoto for his skilful assistance in the X-ray diffrac-

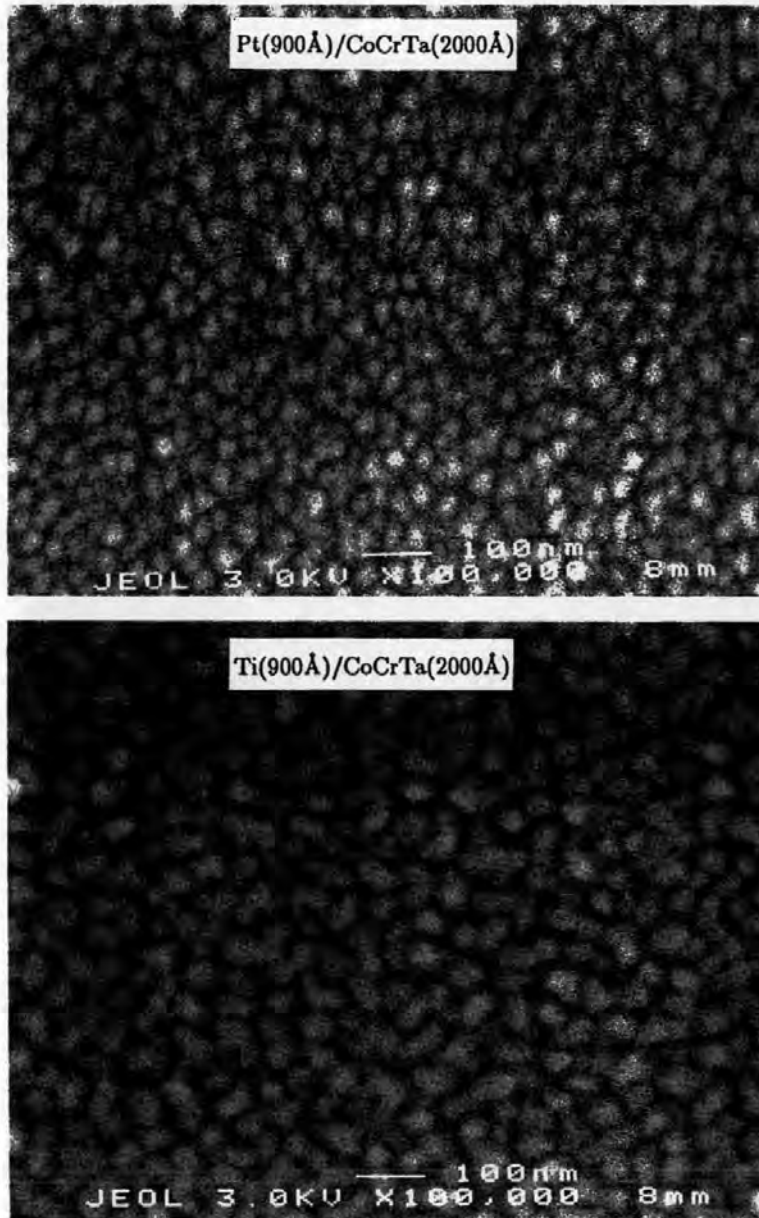


Fig. 5. SEM surface micrographs of Ti (900 Å)/CoCrTa (2000 Å) and Pt (900 Å)/CoCrTa (2000 Å) films.

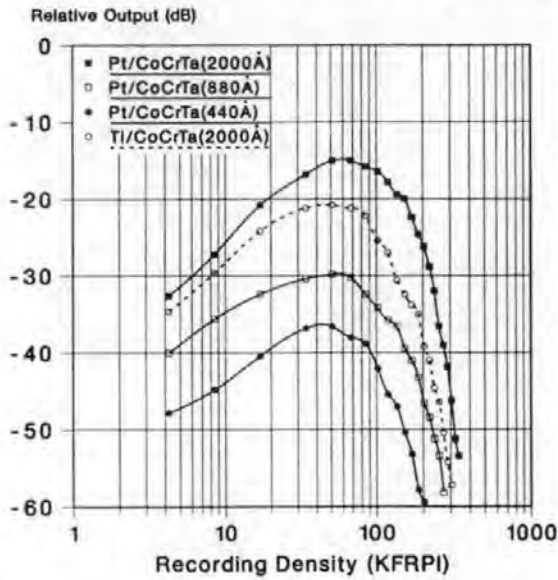


Fig. 6. Bit density response of three disks with different thickness CoCrTa media on Pt underlayers. Also shown are the results of a Ti/CoCrTa disk with medium thickness of 2000 Å.

tion measurements, Dr. Kazuhiko Hayashi and Naoki Honda for their useful advice and discussion. They also wish to express their deep appreciation to Dr. Koichi

Aso and Dr. S. Watanabe for their continuous support to the work. The SERC and Pilkington plc. are acknowledged for providing financial support and glass disk substrates for the project.

References

- [1] T. Yogi, C. Tsang, T.A. Nguyen, K. Ju, G.L. Gorman and G. Castillo, IEEE Trans. Magn. MAG-26 (1990) 2271.
- [2] M. Futamoto, Y. Honda, H. Kakibayashi and K. Yoshida, IEEE Trans. Magn. MAG-21 (1985) 1426.
- [3] G. Pan, D.J. Mapps, M.A. Akhter, J.C. Lodder, P. ten Berge, H.Y. Wong and J.N. Chapman, J. Magn. Magn. Mater. 113 (1992) 21.
- [4] S. Onodera, S. Okijima, K. Ouchi, Y. Nakamura and S. Iwasaki, J. Magn. Soc. Jpn. 15 (1991) S2-287.
- [5] D.J. Mapps, N. Mahvan and M.A. Akhter, IEEE Trans. Magn. MAG-25 (1989) 4192.
- [6] J.G. Zhu and H.N. Bertram, J. Appl. Phys. 66 (1989) 1291.
- [7] J.A. Thornton, Ann. Rev. Mater. Sci. 7 (1977) 239.
- [8] J.K. Howard, J. Vacuum. Sci. Technol. A4 (1986) 2975.
- [9] K. Ouchi and S. Iwasaki, IEEE Trans. Magn. MAG-23 (1987) 2443.
- [10] K. Hayashi, M. Hayagawa, H. Ohmori, A. Okabe and K. Aso, J. Appl. Phys. 67 (1990) 5175.
- [11] S. Iwasaki, J. Appl. Phys. 69 (1991) 4739.
- [12] H.N. Bertram, NATO-ASI Summer School in Applied Magnetism, July 1992.

Microstructure and magnetic properties of very thin CoCr films deposited on different underlayers by rf-sputtering

G. Pan, D.J. Mapps, M.A. Akhter

School of Electronic, Communication and Electrical Engineering, Polytechnic South West, Plymouth, Devon, PL4 8AA, UK

J.C. Lodder, P. ten Berge

Faculty of Electrical Engineering and Applied Physics, University of Twente, P.O. Box 217, 7500 AE Enschede, The Netherlands

H.Y. Wong and J.N. Chapman

Department of Physics and Astronomy, The University of Glasgow, Glasgow, G12 8QQ, UK

Very thin CoCr films deposited on different underlayers on glass disk substrates were studied by the magneto-optic Kerr effect, VSM, torque magnetometry and TEM selected area diffraction. Square or near square perpendicular loops were obtained from Co/Ti, CoCr/Au, CoCr/Al, CoCr/C and CoCr/Si films. TEM SAD study revealed that the crystalline structure is a key factor determining the magnetic anisotropy of the very thin CoCr films. In particular, the *c*-axis of the hcp CoCr films which exhibit square perpendicular loops is perpendicular to the film plane whilst that of the CoCr films which exhibit a thin and flat perpendicular loop lies in the film plane. The texture of the very thin CoCr films deposited on different underlayers is mainly dependent on the structure and texture of underlayers. The relation between the structure of CoCr and its underlayers is discussed.

1. Introduction

There is a considerable current interest in the effect of underlayers on the magnetic properties of both perpendicular and longitudinal magnetic recording media [1,2]. In a previous paper [1] we have reported on the magnetic properties of very thin CoCr films deposited on Ti underlayers. Very pronounced effects of Ti underlayers on the shearing and the squareness ratio of the perpendicular loops have been observed in such CoCr films. In order to understand the origin of the underlayer effect, further experimental investigation into the microstructure, micromagnetics and magnetic properties of these films have been un-

dertaken. We report here on a detailed experimental programme of magnetic measurements together with microstructural examinations by TEM of the 160 Å thick CoCr films with different underlayers.

2. Experimental details

Very thin CoCr films were deposited on different underlayers or directly on to glass disk substrates. The film thickness was measured by a talystep and a Scanning Auger microprobe (SAM). The Cr content of the CoCr films is 23 at% by Auger. The magnetic properties of the CoCr films were studied using a magneto-optic Kerr effect (MOKE) system, a vibration sample magnetometer (VSM) and a torque magnetometer. The film structure and crystal orientation

Correspondence to: Dr. G. Pan, School of Electronic, Communication and Electrical Engineering, Polytechnic South West, Plymouth, Devon, PL4 8AA, UK.

0304-8853/92/\$05.00 © 1992 – Elsevier Science Publishers B.V. All rights reserved

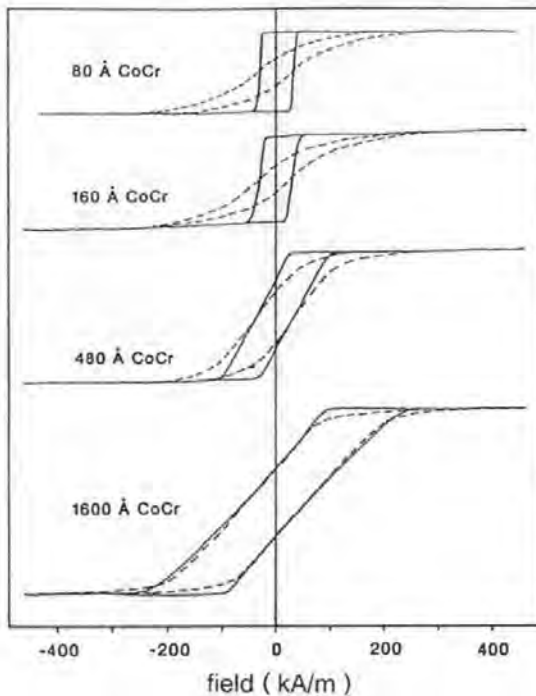


Fig. 1. Perpendicular MOKE loops of different thickness CoCr films with and without Ti underlayers (solid and dashed line respectively). Vertical axis is in arbitrary units.

were investigated by selected area diffraction (SAD) on a JEOL 2000FX TEM. For the preparation of TEM specimens, glass disk substrates were precoated with carbon films before the deposition of underlayers and the CoCr films themselves. The films were then floated off in water.

3. Results

3.1. Magnetic measurements

Fig. 1 shows the perpendicular MOKE loops of different thickness CoCr films with Ti underlayers (solid line) and without Ti underlayers (dashed line). For the 1600 Å thick CoCr films, the principal difference of the MOKE loops of CoCr films with and without Ti underlayers is only in the "shoulder" of the loop. As the CoCr film thickness reduces, the MOKE loops of the CoCr films deposited directly on glass become

more rounded. On the other hand, the MOKE loops of CoCr films on Ti underlayers become steeper and squarer. The shearing of the perpendicular loops has been discussed in the light of a stripe domain model suggested by Weilinga and Lodder [3] and a particulate model suggested by Chang and Fredkin [1,4].

Fig. 2 shows the Ti underlayer thickness effect on the perpendicular loops of 160 Å thick CoCr films, which indicates that the squareness and the shearing of the loops are strongly affected by the existence of even a very thin Ti underlayer. The minimum Ti thickness to obtain a square loop is about 250 Å.

The perpendicular $M-H$ loops of 160 Å thick CoCr films without Ti underlayer and with Ti underlayer were also measured by VSM and results are shown in fig. 3. The square VSM perpendicular loop for the 160 Å thick CoCr film on Ti and a thin and curved one for the films without Ti are in good agreement with the corre-

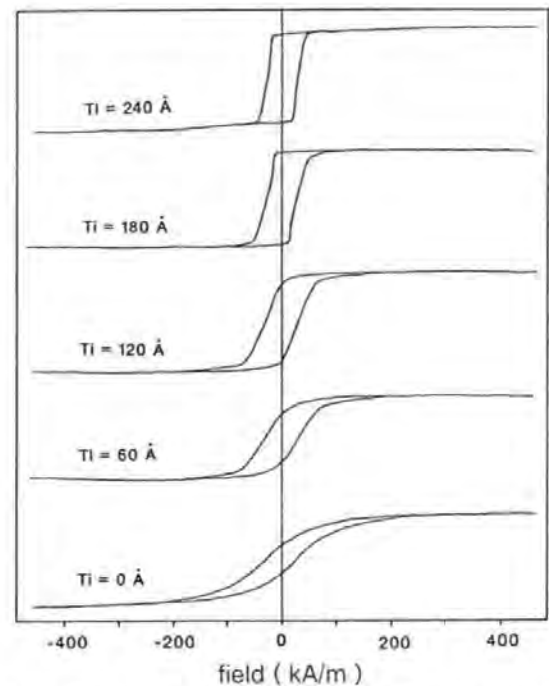


Fig. 2. Ti underlayer thickness effect on the perpendicular MOKE loops of 160 Å thick CoCr films. Vertical axis is in arbitrary units.

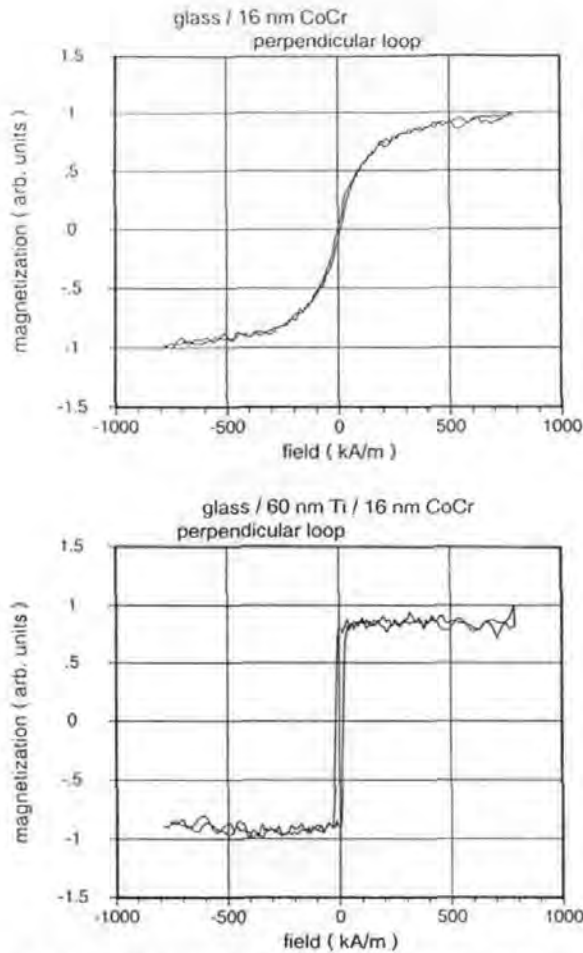


Fig. 3. $M-H$ loops of 160 Å thick CoCr films with and without Ti underlayers measured by VSM.

sponding MOKE loops, indicating an improved perpendicular easy axis behavior of the CoCr films grown on Ti underlayers.

Fig. 4 shows the torque magnetometer plots of the 160 Å thick CoCr films with and without Ti underlayers. Torque curves for both samples were initiated with the applied field in the plane of the sample. Under this condition, torque curves which start at zero degree with negative slope indicate an anisotropy perpendicular to the film plane and with a positive slope indicate an anisotropy in the plane of the films. As shown in fig. 4, the CoCr on glass exhibits a typical in-plane anisotropy torque curve, while the CoCr film on Ti exhibit a near perpendicular anisotropy torque curve. It is obvious that the magnetization easy axis of such thin CoCr film is dependent on the Ti underlayer.

Further experiment on the very thin CoCr films with other different underlayers was undertaken and fig. 5 shows the perpendicular MOKE loops of 80 Å thick CoCr films on different underlayers. Among them, the 80 Å thick CoCr films on Ti, Au, Al and C underlayers or directly deposited on Si substrate exhibit square or near square perpendicular MOKE loops. By contrast the CoCr film on a Cr underlayer exhibits a thin and flat perpendicular loop. The different height of the vertical axis of the loops is believed to be caused by the underlayer enhancement [5]. The effect of different underlayers on the magnetic properties of the initial growth layer of CoCr films can be clearly seen from this figure.

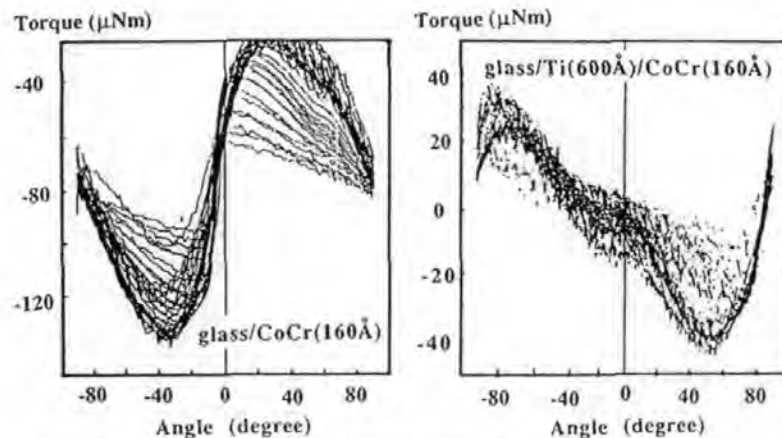


Fig. 4. Torque curves of 160 Å thick CoCr films with and without Ti underlayers.

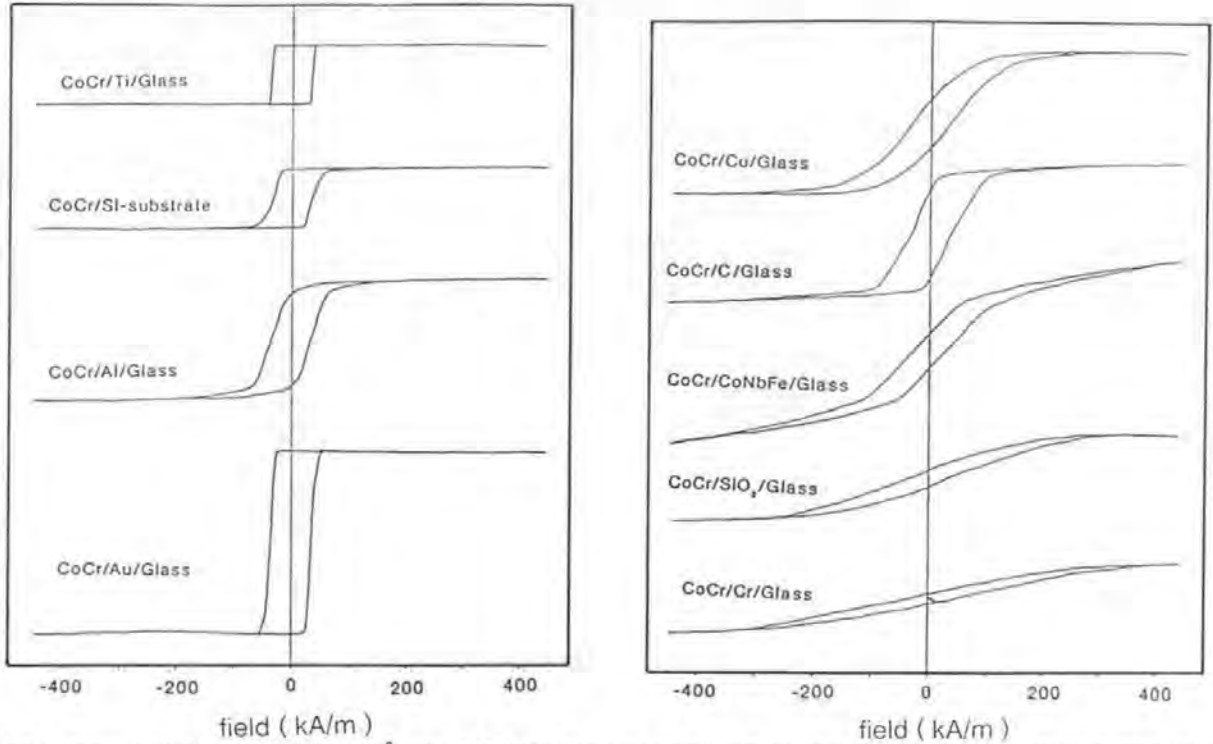


Fig. 5. Perpendicular MOKE loops of 80 Å thick CoCr films deposited on different underlayers, the Y axis is in arbitrary units, but in the same scaling.

3.2. Film microstructure and texture

In order to understand the structural origin of the underlayer effect, the CoCr films and their underlayers were studied by observing selected area diffraction (SAD) patterns with the specimen untilted and tilted through 30° on a JEOL 2000FX TEM.

Let us start with a brief review of the electron diffraction techniques for polycrystalline thin films [6]. In electron diffraction, only those planes which are near parallel to the incident electron beam contribute to the diffraction patterns because the Bragg angle in electron diffraction is very small (less than 1° or 2°).

Fig. 6a is a schematic drawing of a [00.1] oriented hcp Co crystal and the SAD pattern of the [00.1] textural hcp Co films. For such films, the main reflection rings are (1 $\bar{1}$ 00), (11 $\bar{2}$ 0), (20 $\bar{2}$ 0), ... all of which are in the form of $\{hki0\}$. Reflec-

tion rings of (0002), (01 $\bar{1}$ 1), ..., $\{hkil\}$ ($l \neq 0$) would not appear. When the specimen is tilted through 30°, the $\{hki0\}$ rings break into arcs along the diameter parallel to the tilting axis; along the perpendicular diameter, arcs such as (01 $\bar{1}$ 1) appear because this plane makes an angle of 28° with the c -axis. The schematic drawing of SAD patterns of the [11.0] and [10.0] textural Co films are shown in figs. 6b and c respectively. When we observe the SAD patterns of the [11.0] and [10.0] textural polycrystalline films with specimen tilted, it is very difficult to predict when arcs will occur for every family of planes because of the complex of angles within each family. However, one of the obvious features for such textural films is that the (0002) ring will break into arcs along the diameter parallel to the tilting axis.

The experimental results of the SAD patterns of 160 Å thick CoCr films on Ti, Cr, C and Cu underlayers with the specimen untilted and tilted

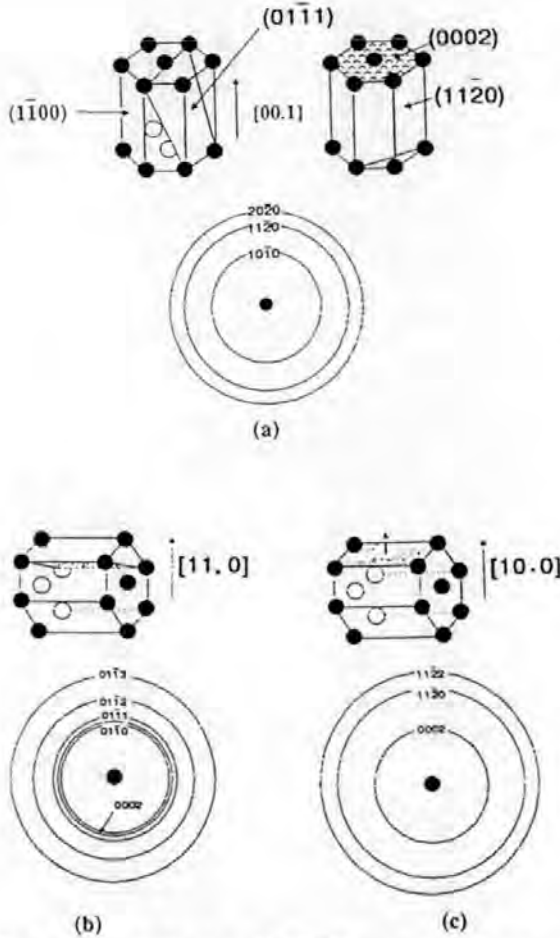


Fig. 6. Schematic drawing of (a) $[00.1]$ zone axis SAD pattern, (b) $[11.0]$ zone axis SAD pattern and (c) $[10.0]$ zone axis SAD pattern of hcp Co polycrystalline films.

through 30° are shown in fig. 7. As mentioned above, these TEM specimens were deposited on a precoated C layers on glass substrates. However, MOKE measurement of these films showed similar loops to those shown in fig. 5. The SAD patterns are indexed in tables 1 to 4. If we examine figs. 6, 7 and tables 1 to 4 carefully, the following conclusions can be drawn.

The SAD patterns of the CoCr films on Ti and C underlayers with the specimen untilted and tilted are as expected from a strong $[00.1]$ textural hcp films. The main reflection rings of the Co on both patterns are $(1\bar{1}00)$, $(1\bar{1}\bar{2}0)$ and $(20\bar{2}0)$ when untilted. Diffraction rings of the form $(000l)$, where $l \neq 0$, are not seen. When the specimen was tilted through 30° , the $(1\bar{1}00)$, $(1\bar{1}\bar{2}0)$ and $(20\bar{2}0)$ rings are broken into arcs along the diameter parallel to the tilting axis. Arcs, such as $(01\bar{1}1)$, appear along the perpendicular diameter. The c -axis of such films is perpendicular to the film plane.

The CoCr on Cr showed a mixed $[11.0]$ and $[10.0]$ zone axis patterns. When the specimen was tilted, the (0002) ring breaks into arcs. The c -axis of such films lies in the film plane. The CoCr on Cu has no texture. Reflection rings from all planes are present on the SAD patterns. When specimen was tilted, no changes to the pattern could be seen.

The underlayer structure can also be clarified from these patterns. The Ti underlayer has a

Table 1
Summary of SAD patterns of C/Ti(300 Å)/CoCr(160 Å) films with specimen untilted and tilted

Ring	Diameter	Plane spacing [Å]		Structure	hkl	Untilted	Tilted
		measured	ASTM				
1	29.0	2.544	2.555	Ti hcp	$10\bar{1}0$	medium ring	ring & arcs
2	31.5	2.342	2.342	Ti hcp	0002	medium ring	unchanged
3	32.9	2.242	2.243	Ti hcp	$01\bar{1}1$	very weak ring	strong arcs \perp
4	34.0	2.170	2.170	Co hcp	$10\bar{1}0$	strong ring	strong arcs
5	38.5	1.916	1.915	Co hcp	$01\bar{1}1$	invisible	strong arcs \perp
6	42.9	1.72	1.72	Ti hcp	$01\bar{1}2$	invisible	weak arcs \perp
7	50.2	1.470	1.475	Ti hcp	$11\bar{2}0$	medium ring	medium arcs
8	55.2	1.337	1.332	Ti hcp	$01\bar{1}3$	very weak ring	unchanged
9	58.6	1.259	1.253	Co hcp	$11\bar{2}0$	strong ring	strong arcs
10	67.5	1.093	1.085	Co hcp	$20\bar{2}0$	very weak ring	weak ring & arcs

Table 2
Summary of SAD patterns of C/Cr(300 Å)/CoCr(160 Å) films with specimen untilted and tilted

Ring	Diameter	Plane spacing [Å]		Structure	<i>hkil</i>	Untilted	Tilted
		measured	ASTM				
1	34.0	2.170	2.170	Co hcp	10 $\bar{1}$ 0	weak ring	unchanged
2	36.2	2.04	2.04	Cr bcc	011	strong ring	ring & arcs
3	36.2	2.038	2.035	Co hcp	0002	strong ring	ring & arcs
4	38.5	1.916	1.915	Co hcp	01 $\bar{1}$ 1	strong ring	ring & arcs
5	49.8	1.481	1.484	Co hcp	01 $\bar{1}$ 2	weak ring	weak arcs
6	51.0	1.447	1.443	Cr bcc	002	strong ring	strong arcs
7	58.6	1.259	1.253	Co hcp	11 $\bar{2}$ 0	weak ring	unchanged
8	62.4	1.182	1.178	Cr bcc	112	weak ring	medium arcs ⊥
9	63.8	1.156	1.15	Co hcp	01 $\bar{1}$ 3	weak ring	unchanged
10	69	1.07	1.067	Co hcp	11 $\bar{2}$ 2	very weak ring	unchanged
11	72	1.02	1.02	Cr bcc	022	weak ring	ring & arcs

Table 3
Summary of SAD patterns of C/CoCr(160 Å) films with specimen untilted and tilted

Ring	Diameter	Plane spacing [Å]		Structure	<i>hkil</i>	Untilted	Tilted
		measured	ASTM				
1	27	2.17	2.17	Co hcp	10 $\bar{1}$ 0	strong ring	strong arcs
2	28.8	2.034	2.035	Co hcp	0002	faint	faint
3	30.5	1.92	1.915	Co hcp	01 $\bar{1}$ 1	faint	strong arcs ⊥
4	46.6	1.257	1.253	Co hcp	11 $\bar{2}$ 0	strong ring	strong arcs
5	53.8	1.089	1.085	Co hcp	20 $\bar{2}$ 0	medium ring	medium arcs
6	55	1.065	1.068	Co hcp	11 $\bar{2}$ 2	faint	strong arcs ⊥
7	61.2	0.957	0.957	Co hcp	02 $\bar{2}$ 2	invisible	weak arcs ⊥
8	71.6	0.818	0.82	Co hcp	12 $\bar{3}$ 0	weak ring	medium arcs

Table 4
Summary of SAD patterns of C/Cu(300 Å)/CoCr(160 Å) films with specimen untilted and tilted

Ring	Diameter	Plane spacing [Å]		Structure	<i>hkil</i>	Untilted	Tilted
		measured	ASTM				
1	34.0	2.170	2.170	Co hcp	10 $\bar{1}$ 0	weak ring	unchanged
2	35.3	2.09	2.087	Cu fcc	111	strong ring	unchanged
3	36.0	2.049	2.038	Co hcp	0002	medium ring	unchanged
4	38.5	1.916	1.915	Co hcp	01 $\bar{1}$ 1	weak ring	unchanged
5	41.0	1.80	1.808	Cu fcc	002	medium ring	unchanged
6	57.8	1.276	1.278	Cu fcc	022	medium ring	unchanged
7	58.6	1.259	1.253	Co hcp	11 $\bar{2}$ 0	medium ring	unchanged
8	68.0	1.085	1.085	Co hcp	20 $\bar{2}$ 0	medium ring	unchanged
9	69.4	1.063	1.067	Co hcp	11 $\bar{2}$ 2	weak ring	unchanged
10	71.0	1.039	1.044	Cu fcc	222	weak ring	unchanged

preferred hcp [00.1] texture. The C layer is amorphous. The Cr underlayer has a preferred bcc [100] texture. The Cu underlayer has a fcc struc-

ture with no texture. The correlation of the underlayer structure and the CoCr texture is schematically given in fig. 8.

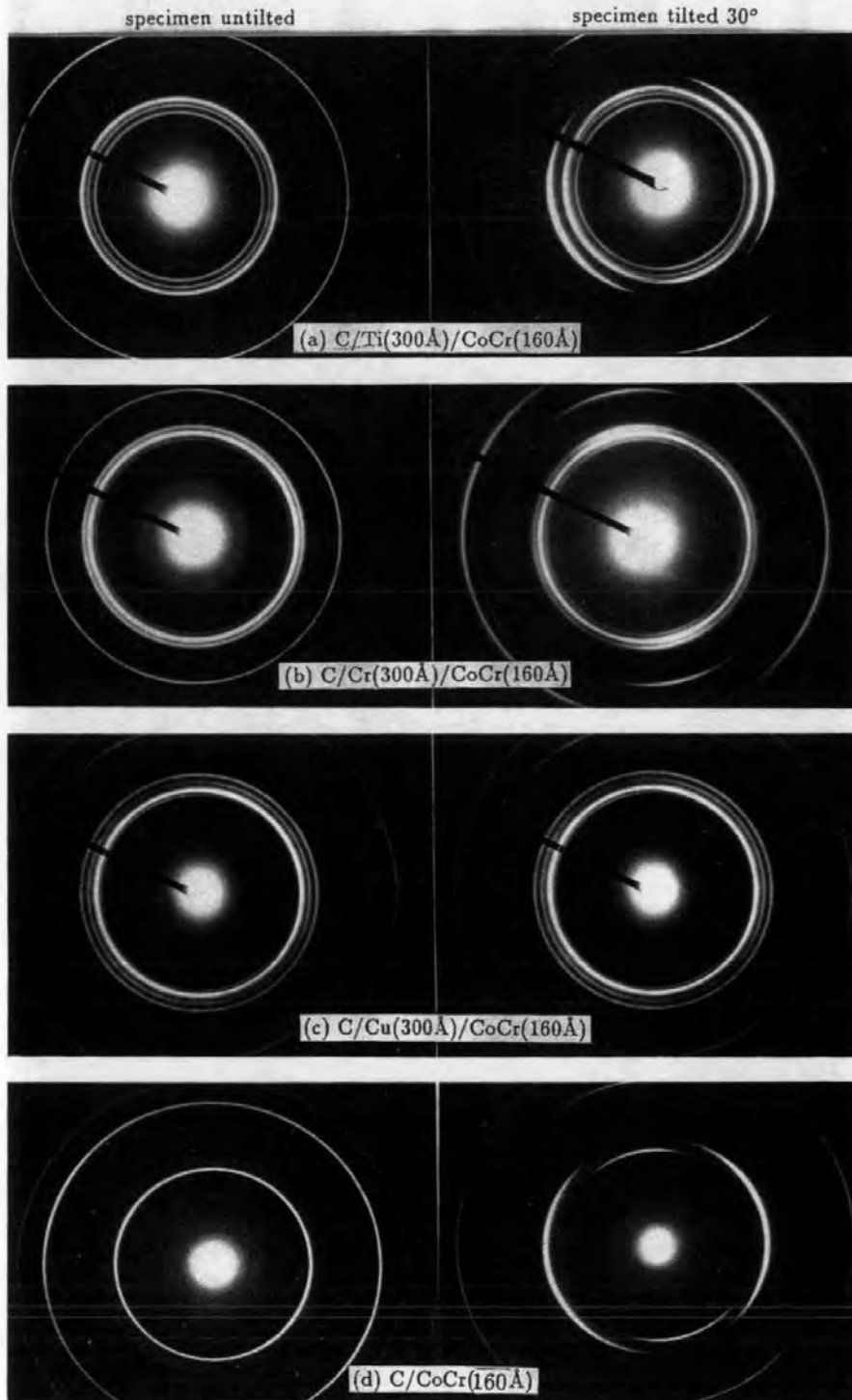


Fig. 7. SAD patterns of 160 Å thick CoCr films deposited on Ti, Cr, Cu and C underlayers.

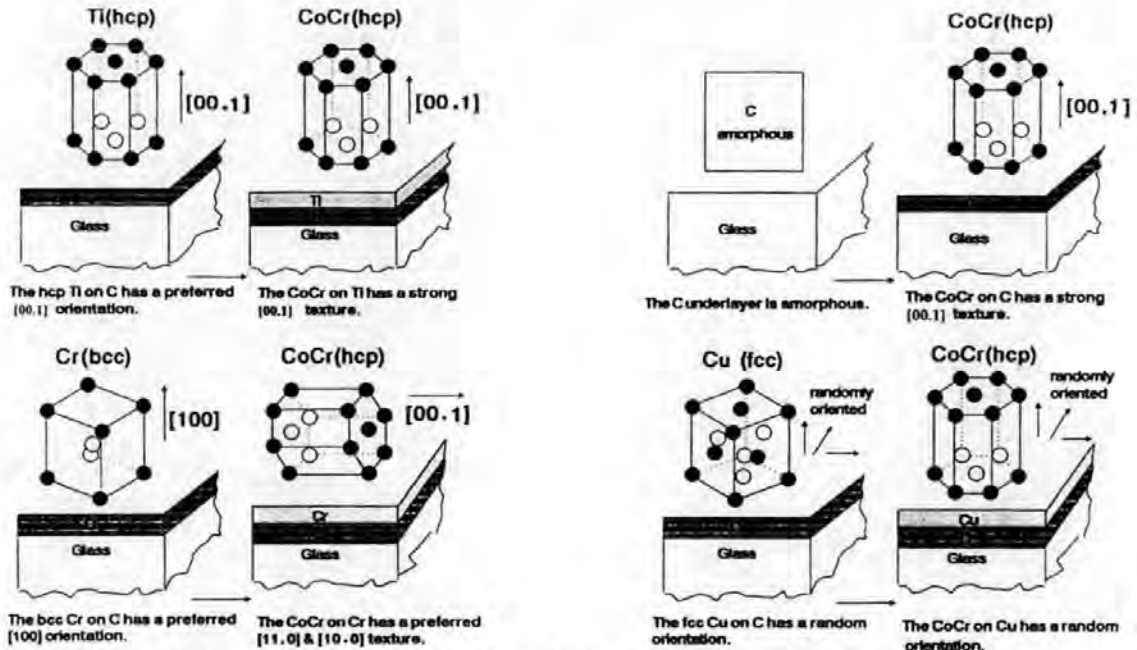


Fig. 8. Schematic representation of the effect of underlayer structure on the texture on CoCr films.

4. Discussion and conclusions

In summary, we conclude that the square or near square perpendicular loops of the very thin CoCr films originate from the improved perpendicular anisotropy of the films due to their growth on appropriate underlayers. Our TEM SAD study revealed that the microstructure is a key factor in determining the easy axis anisotropy of the very thin CoCr films. The c -axis of those hcp CoCr films which exhibit square perpendicular loops, such as CoCr/Ti and CoCr/C, are perpendicular to the film plane. The c -axis of the hcp CoCr films which exhibit poor perpendicular loops, such as CoCr/Cr, lies in the film plane.

The texture of the very thin CoCr films deposited on different underlayers is dominated by the structure and texture of the underlayers. The Ti underlayer which has a preferred hcp [00.1] texture encourages the hcp CoCr to grow epitaxially into a strong c -axis texture. The amorphous C is another suitable underlayer for the growth of [00.1] textural CoCr films. This may be explained by the fact that the CoCr film itself has the potential to grow into a c -axis texture because its

(0002) plane has the lowest surface energy [2], and the amorphous C underlayer provides a free-growth substrate condition for the CoCr. The CoCr films on the [100] textural bcc Cr underlayer were forced to grow into a mixed [11.0] and [10.0] texture. This is perhaps due to the bcc [100] texture being more suitable for the epitaxial growth of hcp CoCr films with c -axis lying in the film plane.

References

- [1] D.J. Mapps, M.A. Akhter and G. Pan, IEEE Trans. Magn. MAG-26 (1990) 1614.
- [2] T. Yeh, J.M. Sivertsen and J.H. Judy, IEEE Trans. Magn. MAG-26 (1990) 1590.
- [3] T. Wielingaa and J.C. Lodder, Phys. Stat. Sol. (a) 96 (1986) 255.
- [4] Ching-Ray Chang and D.R. Fredkin, IEEE Trans. Magn. MAG-23 (1987) 2052.
- [5] J. Zak, E.R. Moog, C. Liu and S.D. Bader, J. Magn. Mater. 89 (1990) 107.
- [6] J.W. Edington, Electron diffraction in the electron microscope, Philips (1975).

The Influence of Different Underlayers on the Microstructure and Magnetic Properties of Very Thin CoCr Films Deposited by RF-sputtering on Glass Computer Disks

D J Mapps, G Pan and M A Akhter

School of Electronic, Communication & Electrical Engineering,
Polytechnic South West, Plymouth, Devon, PL4 8AA, U.K.

Abstract

Very thin CoCr films deposited on different kinds of underlayers on glass disk substrates were studied in order to understand the origin of underlayer effects. Nearly rectangular perpendicular magneto-optic Kerr effect (MOKE) loops were obtained from CoCr films on Ti, Au and Al underlayers on glass substrates and CoCr films on Si substrates. TEM electron diffraction studies of Ti(300Å)/CoCr(160Å) (which exhibits a rectangular loop) and Cr(300Å)/CoCr(160Å) films (which exhibits a poorly shaped perpendicular loop) showed that the texture of the CoCr film was dominated by the texture of its underlayer. The "epitaxial-growth" model applies to these films.

Introduction

It is well known that underlayers can be used to improve the magnetic properties of high density magnetic recording media in both perpendicular or longitudinal magnetic recording[1-4]. In a previous paper[1], we reported that very thin CoCr films (less than 200 Å) on hcp Ti underlayers exhibit nearly rectangular perpendicular M-H loops. We present in this paper the magnetic properties of the very thin CoCr films deposited by rf-sputtering on different underlayers together with a detailed study of the texture of Ti/CoCr and Cr/CoCr films by TEM electron diffraction. The relation between the texture of underlayer and the texture of CoCr films is discussed.

Experimental Details

CoCr films and their underlayers were deposited on to strengthened glass disk substrates in a Nordico NM-2000 system in the same evacuation. Deposition conditions are as stated in [1]. The electron diffraction studies were undertaken in a JOEL 2000 FX TEM. For the preparation of TEM specimens, glass disk substrates were precoated with carbon films before the deposition of underlayers and CoCr films. The films were then floated off in water. The CoCr films for TEM study were 160 Å-thick and underlayers 300 Å-thick. The magnetic properties of Ti/CoCr and Cr/CoCr films for the TEM study were measured by the magneto-optic system prior to floating off the substrates

and assured to be the same as those without carbon layers. The Cr content of the CoCr films is 23 at% by Auger.

Results and Discussions

Figure 1 shows the perpendicular MOKE loops of the 80 Å-thick CoCr films on different underlayers on glass disks. Among these underlayers, 80 Å-thick CoCr films on Ti and Au exhibit very square perpendicular MOKE loops, CoCr films on Al and on Si(substrate) exhibit nearly square MOKE loops, and CoCr films on other underlayers exhibit very poorly shaped perpendicular MOKE loops. The different height of the of the y-axis of the loops is believed to be caused by the underlayer enhancement [5].

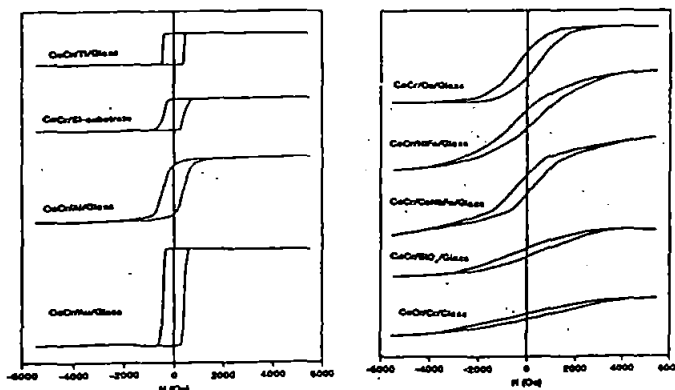


Figure 1, Perpendicular MOKE loops of 80 Å-thick CoCr films deposited on different underlayers, Y-axis is arbitrary unit, but in the same scaling.

Figure 2 and tables 1 and 2 are the TEM electron diffraction results of Ti/CoCr and Cr/CoCr films with specimen untilted and 30° tilted. As is well known in electron diffraction, only those electron beams scattered from the lattice planes parallel to the direction of incident beam form reflection rings because the Bragg angle in electron diffraction is very small (less than 1° or 2°) [6]. Considering an hcp film with a strong c-axis texture, its diffraction pattern with specimen untilted is a typical [0002] zone axis pattern, i.e., its main reflection rings are (10 $\bar{1}$ 0), (11 $\bar{2}$ 0), (20 $\bar{2}$ 0) and etc., all of which are of the form (hk \bar{i} 0). Diffraction rings of the form (000l) would not be observed for such a sample. If the specimen is tilted, the ring pattern is broken into series of arcs. Along the diameter parallel to the axis of tilt, the arcs coincide with the

original ring pattern. Along the perpendicular diameter, the original rings disappear, and new ones [for example, the (011) arcs and etc.] appear as the tilting causes the sphere of reflection to cut the planes of reciprocal lattice circles $h \cdot 0 + k \cdot 0 + i \cdot 0 + l \cdot 2 = 1, 2, 3$, etc.[7]. As shown in figure 2 (a) and table 1, the electron diffraction patterns for Ti/CoCr films with specimen untilted and tilted are precisely what a strong c-axis textural hcp film looks like. The main diffraction rings of Co hcp are (1010), (1120) and (2020) when untilted. Diffraction rings of the form (000*l*) are not seen. When tilted, the (1010), (1120) and (2020) rings are broken into arcs along the parallel diameter. The (011) arcs appear along the perpendicular diameter. This suggests that the 160 Å-thick CoCr films deposited on Ti underlayer has a very strong c-axis texture.

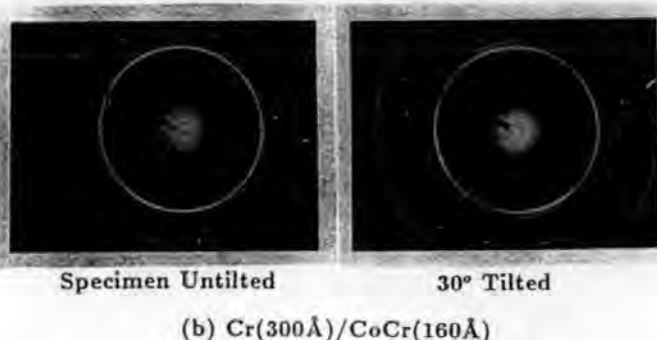
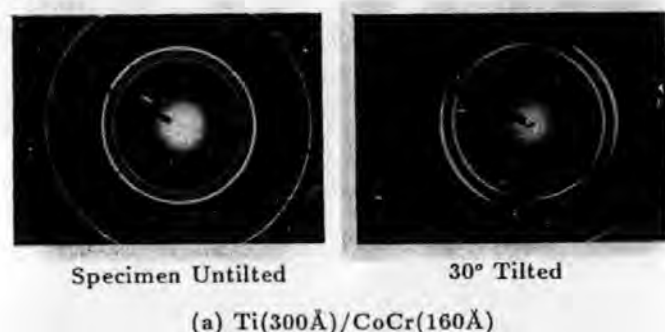


Figure 2, Electron diffraction patterns of Ti/CoCr (a), and Cr/CoCr (b) with specimen untilted and tilted.

The diffraction patterns also show the Ti underlayer has a hcp structure. Both the [0002] and [1010] zone axes reflection rings can be seen on the pattern with the specimen untilted. However, when specimen was tilted, the [0002] zone axis rings, such as (1010) and (1120), are broken into arcs along the parallel diameter. And the (011) arcs appear along the perpendicular diameter. The (0002) ring remains unchanged. This indicates that the c-axis of the hcp Ti in the underlayer has a preferred perpendicular orientation and also some spatial random orientation.

The pattern of Cr/CoCr films with specimen untilted [figure 2(b) and table 2] has two strong reflection rings of (0002) and (0111), which are from Co hcp [1010] zone axis. It also has a few weak hcp Co reflection rings from the [0002] zone axis, such as (1010) and (1120) rings. This suggests that the CoCr films on Cr do not have a strong

texture as the CoCr film on Ti does. However, the different intensity of the two zone axes reflection rings may suggest that the CoCr film has a preferred in-plane [1010] orientation. The slight arcs on the [1010] zone axis reflection rings when the specimen was tilted confirm the existence of the [1010] preferred orientation in the CoCr film.

There are two strong intensity reflection rings for the Cr underlayer in the untilted pattern, the {011} and {002} rings. These two rings could be a result of both [100] and [110] zone axis reflection. There are some other weak Cr bcc rings on the pattern. The {112} ring could result from the [110] zone axis reflection. The {022} could be the [100] zone axis reflection. This indicates that the Cr underlayer has a mixture of [100] and [110] oriented bcc crystals. On the tilted pattern, the parallel arcs on the {011}, {002} and {022} rings and the perpendicular arcs on the {112} rings suggest that the Cr underlayer has a preferred [100] orientation.

Table 1, Summary of Electron Diffraction Patterns of Ti(30nm)/CoCr(16nm) Films with Specimen Untilted and Tilted

Ring No	Diameter	Plane Spacing (Å)		Structure	hkl	Untilted	Tilted
		Measured	ASTM				
1	29.0	2.544	2.555	Ti hcp	1010	medium ring	ring/arcs//
2	31.5	2.342	2.342	Ti hcp	0002	medium ring	unchanged
3	32.9	2.242	2.243	Ti hcp	0111	very weak ring	strong arcs⊥
4	34.0	2.170	2.170	Co hcp	1010	strong ring	strong arcs//
5	38.5	1.916	1.915	Co hcp	0111	invisible	strong arcs⊥
6	42.9	1.72	1.72	Ti hcp	0112	invisible	weak arcs⊥
7	50.2	1.470	1.475	Ti hcp	1120	medium ring	medium arcs//
8	55.2	1.337	1.332	Ti hcp	0113	very weak ring	unchanged
9	58.8	1.259	1.253	Co hcp	1120	strong ring	strong arcs//
10	87.5	1.093	1.093	Co hcp	2020	very weak ring	weak ring/arcs//

Table 2, Summary of Electron Diffraction Patterns of Cr(30nm)/CoCr(16nm) Films With Specimen Untilted and Tilted

Ring No	Diameter	Plane Spacing (Å)		Structure	hkl	Untilted	Tilted
		Measured	ASTM				
1	34.0	2.170	2.170	Co hcp	1010	weak ring	unchanged
2	36.2	2.04	2.04	Cr bcc	011	strong ring	ring/arcs//
3	36.2	2.038	2.035	Co hcp	0002	strong ring	ring/arcs//
4	38.5	1.916	1.915	Co hcp	0111	strong ring	ring/arcs//
5	51.0	1.447	1.443	Cr bcc	002	strong ring	strong arcs//
6	58.8	1.259	1.253	Co hcp	1120	weak ring	unchanged
7	62.4	1.182	1.178	Cr bcc	112	weak ring	medium arcs⊥
8	83.8	1.156	1.15	Co hcp	0113	weak ring	unchanged
9	69	1.07	1.08	Co hcp	2020	very weak ring	unchanged
10	72	1.02	1.02	Cr bcc	002	weak ring	ring/arcs//

From the above results we may conclude that the texture of the very thin CoCr films deposited on Ti and Cr underlayers is dominated by the texture of underlayers because of the "epitaxial-growth" mechanism. The Ti underlayer which has the (0002) texture encourages the CoCr to grow epitaxially into a strong c-axis texture. The Cr underlayer which has a bcc (100) and (110) texture is perhaps more suitable for the CoCr film to grow into (1010) texture because of the similarity of the reciprocal lattice patterns of the bcc [100], [110] and hcp [1010]. We may also speculate that because the CoCr film itself has the potential to grow into a c-axis texture [the (0002) plane has the lowest surface energy] [3], the CoCr films on Cr underlayer still have some fraction of the (0002) texture. The fraction of (0002) texture may increase with the CoCr film thickness because of the decrease of the "epitaxial-growth effect" with the increase of film thickness[3]. On the other hand, the CoCr films on hcp Ti underlayer would not have any fraction of (1010) texture. Its (0002) textural growth potential becomes much stronger

because of the support from the (0002) texture of the Ti underlayer. As a result of this, it grows into a dominant (0002) texture.

The square perpendicular loop of the Ti/CoCr films originates from the dominant c-axis texture of the CoCr films. Because of the excellent perpendicular orientation of the hcp Co crystals in the film, the CoCr film exhibits the easy axis magnetization behaviour of hcp Co crystals in the perpendicular magnetization direction. The poorly shaped perpendicular loop of Cr/CoCr films results from the preferred in-plane orientation of the CoCr films. Because of the preferred in-plane orientation of the Co crystals, the CoCr film exhibits the hard axis magnetization behaviour of the hcp Co crystals in the perpendicular magnetization direction. However, such films may have excellent in-plane anisotropy because of its (10 $\bar{1}$ 0) texture, which is very suitable for high density longitudinal recording. It may therefore be speculated here that underlayers which have the texture with the zone axis reciprocal lattice sections similar to that of the hcp [0002] can be used for depositing (0002) textural Co based films for perpendicular magnetic recording; underlayers which have the texture with the zone axis reciprocal lattice pattern similar to that of the hcp [10 $\bar{1}$ 0] can be used for depositing (10 $\bar{1}$ 0) textural Co based films for longitudinal recording. It may also be argued that the low recording noise characteristic of Co based magnetic films deposited on Cr underlayers may be attributed in part to the improvement of film texture by Cr underlayer rather than merely due to the reduction of the inter-grain exchange coupling by the Cr underlayer[8-9]. The effect of the Co crystals' orientation on the recording performance may not be negligible.

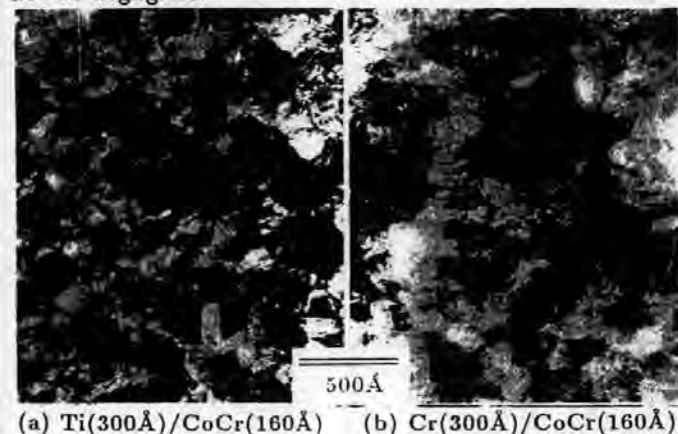


Figure 3, TEM bright field images of Ti(300Å)/CoCr(160Å) and Cr(300Å)/CoCr(160Å) films.

Figure 3 is the TEM bright field images for the above two films. The bright field image of Ti/CoCr shows very clear grains. The average grain size is about 120 Å. The clear grains may originate from the strong c-axis texture of the CoCr films. The CoCr films grown on Cr underlayers exhibit a more continuous structure. No clear grains or grain boundaries can be seen.

Conclusions

(1) Very thin CoCr films deposited on Ti, Au, Al underlayers on glass disks, or deposited on Si substrates exhibit nearly square perpendicular MOKE loops, while when deposited on Cr, Cu, NiFe, CoNbFe, SiO₂ underlayers they exhibit poorly shaped perpendicular loops.

(2) TEM microscopy study showed that the texture of the underlayer played an important role in the forming of texture of the CoCr films. The "epitaxial-growth" model applies to the Ti/CoCr and Cr/CoCr films.

(3) The square perpendicular loops of Ti/CoCr films originated from excellent c-axis texture of the CoCr films. The poor perpendicular loop of the Cr/CoCr results from its (10 $\bar{1}$ 0) texture.

(4) The TEM micrographs showed that the Ti/CoCr films have much clearer grain structures than the Cr/CoCr films.

Acknowledgement

We wish to thank Pilkington Micronics for their supply of glass disk substrates. We are also very grateful to Professor J N Chapman at University of Glasgow, Mr B Lakey at Polytechnic South West for their helpful discussions and generous technical assistance in the TEM experiment.

References

1. D J Mapps, M A Akhter and G Pan, IEEE Trans. Magn., MAG-26, No.5, 1614(1990).
2. G Pan, D J Mapps, M A Akhter, J C Lodder, P Berge, H Y Wong and J N Chapman, to be submitted to ICMFS'91 at Glasgow.
3. Y Hsu, J M Sivertsen and J H Judy, IEEE Trans. on Magn., Vol. 26, No. 5, 1599 (1990).
4. M. Futamoto, Y. Honda, H. Kakibayashi and K. Yoshida, IEEE Trans. on Magn., Vol. MAG-21, No. 5, 1426 (1985).
5. J Zak, E R Moog, C Liu and S D Bader, J. of Magnetism and Magnetic Materials, Vol. 89, 107(1990).
6. B E P Beeston, et al., "Electron Diffraction and Optical Diffraction Techniques", 1972.
7. P B Hirsch, et al., "Electron Microscopy of Thin Crystals", 1965.
8. Jian-Gang Zhu and H Neal Bertram, IEEE Trans. on Magn., Vol.26 No.5, 2141(1990).
9. Tu Chen and Tom Yamashita, IEEE Trans. on Magn., Vol.24, No.6, 2700(1988).

VERY THIN PERPENDICULAR FILMS ON GLASS DISCS

D.J. MAPPS, G. PAN and M.A. AKHTER

Centre for Research in Information Storage Technology, Polytechnic South West,
Plymouth PL4 8AA, U.K.

Abstract. This paper summarizes work carried out on thin-films of CoCr deposited on glass surfaces. The use of negative biasing during RF sputtering is reported, especially as it affects impurity gas contamination and the promotion of good microstructure. To reduce contamination from the glass, a gold or titanium underlayer is used. The effect of titanium is extensively studied. Magnetic domain measurements show that the CoCr/Ti/glass system is suitable for high-density perpendicular recording.

Introduction

The popular base material choice for hard computer discs is aluminium but as head flying heights decrease and personal computer systems include more 'laptop' type applications, alternative materials have been sought. One such material is glass which has high smoothness and flatness, is light in weight and has superior mechanical properties. The trend towards flying heights of 50 nm [1] and in-contact systems at better than 25 nm [2] means that perpendicular recording, in particular will benefit from glass substrates since it is known that the areal density capability of perpendicular recording overtakes that of longitudinal recording for flying heights below 100 nm [3]. The many advantages of glass over Al/Ni-P have been summarised in a recent paper by Matsudaira et al. [4]

The purpose of this paper is to describe experiments involving typical perpendicular recording films on glass surfaces and chemically toughened glass discs. The influence of various underlayer films is reported and explained as well as some studies of the effect of impurities which may enter the films during film growth.

Experiments with Glass Substrates

The simplest perpendicular recording system is one which has a single storage layer of

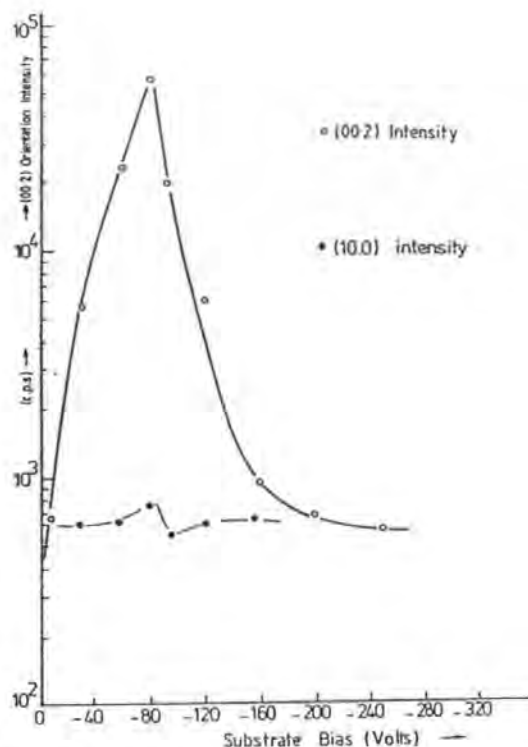


Figure 1. x-ray intensity count for CoCr film on glass as a function of negative substrate bias voltage.

perpendicular anisotropy, capable of supporting perpendicularly oriented magnetised volumes. This can be recorded with a conventional gapped recording head as

long as the coercivity is low enough so that the head fields are high enough to record, and the coercivity high enough to overcome the demagnetising effects which shear over the B-H loop and reduce the remanent magnetisation. The requirements for good perpendicular microstructure are affected by various factors in the deposition process, especially impurity atoms of oxygen and nitrogen [5]. Oxygen, silicon and calcium are present in the glass and oxygen and nitrogen available in small traces in the sputtering chamber. One method of reducing impurity atoms embedded in the film is to preferentially re-sputter these from the

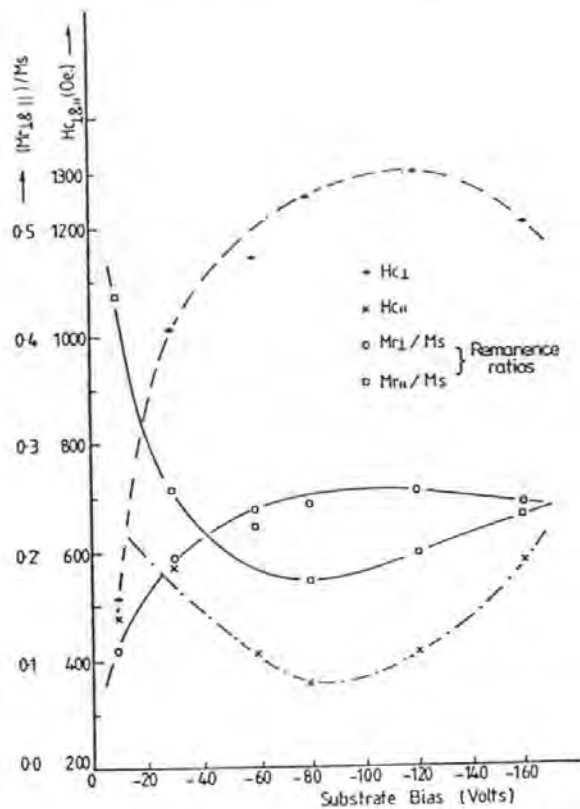


Figure 2. Perpendicular and in-plane magnetic properties for the films of figure 1.

information storage film by diverting part of the sputtering power from the target to the substrate. This creates a negative bias potential on the substrate during the film

growth process. The effect of negative bias is shown in figure 1 where the (00.2) intensity shows a peak (corresponding to good perpendicular microstructure) at a substrate potential of -100 volts. The corresponding effect on the magnetic properties, shown in figure 2, is to produce a peak in the perpendicular coercivity and squareness ratio. Other work [5] shows a correlation between oxygen and nitrogen impurity concentrations in the CoCr films and the oxygen and nitrogen partial

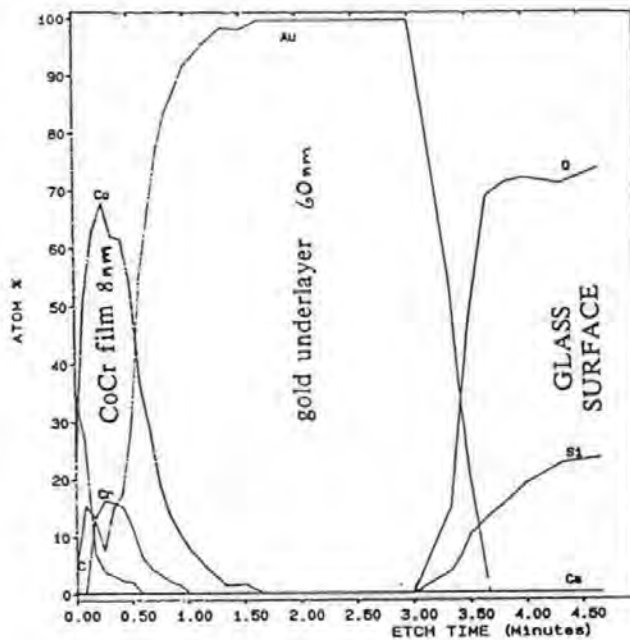


Figure 3. Auger microanalysis plots of elements in CoCr and gold films on glass surfaces.

pressures present in the chamber before sputtering commences. Therefore, for CoCr perpendicular recording, the use of RF bias sputtering is advantageous in reducing impurity gas atom concentration.

Other contaminants, however, enter the film from the glass as shown by Auger microanalysis. The glass surface is rich in oxygen which persists through the CoCr film starting at a high level, decreasing slightly and being added to by surface oxidation after the film is removed from the sputtering chamber. This suggests the need

for some kind of barrier layer to hold back oxygen at the substrate surface.

The effect of a barrier layer of pure gold is shown in figure 3. The effect of the gold is to completely remove the oxygen from the substrate, whilst providing an excellent surface for the growth of very thin (8 nm) perpendicular CoCr films with nearly square magneto-optic M-H loops as shown in figure 4. These films show remarkable squareness considering that they are very thin and magnetised in the perpendicular direction. The squareness would be excellent for perpendicular recording with no need for a high coercivity to compensate for loop shearing resulting from demagnetising fields. The high squareness suggests that the gold layer may be providing an atomic match at the interlayer causing the CoCr to adopt an h.c.p. microstructure. This was confirmed by TEM studies.

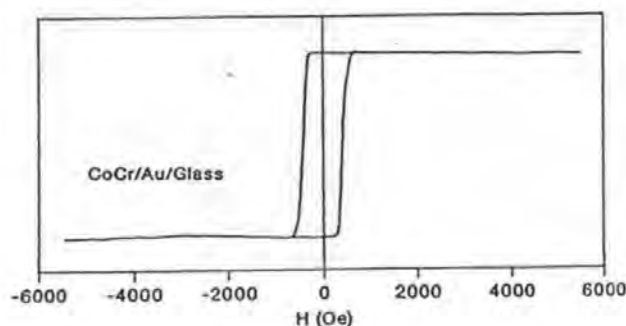


Figure 4. Perpendicular magneto-optic loop for CoCr film deposited on a gold underlayer.

Experiments with Titanium Underlayers

Titanium is known to promote good perpendicular microstructure in over-deposited CoCr films [6]. However, the effect on very thin CoCr films is to produce, surprisingly, an even squarer loop than for thick CoCr films. This is shown in the M-H loop comparison of figure 5. The phenomenon is explained if the CoCr grains are separated and grow as individual magnetic units until they merge together as the film thickens. Using the theory of Wielinga et al [7] and, Chang and Fredkin

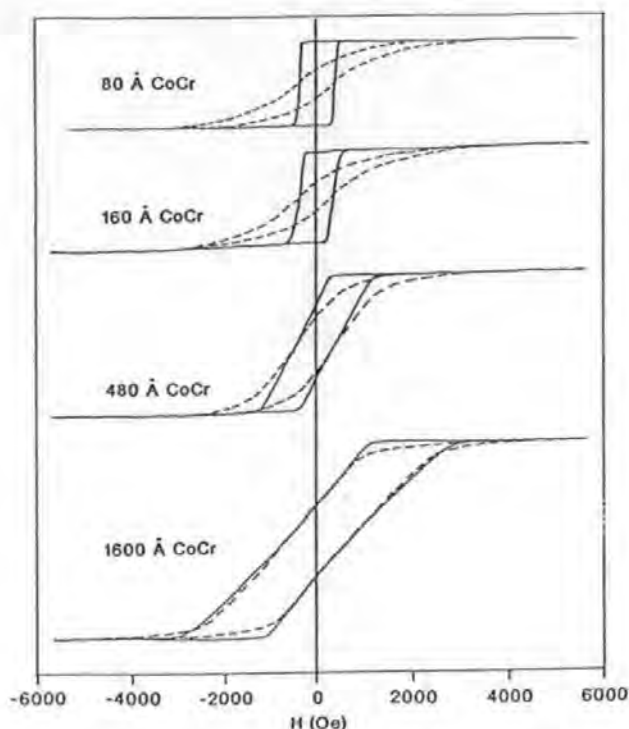


Figure 5. Perpendicular M-H loops of different thickness CoCr films with and without Ti underlayer (solid and dashed line respectively).

[8] the shearing of a perpendicular loop can be indicated by the rate of change of the magnetisation with field dM/dH . The general equation for this is,

$$\left(\frac{dM}{dH}\right)^{-1} = \frac{D}{D+a} \left\{ 1 - \left\{ N_z (D+2a) \right\} + \left[N_z (3D+4a) - N_z (3D+2a) \right] + \dots \right\}$$

where D is a thickness-dependent grain diameter, a is a non-magnetic gap between grains and N_z the grain demagnetising factor in the perpendicular direction which is a function of D and a .

Using the theory above a series of calculations were made for values of a of between 0 and 5 nm for various thicknesses. These are plotted as dotted lines in figure 6. Also plotted on figure 6

are three experimental curves. The lower curve is for a CoCr film on glass only with no underlayer and no RF bias during deposition. There is no evidence in this case of CoCr segregation. The middle curve shows some segregation caused by the use of titanium but the squareness is not perfect until the impurity gas atoms have been removed (by bias-sputtering) and segregation well defined (upper curve). Under these conditions there is a good fit with the theoretical data with a non-magnetic gap spacing of about 5 nm between CoCr columns. The Auger results for CoCr films on Ti underlayers, show that the Ti does reduce contamination from the glass surface but not as much as by using gold (see figure 3). The combination of Ti and bias-sputtering is able to produce good films as long as the Ti is at least 20 nm thick in our experiments.

The mechanism by which CoCr h.c.p. grows on Ti was investigated using transmission electron microscope techniques. The results

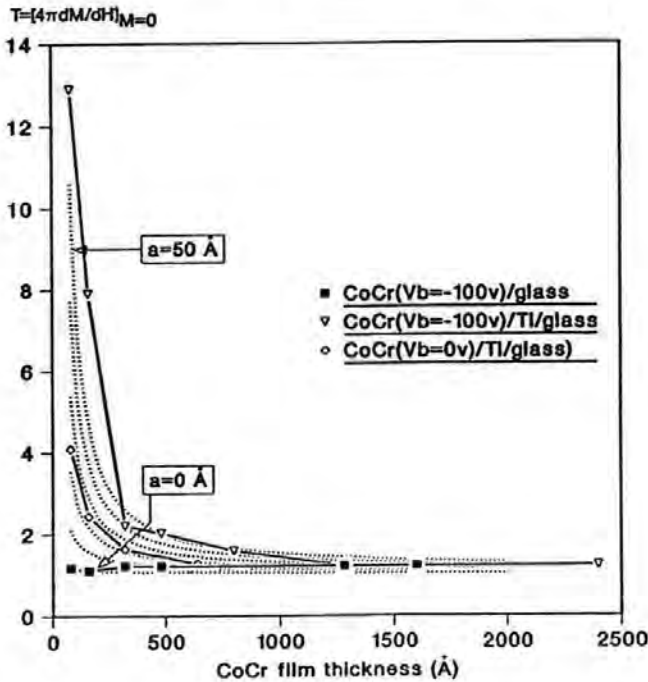


Figure 6. Hysteresis loop slope T of CoCr films as a function of film thickness. Dotted lines are calculated results by particulate model for $a = 0$ to 50 \AA .

show that the c -axis of the Ti underlayer is strongly perpendicular and this provides atomic matching for the upper CoCr layer. The CoCr therefore grows with a good hexagonal microstructure within the first few atoms and this explains why the very thin, CoCr films have such a good square loop compared with the thicker films whose demagnetising factors are increased when the columns eventually grow together.

Magnetic Domain Structure

The stable magnetic domain structure which the CoCr films support is a measure of the eventual information bit density on the computer disc. This was studied using Lorentz Microscopy and the results are shown in figure 7. Figure 7(a) is a perpendicular Fresnel image with low domain contrast. The low contrast is expected if the domains are

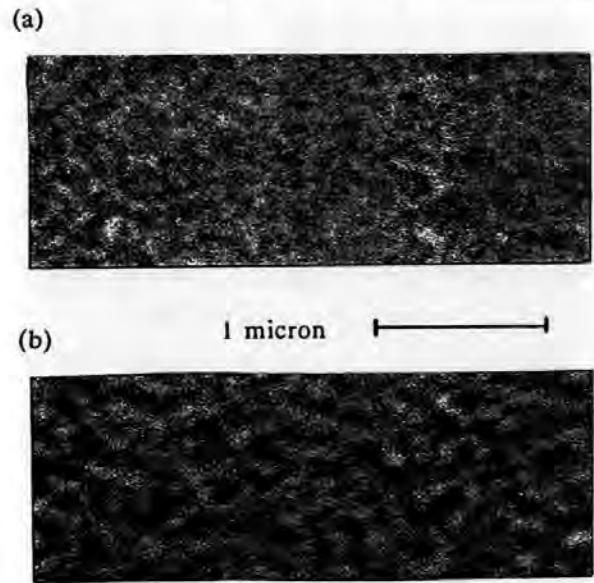


Figure 7. Fresnel images of magnetic domains in CoCr for the case of (a) normal incidence and (b) 20° tilted.

perpendicularly magnetised. To improve domain contrast the specimen is tilted at an angle of 20° in figure 7(b). Measurements from figure 7(b) show a maximum domain spacing of 80 nm ($>300,000$ domains/inch). This confirms that the CoCr

film is suitable for high-density magnetic recording.

Conclusions

Measurements of CoCr thin films on glass disc surfaces show that exceptionally good microstructure can be produced in very thin films deposited on gold and titanium underlayers. The best microstructure is produced with RF bias sputtering combined with a suitable underlayer. Domain studies confirm that these films are suitable for high-density magnetic recording.

References

- [1] C. Tsang, American Journal of Applied Physics, "Design and performance considerations in high areal density longitudinal recording." Vol 69, 8, April 1991.
- [2] H. Hamilton et.al. Proceedings of 1991 Intermag/MMM Conference. "Contact perpendicular recording on rigid media." Paper No EA01, p122. June 1991.
- [3] D.J. Mapps et.al. O.S.T.E.M. report, Magnetic Recording Technology. BNF6.106.0/3 p28. May 1988.
- [4] T. Matsudaira et.al. Proceedings of the International Convention on Glass for Magnetic Recording" - TC20, (Glass optoelectronics), Tokyo, December 1989.
- [5] D.J. Mapps et.al. I.E.E.E. Transactions on Magnetics. "The influence of nitrogen and other gases on the magnetic properties of bias-sputtered CoCr perpendicular films for computer memory applications." Vol. Mag-23, No.5, pp 2473-2475, Sept 1987.
- [6] Y. Sakamoto et.al. I.E.E.E. Trans.Mag. "A magnetic and microstructural study on high-rate evaporated CoCr Films with Ti underlayer." Mag-23 No.5, pp 3654-3656, Sept 1987.
- [7] T. Wielinga et.al. I.E.E.E. Trans.Mag. Mag-18, 1107, 1982.
- [8] C. Chang et.al. I.E.E.E. Trans Mag. "The shearing of perpendicular loop with columnar microstructure." Mag-22, pp 2052-2054, Sept 1987.

Acknowledgements

Thanks is extended to Pilkington Micronics (U.K.) for the supply of glass discs, the Science and Engineering Research Council and Pilkington Group Research for financial support, Mr. B. Lakey and Prof. J.N. Chapman for help with the electron microscopy measurements.

VERY THIN CoCr FILMS ON TITANIUM UNDERLAYERS FOR HIGH-DENSITY PERPENDICULAR RECORDING COMPUTER DISCS

D.J. Mapps, M.A. Akhter and G. Pan
Department of Electrical & Electronic Engineering,
Polytechnic South West, Plymouth, Devon, PL4 8AA, U.K.

Abstract

Very thin CoCr films with and without Ti underlayer were deposited on strengthened glass disc substrates by bias RF-sputtering. Perpendicular M-H loops were successfully measured by polar Kerr M-O loop plotter. Very pronounced effects of Ti underlayer and bias on the shearing of the loop and the perpendicular remanence ratio were observed. X-ray diffraction results show excellent (002) orientation of CoCr films with Ti underlayer. Experimental results are discussed in the light of particulate model and stripe domain model.

Introduction

There is a trend towards the use of thinner films of CoCr for high-density perpendicular magnetic recording. In addition, there is a strong current interest in the effect of underlayers such as germanium and titanium [1 - 6] as microstructure "growth promoters". It was believed that the initial nucleation stage of the hcp CoCr crystallites, which is directly influenced by the substrate conditions, is very important for the growth of highly c-axis oriented CoCr films[1]. However, no investigation has been made so far into the very small thickness region of such films.

In this paper, very thin CoCr films (below 100 Å) with and without Ti underlayer are studied. Very pronounced improvements in magnetic properties by the existence of Ti underlayer under our optimum bias sputtering conditions[7] are reported.

Experimental details

Ti and CoCr films were deposited by RF-sputtering on to a strengthened glass disc substrate in a Nordico NM-2000 system in the same evacuation. The chamber was evacuated to a base pressure below 2×10^{-7} Torr by a diffusion pump system equipped with a liquid-nitrogen trap. The experiments were undertaken in a class 1000 clean room. The surface roughness Ra of the substrate was less than 30 Å. Substrates were cleaned by Decon solution in an ultrasonic bath, placed on a water-cooled substrate holder and then cleaned further by sputter etching just before sputtering. The CoCr target was an 8" diameter high purity Co disc on which 1 cm Cr pieces were uniformly arranged. Argon pressure during sputtering is 3 mTorr for CoCr, 4 mTorr for Ti respectively. Sputtering power was 600 W and deposition rate 160 Å/min for CoCr and 60 Å/min for Ti respectively.

The film composition was analysed by SAM (Scanning Auger Microprobe) depth profiling. The c-axis orientation of CoCr films was estimated by X-ray diffraction using Cu-K α radiation (40 kv 30 mA). Magnetic properties were measured by polar Kerr M-O loop plotter, vibrating sample magnetometer and torque magnetometer. Film thickness was measured by Talystep.

Results

CoCr films of different thickness (varied from 80 to 3000 Å) were deposited on 600 Å-thick Ti underlayers or directly on glass substrates. The Cr content of the CoCr films is 23 at% by Auger. Saturation magnetization is 200 emu/cc by VSM, neither affected by Ti underlayers nor film thickness.

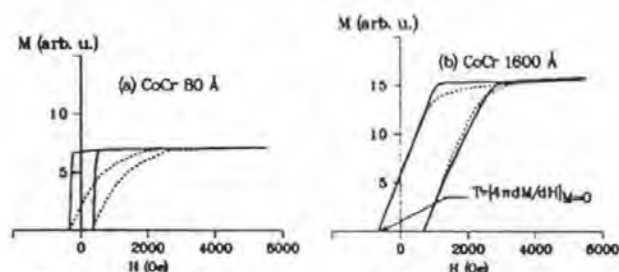


Figure 1, Perpendicular M-H loops of different thickness CoCr films with and without Ti underlayer (solid and dashed line respectively).

Figure 1 shows the typical perpendicular hysteresis loops of 80 Å-thick and 1600 Å-thick CoCr films with Ti underlayers (solid line) and without Ti underlayers (dashed line) measured by polar Kerr M-O system. The height of the perpendicular loops of 80 Å-thick CoCr films is only about half of that of 1600 Å-thick films. This probably is due to the skin depth effect on such small thickness films (the skin depth of HeNe laser is 150 Å[11]). As shown in figure 1(a), an 80 Å-thick CoCr film deposited directly on glass substrate exhibits a very poor perpendicular loop. While the same thickness CoCr film deposited on Ti underlayer exhibits a nearly square perpendicular hysteresis loop. The shearing of the loop is very small and the perpendicular remanence ratio is near unity. Such a nearly square loop was also observed in our 160 Å-thick CoCr films on Ti underlayer. For 1600 Å-thick CoCr films (figure 1(b)), the principal difference of their perpendicular loops is only in the "shoulder"

of the loop. CoCr film with Ti underlayer exhibits a bigger "shoulder" in its perpendicular loop. We plotted the slope $T (=4\pi dM/dH)$ of the perpendicular loops at $M=0$ (which indicates the shearing of the loops[8]), the perpendicular remanence ratio and coercivity versus CoCr film thickness in figure 2 and figure 3. It can be seen from figure 2 and figure 3 that the Ti underlayer effects on the magnetic properties become very pronounced in the thinner film region. The slope T of the perpendicular loop of an 80 Å-thick CoCr film with Ti underlayer is about 13 and perpendicular remanence ratio 0.9, while for the same thickness CoCr film without Ti underlayer, only about 1.2 and 0.28. However, the perpendicular coercivity appeared to be not affected by the Ti underlayer and it is only a function of CoCr film thickness.

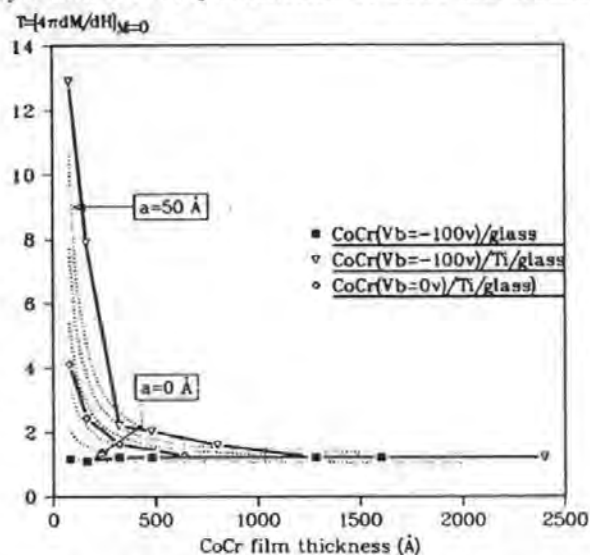


Figure 2, Hysteresis loop slope T of CoCr films as a function of film thickness, dotted lines are calculated results by particulate model for $a=0$, to 50 Å.

The substrate bias effect on the slope T and remanence ratio of CoCr films at small thickness is also shown in figures 2 and 3. The shearing of the loop of CoCr films made without bias is bigger (T smaller) than that deposited with bias and the perpendicular remanence ratio smaller. The nearly square loops can only be obtained from samples made under optimum bias conditions.

The X-ray diffraction patterns showed that the CoCr films have an hcp structure and the main reflection peak is (002) and the Ti underlayer has an hcp structure with a main reflection peak of (010). The (002) reflection peak intensity of different thickness CoCr films with and without Ti underlayer is shown in table 1, from which we can see that the (002) peak intensity of any thickness CoCr films deposited on Ti underlayer is much higher than that without Ti underlayer. This means CoCr films deposited on Ti underlayer have excellent c -axis orientation. The excellent perpendicular loops of very small thickness CoCr films could be attributed to this excellent (002) orientation. For thick CoCr films the better c -axis

orientation results in a bigger shoulder in the perpendicular loop.

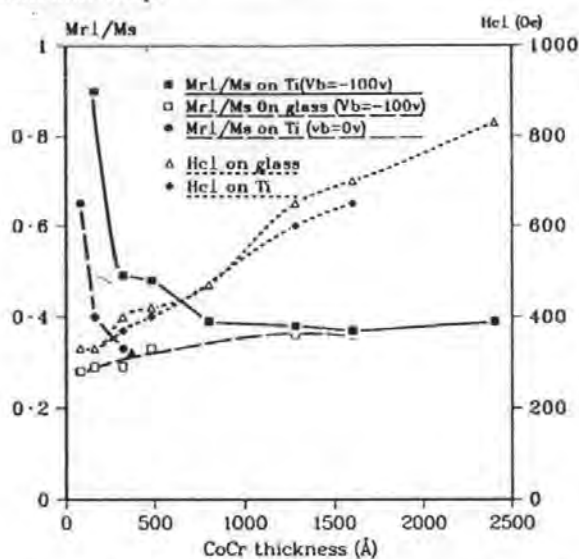


Figure 3, Perpendicular remanence ratio and coercivity as a function of CoCr film thickness.

Table 1, (002) reflection peak intensity of CoCr films with and without Ti underlayer.

Film thickness	160 Å	640 Å	960 Å	1280 Å	1920 Å
$I(002)$ c.p.s. CoCr/Ti/glass	614	1,548	4,474	4,670	11,710
$I(002)$ c.p.s. CoCr/glass	162	934	1,778	1,946	3,824

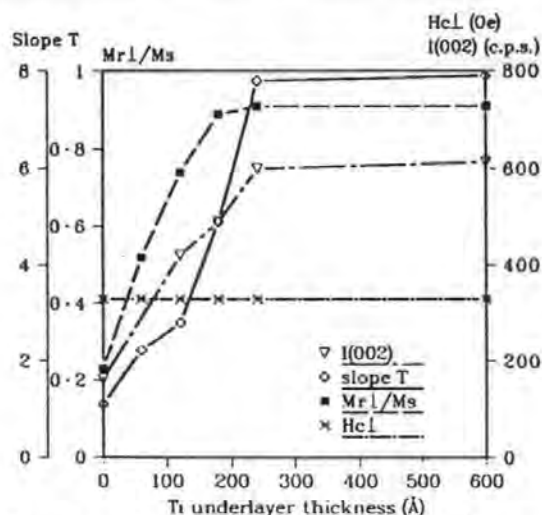


Figure 4, Effects of Ti underlayer thickness on perpendicular magnetic properties and (002) intensity of 160 Å-thick CoCr films.

The Ti underlayer thickness effects on the magnetic properties of very small thickness CoCr films (160 Å) are shown in figure 4. The perpendicular remanence ratio and the slope T can be in some degree improved by the existence of even a very thin Ti underlayer. This improvement is again related to the improvement of the (002) orientation of the CoCr films, reaching the maximum at the Ti thickness of about 250 Å.

CoCr films deposited on 250 or 600 Å-thick Ti underlayers exhibit little difference in their perpendicular loops. Therefore, a 250 Å-thick Ti underlayer is sufficient to provide a good substrate condition for the growth of highly (002) oriented CoCr films. It can also be seen from figure 4 that the coercivity of a 160 Å-thick CoCr film is about 330 Oe and not affected by the Ti underlayer thickness.

Discussion and conclusions

A very thin CoCr film deposited on Ti underlayer exhibited a nearly square perpendicular loop. These excellent perpendicular magnetic properties originated from the improvement of the (002) orientation of the hcp CoCr crystallites by the existence of the hcp structure Ti underlayer. It has been reported by several authors that the (002) oriented hcp structure Ti and Ti-M alloy underlayer or amorphous-like Ge underlayer [1,6] could greatly improve the c-axis orientation of CoCr films. An epitaxial growth model had been proposed for this. However, the Ti underlayer made in this study, which has a strong effect on the structure of CoCr films, was not (002) oriented, its main reflection peak of X-ray diffraction pattern was (010). A similar result has been reported by D. Jeannot et al [4]. It seems that the high (002) orientation of the underlayer is not essential for the growth of highly (002) oriented CoCr films. More detailed studies are necessary to clarify the growth mechanism of CoCr film on underlayers.

Wielinga et al have reported that the slope T of the perpendicular loops of CoCr films was a strong function of film thickness [8]. The maximum T for their 250 Å-thick CoCr films was about 2. A stripe domain model by Wielinga and Lodder [8,9] and most recently, a particulate model by Chang and Fredkin [10] have been proposed, both of which could explain Wielinga's results successfully. It is worth noticing that the slope T of very thin CoCr films in this study is not only a function of CoCr film thickness, but also a function of the c-axis orientation of the films which was affected by underlayer and substrate bias. For comparison, we calculated the slope T by the particulate model. The slope T was given by equation (1),

$$T^{-1} = \frac{D}{D+a} \{1.0 - \{Nz(D+2a) + [Nz(3D+4a) - Nz(3D+2a)] + \dots\} \} \quad (1)$$

where, the demagnetization factor $Nz(x)$ (here $x=D+2a, 3D+2a, 3D+4a, \dots$) was calculated from equations (3) and (4) of reference [10]. The crystal diameter D of the CoCr films was taken from Wielinga's experimental data. The non-magnetic gap "a" took values of 0, 10, 20, 30, 40, and 50 Å respectively. The calculated results were plotted in figure 2 (dotted line). As shown in figure 2, the tendency of slope T towards film thickness coincides with the calculated results of different nonmagnetic gap distance. This might be interpreted as that CoCr films deposited

on glass substrate is not a columnar structure because of the lack of c-axis orientation and therefore the non-magnetic gap between particles is zero. Their slope T coincides with that of $a=0$. While CoCr films deposited on Ti underlayer exhibit good columnar structure because of the excellent c-axis orientation of the hcp crystallites and therefore the non-magnetic gap may exist between the columns. This non-magnetic gap reduces the shape anisotropy and consequently reduces the shearing of the perpendicular loops in the very small thickness region. The fact that the coercivity of the very thin CoCr films is independent of the c-axis orientation of the films also supports the particulate model which concluded that the interaction field shears the perpendicular loop, but does not affect the coercivity [10]. More structure evidence is needed to confirm this.

We conclude: A CoCr film thinner than 200 Å, deposited on Ti underlayer under optimum bias sputtering conditions exhibits a nearly square perpendicular loop. These excellent perpendicular magnetic properties originate from the improvement of the (002) orientation by the Ti underlayer. The Ti underlayer effect on the magnetic properties becomes very pronounced in the very small thickness region. A particulate model could be used to explain the shearing of the perpendicular loop.

Acknowledgements

We gratefully acknowledge Dr K. O'Grady for VSM measurement, Dr J.M. Bradshaw for Auger analysis and Dr M. Boles for X-ray diffraction analysis.

References

1. M. Futamoto, Y. Honda, H. Kakibayashi and K. Yoshida, IEEE Trans. Magn., MAG-21, 1426 (1985).
2. T. Tanaka and H. Masuya, Jap. J. Appl. Phys., 26(6) 897 (1987).
3. O. Kitakami, Y. Ogawa, H. Fujiwara, F. Kugiya and M. Suzuki, IEEE Trans. Magn., MAG-25 2607 (1989).
4. D. Jeannot and J. Bouchand, IEEE Trans. Magn., MAG-24, 2356 (1988).
5. C.P.G. Schrauwen and J.P.C. Bernardis, IEEE Trans. Magn., MAG-24, 1901 (1988).
6. Y. Matsuda, Y. Shiroishi, T. Shimotsu and K. Takagi, J. magn. soci. Japan, Vol. 13, Supplement S1, 391 (1989).
7. D.J. Mapps, N. Mahvan and M.A. Akhter, IEEE Trans. Magn., MAG-23, 2473 (1987).
8. T. Wielinga, J.C. Lodder and J. Worst, IEEE Trans. Magn., MAG-18, 1107 (1982).
9. T. Wielinga and J.C. Lodder, Phys. Stat. Sol.(a)96, 255 (1986).
10. Ching-Ray Chang and D.R. Fredkin, IEEE Trans. Magn., MAG-23, 2052 (1987).
11. K. Hemmes, et. al., J. Appl. Phys. 19, 1311 (1986).

CoNbFe soft magnetic thin-film backlayers for glass computer disks

D. J. Mapps, M. A. Akhter, and G. Pan

School of Electronic, Communication and Electrical Engineering, Polytechnic South West, Drake Circus, Plymouth, Devon PL4 8AA, United Kingdom

$\text{Co}_{84}\text{Nb}_{12}\text{Fe}_4$ films with very low coercivity down to 1 A/m, anisotropy field 1100 A/m, and saturation magnetic induction 1.1 T have been deposited by rf sputtering onto chemically strengthened glass disk substrates as a backlayer for perpendicular recording Winchester disks. Values of coercivity and anisotropy field were studied over a thickness range from 30 to 15 000 Å and found to be a strong function of film thickness. Comparisons between Néel's prediction for wall motion coercivity mechanism and the experimental data were made. The experimental coercivity fits the Néel formula when films are thicker than 400 Å. The dependence of coercivity and anisotropy field on deposition conditions was also characterized. The thermal stability of the films was studied by differential scanning calorimetry (DSC) and by thermal annealing up to 500 °C. The crystallization temperature of the CoNbFe films is about 450 °C determined from DSC analysis. Thermal annealing revealed that the magnetic properties were very stable when the annealing temperature was below 400 °C.

I. INTRODUCTION

Various soft magnetic thin films have been used as a "soft" backlayer in perpendicular magnetic recording systems.^{1,2} These films are required to have excellent soft magnetic properties such as high saturation magnetization, small coercivity, and high permeability. It has been reported by different authors^{3,4} that CoNbFe amorphous films exhibit much better properties than Permalloy and other soft magnetic films, such as zero magnetostriction, very small coercivity, very high saturation magnetization and permeability, good corrosion resistance, and high resistivity. In this paper we report some of the magnetic properties of $\text{Co}_{84}\text{Nb}_{12}\text{Fe}_4$ amorphous films deposited by rf sputtering on a toughened glass disk substrate as a "soft" backlayer of perpendicular recording Winchester disks.

II. EXPERIMENTAL DETAILS

CoNbFe films were prepared by a rf-sputtering system located in a class 1000 clean room. Two types of substrates (chemically strengthened glass disk substrates with average surface roughness R_a of 50 Å and microscope glass slides) were used for film depositions. The CoNbFe target was an 8-in.-diam high-purity Co disk on which $1 \times 1\text{-cm}^2$ Nb pieces and $0.5 \times 0.5\text{-cm}^2$ Fe pieces were uniformly arranged to give the desired composition. The chamber was evacuated to a base pressure below 2×10^{-7} Torr by a diffusion pump system equipped with a liquid-nitrogen trap. Argon pressure during sputtering was 3 mTorr. Target-to-substrate distance was 7 cm. No external magnetic field was applied during film deposition. The substrate temperature during sputtering was measured by a thermocouple fixed on a glass substrate surface.

The film composition was determined by EDAX on a scanning electron microscope (SEM) and film thickness by Talystep. The film structure was analyzed by x-ray diffraction using $\text{CuK}\alpha$ radiation (40 kV, 30 mA) and by electron diffraction on TEM. Magnetic properties were measured by transverse Kerr magneto-optic M - H loop

plotter and inductive B - H loop plotter. The crystallization temperature was determined by differential scanning calorimetry (DSC) using a Dupont Model 910 DSC.

III. RESULTS AND DISCUSSIONS

A. Magnetic properties

The as-deposited $\text{Co}_{86}\text{Nb}_{12}\text{Fe}_4$ films exhibit a uniaxial anisotropy. The saturation magnetic induction is about 1.1 T. Both the electron diffraction and the x-ray-diffraction analysis showed that the film structure was amorphous. A very thin Ti adhesion layer could be used to improve the adhesion between the CoNbFe film and the glass disk substrate. No effect of this adhesion layer on the magnetic properties was observed.

Figure 1 shows the dependence of coercivity H_c on the thickness of CoNbFe films deposited on strengthened glass disk substrates ($R_a = 50$ Å) and on microscope slide substrates without Ti adhesion layer in the thickness range of 30–13 800 Å. The coercivity was measured by a transverse Kerr magneto-optic system for the thinner films (from 30 to 5000 Å) and by inductive B - H loop plotter for thicker films (from 400 to 13 800 Å). No significant difference between these two measurements was observed, as can be seen from Fig. 1. The coercivity is also independent of the surface roughness on these two substrates, but a strong function of the film thickness. The value of H_c changes from 1100 A/m for 30-Å-thick films to 1.0 A/m for 13 800-Å-thick films. We also plotted (Fig. 1) the thickness dependence of H_c of CoZr films⁵ and Néel's theoretical predictions⁶ for wall motion coercivity mechanism ($H_c \propto t^{-4/3}$). The thickness dependence of coercivity could be divided into three regions throughout the thickness range shown in Fig. 1. The first region is from 15 000 to 400 Å, where the experimental coercivity of both CoNbFe and CoZr films approximately follows the Néel formula. The dominant coercivity mechanism for this region could, therefore, be assumed to be the wall motion coercivity mechanism as predicted by Néel.^{5,6} The second

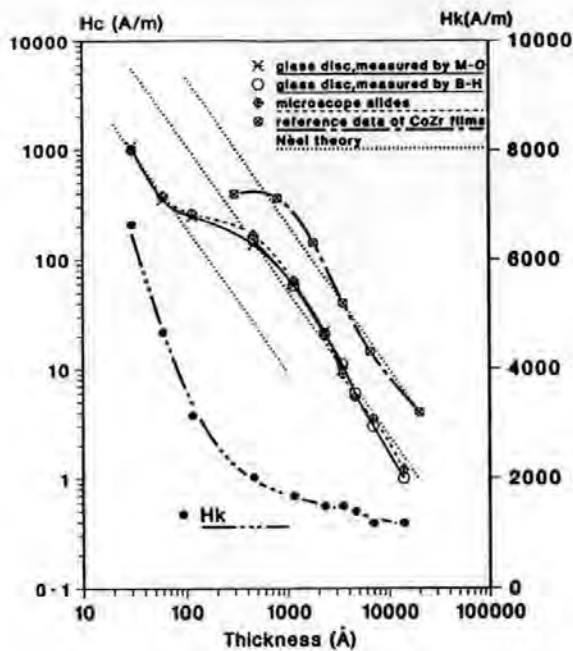


FIG. 1. Thickness dependence of coercivity H_c and anisotropy field H_k of $\text{Co}_{84}\text{Nb}_{12}\text{Fe}_4$ films.

region is from 400 to 100 Å, where the experimental coercivity of both CoNbFe and CoZr films shifts from the $t^{-4/3}$ law, showing less thickness dependence. Jagielinski⁵ attributed the deviation from the Néel formula to the existence of a Néel wall rather than a Bloch wall in this region because for Néel walls, the coercivity was found to be thickness independent⁷ and the Néel wall might be expected to occur in this thickness range according to the wall energy theory.⁶ The third region is when films are thinner than 100 Å, where the coercivity of the CoNbFe films increases sharply as film thickness decreases, approximately fitting the $t^{-4/3}$ law again. However, it might not be reasonable to assume the coercivity mechanism to be Néel's wall motion mechanism for this region because Bloch walls might not exist in these extremely thin films due to the very high wall energy. The interface effect on the magnetic domains might be mostly responsible for the sharp increase of coercivity in this region. Further studies are needed to understand this.

The coercivity of CoNbFe films is always smaller than that of CoZr films in the whole thickness range, as shown in Fig. 1. This could be attributed to the nearly zero saturation magnetostriction of the $\text{Co}_{84}\text{Nb}_{12}\text{Fe}_4$ films due to the addition of the small amount of Fe.³

The thickness dependence of the anisotropy field H_k is also shown in Fig. 1. The value of H_k changes from 6600 A/m for 30-Å-thick films to 1100 A/m for about 10 000-Å-thick films. The dependence of H_k on film thickness of thinner films is much stronger than that of thick films. No significant effect of the two different substrates on H_k was observed in this study.

Figure 2 shows the substrate bias effects on H_c and H_k of 4600-Å-thick as-deposited films. The coercivity of the as-deposited films does not appear to be affected by

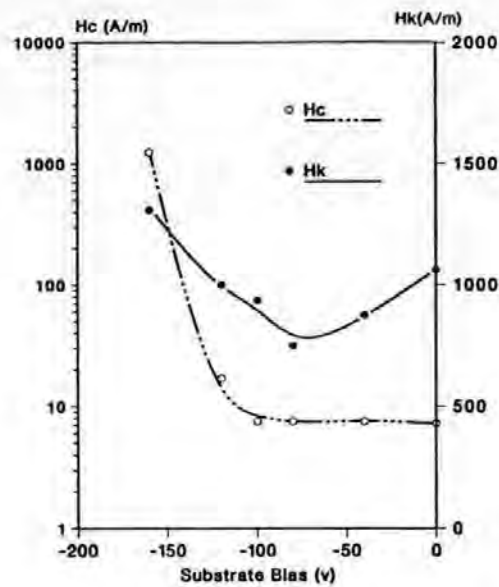


FIG. 2. Substrate bias effects on H_c and H_k of 4600-Å-thick $\text{Co}_{84}\text{Nb}_{12}\text{Fe}_4$ films.

substrate bias when the substrate bias is between 0 and -100 V. The anisotropy field H_k shows a slight decrease as substrate bias increases from 0 to -80 V. A further increase of substrate bias from -100 V results in a sharp increase of the coercivity (1200 A/m for $V_b = -160$ V) and a slight increase of H_k .

Figure 3 shows the sputtering power dependence of H_c and H_k of 8500-Å-thick CoNbFe films. These films were made under different sputtering power, but the same thickness by controlling the deposition time. The deposition rate and the final substrate temperature under different sputtering power is also shown in Fig. 3. As can be seen, when sputtering power increases, both the deposition rate and substrate temperature increase. However, the magnetic properties are insensitive to these changes.

B. Thermal stability

The thermal stability was studied by differential scanning calorimetry (DSC) and by thermal annealing. Samples for DSC measurements were 30 000-Å-thick CoNbFe films peeled off from a glass disk substrate, about 10 mg weight for each run. Figure 4 is the DSC curves of the CoNbFe films measured at two different heating rates, i.e., at 5 and 10 °C/min. Two main exothermic peaks in each curve were observed, 470 and 557 °C for the run at 5 °C/min, and 482 and 570 °C for the run at 10 °C/min. The first peak was resulted from the crystallization of the film from amorphous to crystalline state. The second peak may be due to the phase change from one crystalline state to another. The different peak temperature values at different heating rate reflect some information on the kinetics of the crystallization process. The thermal annealing was undertaken by heating samples in an oven with an air atmosphere from room temperature to 300, 400, 450, and 500 °C and holding on each temperature for 30 min respectively. The samples for thermal annealing were 10 000-Å-thick

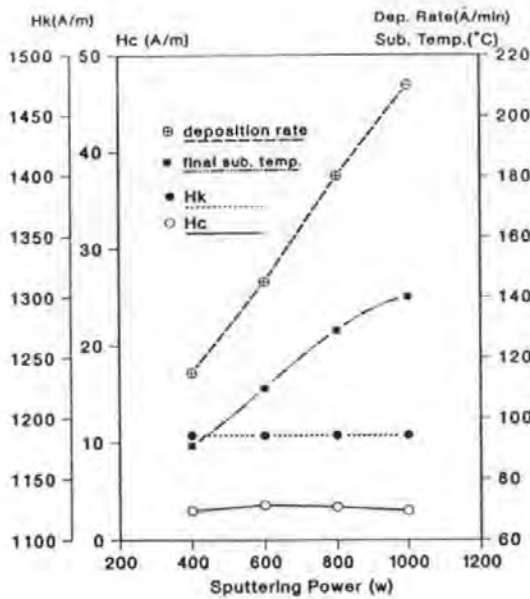


FIG. 3. Sputtering power dependence of H_c and H_k of 8500-Å-thick $\text{Co}_{84}\text{Nb}_{12}\text{Fe}_4$ films and the deposition rate and final substrate temperature.

CoNbFe films deposited on a glass disk substrate and coated with an 800-Å-thick SiO_2 top layer to prevent the film from oxidation during annealing. The coercivity H_c and anisotropy field H_k were measured after annealing and results are shown in Fig. 5. From Fig. 5 we can see that the magnetic properties of the films are quite stable when the annealing temperature is below 400 °C. A slight decrease of H_k after annealing could be attributed to the stress release by the thermal annealing process. When the annealing temperature increases to 450 °C or over, both the H_c and H_k increase sharply. These results agree very well with the

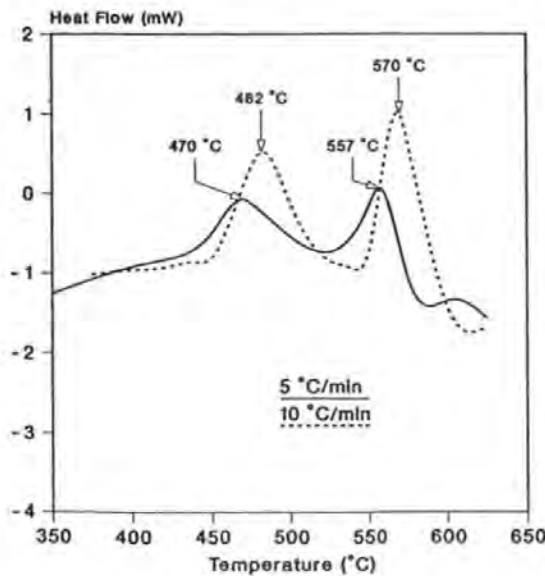


FIG. 4. Differential scanning calorimetry curves of $\text{Co}_{84}\text{Nb}_{12}\text{Fe}_4$ films at a heating rate of 5 and 10 °C/min, respectively.

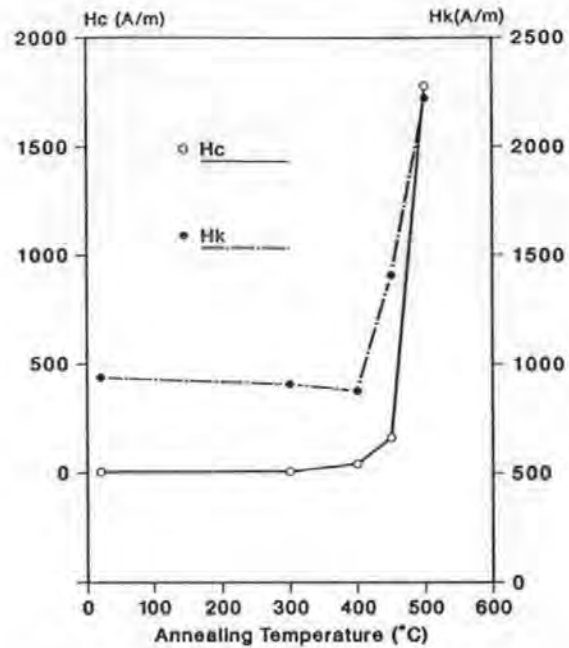


FIG. 5. Annealing temperature dependence of H_c and H_k of $\text{Co}_{84}\text{Nb}_{12}\text{Fe}_4$ films.

DSC results, both of which suggest that crystallization process occurs in the CoNbFe films when temperature is above 450 °C.

IV. SUMMARY

$\text{Co}_{84}\text{Nb}_{12}\text{Fe}_4$ amorphous films were deposited by rf sputtering onto chemically strengthened glass disk substrates as a backlayer for perpendicular magnetic recording computer disks. Very low coercivity down to 1 A/m was achieved for films 10 000 Å thick with a uniaxial anisotropy field of 1100 A/m and saturation magnetic induction of 1.1 T. The coercivity and anisotropy field were studied over a thickness range from 30 to 15 000 Å and found to be a strong function of film thickness. The thickness dependence of coercivity follows the Néel formula ($H_c \propto t^{-4/3}$) when films are thicker than 400 Å. A low substrate bias during sputtering has no effect on coercivity and reduces H_k slightly. A high substrate bias (above -120 V) is detrimental to the soft magnetic properties of the films. The crystallization temperature of the amorphous films is about 450 °C. The thermal stability of the film is very good from room temperature to 400 °C.

¹K. Ouchi and S. Iwasaki, *J. Appl. Phys.* **57**, 4013 (1985).

²M. Takahashi, H. Uwazumi, T. Miyazuki, T. Sato, M. Takahashi, and T. Wakiyama, *J. Magn. Soc. Jpn.* **13**, 743 (1989).

³H. Sakakima, *IEEE Trans. Magn.* **MAG-19**, 131 (1983).

⁴G. Pan, A. G. Spencer, and R. P. Howson (unpublished).

⁵T. Jagielinski, *J. Appl. Phys.* **61**, 3237 (1987).

⁶M. Prutton, *Thin Ferromagnetic Films* (Butterworths, London, 1962).

⁷R. F. Soohoo, *Magnetic Thin Films* (Harper & Row, New York, 1965).